A Positive Ion Beamline for Space Qualification of Birefringent Materials

A Thesis Submitted to the
College of Graduate and Postdoctoral Studies
in Partial Fulfilment of the Requirements
for the Degree of Doctor of Philosophy
in the Department of Physics and Engineering Physics
University of Saskatchewan
Saskatoon

By

Barrett J. A. Taylor

Permission to Use

In presenting this thesis in partial fulfilment of the requirements for a Postgraduate degree from the University of Saskatchewan, I agree that the Libraries of this University may make it freely available for inspection. I further agree that permission for copying of this thesis in any manner, in whole or in part, for scholarly purposes may be granted by the professor or professors who supervised my thesis work or, in their absence, by the Head of the Department or the Dean of the College in which my thesis work was done. It is understood that any copying or publication or use of this thesis or parts thereof for financial gain shall not be allowed without my written permission. It is also understood that due recognition shall be given to me and to the University of Saskatchewan in any scholarly use which may be made of any material in my thesis.

Requests for permission to copy or to make other use of material in this thesis in whole or part should be addressed to:

Head of the Department of Physics and Engineering Physics
116 Science Place
University of Saskatchewan
Saskatoon, Saskatchewan S7N 5E2 Canada

OR

Dean
College of Graduate and Postdoctoral Studies
University of Saskatchewan
116 Thorvaldson Building, 110 Science Place
Saskatoon, Saskatchewan S7N 5C9 Canada

Abstract

The constant advancements in spaceborne technology have provided an immense increase to the boundaries of human knowledge in a variety of research fields. As these continue, and new technologies arise, their suitability for deployment in the space environment must be assessed due to the harsh operating environment of space. One component of the space environment is intense radiation, specifically charged particle radiation, which can cause damage to a variety of system components. Effects include changes to electrical, structural, and optical properties, the latter of which is the focus of this work.

A recently introduced technology to spaceborne imaging instrumentation is Acousto-Optic Tunable Filters. These devices use the Acousto-Optic effect and birefringent materials, such as tellurium dioxide and lithium niobate, to create narrow band image quality tunable filters. As common radiation damage effects include changes to transmittance, reflectance and absorbance of optical materials, as well as changes to the atomic structure causing changes to refractive indices and birefringence, radiation testing of these devices to assess long term performance is critical to further development of the technology for space applications.

Radiation testing involves accelerated lifetime testing of materials under multiple years' worth of equivalent radiation in much shorter time frames (hours), using charged particle radiation provided by an ion accelerator. This work details the development of a positive ion accelerator and its use for radiation testing. The accelerator can provide beam energies from 5 - 20 keV, beam diameters of 0.8 - 2.5 cm and beam currents from 0.5 - 15 μA, all adjustable by user input settings. The system can also accommodate other ion species such as helium ions. The system was primarily used with proton radiation, due to its dominance in the solar wind and general space environment, to examine induced damage effects in silicon, quartz, lithium niobate and tellurium dioxide as a function of fluence (protons/cm^2). Measurements of transmittance, reflectance and absorbance, as well as an investigation with Raman spectroscopy, were completed for all materials at varying fluences. Comparison of results to those in the literature shows good agreement, however, not all results have comparable data available in the current literature. Results are used to assess space mission suitability and show that tellurium dioxide has the highest radiation resistance of the investigated materials.

Acknowledgements

This work was made possible by financial funding from the Canadian Space Agency's Flights for the Advancement of Science and Technology program, the NSERC Discovery grants program and the University of Saskatchewan.

Special thanks to Ted Toporowski and all the wonderful workers in the University of Saskatchewan Physics Machine Shop who provided mechanical design guidance on, and machined, the custom parts used in the beamline system. They also provided support on a number of day to day mechanical challenges without hesitation and were always available to help troubleshoot mechanical issues. Without their expert knowledge and craftsmanship, as well as accessibility, the system would not be what it is today and many 'quick-fix' issues would have become stressful, longer term issues.

Thank you to the Saskatchewan Structural Science Center and corresponding personnel for use of the Raman spectrometer and the accompanying technical support throughout the measurement process.

My deepest gratitude is reserved for my supervisors, Drs. Michael Bradley and Adam Bourassa, who provided me with every opportunity I could have imagined in this project and facilitated the learning and understanding that I have gained through this work. Without their continued support, vast knowledge, and most importantly, time dedication, this work would not be what it is today. I will always be grateful for the many lessons, technical skills, and general understanding of topics that I gained through many discussions with both Mike and Adam, as well as through the general project work.

Finally, thank you to my family, especially my wife, my parents and my friends, for their unwavering support and belief in me and my abilities.

To my parents, Gordon and Diane,

My wife, Danielle,

and my son, James

Contents

List of Tables

List of Figures

List of Abbreviations

ALI	Aerosol Limb Imager
AO	Acousto-Opitic
AOTF	Acousto-Optic Tunable Filter
a-Si	Amorphous Silicon
CCD	Charge Coupled Device
CF	ConFlat
c-Si	Crystalline Silicon
c-SiO_2	Crystalline Silicon Dioxide (Quartz)
CSA	Canadian Space Agency
EPR	Electron Paramagnetic Resonance
HV	High Voltage
GCR	Galactic Cosmic Ray
$LiNbO_3$	Lithium Niobate
MFC	Mass Flow Controller
PKA	Primary Knock-on Atom
PWM	Pulse Width Modulation
RF	Radio Frequency
STP	Standard Temperature and Pressure
TeO_2	Tellurium Dioxide

Chapter 1

Introduction

1.1 Project Motivation

In today's world, the dependence of modern society on spaceborne instrumentation is undeniable. From satellites that provide GPS and global communication to instruments studying the Earth environment to instruments viewing the solar system and deep space objects, space technology is a huge part of everyday life and the lives of many researchers in various fields. As science continues to push the boundaries of human knowledge, the dependence on spaceborne measurements will continue to increase. This may include new everyday technology, the verification of fundamental theories, or discoveries of new observations that lead to major revelations on how the universe works. Regardless of the purpose of spaceborne instrumentation, a major concern for its operation and mission lifetime is the high levels of particle and photon radiation experienced in the harsh space environment. Radiation can inflict damage in a variety of ways including the creation of erroneous signals in electronics and changing physical properties of materials that disrupt their intended functionality.

One of the first radiation issues experienced with spaceborne technology was false triggering in electrical systems due to additional charge creation from incident radiation. This caused a range of effects from data corruption to complete system malfunction. The connection of these issues to radiation damage led to the need to understand radiation damage effects and to characterize the space environment. For electronics specifically, this led to the development of radiation hardened electronics [1]. Once the potential threat of radiation damage was fully understood, radiation readiness testing became a mandatory part of space qualification for any new spaceborne technology. This typically requires accelerated lifetime testing of materials, *i.e.*, providing multiple years' worth of radiation in a short period of

time and examining the results. Depending on the damage severity and the relationship to instrumentation operation, a new technology may be deemed unsuitable for space. Results could show that a device simply will not work in space or, alternatively, that its working lifetime is too short to justify the costs of development, launch and upkeep.

Along with electronic issues, the optical and mechanical properties of a material can also be adversely affected by radiation damage. In both cases, the majority of early experimental data came from nuclear labs where experiments naturally provided high levels of various radiation types. Examples from early nuclear research include metals becoming brittle [2] and breaking under mechanical stress, and transparent optical components, such as quartz windows, becoming darkened [3]. While only the former was a substantial safety concern to nuclear research, both results created extreme interest and motivated research into radiation damage processes (particle penetration theory) and corresponding induced effects. Optical properties, the subject of this thesis, that can be affected include, but are not limited to, spectral transmission range and quality, reflection, absorption, index of refraction and birefringence. These properties can change at variable rates as radiation damage accumulates.

The term radiation is very broadly used to refer to a variety of types of electromagnetic radiation and energetic particles. For example, both optical photons and microwaves can be classified as radiation. In terms of radiation damage, radiation refers to either energetic charged particles, which includes both positively and negatively charged ions (atomic nuclei) and electrons, energetic neutrons (prevalent in nuclear research), or gamma radiation (very high energy photons). Each of these can cause damage to a material via their own interaction mechanisms. Both charged particle and neutron radiation cause damage by interacting with target material lattice atoms and physically removing them from lattice sites. This causes substantial structural damage and can lead to changes in chemical composition and complete amorphization of crystal materials. Complete amorphization of a crystal material in the damaged layer serves as an upper limit for induced radiation damage. Charged particles can also interact with the electrons of a target material to cause target ionization. Electron radiation can also cause lattice atom displacement, but this occurs at a much lower rate. Instead, the most common damage type from incident electrons is target ionization, which can lead to optical effects, specifically changes to absorption and transmission. Gamma

radiation is very different from particle radiation as interactions between photons and target atoms result in electronic excitation and ionization rather than lattice displacements. These interactions create secondary electrons via the photoelectric effect, Compton scattering or positron-electron pair production reactions [1]. These electrons travel through the material and cause damage as described for incident electrons. As with pure electron radiation, the most common optical results of gamma radiation are changes to absorption and transmission.

The University of Saskatchewan is currently developing the Aerosol Limb Imager (ALI) [4], a proposed new satellite instrument funded by the Canadian Space Agency (CSA). ALI is an imaging device used to measure scattered sunlight from the limb of the Earth's atmosphere in order to determine atmospheric content concentrations, specifically atmospheric aerosols. Atmospheric aerosols are particles suspended in the atmosphere that have a diameter between approximately 0.002 and 100 microns. This includes water droplets, ice crystals, dust particles, and sulfates to name a few. The importance of measuring atmospheric concentrations is to learn about processes that occur in the atmosphere that affect daily life on Earth such as better understanding and predicting weather patterns, understanding global warming and ozone depletion, and learning how to combat these negative effects. The specific importance of aerosols in the stratosphere is that they create a global cooling effect by reflecting incoming light from the Sun back into space. The primary component of ALI is a tellurium dioxide (TeO_2) Acousto-Optic Tunable Filter (AOTF), that is used to select specific wavelengths of interest from scattered sunlight for measurement of these stratospheric aerosols.

An AOTF is an imaging device that uses the Acousto-Optic (AO) effect to create a tunable diffraction grating that can select specific wavelengths of light from a broad incoming source, generally in the visible and near-infrared. The AO effect is a specific case of photoelasticity, which describes the optical properties of a material while under mechanical strain [5]. The result of this strain is an induced change to the material permittivity that causes a change in the optical refractive index. In the AO effect, the mechanical strain is provided by coupling a standing radio frequency (RF) acoustic wave into the material. As the RF wave travels through the material, it causes the lattice atoms to vibrate in a pattern corresponding to the standing wave. This results in a periodic modulation of the local atomic density that causes a periodic modulation of mechanical strain and thus, the refractive index. This refractive

index variation creates a diffraction grating that can be tuned to select a specific wavelength of light by changing the acoustic frequency and the periodic variation of the refractive index. The major benefit of this effect is that it is completely reversible and does not harm the material. Once the RF wave is removed, the atoms return to their original lattice positions. For space applications, AOTF technology is highly desired as it has no moving parts.

The main component of an AOTF is the material through which the light and acoustic wave propagates. While the AO effect can technically occur in any optical material, the effect is enhanced in anisotropic, birefringent materials. Materials with stronger birefringence exhibit a stronger AO effect and thus AOTF devices typically use birefringent materials. The current 'industry standard' for AOTF crystals, both on ground and in space, is TeO_2. This is primarily due to its high figure of merit; a measure of how well a material will work in an AO device. Multiple calculations exist for defining the figure of merit, each of which uses either a different combination of multiple optical factors or different powers of the factors. This leads to different figures of merit and potential disagreement in which material is the best for a given application. However, the most commonly used figure of merit puts TeO_2 at the top of the list [5] for materials that can currently be manufactured into an AO device (there are materials with higher figures of merit but they pose issues to the manufacturing process - ongoing work is being conducted on these 'new' materials [6]). Given the dependence of AOTF operation on material birefringence, and of birefringence on crystal structure, AOTF devices are, in theory, highly susceptible to performance altering, radiation induced damage. Furthermore, the optical imaging nature of AOTF devices requires known transmission behavior, which also increases device vulnerability. Damage to the AO crystal that results in changes to, or loss of, either birefringence or transmission of desired wavelengths, could result in distorted data collection or complete system failure. Currently, the knowledge on radiation induced effects in TeO_2 is limited and there is little heritage for its use in the space environment in comparison to that of other, more mature, optical materials and technologies.

The primary motivation for this work is the radiation testing of TeO_2 and other relevant birefringent materials, quartz (SiO_2) and lithium niobate ($LiNbO_3$). This was further narrowed to charged particle radiation, specifically positively charged particles, due to the high presence of energetic protons in the space environment and the limited research on proton

induced damage in TeO_2 and $LiNbO_3$. Therefore, other types of radiation damage, neutron, electron and gamma, will not be discussed other than to say that they exist and are also an issue for spaceborne optics. Quartz was chosen for its rich history of charged particle radiation damage research to provide results to compare with the present research results and verify implemented techniques. $LiNbO_3$ was chosen for study alongside TeO_2 as prior to the dominance of TeO_2 in AO technology, the standard material was $LiNbO_3$, making it an obvious choice to include in the research. The limited amount of published research on $LiNbO_3$ charged particle radiation damage also provided a good opportunity to contribute meaningful results alongside the meaningful results of TeO_2. While research does exist on TeO_2, as well as some implementation heritage with recent space applications, this work was funded by the CSA as an independent study to add to the current body of knowledge to support the development of the ALI instrument for space deployment.

1.2 Charged Particle Radiation in Space

Charged particle radiation in the local space environment (within our solar system) comes from one of two sources. The most dominant source is the solar wind; a constant flux of energetic charged particles emitted from the Sun in all directions. The solar wind is composed of 96% protons, 4% alpha particles (helium nuclei), trace amounts of other ionized elements ($< 0.1\%$) and enough electrons to maintain approximate charge neutrality [7, 8]. The characteristic energy of the positively charged particles in the solar wind is 10 keV (but also includes a range of energies down to a few eV, in varying proportions) and the average flux is $3{\times}10^8$ particles/cm^2/s [7]. The other source of charged particle radiation is Galactic Cosmic Rays (GCRs), which are extremely high energy (> 100 MeV) charged particles originating from deep space, most commonly from supernova events. GCRs consist of 90% protons, 9% alpha particles and 1% other ionized elements as well as electrons [9]. The GCR flux is energy dependent and monotonically decreases with increasing energy above 1 GeV. At 1 GeV the flux density is ≈ 0.1 particles/(cm^2 s sr GeV) ≈ 1 particle/cm^2/s. This high end flux value of GCR particles is on average 7 orders of magnitude less than the solar wind flux. The majority of charged particles are deflected by the Earth's magnetic field and are thus a low concern to satellites that orbit inside of Earth's magnetic field.

However, for Earth orbiting satellites, there is a third 'source' of charged particle radiation: radiation located in the Van Allen belts. These belts are regions of trapped charged particles, originally from the solar wind or GCRs, confined by the Earth's dipole magnetic field. The inner radiation belt consists mostly of energetic protons with high keV - 100 MeV energies [10], while the outer belt is primarily energetic electrons with energies up to 10 MeV [8]. Satellite missions orbiting Earth generally avoid the radiation belts as the average orbit altitude (∼600 km) is below the radiation belts. However, there is a region near Brazil, called the South Atlantic Anomaly, where the inner radiation belt comes to within ∼300 km of the Earth's surface, due to the tilt angle of the Earth's magnetic field. Space missions passing through this region are subject to higher fluxes of energetic charged particles [11].

1.3 Review of AOTF Radiation Damage Studies

To date, the amount of radiation testing conducted on AOTF crystal materials has been relatively minimal. As TeO_2 is the present AOTF material standard, it has received some space qualification studies, while information on radiation damaged $LiNbO_3$ is harder to find. Given the dominance of TeO_2, its interaction with radiation is of great interest to future AOTF technology, and the present research. The most widely referenced and accredited TeO_2 charged particle damage study [12] [13] used proton radiation to examine TeO_2 Bragg cells and monitored changes in the Stokes parameters during irradiation. The study used energies of 63.0 and 39.9 MeV with a beam flux of 1.885×10^{10} protons/cm^2/s and 1.897×10^{10} protons/cm^2/s respectively. Irradiation times were of the order of 1 - 2 minutes. This produced fluences in the range of 1.5×10^{12} protons/cm^2. During irradiation, the Stokes parameters were observed to change but after the proton beam was removed from the target, all parameters returned to normal values after a few minutes of recovery time. Follow up studies have cited this proton radiation work and focused instead on Cobalt 60 gamma radiation induced damage [14] [15]. Another, more recent, study on effects of Cobalt 60 gamma radiation was also completed on a TeO_2 AOTF device [16].

The conclusions of these studies have all been that TeO_2 is a very suitable material for space applications. In the case of gamma radiation, minimal to no effects were observed and in the case of proton radiation, any changes to the material were reversible, which

leads to minimal long term damage. Based on the results of the earlier studies, the use of TeO_2 AOTF devices in spaceborne missions began with implementation on the Spectroscopy for Investigation of Characteristics of the Atmosphere of Mars/Venus missions [17][18]. To date, no degradation in operation has been reported and a very recent review article on the use of AOTF devices for space missions was published in 2018 where the author cites the above studies and missions to conclude, "the most used TeO_2 crystal is inherently immune to radiation" and that "Mars Express and Venus Express instruments ... have confirmed the AOTF robustness during long term space operations" [19].

While the reported evidence from both studies and implementation in spaceborne instrumentation appears to be conclusive and is accepted as a general consensus, especially in regard to gamma radiation, it is not as obvious for charged particle radiation as only one major study exists. Furthermore, this study used low fluxes and irradiation times, leading to low fluence values, which from general damage and ion implantation knowledge, would not be expected to cause significant damage. The study itself even suggests that observed effects could have been due to sample heating rather than measurable radiation damage, which would account for the fast recovery time in the Stokes parameters. This leaves an open question of the effects of substantial damage at much higher fluences; a question that the present work will investigate. Based on the flux of the solar wind, 3×10^8 particles/cm^2/s, the delivered fluence in [13], $\sim1.5\times10^{12}$ protons/cm^2, is equivalent to only a few hours of exposure, much less than any space mission lifetime. This work presents evidence that these fluences are too low to conclude on space qualification issues and that higher fluences, equivalent to multiple years' worth of solar wind irradiation, delivered with accelerated lifetime testing, is required to fully address the issue of space qualification.

1.4 Project Overview

As mentioned, the primary research goal is to examine effects of high fluence charged particle radiation on birefringent materials, specifically TeO_2, to assess suitability for use in space applications with accelerated lifetime testing. Protons were chosen as the primary radiation type of interest for this research based on their prevalence in the space environment, their theoretical significance in regard to both particle mass and energy scaling rules to predict

other types of damage [20] and because they are simple to create with a hydrogen plasma. The proton energy was chosen to be 10 keV to match the characteristic energy of the solar wind, which is the dominant charged particle radiation source in the space environment. This energy is also obtainable in the laboratory setting and provides surface level damage that aids characterization techniques and calculations. Particle energy primarily affects the penetration depth of incident particles, *i.e.*, the location and width of the damage layer. This can be scaled to other energies and permit calculations of various expected results, especially in terms of optical properties (multi-layer reflection/transmission). Furthermore, while potentially counterintuitive, it is actually lower energy particles that cause the most damage as very high energy particles can pass through targets with minimal induced damage. This will be further detailed in Chapter 2. Based on this last point, and their relative low abundance, GCR particles are generally a low level concern for induced damage. In cases where GCRs become significant, damage is modeled based on theoretical or lower energy experimental results as creation of GCR energies is not a simple task.

To create and deliver the proton radiation, a positive ion accelerator was designed, built, and characterized. Inside the system, a plasma source creates hydrogen plasma from hydrogen gas and the remainder of the system accelerates the positive ions into a beamline directed toward the target material. As the second most common positively charged energetic particle in the solar wind is helium, the system was also designed to run as a helium beamline. Furthermore, the beamline was designed to operate at different beam energies (5 - 20 keV), have an adjustable beam size, and provide adjustable beam current. Each of these adjustable features are 'programmed' into the system by various user input settings.

Given the large number of possible ion beams the system can produce, some minimum requirements are necessary to aid beam choice for radiation damage research. The first requirement was to create a broad beam capable of irradiating sample sizes of the order of 1×1 cm and providing an approximate uniform implant throughout the sample area. In terms of total beam current values, the system was designed to deliver multiple years' worth of protons at solar wind flux values on the time scale of hours. A baseline benchmark was calculated from a general 'rule of thumb' in the ion implantation world. This rule is referred to as the 'amorphizing dose', which says that the typical minimum fluence to amorphize a crystal

material is of the order of $1{\times}10^{16}$ particles/cm^2 [21]. Another interpretation of this rule says this is the fluence at which the target material can no longer considered to be pure and has a substantial quantity of implanted ions, which can be extended to mean, has experienced substantial damage. With this second definition, this fluence signals an approximate value at which substantial changes to measurable macroscopic properties should become apparent. This fluence is four orders of magnitude higher than the fluence used in [13]. Therefore, it is not surprising that this study did not find substantial retained damage in their samples.

For accelerated lifetime testing, the minimum required beam current density (J_{beam}) must be able to deliver a fluence equal to the amorphizing dose (10^{16} particles/cm^2) in a short time period, say, one hour. Interestingly, 10^{16} is also the acquired fluence of protons in one year from the solar wind average flux.

$$J_{beam} = \frac{(1.602 \times 10^{-19}\ \mathrm{C})\,(10^{16}\ \mathrm{cm}^{-2})}{(3600\ \mathrm{s})} = 0.445\ \frac{\mu\mathrm{A}}{\mathrm{cm}^2} \tag{1.1}$$

To deliver multiple years' worth of protons, say 10 years (10^{17} protons/cm^2), J_{beam} must be higher to allow delivery in a few hours of time. However, this minimum required value would still be able to provide this fluence in 10 hours of run time, which is acceptable.

Once the beamline was fully operational and characterized, it was used to irradiate sample materials beginning with crystalline silicon (c-Si) and quartz (c-SiO_2) to compare results with previously reported radiation induced effects. Following quartz, both $LiNbO_3$ and TeO_2 were irradiated and measured. Results were used to assess the lifetimes and performance of these materials and to provide a conclusion on space suitability at high proton radiation fluences.

Chapter Two presents the development of radiation damage theory, specifically charged particle penetration theory, as well as a discussion on physical damage effects and induced changes. The application of theory to experiment and development of empirical models is also discussed. Chapter Three discusses the background required to design an ion accelerator from start to finish while Chapter Four details the specific design choices of the present system. Chapter Five discusses beamline characterizations and presents performance results in regard to beam size, uniformity and current density system requirements. Chapter Six presents sample irradiation details and subsequent induced damage measurements. Finally, Chapter Seven provides a summary of the work, results and future work for this project.

Chapter 2

Charged Particle Radiation Damage Theory and Effects

The theory of how both energetic charged and neutral particle radiation interacts with solid targets is referred to as particle penetration theory. Modern penetration theory began with derivation of the Rutherford scattering formula [22]. The importance of understanding physical mechanisms and effects of energetic particles interacting with matter increased with the development of nuclear research. This field was a driving force in furthering the understanding of particle penetration as knowledge and minimization of effects was essential for safe nuclear research. Charged particle and neutron radiation are now both known to induce a variety of effects in target materials including changes to electrical, mechanical and optical properties. Examples include ion implantation to dope semiconductors [23], induced structural damage in metals causing enbrittlement [2, 24], and darkening of transparent materials [25] in both nuclear [3] and space [26] applications. Understanding these effects has led to mitigation techniques as well as harnessing beneficial effects.

Following Rutherford's work, Bohr [27], Bethe [28] and Bloch [29, 30] each had significant contributions to the field. Following their work, Lindhard [31] took a whole new approach to the problem and developed a universal theory that is still widely used today. While experimental research has always attempted to use theory to design or explain experiments, Lindhard's universal theory sparked an increased interest in comparing experiment to theory. Unfortunately, theory has never been able to fully verify or predict experimental results, primarily due to the vast complexity and intricacies required to explain different interactions. This led to empirically based models for experimental prediction, which have had significant success and have become a standard in related industries. The following presents the basic

historical development of particle penetration theory, empirically based computer simulation models, and an introduction to potential observable effects in materials as a result of charged particle radiation damage. All presented formulas use CGS units rather than SI units as this is the standard in theoretical particle penetration due to the simplification of removing the $1/4\pi\epsilon_0$ factor from most equations.

2.1 The Basic Interaction Description

A simplistic and intuitive description of radiation damage treats both the target material lattice atoms and the incoming energetic particles as hard spheres. This is the hard-sphere, or 'billiard ball' model. When incoming particles interact with the target material, the hard spheres collide in elastic collisions that result in a transfer of energy and momentum. Depending on the transfer magnitude, the target atom may become displaced from its lattice site. The colliding spheres continue along new trajectories after the collision and potentially cause more collisions with other target material spheres in a cascade effect. This continues until all kinetic energy is dissipated and all atoms have come to rest. Once at rest, the projectile atoms are unlikely to occupy a lattice position. Instead, they will exist somewhere within the material, in no particular position, with no long-range order. These are called interstitial atoms. The removal of target atoms from their lattice sites (creation of vacancies) causes disorder in the crystal structure. The degree of disorder scales proportionally with radiation flux and exposure time. After many collisions, the final material state is a state of complete disorder. As many material properties depend on a specific lattice structure, this disorder causes substantial property changes. Incident particles that come to rest inside the material are impurities that change the material composition and can further alter material properties. In this classical description, induced damage is directly proportional to the size and energy of the incoming particle; larger and faster particles should cause more destructive collisions. For a macroscopic analogy, imagine a fast moving bowling ball and a slow moving baseball incident upon a pile of baseballs; the bowling ball will cause more damage.

While this description is intuitive on a macroscopic level, it does not completely transfer to atomic interactions. The theory does explain the majority of damage caused by energetic neutrons, as well as a portion of charged particle damage, but does not give the full picture

for charged particles. In the charged particle regime, this theory has challenges accounting for long-range Coulomb interactions with the charged target particles, especially electrons.

2.2 Stopping

Stopping is the term used to describe the ability of a material to remove kinetic energy from an incident energetic particle through different energy transfer interactions causing it to slow down and eventually stop moving. It is defined as a retarding force that opposes the motion of an incident particle. There are three types of stopping, nuclear, electronic and radiative. Radiative stopping is caused by the emission of bremsstrahlung radiation and is only significant for high energy electrons and very high energy charged particles. As the present work uses low energy charged particles, radiative stopping is insignificant. However, nuclear and electronic stopping are significant and are discussed in the following sections.

2.2.1 Nuclear Stopping

Nuclear stopping describes incident energetic particle stopping via elastic collisions with the target material nuclei. In a simplistic form, it is similar to the hard-sphere model but also accurately handles Coulomb interactions. When an incident energetic particle collides with a lattice atom (nucleus), the energy transferred (E_T) to the target particle depends on collision details such as mass ratio and angle of incidence. Based on the magnitude of E_T, the effect on the lattice atom will vary. In order to knock an atom out of a lattice position, a minimum energy is required to break lattice bonds and send the atom away from the lattice site such that it does not 'fall back into place'. This minimum energy is called the threshold displacement energy (E_d). While this is different for every material, a common rule of thumb value is five times the energy of sublimation, E_s, which is typically of the order of 5 eV, *i.e.*,

$$E_d = 5E_s = 25 \text{ eV} \tag{2.1}$$

This rule and value comes from the Kinchin-Pease model [32] for radiation damage. Based on this rule, if $E_T > 25$ eV, the target atom will be displaced and move away from the lattice site with an energy of approximately $(E_T - 25)$ eV on a trajectory determined by collision properties. An atom displaced by an incident particle is called a Primary Knock-on Atom (PKA). A PKA will travel through the material until it has depleted its energy through interactions with the rest of the material. Depending on the type of interaction and energy

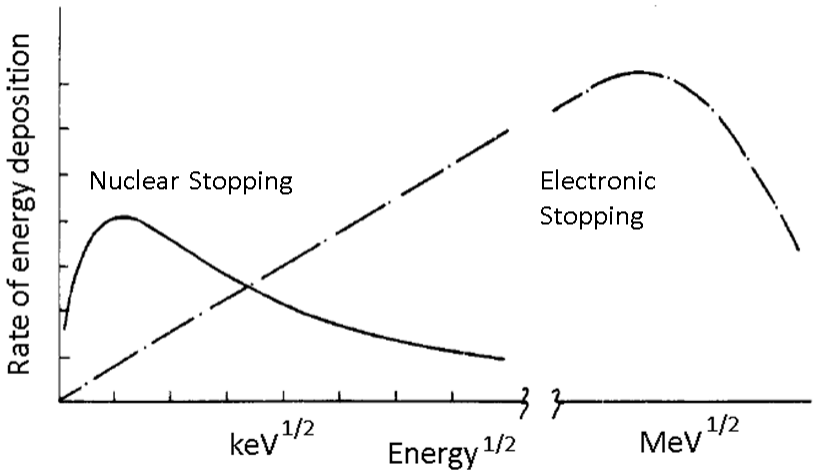

Figure 2.1: Example nuclear and electronic stopping as a function of energy. Nuclear stopping is negligible at high energies when incident particles have low interaction times with a single target. Electronic stopping dominates high energy when incident velocity becomes of the order of target electron velocity. Past this point, electronic stopping falls off as the incident particle becomes too fast to interact with electrons. Image adapted from [21].

transfer, it may cause future displacements resulting in a cascade effect that continues until all affected atoms come to rest. If a collision occurs where $E_T < E_d$, the target atom is not displaced and is instead put into an excited vibrational state. This energy is dissipated into the material through vibrations as phonons and effectively leads to target heating.

Along with hard-sphere elastic collisions, elastic Coulomb interactions also contribute to nuclear stopping. A Coulomb interaction inside the material happens when an incident particle passes by a positively charged lattice atom (nuclei). Coulomb interactions also occur between the incident particle and target electrons, but these interactions are called electronic stopping and are discussed in the next section. In a Coulomb interaction, energy transfer depends on the magnitude of the Coulomb force, which depends on the distance between particles, the charge states and the interaction time, which is controlled by the incident particle velocity. Energy transfer is proportional to momentum transfer given by the product of the force and the interaction time as will be shown in Section 2.3.3. Therefore, in order to have a significant energy transfer, the force-time product needs to be large. As the Coulomb force can be long-range, interactions can exist where the force is small due to the distance. However, if the interaction time is long enough, the momentum exchange can become large

enough to produce significant energy transfer. The interaction time refers to the time spent by the incident particle in the vicinity of the target particle. This is completely governed by the incident particle velocity as the target atom can be considered to be at rest. If the incident velocity is too high, the interaction time will be too small to cause significant energy transfer. Therefore, high energy particles, with short interaction times, must have close approaches to the target atoms to increase the force in order to create significant energy transfer. This means the effective target area, or cross section, for nuclear Coulomb stopping decreases with increasing energy. The opposite is true for low velocity particles with high interaction times. The increased interaction time increases effective target area, which allows weak, long distance forces to cause significant energy transfers. The increase to effective target area (cross section) increases the interaction probability. Therefore, as shown in Figure 2.1, nuclear stopping dominates at low energies and becomes insignificant at high energies.

2.2.2 Electronic Stopping

Electronic stopping describes incident particle stopping through interactions with the target material electrons. This energy transfer occurs solely through Coulomb interactions and thus only applies to incident charged particles. The interaction results in the incident charged particle either attracting or repelling the target electrons. If the force between the two is strong enough, the electron is ripped from the target atom and becomes a free electron. This ionizes the target atom and causes damage. Given that the interaction is through the Coulomb force, it is again dependent on distance and interaction time. As the electrons move around the target atom at very high speeds, the incident particle must also be traveling at a high speed, otherwise the electron passes by too quickly to feel any significant force. Therefore, electronic stopping dominates at higher energies as depicted in Figure 2.1.

2.3 Penetration and Stopping Theory Essentials

2.3.1 Stopping Cross Section

The idea of a cross section used in penetration and stopping theory is a key component to the description and understanding of the topic. A macroscopic cross section is quite simple; it is the physical area of a target that can be hit by a projectile. The atomic level definition is not as intuitive due to the long-range nature of the Coulomb force. A target atom is considered

to be 'hit' if the interaction of the projectile with the target has some measurable effect [33]. Therefore, the cross section depends not only on the target and the projectile, but also on the effect to be measured. In stopping theory, the measured effect is material stopping power, which is the loss of projectile kinetic energy to the material divided by distance traveled in the medium. Therefore, this is referred to as the stopping cross section.

2.3.2 Energy Loss and the Differential Cross Section

When a projectile interacts with a target particle, the projectile may transfer all, or part of, its kinetic energy to the target atom depending on interaction details. This decreases the kinetic energy and velocity of the incident particle. This process continues until the projectile experiences enough interactions to lose all kinetic energy, or passes through the material. The energy lost by an incident projectile in any interaction is a discrete amount, T_j, where $j = 1, 2, 3...$ to represent all possible energy transfers. If the projectile penetrates a layer of thickness Δx, which is small compared to the total penetration depth, then within that layer, the projectile will lose kinetic energy, ΔE, given by

$$\Delta E = \sum_j n_j T_j \tag{2.2}$$

where n_j is the number of collisions of type j that occur within Δx and lead to a kinetic energy transfer, T_j. The expected value of n_j is defined as

$$\langle n_j \rangle = N \Delta x \sigma_j \tag{2.3}$$

where N is the number density of target particles in a slab of the target material of depth Δx and σ_j is the *energy-loss cross section*. This theory of energy loss can be applied to a large number of projectiles to find the average energy loss $\langle \Delta E \rangle$.

$$\langle \Delta E \rangle = \sum_j \langle n_j \rangle T_j \tag{2.4}$$

Substituting (2.3) into (2.4) leads to

$$\langle \Delta E \rangle = N \Delta x \sum_j T_j \sigma_j \tag{2.5}$$

Here the stopping cross section, S, is defined as

$$S = \sum_j T_j \sigma_j \tag{2.6}$$

The *stopping force* or *stopping power* is defined in (2.7). This ratio describes the energy lost per distance traveled in the medium. It is used to calculate the distance, or the range, that an energetic particle will travel in a specific medium.

$$F = \frac{\langle \Delta E \rangle}{\Delta x} = NS = N \sum_j T_j \sigma_j \tag{2.7}$$

The discrete cases of energy loss in (2.6) can be turned into a continuous spectrum of energy losses by letting the interval size, ΔT_j, become sufficiently small to replace the summation with an integral. With this substitution, the stopping cross section becomes

$$S = \int T d\sigma \tag{2.8}$$

where $d\sigma$ is the *differential energy-loss cross section* defined as

$$d\sigma = \frac{d\sigma\,(T)}{dT} dT \tag{2.9}$$

2.3.3 Rutherford Scattering

Rutherford scattering describes the elastic scattering of charged particles through the Coulomb interaction. The elementary interaction, sketched in Figure 2.2, is an incident point charge, q_1, with mass, m_1, and velocity, v, interacting with a target particle, q_2, with mass m_2. The projectile may be positively or negatively charged and the target may be a nucleus or electron. The different combinations result in Coulomb attraction or repulsion. The following discussion assumes a positively charged projectile interacting with a nucleus causing a repulsive force. The end result is an expression for the differential energy-loss cross section of the basic interaction which is used with (2.7) and (2.8) to find the stopping force of a material.

Rutherford's formula is derived through calculation of the interaction momentum and energy transfer. If the projectile is moving fast enough, the target particle can be considered to be at rest for the duration of the interaction. The momentum transfer is given by

$$\Delta P = \int_{-\infty}^{\infty} F(t) dt \tag{2.10}$$

where $F(t)$ is the Coulomb force between the two charges as a function of time.

$$F(t) = \frac{q_1 q_2}{\mathrm{b}^2 + (\mathrm{v}t)^2} \tag{2.11}$$

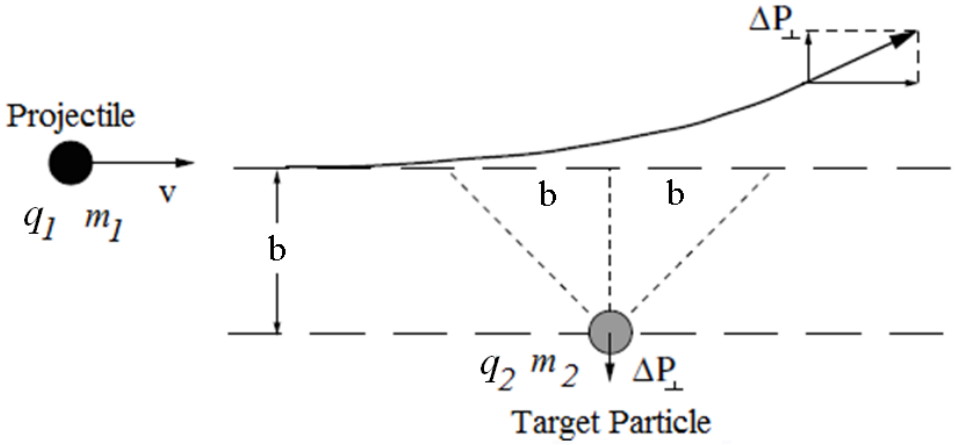

Figure 2.2: Elementary collision event of a charged projectile, q_1, with mass, m_1, and velocity, v, interacting with a charged target particle, q_2, considered to be at rest with mass m_2. The impact parameter, b, is also referred to as 'p' in some sources. Image adapted from [33].

Momentum transfer has two components: parallel and perpendicular to projectile velocity.

$$\Delta P_{\parallel} = q_1 q_2 \int_{-\infty}^{\infty} \frac{\mathrm{v}t}{(\mathrm{b}^2 + \mathrm{v}^2 t^2)^{\frac{3}{2}}} dt = 0 \tag{2.12}$$

$$\Delta P_{\perp} = q_1 q_2 \int_{-\infty}^{\infty} \frac{\mathrm{b}}{(\mathrm{b}^2 + \mathrm{v}^2 t^2)^{\frac{3}{2}}} dt = \frac{2|q_1 q_2|}{\mathrm{bv}} \tag{2.13}$$

The *impact parameter*, b, in these equations, is defined as the distance between the straight line trajectory of the projectile and the initial position of the target. For simplicity, it is assumed that this distance is reached at time $t = 0$. Due to the symmetry of the Coulomb interaction, the momentum transfer parallel to the the direction of velocity, $\Delta P_{\parallel}$, vanishes as seen in (2.12). Therefore, all momentum transfer is in the perpendicular direction. An *effective collision time*, τ, is defined from an approximate momentum transfer equation

$$\Delta P_{\perp} \simeq F_{\max} \tau \tag{2.14}$$

where $F_{\max} = |q_1 q_2|/\mathrm{b}^2$ is the force at closest approach ($t = 0$) and is directed normal to the direction of initial velocity. Using this along with (2.13) and (2.14), gives

$$\tau \simeq \frac{2\mathrm{b}}{\mathrm{v}} \tag{2.15}$$

This says the two particles interact over an effective length $\simeq 2\mathrm{b}$ on the incoming trajectory. Converting momentum transfer from (2.13) to kinetic energy transfer gives an equation for

the energy lost, T, as a function of b.

$$T = \frac{\Delta P_{\perp}^2}{2m_2} \simeq \frac{2q_1^2 q_2^2}{m_2 \mathrm{v}^2 \mathrm{b}^2} \tag{2.16}$$

With this result, Rutherford's differential scattering cross section for the Coulomb potential can be determined. The full cross section is found by integrating over a circular 'target area' of radius b increasing by db. Therefore, the differential cross section is the integrand.

$$d\sigma = 2\pi \mathrm{b} d\mathrm{b} = \left| \frac{d(\pi \mathrm{b}^2}{dT} \right| dT \tag{2.17}$$

Differentiation of (2.16) and substitution into (2.17) yields Rutherford's formula.

$$d\sigma \simeq 2\pi \frac{q_1^2 q_2^2}{m_2 \mathrm{v}^2} \frac{dT}{T^2} \tag{2.18}$$

This derivation has assumed that moving particles are classically described and that target material electrons also behave classically, *i.e.*, quantum and relativistic effects are ignored. While actual motion will obviously differ from the classical case, within certain limits, it can be argued that the difference is insignificant. Outside these limits, the assumption fails and both quantum and relativistic considerations are required. In order for a momentum transfer occurring at b $\pm$ δb to be considered classical and well-defined, it is required that

$$\frac{\delta P}{\Delta P_{\perp}} \sim \sqrt{\frac{\hbar \mathrm{v}}{2\left|q_1 q_2\right|}} \ll 1 \tag{2.19}$$

where δP is the error in P due to δb. This condition was formulated by Bohr as

$$\kappa = \frac{2\left|q_1 q_2\right|}{\hbar \mathrm{v}} \gg 1 \tag{2.20}$$

which can be rewritten as

$$\mathrm{v} \ll 2\mathrm{v}_0 \left| \frac{q_1 q_2}{e^2} \right| \tag{2.21}$$

where v_0 is the Bohr velocity, $\mathrm{v}_0 = e^2/\hbar = c/137$, which is the orbital speed of an electron in the ground state of a hydrogen atom with c being the speed of light in vacuum. This is an upper bound on projectile velocity. If the target particle is an electron, the limit becomes

$$\mathrm{v} \ll 2Z_1 \mathrm{v}_0 \tag{2.22}$$

and if the target is the atomic nucleus, the limit becomes

$$\mathrm{v} \ll 2Z_1 Z_2 \mathrm{v}_0 \tag{2.23}$$

where Z_1 and Z_2 are the atomic numbers of the projectile and target respectively. A lower bound for projectile velocity is required to ensure the projectile is fast enough to consider the target particle to be at rest. When the target particle is the nucleus, a lower bound essentially does not exist, as the nucleus can effectively always be considered at rest. However, when the target particle is an electron moving around the nucleus, a lower bound is required. According to Bohr, the projectile must have a velocity much greater than v_0.

$$\mathrm{v} \gg \mathrm{v}_0 \tag{2.24}$$

By inspection, it may be noticed that there are cases when (2.21) and (2.24) contradict one another, especially for electron targets and low Z projectiles. When this occurs, the assumption of pure classical interactions will not suffice and quantum interactions must be considered. When the upper velocity limit is surpassed, relativistic corrections are required.

2.4 Stopping Theories

2.4.1 Bohr Stopping Theory

Bohr's stopping theory [27] assumes the target electrons behave as classical harmonic oscillators with a resonance angular frequency, ω_0. When an external force, F, acts on the target electron during a time τ, the momentum transfer depends on the magnitude of τ compared to the oscillation period of the target electron, $2\pi/\omega_0$. If $\tau \ll 2\pi/\omega_0$, the oscillator will receive an impulse of $\sim F\tau$ as if it were a free particle. In the opposite case, $\tau \gg 2\pi/\omega_0$, the target electron responds adiabatically to the external force and will tend to relax as the disturbance diminishes even without the aid of dampening forces. Therefore, the momentum received by the target electron will be much smaller than in the first regime. Bohr used this basis, the classical equations governing a harmonic oscillator, and Rutherford's law of free-Coulomb scattering for close collisions to derive his famous stopping formula for the stopping cross section of a target electron and a uniform stream of point charges.

$$S = \frac{4\pi e_1^2 e^2}{m\mathrm{v}^2} \ln\left(\frac{Cm\mathrm{v}^3}{|e_1 e|\,\omega_0}\right) \text{ with } C = 1.1229 \tag{2.25}$$

2.4.2 Bethe Stopping Theory

Bethe's approach to stopping theory [28] is similar to Bohr's except that Bethe included quantum mechanic descriptions and equations in his theory including modeling the electron as a quantum harmonic oscillator, $\hbar\omega_0$. Bethe also classified his interaction in momentum space. This led to momentum transfers of $\hbar q$. The theory operates in the regime where the dipole approximation is assumed valid which is when $q < q_0$ or $Q < Q_0$ where Q is a simplification variable defined as $Q = \hbar^2 q^2/2m$. Bethe used the Plane-Wave Born Approximation (first order) to write the stopping cross section as generalized oscillator strengths in the form

$$S = \int Q d\sigma_R(Q) \sum_j f_{j0}(Q) \tag{2.26}$$

where $d\sigma_R(Q)$ is the free-Coulomb cross section for energy transfer as a function of Q and $f_{j0}(Q)$ is a function for the quantum dipole oscillator strengths. Using a harmonic oscillator model, these oscillator strengths are[1]

$$f_{j0}(Q) = \frac{1}{(j-1)!}\left(\frac{Q}{\hbar\omega_0}\right)^{j-1} e^{-Q/\hbar\omega 0} \tag{2.27}$$

Performing a general evaluation of (2.26) using (2.27) leads to the *Bethe stopping formula.*

$$S = \frac{4\pi e_1^2 e^2}{m\mathrm{v}^2} Z_2 \ln\left(\frac{2m\mathrm{v}^2}{I}\right) \tag{2.28}$$

Here, I is called the *mean logarithmic excitation energy* and is defined as

$$\ln(I) = \sum_j f_{j0} \ln(\epsilon_j - \epsilon_0) \tag{2.29}$$

where ϵ_j and ϵ_0 denote the j energy levels of the target and the ground state respectively.

2.4.3 Bloch Stopping Theory

In Bloch stopping theory [29, 30] the goal was to use a semi-classical treatment to derive a stopping formula to combine Bohr and Bethe theory into one theory. Combining these theories was possible because Bohr theory is more accurate at lower velocities and Bethe theory is more accurate at higher velocities approaching the relativistic limit. Bloch combined the two with correction factors in the mid-range velocity region. These correction factors

[1]The origin of this equation can be found in books such as [33].

approach zero in the upper and lower velocity limits. The outcome of this theory was an overall increase in accuracy. The correction factor derivations are fairly involved and will be omitted for brevity, but can be found in [33].

Stopping Number and Bloch Equations

The Bloch equations are generally stated in terms of a stopping number, L, which was introduced by Lindhard and Scharff [31]. They determined that any stopping formula can be written as a universal prefactor multiplied by a theory dependent logarithmic term.

$$S = \frac{4\pi Z_1^2 Z_2 e^4}{m\mathrm{v}^2} L \tag{2.30}$$

Comparing this equation to Bohr (22) and Bethe (26), it is obvious that

$$L_{Bohr} = \ln\left(\frac{Cm\mathrm{v}^3}{Z_1 e^2 \omega_0}\right) \tag{2.31}$$

$$L_{Bethe} = \ln\left(\frac{2m\mathrm{v}^2}{I}\right) \tag{2.32}$$

The Bloch equations for 'fast' and 'slow' velocity regimes (Bethe and Bohr respectively) are

$$L_{Bloch-Bethe} = L_{Bethe} - 1.202\left(\frac{Z_1 v_0}{\mathrm{v}}\right) \tag{2.33}$$

$$L_{Bloch-Bohr} = L_{Bohr} - \frac{1}{12}\left(\frac{\mathrm{v}}{Z_1 v_0}\right)^2 ... \tag{2.34}$$

2.4.4 Lindhard Stopping Theory

The previous theories treated the interaction of a single projectile and target particle as the elementary event. The sum of all elementary events is assumed to be governed by Poisson statistics and is considered to produce the total energy transfer and ultimately, stopping. There are three problems with this approach. First, it does not consider the effect of projectile or target particles interacting with themselves. Second, polarization effects on electrons in the medium due to electric fields may be significant. Third, assuming Poisson statistics accurately represents the collision distribution in space and time may not be accurate. This stems from only considering single events and not the effects of past events on future interactions.

One fairly successful attempt to overcome these issues was by Fermi [34] based on a suggestion in [35] to describe particle stopping as a polarization phenomenon in terms of Maxwell's equations. Lindhard took this one step further and developed a stopping theory

that claimed all collisional stopping could be described in terms of electromagnetic field equations regardless of regime or other assumptions. He introduced his dielectric function, $\epsilon(k,\omega)$, which depended on the wavenumber k and the frequency ω whereas other models at the time did not use both functional parameters. With this structure, Lindhard developed the first universal stopping theory applicable to all regions of interaction. The derivation of Lindhard's theory is quite involved and again is omitted for brevity. A full derivation can be found in [33]. The primary outcome from Lindhard theory is the following universal integral equation for the stopping force as a function of the dielectric function.

$$-\frac{dE}{dx} = \frac{ie_1^2}{\pi v^2}\int_0^\infty \frac{dk}{k}\int_{-kv}^{kv} d\omega\ \omega\left(\frac{1}{\epsilon_l(k,\omega)} - \frac{v^2}{c^2}\ \frac{k^2 - {\omega^2}/{v^2}}{k^2 - \epsilon_t(k,\omega){\omega^2}/{c^2}}\right) \tag{2.35}$$

When longitudinal and transverse dielectric functions are equal, $\epsilon_t = \epsilon_l = \epsilon$, (2.35) becomes

$$-\frac{dE}{dx} = \frac{ie_1^2}{\pi v^2}\int_0^\infty dk\ k\int_{-kv}^{kv} d\omega\ \omega\left(\frac{{1}/{\epsilon} - {v^2}/{c^2}}{k^2 - {\epsilon\omega^2}/{c^2}}\right) \tag{2.36}$$

Although this result is more complicated than that of Bohr, Bethe or Bloch, the beauty of the Lindhard equation is that it is a universal equation that does not suffer from problems that plague other theories. For this reason, and the success of the theory with dielectric functions developed by Lindhard, Lindhard theory became very popular. A modification to this theory by Lindhard, Scharff and Schiøtt, called LSS theory [36], has become the most commonly used in the field of theoretical stopping.

2.4.5 Validity of Theory in Practice

With an assumed understanding of particle penetration, the theory was implemented in the experimental world for validation and prediction purposes. This involved implementing theoretical equations into computer simulation models to calculate stopping powers and penetration depths of different projectile-target combinations at varying energies. The challenge with validating the Bohr, Bethe and Bloch theories was that experimental applications were limited to energies that could be produced by man made machines, which, at the time, were typically energies too low to meet velocity criteria for interactions with the target electrons. Therefore, these theories could not be directly validated experimentally. For the Lindhard theory, which has no velocity constraints, theoretical predictions did not match experimental results at these low energies to an acceptable level. The best results were observed in using

the LSS model which was correct to within a factor of 2. These issues at low energies (keV and MeV) led to the creation of empirically based models to predict outcomes at other energies and projectile-target combinations through interpolation and extrapolation of accepted experimental results. Through primarily empirical data and modeling, many approximate scaling rules started to be uncovered and as more trusted data was measured, the more accurate the models became. This led to very successful results of models predicting future experiments. Noteworthy programs include Pstar, Astar, Estar (for protons, alpha particles and electrons respectively) developed by ICRU and NIST [37] which uses Bethe theory with empirical input for I values and correction values, CasP code [38] (no longer available) and the SRIM code [39] which has become the most popular of the empirical models.

Although the empirical models have become the most accurate method for low energy projectiles due to the availability of experimental data, the theoretical approach is still the most accurate at high energies. For these high energy particles, Bethe theory is considered to be correct and is used by many programs to calculate high energy stopping. The question for these models becomes, where is the transition between low energy empirical models and high energy theoretical models? For most programs, the boundary exists where the two models converge in their respective results and a smooth transition can be made from one to the other. For example, this typically happens around 0.5 MeV for protons and 2 MeV for alpha particles [37]. This transition energy is different for every projectile type and, to a lesser extent, target particle type.

2.4.6 SRIM

The Stopping and Range of Ions in Matter (SRIM) code is an empirically based simulation model written and maintained by J. F. Ziegler [39, 40, 41]. New versions of the software were periodically released with the most recent version having been released in 2013. The primary, and arguably most useful, output is the projectile range distribution. Other outputs include collision events, target ionization, energy lost to target recoils and energy lost to target phonon distributions to name a few. The projected range is the primary output due to its use in ion implantation where experiments are designed to implant materials with ions at specific depths and concentrations. This is highly used for semiconductor doping, thin film technology, and creation of embedded layers for electrical applications.

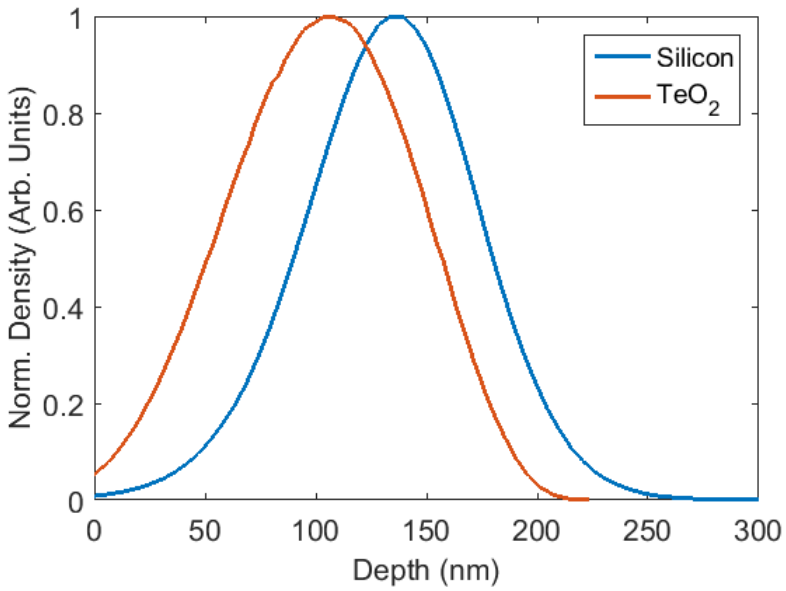

Figure 2.3: Normalized example SRIM expected range profiles of 10 keV protons into silicon and TeO_2. Area can be scaled to equal incident fluence. Typically heavier targets have more shallow penetration depths, as shown here.

SRIM is a fully empirical model that uses careful interpolation and extrapolation techniques of experimental data along with empirically identified scaling rules to predict the stopping of any projectile-target combination up to an energy of 10 GeV/amu. The foundation of the SRIM empirical database is a robust data set of hydrogen and alpha particle stopping data acquired at a large variety of energies for a variety of target materials by Andersen and Ziegler in 1977 [42]. The first iteration of the SRIM code was based solely on this data set using techniques to extend predictions to all projectile-target-energy combinations. Since inception, SRIM has been continually adjusted and calibrated by the addition of an increasing number of data sets as reliable stopping measurements became increasingly abundant for various experimental combinations. This data is incorporated into the SRIM database and is used to increase the accuracy of the model. Details of this incorporation and adjustment are not public knowledge. However, over the years, Ziegler has had an open invitation to submit reliable experimental data to him for use in the model. As per the SRIM official website, the SRIM model contains "100 years of Ion Stopping Data" and has been used in over 2300 publications. Figure 2.3 shows an example output of SRIM for the ranges of 10 keV protons into silicon and TeO_2. Note that SRIM does make a few assumptions that

theoretically will skew results, however the agreement with experimental data is undeniable. These assumptions include a target temperature of 0 K *i.e.*, target atoms are stationary, each simulated trajectory is simulated with an undamaged material *i.e.*, previous damage events are not taken into consideration and high level structure dependent effects are not considered as SRIM takes as input only the chemical formula and density of the target. As can be seen in Figure 2.3, the more dense target (TeO_2) has a lower penetration depth as expected.

2.5 Induced Damage Background

As previously mentioned, when an incident energetic particle interacts with a target particle, there is a transfer of energy, E_T. If $E_T > E_d$, the target particle is removed from the lattice site and can go on to cause more collisions. If $E_T < E_d$, the interaction results in a vibrating lattice atom that dissipates its energy into lattice phonons (lattice heating). When $E_T = E_d$, the target particle is displaced but does not have enough energy to cause future damage and thus comes to rest nearby as an interstitial atom. In this case, a vacancy-interstitial pair is created. This is called a Frenkel pair, or a Frenkel defect. In regard to what happens to the incident particle after the interaction, there are three cases. If the incident particle still has significant energy, it will continue on to cause more collisions. If the leftover energy is moderate, close to, but less than E_d, the incident particle will travel a short distance from the collision site, have one final interaction where the energy transfer will cause a lattice vibration and the incident particle will come to rest as an interstitial. Finally, if the leftover energy is small, much less than E_d, the particle will fall into the empty lattice site and attempt to bond with adjacent atoms. If the incident atom in the collision is a different species from the target atom of the collision, this is an impurity replacement collision. However, if the projectile and target are the same species, e.g., in self-ion implantation or when the incident particle is a secondary projectile from another collision, this is called a replacement collision. In a replacement collision, there is no increase to overall material damage, other than potential lattice heating, as the collision lattice site has maintained the ion species and there is no net increase to the number of projectiles. Figure 2.4 shows an illustration of a charged particle incident on a material and the resulting cascade effect along with different possible interaction event outcomes.

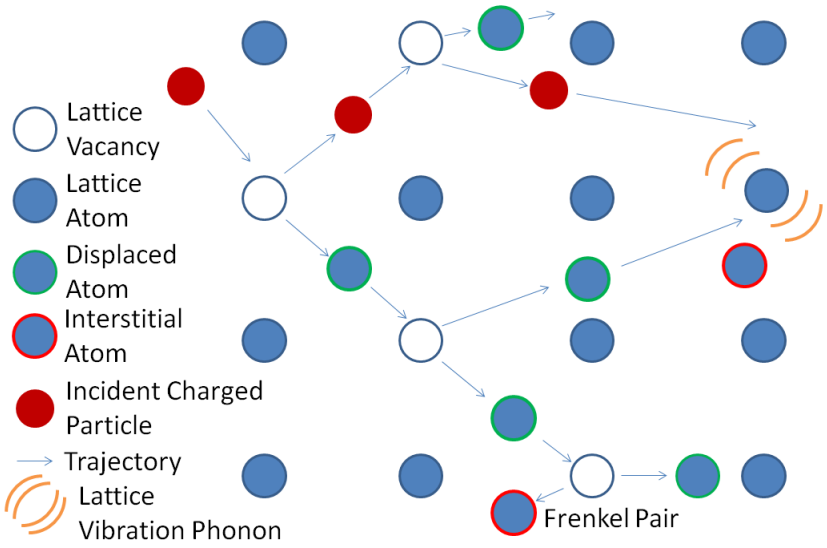

Figure 2.4: Illustrative example diagram of an incident charged particle creating a damage cascade and different possible interaction event outcomes.

2.5.1 The Bragg Curve and Bragg Peak

Figure 2.1 showed a plot of energy deposition rate as a function of energy for both nuclear and electronic stopping. This information can be used to create plots, called Bragg curves, of stopping power (energy/distance) as a function of distance traveled through a material for a specific incident energy. Example Bragg curves for variable energy protons into a high density polymer are shown in Figure 2.5. As can be seen, the Bragg curves have a sharp characteristic peak near the particle end of range. This is the Bragg peak and exists due to the energy dependence of nuclear and electronic stopping. As the particle passes through the material, it slows down. This increases the interaction time of Coulomb interactions with the target nuclei thus increasing the nuclear stopping probability. At the same time, electronic stopping probability decreases with the velocity reduction. The increased nuclear interaction probability decreases the mean free path of the incident particle. The result is a substantial amount of energy deposited to the material by the incident particle, due to high energy transfers in nuclear collisions, in a short distance, thus creating the Bragg peak.

The existence of the Bragg peak is paramount to understanding charged particle radiation damage not only in regard to where substantial energy transfer occurs (predominantly at the end of range) but also on the type of transfer. As briefly mentioned earlier, nuclear stopping

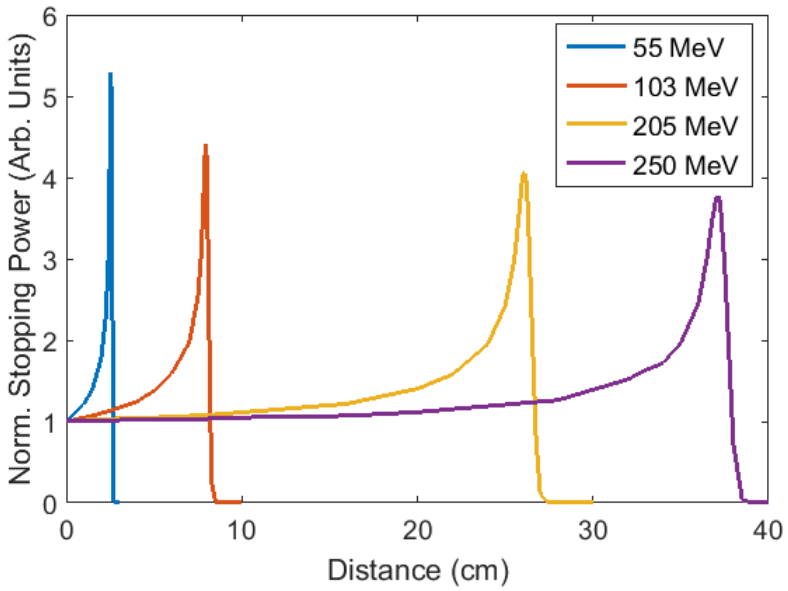

Figure 2.5: Example Bragg curves for energetic protons incident on a high density polymer. Data from [43]. As energy is increased, the position of maximum energy transfer increases. In comparison to SRIM plots, maximum energy transfer occurs just prior to the particle end of range, or depth.

collisions are the most significant in terms of material property altering radiation damage as they have the highest rate of lattice atom displacement and cascade effects. Electronic stopping and energy transfers typically only affect the ionization state of target atoms, which can lead to an increased probability of a nuclear collision in the future, but rarely causes atomic displacements and significant structural damage. Therefore, knowledge of the position where maximum nuclear stopping occurs, the Bragg peak, gives positional knowledge of the primary damage region. The curves of Figure 2.5 should look very similar to the SRIM curves in Figure 2.3 that show where the implanted ions comes to rest; they come to rest immediately following the Bragg peak, when they have depleted their energy.

The most significant information to take away from stopping theory and the Bragg curve is that, in terms of structural material damage, nuclear stopping is the most significant due to the displacement of target atoms. Therefore, information on where this stopping occurs, the Bragg peak, as well as where the incident particles end up, their end of range - SRIM, is crucial knowledge. A secondary result is information on required target thickness to stop an incident particle at a given energy. If the material thickness is larger than the Bragg peak

depth, no radiation will be able to pass through. If the thickness is much smaller than the Bragg peak position, all particles will pass through and insignificant damage, dominated by electronic stopping, will occur. In some cases, there will be no induced measurable effect.

2.5.2 Measurable Effects

The definition of a measurable effect can be highly variable and can depend on measurement equipment sensitivity. In cases where atomic level measurements are possible, the number of measurable effects increases as measurement can focus on very specific damaged areas. This level of measurable effect can also be observed with very low doses of radiation if exact positioning of collision events is known. For the purpose of this work, a measurable effect refers to a macroscopic effect, *i.e.*, an effect measurable by examining bulk sections of the material. For this definition, substantial radiation damage is required to manifest in observable property changes as low amounts of damage will not have a high enough concentration to change bulk material properties. This means scenarios such as high energy particles incident on a thin material will not produce measurable damage and, on a macroscopic level, the particles can essentially be considered to have passed through the target with no effect.

The number of observable measurable effects is quite large, and all effects will not be mentioned or discussed in detail. A thorough review of effects can be found in many references such as [21]. As has been mentioned, optical properties are the primary interest of this work. Optical property effects can include changes to the refractive index, degree of birefringence (total loss of birefringence in some cases), luminescence, reflectance, transmittance and absorbance to name a few. In the case of birefringent materials, the degree of birefringence is altered by disrupting the lattice structure and birefringence is lost when the damaged layer reaches a state of total disarray. In some cases, amorphization of the damaged layer is possible. Also in birefringent materials, choice of polarization sensitive optical properties can lead to detailed property information or use of unpolarized light can be used to investigate a high level presence of damage, *i.e.*, changes in the optical properties. The latter will be used later in this work to investigate if radiation damage occurs as a result of proton irradiation of specific materials and at what fluence these changes occur. More in depth measurements that require specific light polarization, crystal orientation knowledge and more sophisticated techniques are left as future work.

2.6 Additional Dependencies and Effects

2.6.1 Annealing

Annealing is a technique used to promote the recombination of interstitial atoms and vacancies by increasing the mobility of the interstitial atoms via a material temperature increase [44]. As the interstitial atoms move through the lattice, they can 'collide' with vacancy sites and reform bonds through recombination; an energetically favorable state. This process repairs induced damage and reduces the amount of retained damage in a material. Annealing, as described, only occurs in crystalline materials where there is a defined structure to reform. Annealing is very common in ion implantation. One common use is the thermal activation of implanted dopants in semiconductors [45]. In this process, additional thermal energy is required to allow interstitial dopant ions to move through the material and combine with lattice vacancies created by the implantation process (radiation damage). This process also increases recombination of original lattice atoms with vacancies. Recombination rates depend on temperature and defect mobility. At room temperature, defect mobility is generally not sufficient to result in substantial, long-range, recombination.

Another common use is to implant an embedded layer of ions, well below the surface, and use annealing to recover the small amount of induced damage in the surface layer above the implanted layer. This is possible due to the damage distribution being sharply peaked at the Bragg peak. When annealed, all damage is reversed to some extent. However, as there is less damage to recover in the upper layer compared to the heavily implanted layer, it is more easily recovered and, as a percentage, more recovery will occur in the minimally damaged upper layer. As a general rule, the more damaged a layer is, the less effective a given annealing technique will be. In some cases, such as amorphization of a crystal material, temperature increases are not always able to restore the original crystal structure. In the opposite case, a lightly damaged crystal structure, with the macro structure still intact, will have high recombination at relatively lower temperatures. Commonly used annealing temperatures (for implanted silicon) are of the order of 500 - 1000 °C, with the most common value being around 800 °C. Required temperatures are material dependent, but are at minimum an order of magnitude above room temperature; substantial annealing does not occur without intent.

2.6.2 Dynamic Annealing and Retained Damage

Dynamic annealing describes the situation in which a material recovers induced damage through recombination by itself without substantial heating outside of the natural ambient temperature or temperature increases due to irradiation. This is more likely to occur at low damage levels where the larger crystal structure is very much intact and only a small amount of heat energy is required to permit recombination. This does not include replacement collisions that were discussed earlier. Self-annealing can happen in one of two ways.

First, a Frenkel pair can be created such that the inherent vibrational energy of the interstitial is enough to cause a recombination interaction. This process depends on material temperature. Therefore, implants that occur at higher substrate temperatures will have less retained damage than lower temperature implants. Retained damage refers to the damage state of the material once equilibrium has been reached in terms of defect mobility and recombination at a given temperature. It is effectively equal to induced damage minus dynamic annealing recombination. In order for retained damage to equal induced damage, the irradiation would need to occur at a material temperature of absolute zero.

The other scenario in which dynamic annealing can occur is due to the incident radiation causing substrate heating. This happens in two ways. First, this can happen locally, at an atomic level, in what are referred to as thermal spikes. Thermal spikes occur when collision events in a small area create large local heating through dense damage cascades or high probability electronic stopping collisions. If enough atoms in a small area become displaced, the area can be considered to be 'melted' and the defects do not behave as individuals but have many-body group dynamics. This heating causes large movement of defects in a very small time frame and as the heat dissipates, annealing effects can occur. These spikes can also create defect clusters that are much harder to anneal than individual defects as the cluster must first be broken up before recombination can occur. In all cases, thermal spikes are very short lived, of the order of ps, and thus long-range annealing does not occur, as the heating quickly dissipates throughout the lattice and results in very minor (almost negligible) macroscopic lattice temperature increases [20]. The second way sample heating occurs is through stopping interactions that produce lattice vibrations (phonons). This causes macroscopic heating and increases to dynamic annealing throughout the implanted region.

2.6.3 Effects on Radiation Damage and Space Qualification

Retained damage and dynamic annealing depend on temperature, incident flux and material properties. As discussed, everything effectively revolves around substrate temperature and heating; retained damage decreases with increasing temperature. In the present work, the substrate ambient temperature is room temperature. While this is not high enough to support active annealing, there are known effects on dynamic annealing and retained damage at room temperature in some materials [46, 47]. The next dependence is on flux. A higher flux will increase sample heating and generally decrease retained damage. However, there are scenarios in which higher flux values will produce higher retained damage than at lower flux values. The argument here is that at a low flux, the material will be in a low damage state where annealing effectiveness is high and the recovery time in between damage events is long enough to never allow the material to reach a high damage state where dynamic annealing becomes ineffective. Therefore, the retained damage is lower than at high flux values where substantial damage occurs in a small time frame and dynamic annealing cannot keep up, thus resulting in a damage state where dynamic annealing becomes ineffective. The details are dependent on a number of factors including incident particle species and target material. For particle species, the dependence is simple, higher mass ions create increased retained damage. The details of each dependence are similar for most crystalline materials. As a reference, details for temperature, flux and species dependence in crystal silicon can be found in [47, 48, 49].

As will be seen in later sections, each of these dependencies can have different effects on the results and conclusions of this work. Given the relative ease to produce substantial damage with heavy ion implantation, majority of studies use heavy ions. In general, current literature suggests that low mass ions (protons) may not be able to induce certain types of damage that are observed with heavy ion irradiation, even with high doses or low temperatures. Therefore, comparison of published heavy ion results, such as Si^+, with low mass ion results obtained in this work is not always straightforward. However, for the purpose of space qualification, these high mass ions are not a concern due to the much higher abundance of low mass ions, specifically protons. In this regard, the flux and fluence dependencies are more important, especially when implementing accelerated lifetime testing at a higher than observed flux to examine multiple years' worth of damage in a much shorter time

frame (hours). Given that the present work occurs at room temperature, the fact that most spaceborne optics are temperature controlled to roughly room temperature, and the fact that induced heating from implemented fluxes is likely too low to cause sample temperatures to reach substantial annealing levels ($\sim$500°C), it is not expected for results to be unrealistic or have large discrepancies between real and experimental environments. However, any differences in dynamic annealing, however small, will affect measurable damage and subsequent lifetime calculations. Based on the large difference in flux values, this is a possibility.

2.6.4 Channelling

Channelling is an effect present only in highly long-range structured materials, such as crystals. Channelling causes an increase to the depth of the damage/implanted layer beyond the expected range (range when channelling is not a factor) [50]. The effect is dependent on particle angle of incidence with respect to the crystal orientation. The incident particles can travel down areas, or channels, in the material without strongly interacting with lattice atoms for long stretches that would not be possible at other angles of incidence. Channelling can be aided by small Coulomb deflections of the incident particle by lattice atoms that can keep the particle contained to a channel for a long period of time. Since its discovery, researchers have learned to used channelling to their benefit to achieve deeper implants at lower energies and reduced damage levels in the upper layer due to decreased interactions.

Channelling is significant for crystal components with cut angles along a principle axis such that normal incidence radiation (typical incidence angle for ion implantation) is aligned with a crystal axis. This is not a significant effect in a natural environment such as in space where radiation is incident from all angles. Some particles will experience channelling but the majority will not and the overall distribution will be relatively unaffected. However, as radiation testing is done in the lab with strongly directed radiation in a small cone of angles, channelling has been observed to affect results when not accounted for [20]. To avoid channelling, ion implantation and radiation damage research simply offsets the sample face from normal incidence by a small amount (standard value is 7°). This practice was implemented in the present work to minimize potential channelling effects.

2.7 Damage Calculations: DPA

As mentioned, the processes for each type of radiation, gamma, electron, neutron and charged particle, are all different and induce variable damage, even at comparable doses. The word dose has different meanings when referring to different radiation types. The SI unit of absorbed radiation dose is the Gray, where 1 Gray = 1 Joule/kg. In charged particle radiation, the more common unit for dose is number of particles per unit area, *i.e.*, fluence. However, in both cases, consideration of absorbed dose alone does not give the full induced damage story as damage processes vary. To bridge this gap, and allow cross comparison of different radiation types, a new unit was developed called DPA, or the *number of displacements per atom in the solid*. This refers to the number of vacancies created by incident radiation per atom in the solid. This unit is very useful for cross comparison of induced structural damage but does not account for electronic excitation and ionization effects. To calculate DPA, let $v(x)$ be the number of vacancies created per unit length along the track of the incident particle. The the total number of vacancies created along the ion track is

$$\int_0^d v(x)\ dx \tag{2.37}$$

This is converted to a number density of vacancies created per second per unit volume by multiplying by particle flux, ϕ, and dividing by total distance, d, traveled by the particle.

$$\frac{1}{d}\int_0^d v(x)\phi\ dx \tag{2.38}$$

Dividing the above volumetric vacancy creation rate by the target particle number density, n, then gives the vacancy creation rate per atom of the target material

$$\left[\frac{DPA}{s}\right] = \frac{1}{d}\int_0^d \frac{v(x)\phi}{n}\ dx \tag{2.39}$$

While DPA is very useful for cross comparison of damage types, it is rarely used outside of this purpose as the individual units within different radiation type fields are still strongly preferred. Therefore, as charged particle radiation is the only radiation type explored in the present work, resulting fluence values are not converted into DPA values. This is left as future work if direct comparisons of damage from different radiation types is desired.

Chapter 3

Beamline Design Background

Design and implementation of an ion beamline system is the culmination of a series of individual design components combined into one large system. Every design choice not only affects the performance of an individual component, but also affects other components and the larger system performance. Therefore, each component must be designed, implemented, tested and characterized both in isolation and within the larger system. System level design considerations may lead to sub-optimal individual component designs but permit increased optimization of other components and the overall system. Given the connections between multiple components and design choices, the overall design process is both linear and iterative, including multiple feedback loops and parallel design branches. This chapter presents required component design background as well as the connections to the larger system level design. Chapter 4 presents final beamline design specifics.

A high level outline of the system design is presented first to provide context for the following discussions. A schematic cross section of the beamline is provided in Figure 3.1 to provide system scale and general layout. The heart of the ion beamline is the plasma source whose role is to create sufficiently dense plasma to supply the beamline with a sufficient number of ions. The plasma source is contained within the ion source whose role is to 'extract' and deliver ions to the downstream beamline components. Extraction is aided by biasing the plasma source positively with respect to the extraction electrode and the remainder of the system, to establish a potential gap. A consequence of the plasma source bias is that it must be electrically isolated from all other system components. Before beginning ion source design, the plasma source must be fully characterized, as plasma properties influence the remainder of the ion source design. The ion source also contains the ion optics, which are responsible for beam formation. The strength and effect of ion optics is dependent on geometry and,

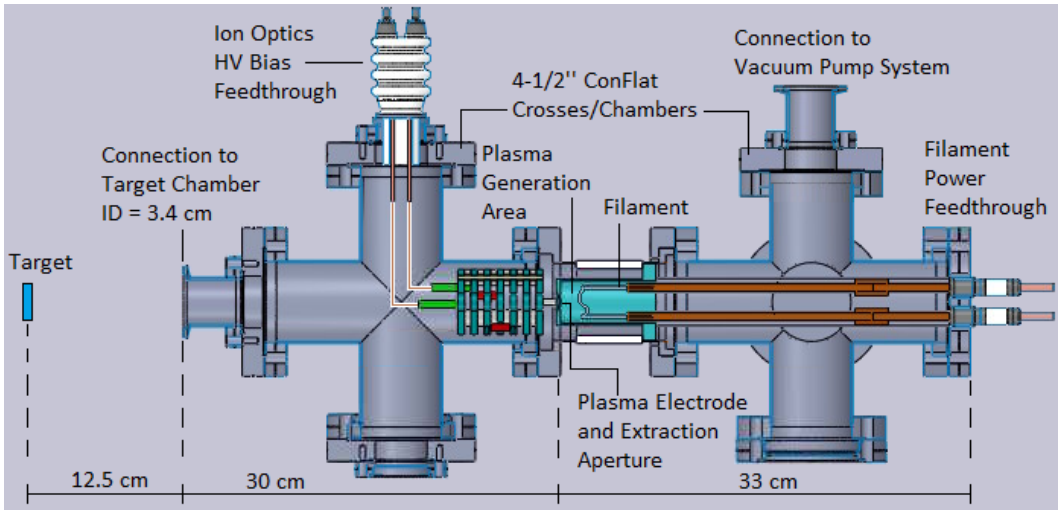

Figure 3.1: Full system cross section of the beamline to illustrate system size and relative positioning of elements including filament, plasma generation area, plasma electrode, extraction aperture, ion optics and target.

for electrostatic optics, the applied electrode voltages. Design of the ion optics is aided by computer simulation packages or programs to account for the large number of codependent variables that exist in the system. The ion optics are found in the transport column; the vacuum component that links the plasma source to the target chamber and supplies access points for required diagnostic or beam modification equipment, prior to the target. The length of the transport column defines beamline length and is typically kept as short as possible. The target chamber contains both the target and system performance diagnostic tools for characterization and monitoring purposes. Performance is measured by the ability to deliver beam current to the target and by the beam current density profile, which are both measured in the target chamber. As the target is typically ground referenced, the ion energy is equal in magnitude to the plasma source bias multiplied by the ion charge state.

3.1 The Plasma Source

The plasma source, characterized by the plasma ion density, n_0, and electron temperature, T_e, is the fundamental component of the ion source and overall system. As a general statement, plasma is a collection of positive ions and free electrons created by supplying energy to a collection of atoms or molecules in the gaseous state causing a portion of the atoms to become ionized. The ionization process in a plasma source occurs through *electron-impact*

ionization. Energy is supplied to the gas by an applied field that accelerates free electrons, which are either naturally present or introduced by an additional source. As these accelerated electrons traverse the gas, some will interact with the gas atoms and cause a transfer of energy. Interaction theory was discussed in Chapter 2. Interactions can be elastic or inelastic and occur through the Coulomb interaction between the incident electron and the target electrons or nucleus. If sufficient energy transfer occurs, the neutral atom expels a new free electron and becomes a positively charged ion. Energy can be provided to free electrons through a variety of processes. Source types include RF inductively coupled, helicon, arc-discharge and filament driven sources to name a few. All plasma sources typically operate inside a vacuum chamber to allow accurate control of background gas composition and pressure. This provides control of both ion density and the type(s) of ion(s) created. The present system uses a hot cathode filament driven source and thus will be the focus source type from here on.

3.1.1 Hot Cathode Filament Source: Principle of Operation

Unlike other source types that require naturally occurring free electrons in the chamber to ignite the ionization process, the hot cathode filament source supplies the required quantity of free electrons to the system through thermionic emission caused by Ohmic heating of the filament. The number of additional electrons added to the system is controlled by filament temperature, which is controlled by altering the filament current. As filament current increases, the filament temperature and thermionic emission rate also increase due to the increased power dissipation of the resistive filament. Control of the number of electrons added to the system provides partial control over the ionization rate as more electrons equates to a higher ionization rate through probability; there are more chances for a collision to occur with more incident projectiles. Ionization rate control then grants control of ion density. A limit to the statement that more electrons equals higher ionization rate is the scenario in which the plasma is already fully ionized. In this case, adding more electrons does not increase the ionization rate or ion density. A fully ionized plasma does not mean a degree of ionization (number of ions/[number of ions + number of neutrals]) of one, as this is not possible to obtain, but instead refers to a state where the electron-ion collision rate is greater than or equal to the electron-neutral collision rate. This is called a *Coulomb-collision dominated regime* and can occur at a degree of ionization as low as 0.01 [51]. Filament driven

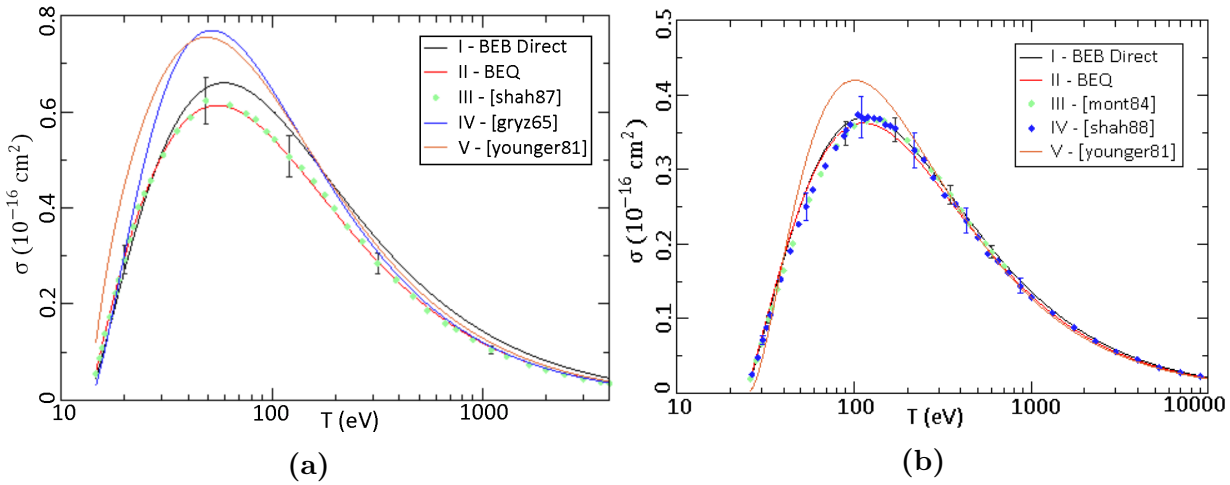

Figure 3.2: Electron-impact ionization cross sections of (a) hydrogen and (b) helium. Obtained from [52].

sources are widely used, especially for high density applications, based on their history of success and achievable plasma densities with comparatively low power consumption.

In order to ionize the background gas, electrons emitted from the filament must be accelerated by the applied field. In the present system, acceleration is supplied by negatively biasing the filament with respect to the chamber walls to create an acceleration gap. Required ionization energy depends on the species of atom or molecule. On top of the minimum required ionization energy, which can be as low as a few eV, the ionization cross section, or probability of an ionizing collision occurring, is energy and species dependent. For hydrogen, the ionization energy is 13.6 eV, but the electron-impact ionization cross section has a maximum value at approximately 80 eV as shown in Figure 3.2a [52]. The maximum being contained in a broad peak with little variation between 50 and 90 eV results in flexibility on bias voltage precision requirements to obtain a high ionization probability. For helium, the cross section peaks at approximately 110 eV and is also contained within a broad peak of minimal variation as shown in Figure 3.2b. Following an ionization collision, both the incident electron and new free electron are accelerated by the applied field and can cause future ionizations. This chain reaction helps to sustain stable plasma.

3.1.2 Filament Design Considerations

Inspiration for the plasma source design was drawn from the Freeman and Bernas hot filament cathode source designs [53]. A cross section view of the plasma source design was

included in Figure 3.1. The filament is immersed in a source gas inside the plasma chamber and is biased negatively with respect to the chamber walls. There are three primary choices for filament system design: distance between the filament and the chamber walls (acceleration gap distance - modified by filament mounting), filament material, and filament coil dimensions. The length of the acceleration gap affects the time and space given to emitted electrons to gain energy before reaching a chamber wall and being electrically lost from the system. If the gap length is too small, the electrons will not reach full energy (optimal cross section) before colliding with the anode. This causes sub-optimal ionization or, in the lower limit, zero ionization if the minimum ionization energy is not obtained. As an upper limit, the gap length can become too long to sustain stable plasma or cause decreases in density by increasing the volume. While plasma can be created in the gaps between the filament and any chamber wall, one wall is chosen as the extraction wall or plasma electrode. The plasma electrode separates the plasma chamber from the remainder of the system and contains the extraction aperture that allows ions to pass into the beamline. The area between the filament and the plasma electrode is the plasma generation area, also referred to as the electron acceleration gap. This gap distance is optimized for plasma creation while all other filament-chamber wall gaps are ignored.

Choice of filament material is limited due to high melting point requirements. The material must be able to withstand high temperatures induced by direct heating from the filament current as well as additional heating from interactions with the plasma. The material must be pliable such that it can be bent into the desired configuration. It must also be capable of supplying thermally emitted electrons, but the emission rate at given temperatures must also be considered. The most common material is tungsten, primarily due to its high melting point and successful history. Other common materials include oxides, borides, and thoriated tungsten. While very popular for a time, due to increased emission rates, concerns of radioactivity and toxicity of the thorium has greatly decreased the use of thoriated tungsten.

The generic filament structure is a coil of n turns. Design choices include wire thickness, number of turns and turn diameter, which dictates the required wire length. The filament resistance and total number of emitted electrons for a given temperature are both influenced by wire thickness and length. The thermionic emission rate is proportional to filament

resistance, which is proportional to wire length and inversely proportional to cross sectional area. If maximum emission rate is top priority, this suggests that a filament should be constructed from a large length of small diameter wire coiled into a large number of turns with large diameters. However, the more important plasma generation factor is the total number of electrons emitted at a given temperature. This is proportional to the emitting area of the filament, *i.e.*, the filament surface area, which is proportional to the wire diameter for a given length. This suggests implementation of large diameter wire, which contradicts the attempt to increase resistance. Adding to this competition, heating a large diameter filament to the same temperature as a smaller diameter filament will require more power due to the decrease in resistance and increase in amount of material to heat. Unless the larger emission area is required to supply enough electrons to the system, the choice of a larger diameter filament is a waste of power and electrons. The design philosophy for the present system was to supply enough electrons to create sufficient ion density with minimal power. Power limitation is desired to maximize the single use operational lifetime of the system as both the negative filament bias and the filament current are supplied by battery sources. This was required due to the high voltage (HV) bias of the plasma source. The single use lifetime of the batteries, prior to requiring a recharge, defines the single use lifetime of the system. As this lifetime depends on power requirements, maximizing the system lifetime required choosing low current, high resistance filament design options.

3.1.3 Vacuum and Gas Management System

The gas management system is composed of vacuum pumps, vacuum connections and gas flow systems. Together, these components create an equilibrium condition inside the chamber that defines the plasma source operating pressure. Variable operating pressures are obtained with a combination of vacuum pump speed throttling and alteration of gas flow rate. As vacuum pumps are not meant to operate at variable speeds, pump speed throttling is obtained with a valve system between the chamber and the pump that can be partially closed to constrict gas flow. Gas flow rate variability is more straight forward as off the shelf mass flow controllers (MFCs) provide calibrated and programmable flow rates over reasonably large ranges.

The primary design concern for source operating pressure is to maximize ion density for a given source configuration. The operating pressure affects ion density by altering the

number of neutrals available to be ionized. In general, ion density will continually increase with increasing source pressure (increased number of ionization targets), but not indefinitely. An upper limit exists that once passed will cause ionization rate and ion density to decrease with increasing pressure. This occurs when the number of targets causes the electron mean free path (λ_e) to decrease to the point where the electrons can no longer achieve optimal ionization energy in between successive collisions. This is similar to the previous issue of a too short acceleration gap. The upper limit occurs when λ_e becomes so short that the electrons cannot obtain the minimum ionization energy and no ionization collisions occur. Optimal performance in this regard is obtained when conditions create λ_e equal to the required electron acceleration distance such that both collision probability and electron re-energizing time are optimized. In practice, systems tend to err to low pressures as this guarantees electrons will reach maximum energy. This also uses less source gas which increases source efficiency.

The gas management system must also take into consideration the HV system design including potential breakdown conditions. The plasma source bias above lab ground means vacuum pumps and MFCs cannot be electrically connected to the plasma chamber as their ground referenced power supplies would cause electrical issues. This requires HV isolation connections between the source and vacuum lines or the use of an insulating material for the vacuum line. Regardless of isolation technique, the result is a positive bias on one side and a ground bias on the other that creates an electrostatic gap filled with gas that could result in electrical breakdown. This is called Paschen breakdown and is discussed in Section 3.3. To avoid Paschen breakdown, all electrostatic gaps must be designed such that conditions inside the gap create a *pd* (pressure times distance) factor that ensures breakdown is not possible. Typically, an operational pressure range is set and gap distance is designed around pressure, but physical constraints may require additional constraints on operational pressure ranges.

Performance of the gas management system is assessed based on the ability to achieve operational pressures and the desired base pressure. The base pressure of a system is the pressure reached with no obstruction to the pumping system and no external gas load. It depends on the quality of vacuum seals, the size of the chamber and the pumping capacity of the vacuum system. The desired base pressure partially influences the number and types of pumps required. As complete evacuation of any chamber is impossible, there will always be

some remnant gas in the system prior to flowing in the source gas. The ratio of base pressure to operational pressure provides a contaminant gas ratio, which is ideally zero. Realistically, the ratio will likely be of the order of 1% or lower, and the requirements for this ratio depend on the plasma purity requirements. As an example, if a source were to operate in the low mTorr range with a base pressure of 10^{-5} Torr, the impurity ratio would be of the order of 1%. Base pressures of 10^{-5} - 10^{-6} Torr can be achieved with basic vacuum system procedures and turbomolecular pumps. If a base pressure less than 10^{-6} Torr is desired, more effort is required. This may include better design or more advanced components, such as better seals.

3.1.4 Plasma Source Testing

Performance of the plasma source design is assessed by measuring n_0 and T_e of the created plasma to ensure sufficient operation for beamline requirements. Sufficient operation is determined by comparing the benchmark value discussed in Section 1.4, 0.445 $\mu A/cm^2$, with the calculated maximum current density obtainable from the source, the *Bohm current density*,

$$J_{Bohm} = Zen_0u_B \tag{3.1}$$

where Z is the ion atomic number, e is the elementary charge and u_B is the *Bohm velocity*, given in (3.2), where m_i is the ion mass.

$$u_B = \sqrt{\frac{T_e}{m_i}} \tag{3.2}$$

If $J_{Bohm} > J_{required}$, the source operation is deemed sufficient. While J_{Bohm} is theoretically obtainable, any real extraction system can rarely reach this value and thus the source is usually required to have a larger than necessary J_{Bohm} calculated value to supply the beam with a sufficient number of ions. While the ion density can usually be increased to increase the extracted beam current, care must be taken to ensure that this increase is not required to compensate for poor design in other areas such as beam transport, where losses can occur and create poor system efficiency.

3.1.5 Langmuir Probe Theory and Analysis

Calculation of J_{Bohm} (3.1) requires values for n_0 and T_e, which can be measured with a *Langmuir probe*, the most commonly used plasma diagnostic tool. A diagram of the basic Langmuir probe design is shown in Figure 3.3. The probe tip must be able to withstand

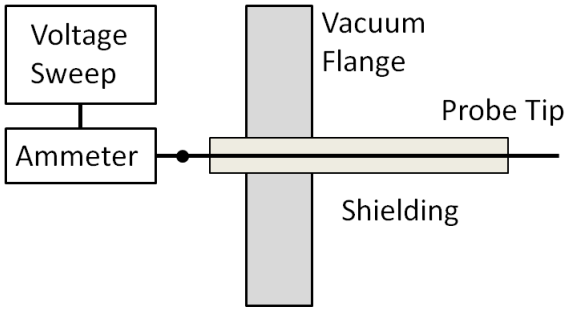

Figure 3.3: Diagram of basic Langmuir probe design elements.

high temperatures as operation involves direct interaction with the plasma and thus the most common material to use is tungsten. In principle, the tip can be any shape, but it is typically chosen to be a thin piece of wire such that it may be modeled as a cylinder in calculations. Once inserted into the plasma, free electrons and ions present in the plasma will naturally collide with the probe creating a measurable current whose magnitude is proportional to the surface area of the probe tip. The current magnitude is also influenced by the applied probe bias, which is scanned over a range of positive and negative voltages in a voltage sweep. The probe tip is kept as small as possible to impose a negligible perturbation on the plasma but still collect sufficient current for a measurable signal. In order to keep the probe tip small but able to reach the desired position within the plasma, insulating shielding is used to cover the part of the probe not meant to collect current.

Depending on the polarity and magnitude of applied probe bias, the collected current magnitude and percentage of collected electrons and ions will vary. A plot of collected current versus applied probe voltage produces an *I-V* curve, or *Langmuir curve*. The upper positive limit of probe bias creates conditions such that only electrons are collected as the applied bias repels all incoming ions and the lower negative limit creates conditions such that only ions are collected as the bias repels all electrons. These conditions create the electron and ion saturation regions respectively. Within these regions, the current value should theoretically plateau and the value of this plateau is the electron or ion saturation current value. In between the saturation regions, in the transition region, the probe collects a combination of electron and ion current leading to charge cancellation and lower current magnitudes. When the probe is biased slightly positive, some ions will still have enough

kinetic energy to overcome the potential hill and still collide with the probe causing them to be collected rather than be repelled. The same statement is also true in the case of a slightly negative probe bias causing some electrons to be repelled but some to still be collected. The number of electrons or ions that can overcome the bias boundary decreases with increasing bias magnitude until saturation occurs at a voltage where all electrons or ions are repelled. In theory, voltage increases past this point further into the saturation regions should not change the measured current magnitude. This is due to the fixed velocity and thus collection rates of electrons and ions, independent of probe voltage except in the case of a repelling boundary. However, in experiment, both regions have a slight slope due to plasma sheath expansion. The plasma sheath is a boundary that exists between the physical probe area and the plasma bulk whose area is determined by probe bias magnitude. Any ion or electron that enters the sheath is considered to be collected by the probe and thus the sheath can be considered as the effective probe collection area. As the bias magnitude increases, so does the sheath area, which is what causes the sloped saturation regions. One fundamental difference between the two saturation regions is the higher magnitude of the electron saturation current. This is due to the electron velocity being substantially higher than the ion velocity as a result of the substantial mass difference. This allows more electrons to be collected in the same amount of time than ions, which creates a larger current (charge/s).

Both T_e and n_0 values can be extracted from analysis of the Langmuir curve. In plasma that obeys the Maxwell-Boltzmann distribution (majority do), the electron current (I_e) grows exponentially with applied voltage in the transition region as described by:

$$I_e = I_{es}\ exp\left[\frac{e\left(\mathrm{V_p} - \mathrm{V_s}\right)}{k_B \mathrm{T}_e}\right] \tag{3.3}$$

where I_{es} is the electron saturation current, e is the elementary charge, $\mathrm{V_p}$ is the applied probe potential, $\mathrm{V_s}$ is the plasma potential (potential developed as a result of the loss rate of electrons and ions to the chamber walls favoring electrons due to their higher velocities which produces a net positive charge and potential in the plasma bulk), k_B is the Boltzmann constant and T_e is the electron temperature in Kelvin. If T_e is instead expressed in electron volts, the factor, $e/k_B\mathrm{T}_e$, becomes $1/\mathrm{T}_e$. Taking the natural logarithm of both sides produces (3.4). From here, a plot of $\ln(I_e)$ versus $\mathrm{V_p}$ results in a line with a slope of $1/\mathrm{T}_e$, where the

units T_e are eV. Taking the inverse of the slope value produces the electron temperature.

$$\ln(I_e) = \frac{1}{T_e} V_p - \frac{V_s}{T_e} + \ln(I_{es}) \tag{3.4}$$

The second parameter to calculate is n_0 which can be found from:

$$n_0 \approx \frac{n_s}{0.61} = \frac{I_{is}}{e u_B A} * \frac{1}{0.61} \tag{3.5}$$

where n_s is the number density in the sheath, I_{is} is the ion saturation current, also extracted from the curve, A is the probe tip surface area and u_B is the Bohm velocity. Technically, A is the collection area of the sheath. However, in many cases, such as the present case, this can be approximated as the probe tip area with minimal effect on calculation results. The factor 0.61 is a constant approximation factor of the difference between the density in the plasma bulk and in the sheath [54]. This is required because direct measurement of the bulk density is not possible. This calculation requires a value for I_{is}, which is a sensitive property to measure as there are multiple acceptable methods that all give slightly different values. Combine this with the fact that the ion saturation region can behave differently in different plasma regimes and obtaining an accurate I_{is} value becomes quite challenging. As Chen puts it, "Only on a good day can one measure n to within 10% using I_{sat}" [55] due to the inaccuracy of the I_{is} measurement. One of the more simple, yet sufficiently accurate for the purposes of this project, methods of obtaining an I_{is} value is to use the ion current value at the floating potential (V_f). This is the point on the Langmuir curve where the ion and electron current are equal and the net current is zero. To find the ion current at V_f, the data from the ion saturation region is fitted with a linear fit and extrapolated back to V_f. Methods such as this are necessary due to the sloped saturation region. If this slope did not exist, all values in the saturation region would be equally viable to use.

This basic implementation of a Langmuir probe and analysis technique does include some intrinsic error. These errors can be addressed in a number of ways such as implementing modifications to the probe system, or more intricate analysis techniques [55], which come at the cost of time and/or money. However, the errors are relatively small and only significant if high precision parameter measurement is required. In the present case, only approximate measurements are required due to large error tolerances that will be discussed later on. Therefore, the Langmuir probe was implemented as has been described.

3.2 The Ion Source

The ion source is comprised of the plasma source and the *extractor*. The plasma source acts as an ion reservoir for the remainder of the system and the extractor is a set of electrodes directly in front of the plasma source inside the transport column. The extractor aids the natural flow of ions from the plasma source and forms a target directed beam via electrostatic forces. A schematic of the *elemental ion source* adapted from [53] is shown in Figure 3.4. This basic design shows the extractor comprised of two electrodes while more sophisticated designs utilize additional electrodes. Electrodes are custom shaped metal plates with applied electrostatic potentials to create electric fields between adjacent electrodes. These fields accelerate or decelerate the ions and exert forces that enable beam control as the ions traverse the system. In the present design, all electrodes, chamber walls and vacuum fittings are stainless steel; a common material choice due to its resistance to out-gassing and ion-impact sputtering. The term extractor is misleading as it implies the need for an active extraction force to pull ions out of the plasma source and into the beamline, which is untrue. As long as the plasma source is positively biased, a natural flow of ions out of the extraction aperture will exist at a rate independent of the potential difference between the plasma source and the remainder of the system. A more accurate term for the extractor is the accelerator. However, due to historical use and intuitive visuals, the terms extractor and extraction are dominant in literature and will therefore be used in this work.

The first electrode in the extractor, the plasma electrode, is held at the same potential, V_{pl}, as the plasma source. This ensures the acceleration gap exists solely inside the extractor. In the present system, it is physically connected to the plasma source as it doubles as a chamber wall. The plasma source chamber geometry is typically cylindrical and extraction can occur from either the flat face or curved sides of the cylinder. The present system extracts from the flat face to avoid potential issues involved with side extraction. The second extractor electrode is electrically isolated from, and negatively biased with respect to, the plasma source. It is typically grounded and thus also referred to as the ground electrode. Circumstances in which a non-ground potential is required include resistance to Paschen breakdown by creating a slow potential gradient and cases that need additional beam for-

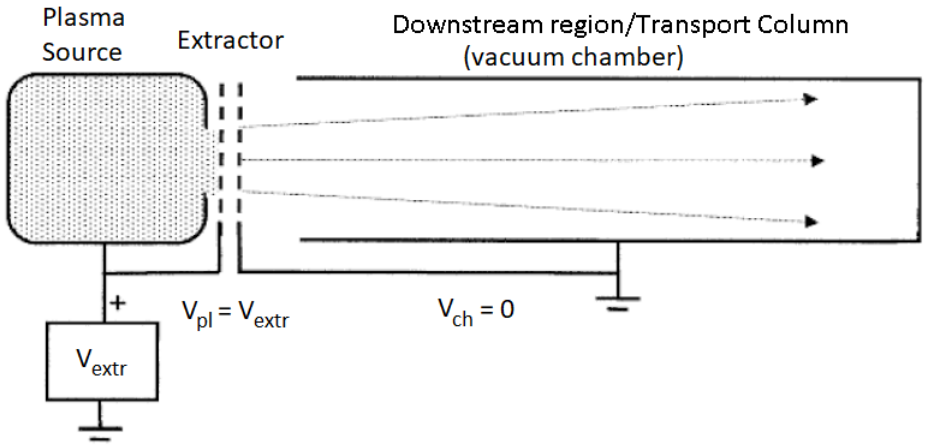

Figure 3.4: *Elemental ion source* schematic adapted from [53].

mation aid. Both the ground and extraction electrodes are flat faced and sit parallel to each other to create an approximate uniform field in the acceleration gap. The field will not be truly uniform as the electrodes contain aperture holes that alter field line geometry.

The extractor is also part of the ion optics chain and aids beam formation by manipulating a property called the plasma meniscus, which has a significant effect on the initially extracted beam. As part of the role of the ion optics is to ensure the beam does not collide with electrodes, the plasma meniscus is designed to aid initial extraction by keeping the beam from colliding with the ground electrode. This requires a converging effect as, upon extraction and throughout the beamline, the beam naturally wants to diverge due to the repulsive Coulomb force experienced by the beam ions due to the beam composition being dominated by positively charged ions. This is called space-charge repulsion and is a significant concern for beamline design [56]. Ion optics are implemented to combat space-charge repulsion and create desired beam sizes throughout the system. With properly designed ion optics, the beam will traverse the entire system without colliding with chamber walls or electrodes. The geometry and field strength design of the two electrode extractor must apply a force opposite to the repulsive space-charge force to allow the beam to pass through the ground electrode aperture and enter the remainder of the system. Once past the ground electrode, most systems employ further ion optics to provide additional beam formation and transport aid. This is the case for the present work and is discussed in Section 3.4.

3.2.1 The Plasma Meniscus

The plasma meniscus is a boundary layer between the bulk plasma and the ion acceleration gap. It defines the emission surface from which ions enter the acceleration gap, the emission angles and the initial extracted beam shape. The plasma meniscus also acts as a boundary for plasma source electrons as it reflects all electrons whose energy is less than the potential drop of the acceleration gap back into the plasma source, keeping them out of the remainder of the system [53]. Figure 3.5 shows a schematic of the two electrode extractor geometry and a representative plasma meniscus. The meniscus shape can be concave, convex, or approximately planar. If the meniscus is convex or overly convergent, the result is an increase to beam divergence within the acceleration gap. Generally, the plasma meniscus is desired to be planar or slightly concave to produce no change to beam divergence, or a slight convergent correction, respectively. The general optimal result is a plasma meniscus that creates parallel ion extraction through the extractor. If this condition is achieved, the ground electrode aperture size can be minimized, which increases the electric field uniformity. This will be elaborated on in Section 3.2.3 when electrode sizes and effects are discussed. While a properly designed plasma meniscus is highly beneficial, most beamlines are too long to have all required beam formation achieved by the meniscus effect alone, primarily due to space-charge repulsion effects experienced throughout the beam. Therefore, additional ion optics are required to maintain and further control the beam.

The plasma meniscus shape depends on ion density and electric field strength and geometry. For a given ion density, the shape can be controlled by the electrode system and for a given acceleration gap, the meniscus can be controlled by varying the ion density. The plasma meniscus shape can be determined with application of a manipulated version of the Child-Langmuir law, which describes the maximum emission current density that can be extracted in a plane parallel diode system separated by a distance, d, and a potential difference of U. This law assumes that both the emission area and the second plate are infinitely planar and that the emitted ions have no initial velocity in the direction of the second electrode. As the extractor electrode system is comprised of two parallel plates whose diameter is much larger than the emission area and whose apertures are small, this can be considered as a close approximation. The Child-Langmuir law is given by Equation 3.6 where ϵ_0 is the permittivity

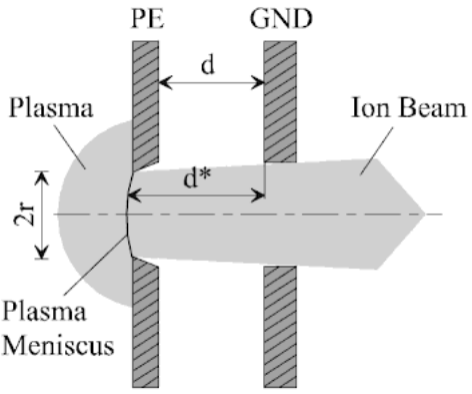

Figure 3.5: Schematic diagram of a two electrode extractor system and an example plasma meniscus. d is the gap distance between electrodes and d* is the true gap distance (distance from emitting area to ground electrode). Extraction aperture tapered to Pierce angle. Image obtained from [53].

of free space, e is the elementary charge, Z is the ion charge state and m_i is the ion mass.

$$j_{CL} = \frac{4}{9}\epsilon_0\sqrt{\frac{2eZ}{m_i}}\frac{1}{d^2}U^{3/2} \tag{3.6}$$

For a given potential drop and ion species, the distance required to extract a given ion density, j_{CL}, can be calculated. Recall that a positively biased positive ion source will produce a natural ion flow, J_{Bohm}. Therefore, the extracted current density in the system is known, and J_{Bohm} can be substituted for j_{CL} to calculate d, the theoretical acceleration gap distance.

$$d = \sqrt{\frac{4}{9}\epsilon_0\sqrt{\frac{2eZ}{m_i}}\frac{1}{J_{Bohm}}U^{3/2}} \tag{3.7}$$

The distance calculated here is the distance between an infinite planar emission area and the second electrode, which, in a real beamline, maps to the distance between the plasma meniscus and the ground electrode. This distance is labeled as d* in Figure 3.5. If the plasma meniscus is desired to be approximately planar, then the acceleration gap distance between electrodes (d in Figure 3.5) should be designed to equal the distance calculated by Equation 3.7 (d*). If the desired meniscus is convex or concave, then d should be greater than or less than d* respectively. The distance, d*, will always adjust such that the electric field at the plasma meniscus is zero. This property allows the d* parameter and plasma meniscus shape to be altered by the acceleration gap electric field.

3.2.2 Plasma Electrode Extraction Aperture

Design of the plasma electrode extraction aperture is critical to multiple different beamline considerations. Design choices include shape, size, and number of apertures. While many designs can benefit from a multi-aperture design, the present work uses a single aperture design and thus details of multi-aperture designs will not be discussed. A cross section of the aperture used in the present beamline was included in Figure 3.1 in Section 3.1.2. While the extraction aperture can have any shape in theory, the typical choice in practice is a circular aperture. This choice ensures an approximate Gaussian beam cross section which is the natural, and typically desired, beam shape. It also promotes symmetry of forces exerted on the ions and allows cylindrical symmetry assumptions to be used to simplify calculations. This choice and reasoning will be used again for the design of the additional ion optics. A further benefit is avoidance of sharp, pointed edges or features, like in a square, that can produce sparking, a safety hazard, due to the increased electric field strength in the immediate vicinity of points. Avoidance of these features requires an aperture with smooth edges. The other consideration for aperture shape is whether or not to use edge tapering on the beamline side of the plasma electrode. When tapering is used, the plasma side edge defines the amount of current (ions) and source gas atoms or molecules that can pass through to the transport column and the beamline side is tapered to alter the shape of the equipotential lines of the applied electric field. This tapering affects the plasma meniscus shape and contributes to initial beam condensing by providing a radially inward force on the ions. An example of tapering is shown in the angled aperture edges of Figure 3.5. Choice of taper angle is different for every system and can be aided with simulation. A commonly implemented angle is the Pierce angle (67.5°), which is derived from theory for use in electron sources where it guarantees parallel extraction of an electron beam [53]. While it does not guarantee the same for positive ions, it is still a common choice that typically produces beneficial results.

The choice of aperture size affects the total number of ions that flow out of the plasma source in a given amount of time (total current). While the initial current density is a fixed value defined by plasma properties, the total current will scale with aperture area. Assuming the final beam size differs from initial size, the final beam current density will also scale with aperture size. Therefore, aperture size increases as total current requirements

increase. However, increasing the aperture size does not come without negative effects on other design considerations. As the aperture links the plasma source to the downstream system components, it supplies a path for source gas to leak into the transport column and the target chamber, which causes an undesirable, yet inevitable, increase in background pressure. In the transport column, the increased pressure results in an increased rate of ion-neutral collisions that can have serious implications on beamline performance if not minimized. This is further discussed in Section 3.6.1. Ideally, the background gas pressure in the transport column and target chamber is zero or, realistically, as low as possible. Pressure minimization is achieved by attaching a second turbo pump to the downstream side of the beamline to remove background gas and by designing the extraction aperture to limit gas flow while still supplying a sufficient current. If sufficient current cannot be achieved without increasing aperture size to the point where gas leakage becomes an issue, plasma source modification is required to produce a higher ion density. This is critical to system performance as high transport column pressure can cripple an otherwise well designed beamline.

3.2.3 Ground Electrode

The ground electrode, also called the accelerator electrode, is the second component in the two electrode extractor design; the first electrode after the plasma electrode. This electrode creates the ion acceleration gap prior to ion beam optics and its position strongly influences the plasma meniscus shape. The design choices are shape, size, and position, of both the electrode itself and the contained aperture. The aperture position is fixed by the plasma electrode design as the aperture centers must align with each other. This ensures cylindrical symmetry of beamline forces and supports lossless transport through the extractor. Misalignment results in asymmetric forces that create asymmetry in the beam distribution.

Similar to the extraction aperture, the ground electrode aperture, and all future system apertures, can be any shape, but the dominant choice is for all apertures to be circular for the same reasons already discussed. The outer shape of the ground electrode is also typically circular. The primary reason is to minimize arcing conditions by removing sharp edge features from conducting surfaces of the system. This choice also makes the electrode match the shape of the transport column, which, if centered, makes the distance between the electrode edge and the transport column wall equal in all directions. While not significant

if the electrode is ground referenced, this allows precise design of gap distance to minimize Paschen breakdown conditions that are present for a non-grounded electrode.

The ground aperture diameter must be large enough to ensure passage of all extracted ions into the transport column. Any ions that collide with the electrode will be lost from the system and will lead to a decrease in operational beam current. The aperture diameter is designed with tolerances to err on the larger side to ensure full beam transport. As a starting point for design, the aperture diameter can be equal to the extraction aperture diameter. This assumes the initial converging forces provided by tapering and the plasma meniscus can overcome the divergent nature of the beam and create a converging or parallel beam. However, even with an initial converging effect, beam divergence can create a beam diameter larger than the extraction aperture within the acceleration gap and thus require a larger ground aperture. The discussion so far suggests that a continually larger ground aperture will give the best performance. However, in order for the fixed potential of the ground electrode to have maximum influence on the ion beam, the physical distance between the electrode and the ions needs to be minimized, *i.e.*, aperture size must be minimized. The effect of the electrode design on the beamline potential can be simulated with ion beam simulation software, such as IBSimu, which is further discussed in Section 4.6. Simulation provides plots of the electric potential in the radial beam center as a function of the distance along the beam trajectory. Figure 3.6 illustrates the effect of reducing the ground electrode aperture by a factor of 2 by comparing the implemented system geometry (blue line) to a system with the ground electrode aperture cut in half (red line). As can be seen, the potential inside the ground electrode at the beam center is not zero as one may expect.

As the beam center is the farthest point from the electrode influence, examination of the potential here yields the maximum deviation from desired potential. At the left edge of the ground electrode, x = 0.03 m on the blue curve, the potential is 430 V rather than the assumed 0 V. Further into the electrode, the potential reaches ground partly due to the width of the electrode and partly due to the rest of the components in this simulation also being ground. Therefore, the ions will still experience the full 10 kV drop, but at the beam center, this drop is distributed over a larger distance, which decreases electric field strength. Moving radially outward from center toward the electrode, the potential will slowly approach zero.

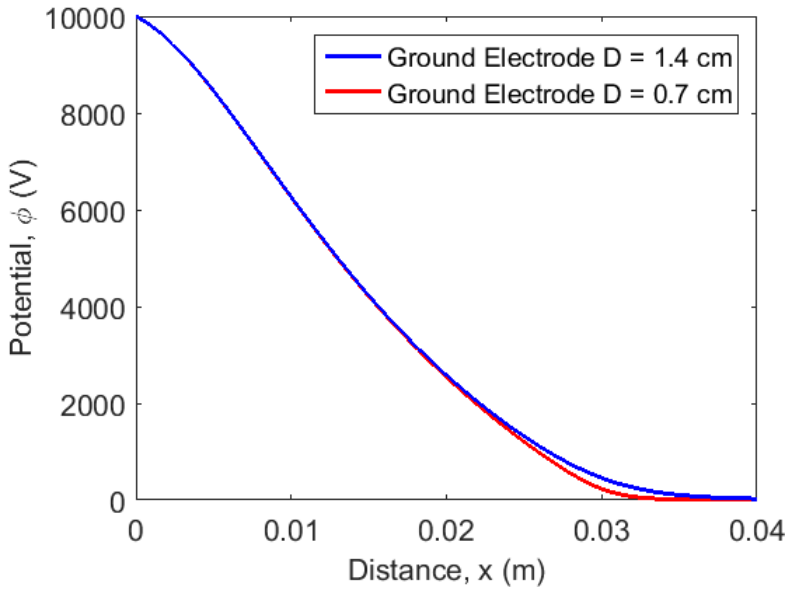

Figure 3.6: IBSimu output of potential (V) at the beam center as a function of distance along the beamline trajectory for the electrode geometry shown in Figure 4.7 (blue curve) and the same geometry with a ground electrode aperture diameter of half the size (red curve). Both simulations use the present operational standard 10 kV plasma source bias.

This results in a varied electric field strength across the beamline. While unavoidable, this has implications on assumptions used in the Child-Langmuir law and on forces applied to different ion trajectories. The main result of this variation is that simple constant equations cannot accurately predict performance or be used for high precision design. Instead, only approximate values come from these equations when done by hand. This type of complexity and variation shows the need and benefits of using computer simulation. In many cases, the variation in electric field across the beamline becomes a small and accepted effect.

If the effect becomes significant, the variation magnitude can be reduced by decreasing the ground aperture diameter. The red curve in Figure 3.6 shows the beamline potential if the diameter decreased by a factor of 2. While the change does not force the potential to zero at x = 0.03 m, it does reduce the deviation (actual value 200 V). Additionally, the potential reaches ground closer to 0.03 m than before. This also lowers the electric field strength deviation and implies a deviation decrease across the beam that results in a more uniform field. As some variation across the beam is unavoidable, acceptable levels become application

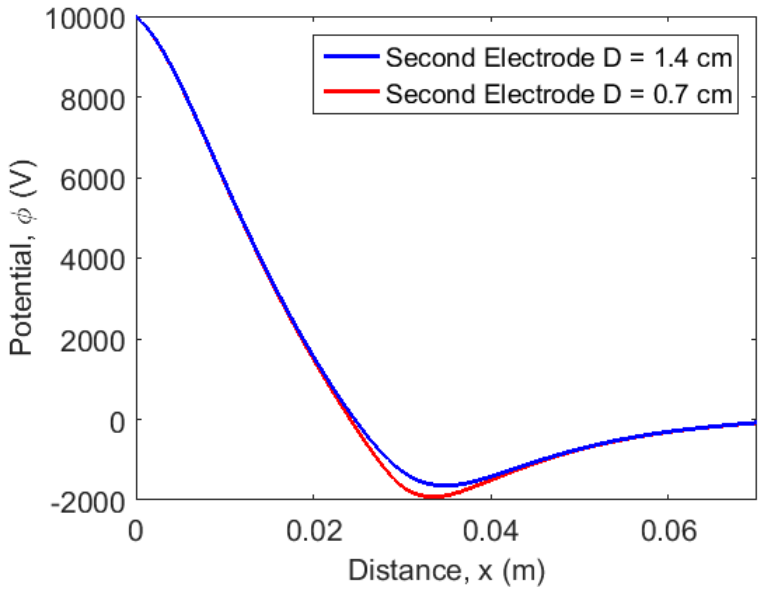

Figure 3.7: IBSimu beam center potential (V) map versus beam distance for the implemented two electrode extractor geometry but with the second electrode at -2 kV. The blue curve has the original second electrode aperture size while the red curve shows the result if the diameter is halved.

specific. As this was just one example of the complex intertwined design choices present in electrode design, the ground aperture size, as well as all electrode apertures in the ion optics are only roughly determined by hand to provide a starting point for simulation. Once in the simulation phase, multiple adjustments and iterations are completed to determine final values suitable for the entire system, not just an individual component.

The consequences of aperture diameter design for electrodes in general, specifically those in the ion optics, are more significant once non-ground potentials are introduced to the electrode system. Figure 3.7 shows the system potential maps if the accelerator electrode were biased to - 2 kV while all other components are left equal, including downstream components being grounded. In this case, neither configuration achieves the full -2 kV potential although the halved diameter design does come close. The difference here is that the remainder of the system is a different potential from the electrode, so the potential does not have extra distance to reach the desired value before being pulled to a higher potential. In this situation, which will occur in the additional ion optics, discussed in Section 3.4, the electric field strength and acceleration potential are both decreased from assumed and desired values. This can be

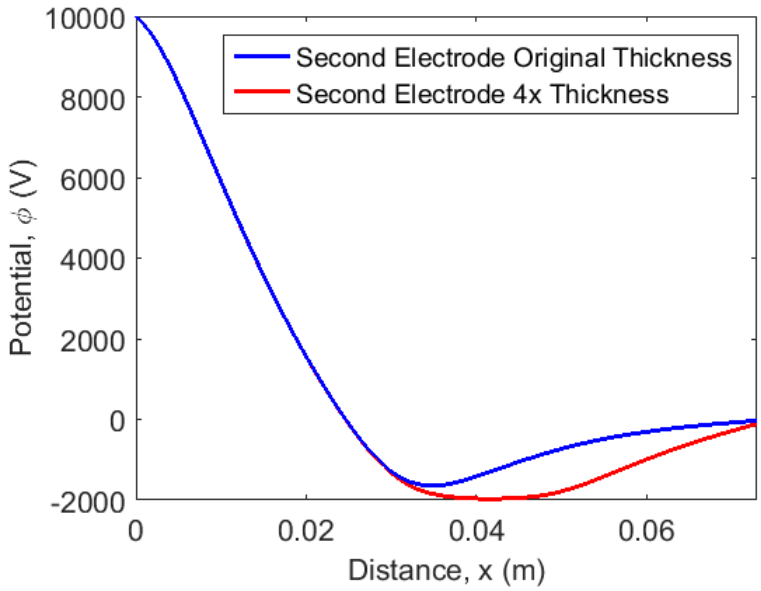

Figure 3.8: IBSimu beam center potential map versus beam distance for the two electrode extractor design geometry but with the second electrode at -2 kV. The blue curve shows the original second electrode thickness while the red curve shows the result with 4x thickness.

decreased by increasing the electrode thickness to allow more distance for the potential to reach the desired value. An example is shown in Figure 3.8 where the original design is shown in blue and a ground electrode 4 times the thickness is shown in red. The increase in thickness does not alter the potential reached at the first electrode face, but does allow the potential to reach the full negative value. The upper limit for electrode thickness stems not only from beamline length and mechanical mounting considerations but also from the avoidance of potential plateaus inside the electrode as has occurred here. When a potential plateau occurs, the ion beam exists in an area of zero external force where it is free to naturally expand due to space-charge repulsion. If the plateau region is large enough, or if the beam is in a condensed state upon entering this region, the result can be a large net divergent force that counteracts the converging effect of the electrode system. Therefore, optimal design avoids plateaus while still allowing the potential to reach the desired value. If this is achieved in the beam center, by definition, it would not be achieved across the beam diameter due to the electrode influence variation. This makes perfect design for all electrode trajectories impossible. Rather than assessing electrode design based on potential maps, or individual

component performance, the ion optics system is considered as one unit and is assessed based on beamline performance. If overall requirements are met, existence of these 'higher order' effects does not matter. The present system further complicates this matter by requiring adjustable beam energies and electrode voltages that change resulting potential maps. The true design challenge is determining areas that can tolerate sub-optimal performance to allow other areas to optimally perform and create an overall sufficient performance system.

3.3 Paschen's Law and Breakdown Voltage

Paschen's law, discovered empirically in 1889 [57], describes the potential difference required to create an electrical breakdown in a gas contained in a gap between two conducting surfaces as a function of pressure, p, and gap length, d. The breakdown voltage, V_B, is the minimum applied voltage drop required to cause a portion of the gas to become electrically conductive and cause an electrical arc. For a pair of conducting materials, such as electrodes, separated only by gas molecules, the gas acts as an insulator, and in general, a very good insulator. For example, in air at atmospheric pressure, the voltage required to cause an arc in a gap of 1 m is 3.4 MV, *i.e.*, an electric field strength of 3.4 MV/m. The physical mechanism of breakdown is analogous to plasma generation described in Section 3.1. Naturally free electrons in the gap are accelerated by the electric field and collide at a rate inversely proportional to λ_e and proportional to the energy gained in between successive collisions [58]. If conditions are such that the electron collides with a neutral gas atom and causes ionization, the result is a positive charge carrier (ion) and an additional free electron. Both the original and the new free electron are accelerated by the electric field and can cause more ionizing collisions. When sufficient conditions are met, this results in an increasing number of ionizing collisions and free electrons described as an avalanche breakdown. This leads to a path of free charge carriers between electrodes that allows current to flow and creates an arc. When desired and controlled, this can be used to create plasma in an arc-discharge source. However, when not intended, these arcs are undesired and typically short lived as bias source electronics will detect their occurrence and shut down to avoid potential damage.

Expressed as an equation, Paschen's law is given as:

$$V_B = \frac{Bpd}{\ln(Apd) - \ln[\ln(1 + {}^1\!/\!_{\gamma_{se}})]} \tag{3.8}$$

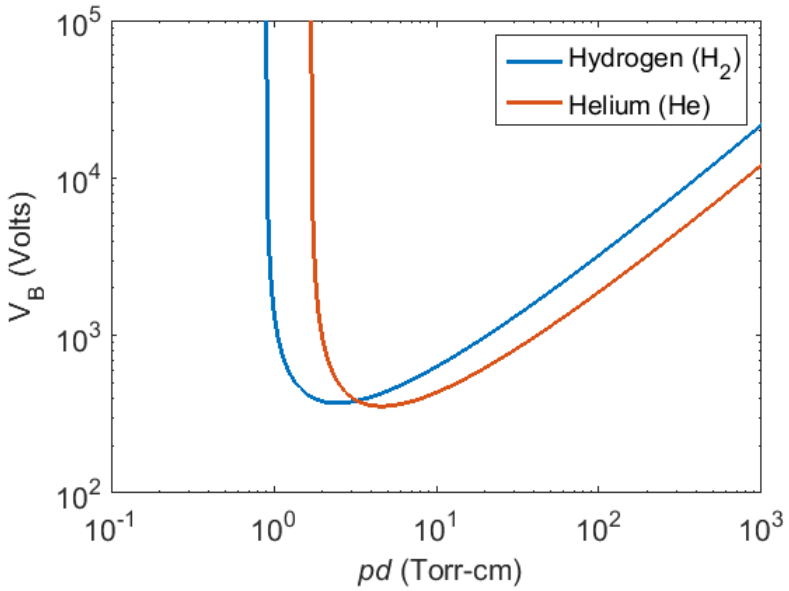

Figure 3.9: Approximate Paschen breakdown curves for hydrogen and helium calculated using A and B values from [54] and a calculated γ_{se}. Curves show the approximate linear trend at high pd and rapid increase at low pd.

where A and B are experimentally determined values. A is the saturation ionization in the gas and B is related to the excitation and ionization energies. Both A and B vary based on operating conditions but are functions of E/p, the electric field strength/pressure. For restricted ranges of E/p, both A and B are approximately constant [54]. The factor γ_{se} is the secondary electron emission coefficient at the cathode. This equation produces curves of V_B as a function of pd, such as those shown in Figure 3.9. These curves were calculated using approximate values of A and B from [54]. From these values, and conditions on the relationship between A, B, γ_{se} and the first Townsend coefficient, an approximate γ_{se} value was determined. The minimum V_B for both hydrogen and helium are roughly equal, with helium being slightly lower in magnitude and occurring at a slightly higher pd value.

Through multiple experiments of different gases, pressures and gap lengths, Paschen discovered two significant results. First, at constant pressure, the voltage required to arc across the gap decreased with decreasing distance but reached a minimum before rising again, at a higher rate than it decreased. Second, at constant distance, the voltage required to arc across the gap decreased with decreasing pressure but also reached a minimum before rising again at an increased rate in comparison to the other side of the minimum.

Paschen's breakdown results for gap length variation at constant pressure both confirm and contradict intuitive expected results. For $d >> \lambda_e$, the proportional increase and decrease to V_B with increasing or decreasing distance respectively, agrees with common intuition of larger gaps requiring higher voltages to induce an arc. However, the result of V_B reaching a minimum before starting to increase again at a rapid rate with continually decreasing distance from this large distance regime is unexpected. This behavior exists due to the relationship between λ_e and d. When $d >> \lambda_e$, a large number of ionizing collisions are required to occur within the gap to create a sufficiently long arcing path. If only a few ionizations occur, individual paths will be too short lived to connect to others and connect the two electrodes. In this regime, as d increases, at a constant p, λ_e stays constant (ignoring energy dependence), but the electric field strength ($\Delta V/d$) decreases with increasing d. Therefore, the voltage must increase to keep electron acceleration constant and create optimal ionization energy. Given that $E = \Delta V/d$, the curve is approximately linear in this regime. Continually decreasing d until minimum V_B is reached enters the regime where $d \approx \lambda_e$. In this regime, d is short enough to require a minimum number of ionizations to create a conductive path, but not so short that electrons can still reach full energy before reaching the anode. This leads to the final regime where $d < \lambda_e$. In this case, electrons are not fully accelerated to optimal ionization energy before reaching the anode and therefore minimal ionizations, if any, occur. Decreasing d also decreases the probability of an electron encountering a neutral before reaching the anode due to constant pressure in a smaller gap decreasing the number of neutrals which further drops the ionization rate. Therefore, the applied field needs to increase to ensure that the electrons reach optimal ionization energy in shorter and shorter gaps so that if a collision occurs, it will be an ionization event that can lead to breakdown.

Paschen's results for pressure variation at constant d also both confirm and contradict intuitive expected results. In the high pressure case, say 1 atm, increasing and decreasing p will cause respective increases and decreases to the required V_B. This again derives from λ_e arguments. As λ_e is inversely proportional to p, an increase to p causes λ_e to decrease, which makes electrons unable to reach the optimal ionization energy unless the effect is compensated by a field strength (voltage) increase. The opposite occurs for a pressure decrease; the λ_e increase results in a required V_B decrease. However, this trend only holds up to a minimum

voltage where λ_e and required acceleration length become approximately equal (optimal breakdown condition). In the low pressure regime, λ_e exceeds d which results in a decreased ionization rate due to electrons being lost to the anode before causing sufficient ionizations. In the absolute lowest limit of zero pressure, an infinite voltage is required to cause breakdown, however, breakdown cannot realistically occur here as there are no atoms in the gap to ionize.

Due to p and d having similar effects on V_B in respective λ_e versus d regimes, V_B can be described as a function of their product, pd. Examples of the Paschen curve for hydrogen and helium were shown in Figure 3.9. Paschen's curve is used in beamline design to ensure that breakdown between conducting surfaces of different potentials will not occur. Significant examples of these areas include the extractor acceleration gap, gaps between electrodes in the ion optics, and the gap between biased electrodes and the grounded transport column chamber wall. Breakdown in these areas can create a number of negative beamline effects, but more importantly, can cause damage to electrical equipment that becomes a safety hazard. Breakdowns can also occur outside of the beamline between HV connection points and ground. These are a direct danger to operator safety and need to be eliminated.

3.4 Ion Beam Optics

Ion optics in the present system are electrostatic lenses composed of electrodes positioned between the plasma source and the target. Electromagnetic lenses also exist and are useful in certain applications such as electron beams. Electrostatic lenses were chosen based on monetary constraints and relative ease of implementation. As electromagnetic lenses are not used in this system, they will not be further discussed. The purpose of ion optics is to apply external forces to the ion beam to control the size and distribution. The name, ion optics, and terminology, such as lens, comes from the similarities between the effects of ion optics on charged particles and the effects of regular optics on light rays. In most cases, the applied external force is used to create a converging effect on the beam. Diverging lenses also exist, but are less common, and are not implemented in this system. Most beamlines require converging optics early in the beam path to ensure lossless beam transport through system components. In a converging lens, the net applied force is directed radially inward, which opposes the space-charge repulsion force. If the applied force can fully overcome space-

charge forces, the result is a converging beam upon exiting the lens. If the lens is not strong enough to create a converging beam, the effect is instead a reduction to beam divergence. As the ions traverse the remainder of the system, space-charge forces will again dominate and beam divergence will increase with travel distance. Therefore, the final beam size depends on the beam size leaving the ion optics and the distance to the target. The constant presence of space-charge repulsion makes its consideration critical to proper beamline design and performance. A consequence of space-charge repulsion is a lower limit on beam size for a given beam current and ion optics configuration, all else equal. This limit occurs when the space-charge force, which increases with decreasing beam size, equals the lens force. Surpassing this limit requires either a lens power increase, a reduction to beam current or introduction of other effects, such as space-charge compensation (Section 3.5.2).

Ion optics design begins with the plasma meniscus and plasma electrode shape as covered in Section 3.2.1. Design continues on with the ground electrode and additional ion optics required to achieve the desired beam size for transport and operational application. The additional optics in the present system are all the same type, known as an Einzel lens. While other lenses exist, this lens was chosen based on implementation ease and history of success. As with magnetic lenses, discussion of these other electrostatic lens types is omitted.

3.4.1 Einzel Lens Principle of Operation

An Einzel lens (from the German word *einzel*, meaning single) is a three electrode lens system where the outer two electrodes are at an equivalent potential, which differs from that of the inner electrode. Together, these three electrodes create a single lens. There are two configurations for the Einzel lens: the accel-decel and the decel-accel, named for the acceleration state in the first and second potential gaps within the lens [59]. The most common configuration for either lens type is to have grounded outer electrodes. In this case, assuming a positive ion beamline, the decel-accel lens has a positive biased center electrode and the accel-decel lens has a negative biased center electrode. Regardless of configuration, an Einzel lens is symmetric and applies no net change to the ion energy; any acceleration in the first gap is offset by an equal and opposite acceleration in the second gap. Also regardless of configuration, an Einzel lens is always a focusing, or converging, lens.

The physical mechanism of an Einzel lens is easiest to describe for the decel-accel con-

figuration. The following explanation uses a positively charged beam, but the mechanism is identical for negatively charged particles with opposite gap polarity. Figure 3.10 shows representative and illustrative figures of a decel-accel lens with an output of equipotential lines from IBSimu in (a), an oversimplified diagram with two illustrative particle paths (black arrows) in (b) and an illustrative plot of radial force strength along the path in (c). Imagine positively charged particles traveling with a velocity component in the positive x direction as shown in Figure 3.10 (b). At position 1, particles encounter a potential hill causing deceleration and a radially outward force, due to the electric field shape, causing the particle trajectories to diverge from the x-axis. As the particles traverse the potential hill, the radial outward force decreases in magnitude before switching to a radially inward force, approximately halfway through the gap at position 2. The force magnitude is illustrated in Figure 3.10 (c) as a function of position in (b) where -1 represents the maximum outward radial force and +1 represents the maximum inward radial force. As particles travel toward position 3, the inward radial force increases in strength and bends the trajectories toward the x-axis (decreases divergence). Once particles reach position 3, they have decelerated to their lowest velocity and now feel a maximum strength inward radial force. As the particles travel down the potential valley, they accelerate while feeling the inward radial force decay and switch to an outward radial force at position 4. While traveling toward position 5, the particles continue to accelerate and now feel an increasing radial outward force. Beyond position 5, the lens has no further effect on the beam. If there is no applied net field in this region, the ions will continue on their trajectories with the exception of space-charge repulsion alterations.

Although the particles experience both inward and outward radial forces of equal magnitude throughout the lens, the net result is a radially inward push, or trajectory convergence. This is a result of particle transit time being greater in the inward force region than in the outward force region. When particles are in the central region (shaded blue in (b)), experiencing the inward force, they travel at their lowest velocity due to the deceleration in the first gap. At the center of the region, the velocity is $v_i - \Delta v$ and at the edges, $v_i - 1/2\Delta v$. In comparison, the velocity ranges from v_i to $v_i - 1/2\Delta v$ outside the shaded region. Given the lower average velocity inside the shaded region and the dimensional symmetry of an Einzel lens, the particle transit time is larger in the shaded region than outside of it. This increased

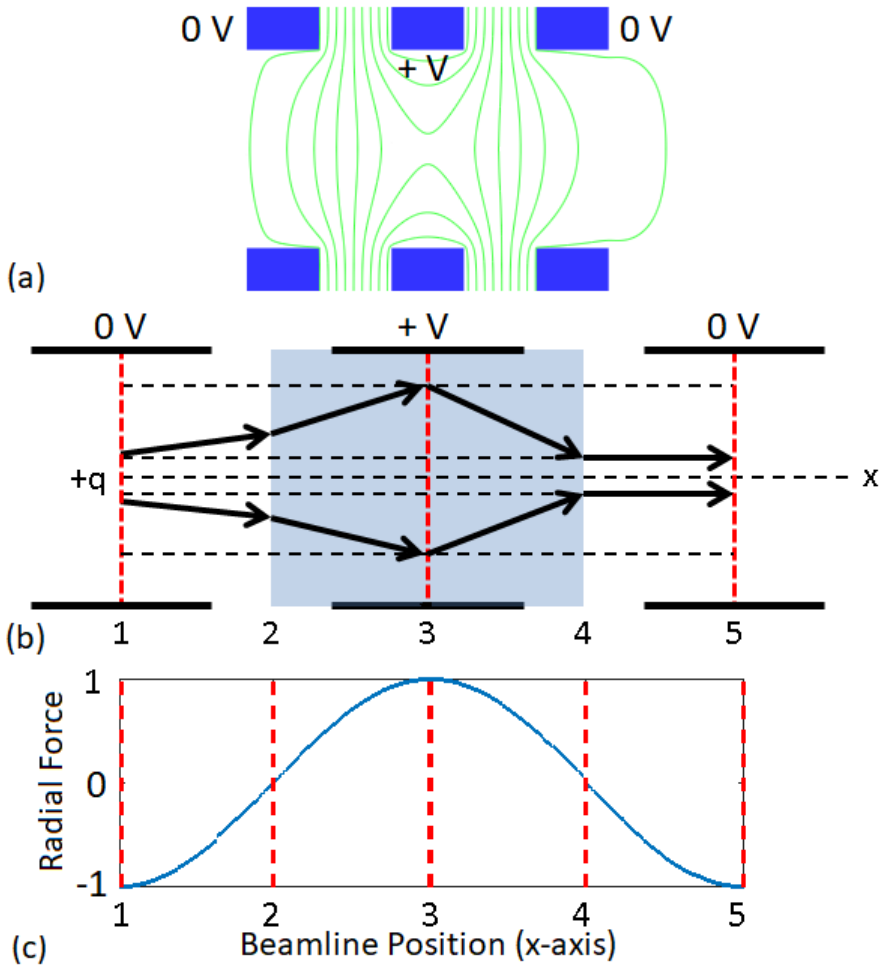

Figure 3.10: Illustrative figures of a positive ion beam traversing a decel-accel Einzel lens with a + V center potential. (a) Example electrode geometry with corresponding equipotential lines in green obtained from IBSimu code. (b) Illustrative diagram of two hypothetical charged particle trajectories to aid Einzel lens explanation. The central area of inward radial force is shaded in blue. (c) An illustrative graph of radial force as a function of position along x-axis. -1 represents maximum outward radial force strength and +1 represents maximum inward radial force strength encountered by a positively charged particle.

time allows the converging force to outweigh the diverging force to result in a focusing lens.

The same logic applies to the accel-decel lens. However, the position of minimum velocity and the converging force area are now outside of the lens center region. When ions in an accel-decel lens leave the first electrode, they see a potential valley and feel an inward radial force. Halfway through the gap, the inward force switches to an outward force and increases in strength until reaching a maximum in the middle electrode. This effect also occurred in the accel gap of the decel-accel lens. Once the particle passes the middle of the lens, it sees a potential hill causing deceleration and a decreasing outward radial force. Halfway through the gap, this switches to an inward force while the particle is still decelerating. When the particle reaches the other side of the lens, it is back to the original velocity.

While both configurations produce beam focusing, the decel-accel configuration is stronger for equivalent voltage gaps. This is because the particle first experiences a deceleration rather than an acceleration which makes the average particle velocity inside the lens less than in the accel-decel configuration. The lower average velocity results in a larger overall transit time that allows all forces to act on the particles for longer and result in a stronger converging power. Therefore decel-accel lenses are used when short focal length lenses are required. The disadvantage of the decel-accel lens is that it is more susceptible to both spherical and chromatic aberrations in comparison to the accel-decel lens. Therefore, if the longer focal length of the accel-decel lens is acceptable, it is typically a better choice.

The relationship between focusing power and the initial ion velocity creates two important Einzel lens design considerations. As the converging power of an Einzel lens depends on the ion transit time, the effect of a given lens decreases with increasing initial velocity. In the present system, it is desired to have an adjustable beam energy, *i.e.*, adjustable ion velocity. In order to maintain a desired lens effect with increasing ion velocity, the lens power must be increased. This means increasing the center electrode bias magnitude or increasing the electrode widths to increase ion travel distance and transit time. Effects of increasing electrode widths was discussed in Section 3.2.3 and the issue of avoiding potential plateaus also applies here. Depending on the state of the ion beam, the effect of a potential plateau can vary from decreasing the overall lens effect to electrode collision beam losses.

The second consideration only occurs in the decel-accel lens when the voltage difference

in the first gap becomes comparable to the initial ion energy. In this case, the ions move very slow through the central region and can technically be stopped. If the lens voltage exceeds ion energy, the ions are reflected back toward the source, which is obviously undesired. While avoidance of this case seems obvious, it becomes an issue when ion-neutral collision effects are added into the mix. As discussed in Section 3.6.1, these collisions cause beam ions to lose energy and potentially fall below the Einzel lens voltage. While these collisions are minimized with proper design, they are never completely eliminated and will lead to inevitable beamline alterations. This effect is rarely significant, as lens voltages typically stay well below ion energy, but it still needs to be kept in mind. A further effect to decelerating ions is that as velocity is decreased, the transit time of ions through the system increases, which increases space-charge repulsion effects. This can be a significant issue in the decel-accel lens and potentially counteract desired converging effects. Based on this time dependency of space-charge, it is easier to obtain a focused beam for higher velocity ions. The fact that these potential effects do not exist in the accel-decel lens, due to ions never dropping below their initial velocity, makes the accel-decel lens a 'safer' choice in many situations.

3.5 Effects of Secondary Electrons

The creation of secondary electrons in an ion beamline is inevitable. These electrons are created through two processes: surface and volume creation. Surface creation occurs when beam ions collide with the target, electrodes, chamber walls or sample holder edges, and 'kick off' surface electrons. Volume creation occurs via ion-neutral collisions in the transport column. These collisions, discussed in Section 3.6.1, result in different outcomes, one of which is the ionization of background gas atoms and the production of free electrons. Depending on the energy, position and trajectory of these free electrons, they can become trapped by the local positive potential of the beamline itself, the space-charge potential. For reference, the secondary electron yield (γ_{se}) from surface creation, especially from a metal surface, is significantly higher than that of volume creation. For surface creation, γ_{se} is the ratio:

$$\gamma_{se} = \frac{N_e}{N_i} \tag{3.9}$$

where N_e is the number of created electrons and N_i is the number of incident particles. This is harder to define for volume creation as each ion-neutral collision can only create one free

electron while surface creation can have multiple electrons per ion. Also, the probability of volume creation is very different from surface creation as it depends on ion energy and background gas pressure (mean free path). Cross sections look similar to those of Figure 3.2, *i.e.*, peaked at a maximum, where as γ_{se} for surface creation is proportional to $V^{1/2}$ [60].

Regardless of creation mechanism, all secondary electrons are accelerated toward the plasma source by the electric field established by the positive plasma source and the grounded target. This results in a stream of electrons with energies varying from a few eV to $e\mathrm{V_{pl}}$, depending on creation location. If these electrons reach the plasma source, they electrically load the source and potentially lower $\mathrm{V_{pl}}$. Electrical loading can also occur in the ion optics electrodes. Another issue is the free electrons traveling back through the transport column, colliding with neutral gas atoms, and causing electron-impact ionization. This creates new ions and additional free electrons that become accelerated toward the plasma source and add to the secondary electron issues. The new ions are a smaller problem. Given that the neutral gas in the transport column is leaked source gas, the created ions will be the same type as that in the beam. Therefore, these ions will be accelerated toward the target and simply add to the overall beam current. However, these ions created throughout the transport column will have intermediate energy values and random trajectories that will create variation in the beam energy and current density profiles. The magnitude of this issue depends on creation rate and application precision requirements of either profile.

3.5.1 The Suppression Electrode

As production of secondary electrons is inevitable, especially surface production at the target, minimization of the related effects is required. This takes the form of a suppression electrode. The suppressor is a negatively biased electrode in the transport column somewhere between the plasma electrode and the target. The negative bias provides a potential hill for the secondary electrons created past the suppressor to climb in order to reach the plasma source. As the energy of secondary electrons is low upon creation (< 200 eV on average), the potential hill does not need to be significantly high. In many cases, a few keV is sufficient to repel secondary electrons away from the source and inhibit the backstream. The suppressor causes the electrons to safely collide with the grounded walls of the target chamber and transport column instead of the plasma source. Even with the suppression electrode, the secondary

electrons will travel some distance within the system before reaching ground and thus ionization of background gas can still occur. As the most significant source of secondary electrons is from the target and target holder, this makes the majority of secondary ions created close to the target. These ions are a low priority concern as the fluence will be low and those that hit the target will have a small energy that creates a minimal effect on beam results. All positive ion beams contain at least one suppression electrode, typically close to the plasma source. The standard position is between the plasma and ground electrodes, making the suppressor the first electrode of the ion optics system. The closer it is to the plasma source, the more secondary electrons it can screen from the source. Any electrons created between the plasma source and the suppressor will cause source loading. Therefore, this gap is generally kept as small as possible and ion optics are used to avoid beam-electrode collisions. This keeps creation limited to ion-neutral collisions, which is typically a low creation rate.

3.5.2 Space-Charge Compensation

While the above discussion presents secondary electrons as a completely negative outcome whose production would ideally be zero, there is a benefit to having a small amount present in the beamline, assuming implementation of a properly designed suppression electrode. This benefit is called space-charge compensation and the result is a decrease to space-charge repulsion effects. When secondary electrons are created within the beamline, they can become trapped in the beam by the local positive potential, the space-charge potential, instead of immediately colliding with a chamber wall. These trapped electrons remain within the beam in the vicinity of creation for an amount of time relative to their initial energy and trajectory. The motion of secondary electrons and whether or not they become trapped by the beam is complicated and will not be fully addressed in the present work. It is sufficient for the present purpose to say that a portion of the secondary electrons will be trapped and remain within the beam for enough time to create a significant screening effect. The result is a decrease to the local positive potential of the beam with a theoretical, final quasi-neutral state depending on creation and trapping rates. This decreases natural beam divergence and decreases requirements on ion optics to create and maintain a specific beam size. Based on this discussion, the creation of secondary electrons, given a suppression electrode to stop source loading and back acceleration, is actually a beneficial effect.

As the trapped electrons are relatively immobile, ion-neutral volume creation throughout the beamline provides a larger space-charge compensation effect to the beamline than surface creation. Even though surface creation will produce many more secondary electrons, they will stay within a localized region around the target or electrode where they were created. This results in areas of the beam with higher space-charge compensation than others. When ion-neutral collisions are discussed in Section 3.6.1, the effect on beamline performance will be negative and will outweigh benefits of space-charge compensation. As collision and secondary electron creation rates are one in the same, the effect as a whole needs to be minimized. As complete elimination is not possible, a small volume creation rate will exist after minimizing the negative effects to an acceptable level. Based on this, space-charge compensation was not specifically designed in the present system but was instead assumed to exist at a beneficial level after limiting the transport column background pressure to limit ion-neutral collision rates. Based on beamline performance, this assumption proved to be successful.

3.6 Beam Transport Considerations

Beam transport is based on ion optics and dealing with space-charge effects. As beams can travel long distances through a variety of components, transport must ensure the absence of ion-loss collisions. Given that increased beamline length increases space-charge repulsion effects by increasing transit time, beamlines are typically kept as short as possible. However, beamline length must be sufficient to accommodate other needs such as beam alteration or measurement, which will inevitably add length. Additional length can be accommodated with ion optics and thus transport column design depends more on the needs of other system components rather than its own effect(s), specifically on beamline length. The primary metric for success is evaluation of what percentage of the beam reaches the target and the corresponding energy and positional distributions. Perfect transport is not possible as some ion-neutral effects will always exist to cause variations in distributions and potentially in delivered current. If the collision rate is properly minimized, the effects should be minimal.

3.6.1 Ion-Neutral Collisions and Beamline Effects

The presence of neutral gas in the transport column has primarily negative effects on beam transport as it creates conditions for ion-neutral collisions to occur between the beamline

ions and the background neutrals. The effect of these collisions on the beamline is dependent on collision type. There are four types of ion-neutral collisions that can occur: elastic scattering, electronic excitation, ionization and charge transfer. Each collision type has a slightly different probability of occurrence as described by the collision cross section, which depends on the specific ion-neutral species combination, incident ion energy, and neutral gas pressure, similar to the electron-impact ionization cross sections previously discussed. These cross sections can be found in references such as [61, 62]. Regardless of collision type, all ion-neutral collisions result in an energy transfer from the incident ion to the neutral that decreases the energy of the beamline ion. The energy reduction affects the energy dependent beam focusing and transport properties that are designed for a specific energy. The trajectory of any ion energy different from the design energy is uncertain and the general result is a broadened beam distribution when slower ions exist. These different energy ions can also obtain trajectories that result in collisions with electrodes or chamber walls. This decreases the beamline fluence. A second result of energy reduction is a broadening of the beamline energy distribution, assuming some of the lower energy ions actually collide with the target. The significance of these effects is application dependent. Changes to the positional beam distribution is more readily handled with design elements, such as additional ion optics, than changes to the energy distribution. However, the best practice is to reduce ion-neutral collisions as much as possible by reducing transport column pressure. It should be noted that the simulation package used for design in this work does not account for ion-neutral collisions. In fact, many ion beam simulation packages ignore this effect as it is assumed to be negligible through proper pressure minimization and given its challenge to accurately model.

3.6.2 Elastic and Electronic Excitation Collisions

Elastic scattering collisions are described by Rutherford scattering. They result in a transfer of energy from the incident ion to the target neutral and a new trajectory for each particle. The energy transfer and resulting particle energies depend on collision details. Regardless of magnitude, the beamline ion will have a reduced energy and a new trajectory that alters focusing and transport. Electronic excitation collisions occur when the incident ion transfers energy to the electrons of the target neutral and causes said electrons to enter an excited state. As the electrons only enter an excited state rather than becoming free of their bond

with the neutral, the transferred energy must be less than the target ionization energy. Based on typical ionization values being of the order of tens of eV, the energy transfer is relatively small compared to typical beamline energies, making the effect relatively small. However, multiple collisions of this type can accumulate and develop a substantial effect.

3.6.3 Ionization and Charge Transfer Collisions

The final collision types, ionization and charge transfer, are closely related processes. Both occur through Coulomb interactions with the target electrons and require the energy transfer to exceed target ionization energy such that a new ion and free electron are created in the beam path. The difference between the two collision types is what happens to the new free electron. In the charge transfer collision, the free electron becomes instantaneously trapped by the incident positive ion, creating a fast neutral, while in an ionization collision the free electron remains free within the system. In an ionization collision, the energy of the free electron depends on the energy transfer but is typically less than a few hundred eV [53]. As per Section 3.5.2, these electrons either become trapped by the beamline potential and contribute to space-charge compensation or collide with electrodes or chamber walls.

Ionization Collision Process

In the present system, the neutral target atoms in the transport column originate in the plasma source and enter through the extraction aperture. For the hydrogen beamline, this means the neutrals involved in collisions will predominantly be H_2 and the incident ion will be either H^+, H_2^+ or H_3^+. The cross sections for collisions of these ions with H_2 and with H are all slightly different but closely related to each other and to H^+ incident on H [60]. The generic ionization collision for a neutral and ion of the same type is:

$$A^+(fast) + A \rightarrow A^+(fast) + A^+(slow) + e^- \tag{3.10}$$

As the energy transfer is typically of the order of a few hundred eV, or less, the energy of the target ion is typically only slightly perturbed, unless the beam energy is also low. In the present system, 5 keV is the operational minimum with general operation at 10 keV, which makes a few hundred eV perturbation negligible. The result of this low perturbation on ion energy is that beam focusing and energy distribution are minimally affected by single collisions. It takes multiple collisions of the same ion to create meaningful changes. Even

then, it is possible for the beam ion to regain lost energy from the electric field depending on where the collision occurred and the ion path length. The bigger issue of a single event is the newly created ion. Upon creation, the energy of this ion is small but it will be accelerated by the electric field between the positive ion source and the grounded target. Depending on where the ion is created in the transport column, the energy will be different. If created close to the plasma source, the ion should be able to obtain an energy close to that of the beamline ions but if created close to the target, the ion will not have time to gain significant energy and may only gain a few hundred eV. On average, the new ion energy will be half the beam energy. This energy range will alter the energy distribution and potentially the positional distribution, depending on creation rate. The focusing and transport of the new ions is uncertain as there are too many variables to fully address.

Charge Transfer Collision Process

Similar to the ionization collision cross sections, the charge transfer cross sections are varied depending on incident ion and target type, but for the hydrogen beam, are roughly similar to the cross sections and collision equation of a proton in atomic hydrogen. The generic charge transfer collision is shown in (3.11). The result is a fast neutral that travels on a straight ballistic trajectory from its point of creation. As this particle is neutral, it will not respond to the focusing or accelerating electric fields in the system. The effect of this neutral colliding with the target is very different from charged particle collisions. If the creation rate were large enough, these collisions could cause significant effects on target damage results. Another issue is presented by the slow ion that is created in the transport column, which has the same effect and considerations as the slow ion produced in the ionization collision.

$$A^+(fast) + A \rightarrow A(fast) + A^+(slow) \tag{3.11}$$

3.6.4 Collision Rate Calculation and Summary

Overall, ion-neutral collisions produce a negative effect on the beamline by altering both the positional and energy distributions of the beamline. While space-charge compensation is a beneficial outcome of ionization collisions, the overall ion-neutral collision negatives outweigh this beneficial effect. To avoid these negative effects and reduce design complexities, the background gas pressure of the transport column is always minimized as much as possible.

As has been discussed, the collision rate will never reach zero, but at reasonable pressures, the effects can be minimal. The collision rate, R, can be calculated by:

$$R = 1 - \exp\left(\frac{-L}{\lambda_i}\right) \tag{3.12}$$

where L is the beamline length and λ_i is the mean free path of the incident ion, given by:

$$\lambda_i = \frac{1}{n\sigma} \tag{3.13}$$

where n is the number density of target neutrals, based on pressure, and σ is the collision cross section [63]. At STP (760 Torr), n for any gas is 2.7×10^{19} molecules/cm^3 [60]. Therefore, in the present system, where transport column pressure is of the order of 0.1 mTorr,

$$n = \frac{2.7 \times 10^{19}}{7.6 \times 10^{6}} \approx 3.55 \times 10^{12} \text{ molecules/cm}^3 \tag{3.14}$$

The cross section, σ, for any ion-neutral collision is typically of the order of 1×10^{-16} cm^{-2}. Specific values for different combinations can be found in references such as [61]. Rather than calculate R for each possible σ, a total R can be calculated by using a total cross section value to represent all possible collision types. As a reference high end estimate, assume the total collision cross section in the present system for hydrogen is of the order of 1×10^{-15} cm^{-2}. Substituting this value, along with (3.14) into (3.13) gives $\lambda_i \approx 312$ cm. Using this value with a beamline length of 42.5 cm in (3.12) gives:

$$R = 1 - \exp\left(\frac{-42.5 \text{ cm}}{312 \text{ cm}}\right) \approx 0.13 \tag{3.15}$$

This shows that, at maximum, 13% of the beam will be involved in an ion-neutral collision of some type during transport, which is an acceptable maximum value. The same calculation can be done for a helium beam using the same assumptions. However, σ values for helium are slightly larger than for hydrogen, so a value of 2×10^{15} cm^{-2} is used instead. This gives

$$R = 1 - \exp\left(\frac{-42.5 \text{ cm}}{156 \text{ cm}}\right) \approx 0.24 \tag{3.16}$$

which is starting to approach a significant value that may be a cause for concern. As will be shown in Chapter 5, the present system operating conditions produce sufficient results in terms of beam profile and thus actual collisions are assumed to occur at acceptable rates.

Chapter 4

Beamline Design

The design theory covered in Chapter 3 provides a solid foundation for the design and implementation of individual system components. Obtaining optimal system design requires components to be designed together using a combination of experience, computer simulation and experimental testing, with the latter being the final authority on the success or failure of any design choice. Moving from the design phase to the implementation phase commonly includes encountering unexpected, design altering effects and practical limitations. These issues are caught, and typically fixed, with experimental testing. This chapter discusses final design choices, the large role of simulation in design and the system implementation including practical issues and solutions that surfaced throughout the process.

4.1 Filament Design

Filament design was completed via trial and error experimental investigation of multiple different filament geometries. Tested filaments were built based on theoretical considerations and experimental experience gained as testing progressed. The plasma created by each design was measured with a Langmuir probe and designs were ranked based on resulting ion density and corresponding required filament current at different pressures. As mentioned in Section 3.1.2, the operational lifetime of the system is limited by filament current and battery capacity. To keep testing contained to a reasonable time frame, a benchmark criterion of obtaining sufficient ion density (of the order of $10^8 - 10^9$ ions/cm^3) without exceeding a filament current of 8 A was imposed. This criterion is based on the filament battery, a $LiFePO_4$ 12 V battery, having an 80 Amp hour capacity. At 8 A, the system can operate for 10 hours, which was deemed sufficiently long. The filament current is variable under operational conditions based on ion density requirements, but this is a good average benchmark value.

While filament current is strongly influenced by the filament resistance, it is controlled in the system by a PWM control circuit (see Appendix A.2) connected between the filament and the battery. Along with current control circuitry, the filament is also connected to a circuit that provides a negative bias with respect to the plasma chamber (see Appendix A.1). The bias range is 64 - 160 V, which includes the optimal bias of -80 V and -110 V for hydrogen and helium plasma respectively. The circuitry allows the potential future implementation of other plasma types with different bias requirements within this range. The source must be capable of maintaining the bias under source loading created by the emitted electrons being absorbed by the chamber wall. As the number of emitted electrons is increased, the source loading increases and can cause the applied bias to decrease. In the upper limit, the emitted electron current is too large for the source to sustain and the potential difference is driven to zero. Any decrease to the applied bias from the optimal setting will decrease the ionization cross section, effectively decreasing the ion density. In the upper limit, when the bias is driven to zero, there is an abundance of electrons, but no ionization occurs as the electrons are not provided sufficient energy. Therefore, source loading is a practical upper limit to the number of electrons that can be added to a system to increase ion density. Source loading is typically desired to be kept to a minimum to increase battery lifetimes and system efficiency. Therefore, optimal system design and performance is not necessarily to maximize ion density but to supply sufficient ion density while minimizing effects like these, which further reinforces the choice to operate in a lower filament current range.

To eliminate an additional variable from the filament design process, the filament material was chosen to be tungsten, the standard choice, and other materials were not considered. The implemented filament is constructed from a 7 cm piece of 0.31 mm diameter tungsten wire coiled in three turns of 1.5 mm diameter to create a 1.5 cm long coiled region and is connected between two 1/4 inch copper rods contained in an isolated vacuum power feedthrough. A picture of the mounted filament and full plasma source assembly is shown in Figure 4.1. The filament legs are wrapped around screws and connected to the copper rods via tapped holes. This mounting method requires a venting mechanism to avoid pockets of trapped gas in the bottom of the screw hole that develop when the screws are inserted at atmospheric pressure. Once under vacuum, this pocket of air will leak out very slowly due to pathway restrictions

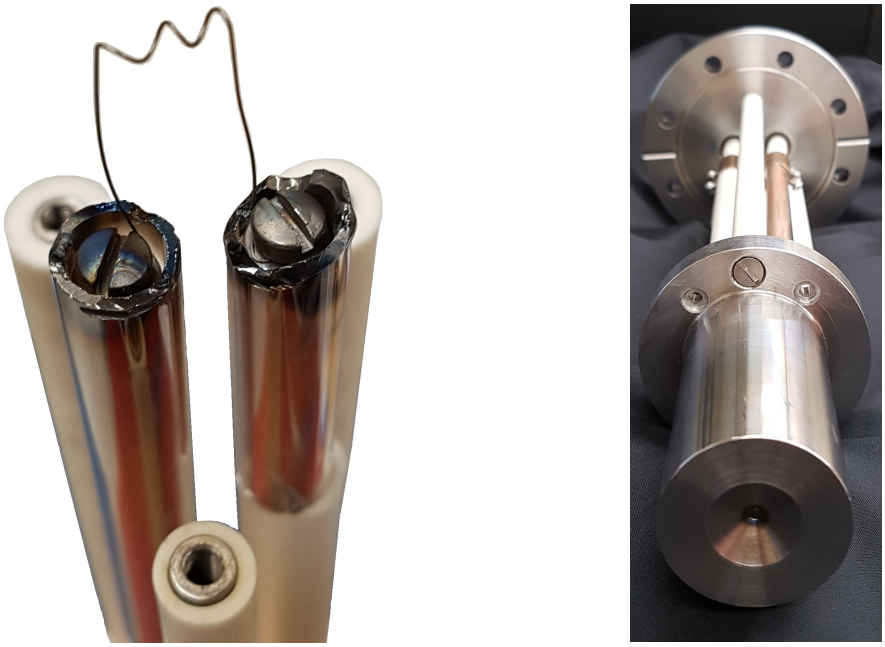

(a) **(b)**

Figure 4.1: (a) Filament mounted to copper feedthrough rods. Rods are covered by a ceramic to inhibit breakdown between rods and other surfaces. The other three rods shown are stainless steel support rods to support the plasma generation cylinder; also covered with a ceramic. (b) Picture of the fully assembled plasma source insert.

and will create a *virtual leak*. A virtual leak is not a true leak, as it does not continuously allow outside air to enter the system, but it gives the appearance of a true leak until the trapped gas is removed. The presence of a virtual leak is thus a diagnostic and operational hassle that can be avoided. Two venting techniques are using vented screws, screws with a central through hole, and venting the tap with a side hole at the bottom of the tap. Both techniques are used throughout the system with the latter being used for filament mounting.

The final filament design choice is the acceleration gap distance between the filament and the plasma electrode. This choice was made via experimental trial and error. Distances in the range of 1.5 to 3.5 cm in steps of 0.4 cm were tested and found to produce similar ion densities. The chosen gap length is 2.5 ± 0.2 cm as it produced the highest ion density.

4.2 Vacuum System, Gas Flow and Operating Pressure

The vacuum system includes the plasma chamber, the downstream components, all vacuum instrumentation, vacuum pumps and the gas flow management system. The first perfor-

mance metric for a vacuum system is assessment of the lowest achievable base pressure. The required base pressure for the present system is 1×10^{-5} Torr, or preferably less. Achieving this pressure requires the series combination of a turbomolecular and roughing pump to be connected to the chamber. The turbo pump attached to the plasma source chamber is an Agilent TV 301 Navigator with a pumping capacity of 200 l/s H_2. The gas flow is handled by an MKS GE50A Mass Flow Controller (MFC) that can provide calibrated flows over a range of 1 to 100 sccm (standard cubic centimeters per minute). The MFC has two operation modes, one that runs from 50 to 100 sccm and one that runs 1 to 50 sccm. The latter mode is currently used. The resolution of the MFC is 0.1% of full scale, *i.e.*, 0.05 sccm, the repeatability is ±0.3%, and the accuracy is ±1.0% of setpoint for the range of 20% to 100% fullscale (10 to 50 sccm) and ±0.2% of full scale (0.1 sccm) for setpoints under 20% fullscale value (1 to 10 sccm). The MFC is connected to the plasma source by an insulating hose as shown in Figure 4.2. In between the plasma chamber and the turbo pump is a gate valve that can be partially closed to limit flow rate and effectively throttle the pumping speed of the turbo pump. This valve, in combination with the controllable flow rate of the MFC, allows the plasma chamber pressure to be accurately controlled from approximately 10^{-1} to 10^{-5} Torr. A second turbo pump, an Alcatel CFF 450 (200 l/s H_2), is attached to the target chamber to remove gas from the downstream region. Both turbo pumps are backed with a 285 l/min Agilent DS 302 roughing pump. The system base pressure is 5×10^{-6} Torr, which is below the maximum allowable base pressure. The downstream turbo does not have a gate valve as it is always fully open to remove as much gas as possible from the downstream region.

Initial values for plasma chamber operational pressure were determined from sources such as [53, 60, 64], which suggested operation in the low mTorr range for this type of source. Trial and error testing began in this pressure range until a pumping speed and flow rate combination was found to provide sufficient operation at a given pressure. In terms of plasma stability and ability to provide sufficient ion density, the best performance was found to occur at a flow rate of 1.0 ± 0.1 sccm and a corresponding plasma chamber pressure of 1.0 ± 0.2 mTorr. This is the operational standard setting for the present research application. With a base pressure of 5×10^{-6} Torr, an operational pressure of 1 mTorr creates a contaminant gas ratio of 0.5%, which is an acceptable value. Even if the operational pressure were doubled to

increase ion density, the contaminant ratio is still an acceptable 1%. The quoted operational pressure has inherent measurement and random error due to potential repeatability error in the MFC. As pressure affects the ionization rate and resulting ion density, the variance in pressure could result in system design problems. However, as will be shown in Section 4.14, the system design can handle current density variations without significant beamline effects and thus this small pressure variation is not a concern to operation.

As shown in Figure 4.2, the connection between the plasma chamber and the source turbo, as well as the plasma chamber and the downstream components, are both 35 kV HV isolation ceramic breaks made of alumina. While these breaks completely suppress potential external arcing (maximum potential difference is 30 kV - source maximum), the same cannot be said for internal arcing where pressure and voltage differences can vary. However, as will be shown in Section 4.8, the mTorr operational pressure range does not allow breakdowns to occur inside the system as the corresponding required distance, at present system voltages, is longer than any distance present in the system. The connection between the MFC and the plasma source does not use a commercial HV break, but instead connects via an insulating plastic hose. As this hose requires some length to span the distance from the HV area to the grounded MFC, the distance starts to approach the required breakdown distance. To avoid breakdowns in this line, a long hose length, 10 m, is used to push the *pd* factor to the far right of the Paschen curve rather than the far left.

The final gas management component is attachment of one or more pressure gauges to calibrate system pressures and verify pressures during operation. Pressure measurement is desired in the plasma source, the transport column and the target chamber. As pressure gauges have ground referenced electronics, direct measurement of the plasma chamber pressure is not possible. Instead, measurement occurs as close as possible to the chamber, on the opposite side of a ceramic break. It is assumed that once gas flow and pressure equilibrium is reached inside the chamber, the pressure measured by the gauge is equal to the pressure inside the plasma generation cylinder. While this assumption may not be 100% accurate, it is sufficient to ensure similar operating conditions across different system runs. The downstream pressure gauge can be attached anywhere throughout the transport column or target chamber as this section is grounded. Source pressures have already been discussed to be

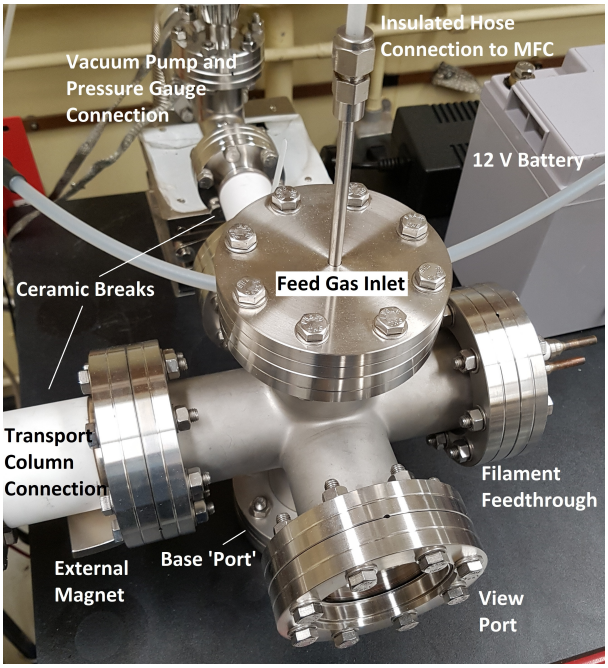

Figure 4.2: Picture of fully connected plasma source chamber highlighting each port connection. Also included in this picture is the 12 V $LiFePO_4$ filament battery and position of external plasma source magnet.

in the 1 mTorr range, but transport column and target chamber pressures are substantially less due to the downstream turbo and small gas flow into a relatively larger volume. The downstream pressure is typically of the order of 0.1 mTorr or less. This pressure increases as the source pressure increases and causes a higher flow rate through the extraction aperture.

4.3 Plasma Source Implementation

The plasma source design places the filament inside a hollowed out cylinder that is then inserted into the larger source chamber. A side-view cross section is shown in Figure 4.3a. The smaller cylinder source supplies a plasma electrode (single flat face) as well as a confined space for plasma creation where the electron acceleration gap can be optimally positioned. The larger source chamber is a 4-1/2″ CF 6-way cross shown with full system connections in Figure 4.2. The six port connections are: the plasma source insert and filament power feedthrough (Figure 4.1), gas supply line, pressure gauge and source vacuum pump line ceramic break, transport column/downstream ceramic break, visual inspection window/additional port and a blanked off base port to allow the chamber to sit on a lab bench. The source cylinder is

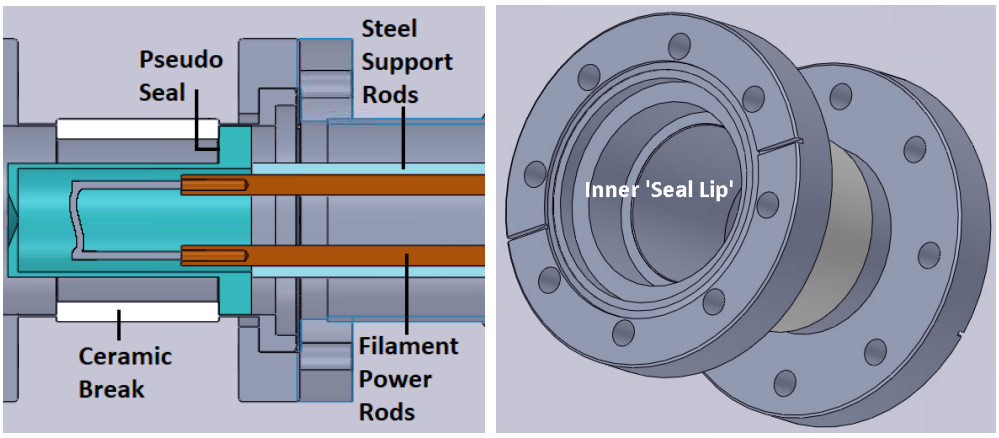

Figure 4.3: (a) SolidWorks cross section view of plasma cylinder inserted into chamber and ceramic break to create the 'pseudo-seal'. (b) SolidWorks drawing of ceramic break showing dimensional features and inner 'seal lip' that enables creation of a 'pseudo-seal' with proper design of plasma cylinder.

electrically connected to the source chamber and structurally supported in 'free-space' by 3 stainless steel rods connected to the power feedthrough flange. This ensures the plasma cylinder and electrode are the same potential as the remainder of the source.

The design discussion so far has focused on theoretical and ideal design scenarios with the exception of the Paschen breakdown discussion. Additional practical issues that developed during the design process include creating a design to limit gas flow from the source chamber to the downstream components and to contain the gas flow path to the extraction aperture. Gas flow restriction to the extraction aperture was achieved by designing the source cylinder to fit partially inside the transport column ceramic break and take advantage of the reduced inner diameter design. The inside of the ceramic break, shown in Figure 4.3b, contains step-like edges that make the inner diameter of the ceramic portion slightly smaller than the inner diameter of the flange connection. This 'lip' is used to create an approximate seal in the system by designing the outer diameter of the source cylinder base to equal the inner diameter of the flange connection and designing the support rod length to make the top of the cylinder base sit flush with the edge of the break lip. Essentially, the plasma cylinder base fits perfectly inside the ceramic break, as shown in Figure 4.3a, and creates an approximate seal. This required high precision machining (completed by the U of S Physics Machine shop) to make everything fit together as tightly as possible.

4.4 Magnetic Field

Although not discussed in Chapter 3, a useful plasma source component is a magnetic field in the plasma generation area. The magnetic field produces a flat increase to ion density while not harming other system component operation by causing the electrons traveling from the filament to the plasma electrode to take helical, rather than straight, trajectories. This increases the electron travel distance and time spent in the plasma generation area before colliding with the plasma electrode, which increases the probability of ionizing collisions and thus, the ion density. In the present design, the magnetic field is applied by an externally mounted 800 ± 30 Gauss pole strength SmCo magnet. The magnet orientation was experimentally varied to find the optimal position that resulted in maximum ion density. The optimal position was found to be approximately 45° off of the filament coil axis. In this position, the ion density increased by a factor between 2 and 8 depending on other conditions.

4.5 Plasma Parameter Measurement

The first plasma source characterization is measurement of ion density and electron temperature using a Langmuir probe and the associated analysis as described in Section 3.1.5. A prototype plasma source was built and included a custom Langmuir probe access port that is omitted from the final design due to the HV bias of the source chamber. Figure 4.4 shows an example measured Langmuir curve. Through analysis of Langmuir curves obtained at varying operating conditions, the source was found to produce ion densities of the order of 2×10^9 ions/cm^3 and T_e between 1.5 and 5 eV. Using (3.1) and (3.2) with this ion density value, an average value of 3 eV for electron temperature and an average ion mass of H_2^+ to account for the presence of H^+, H_2^+ and H_3^+, with H_2^+ dominating in hydrogen plasma, the calculated J_{Bohm} is of the order of 400 μA/cm^2, or 4 A/m^2. Comparison with the minimum target value of 0.445 μA/cm^2 from Section 1.4 shows that the source will easily meet the J_{beam} requirement. As mentioned, the calculated J_{Bohm} value is always desired to be higher than the minimum required value as perfect extraction of J_{Bohm} rarely occurs. Based on the value calculated here, this is the case and the source will provide sufficient room to permit practical beam current extraction. This analysis assumes that T_e follows a Maxwellian distribution. If this is not true, calculated values will be slightly skewed. However, as these

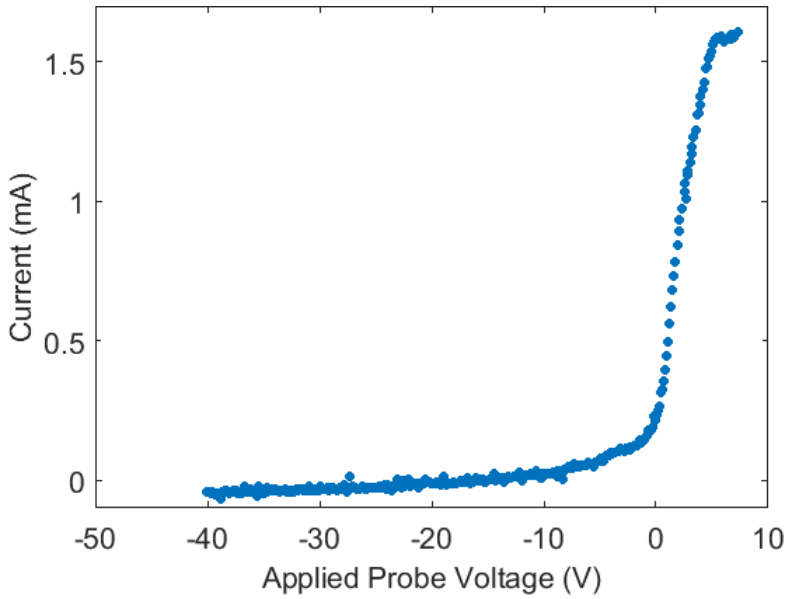

Figure 4.4: Example Langmuir curve from prototype plasma source. Obtained from hydrogen plasma created at 1.3×10^{-4} Torr with filament current of 6 A. Analysis yields $n_0 = 3.4\times10^{8}$ protons/cm^3 and $T_e = 1.5$ eV.

measurements are only used to initially assess source performance, and are not used after beam current measurements are available, there will be no affect on system level results.

4.6 Using Simulation in Design

The computer simulation code used to complete the beam transport and ion optics design, IBSimu [65, 66], was written by Taneli Kalvas. This code is a free to use ion beamline simulation package written in C/C++ and designed to run on Linux. The output of IBSimu is equivalent to more industry standard programs such as SIMION or PBGUNS. Simulations were completed using the cylindrical symmetry mode to produce a two dimensional output of the upper half of the beamline system. Input and output parameters are all reported as radii rather than diameters. This includes electrode and aperture sizes as well as beam size results. IBSimu only simulates the transport column, or beamline, portion of the system and does not include the plasma source. It assumes that a plasma source exists with parameters provided as inputs to the code. Specifics of these parameters are discussed in Section 4.13.

Along with knowledge of plasma source properties, another prerequisite for beamline simulation is a defined metric for successful beam design to permit objective evaluation of

simulation results. The present design goal was to produce a beamline whose size at a given energy is adjustable by alteration of ion optics voltages, *i.e.*, focusing power. Based on the ability to adjust the ion optics power, the beamline should be able to maintain a given size across multiple different energies. Given the sample size of approximately 1×1 cm for the SiO_2, $LiNbO_3$ and TeO_2 samples, and the requirement of a beam larger than the sample area to achieve an approximate uniformly irradiated area, an initial estimate for beam size is of the order of 1 - 2 cm. Further restriction to beam distribution comes from the goal of limiting beam variability across the irradiated area to 15% and to minimize wasted beam current (ions that do not irradiate the target). This restriction depends on sample area, which, as will be discussed in Section 4.12.1, is limited to 8×8 mm by the sample holder cover 'mask'. The area of interest is even further restricted when measurement area is considered. To avoid potential measurement skewing edge effects, an edge buffer of 1.0 - 1.5 mm was used and limited the measurement area to 5×5 - 6×6 mm. This area is still sufficiently large to allow averaging of multiple measurements within the irradiated area. Therefore, the goal was to design a system that can create a beam with a central region variance under 15% that spans at least the central 5 mm of the beam profile and has limited wasted beam current outside of the measurement area. A simulated profile that meets and exceeds these expectations, complete with boundary lines, is shown in Figure 4.5 as an illustrative example.

To begin simulation, values for the plasma source parameters are required. As the system was designed to handle variable beam current, the plasma properties change from one run to the next. In the beginning, it was unknown how sensitive the design would be to variation of these parameters, especially ion density. In the early design stages, a possible outcome was evidence that a system capable of handling variable parameters, within beam constraints, was not possible. If this happened, new beam requirement definitions would have been required.

The first step was to create a working design for average values, obtained from Langmuir probe measurements of the prototype system. From here the design and parameter sensitivity could be evaluated. Many failed designs were simulated in this first step that produced significant understanding of how changing components affected the system. It also led to a systematic study of simulation parameter sensitivity and variance effects that will be discussed in Section 4.14. This study shows that the regime in which the final beamline

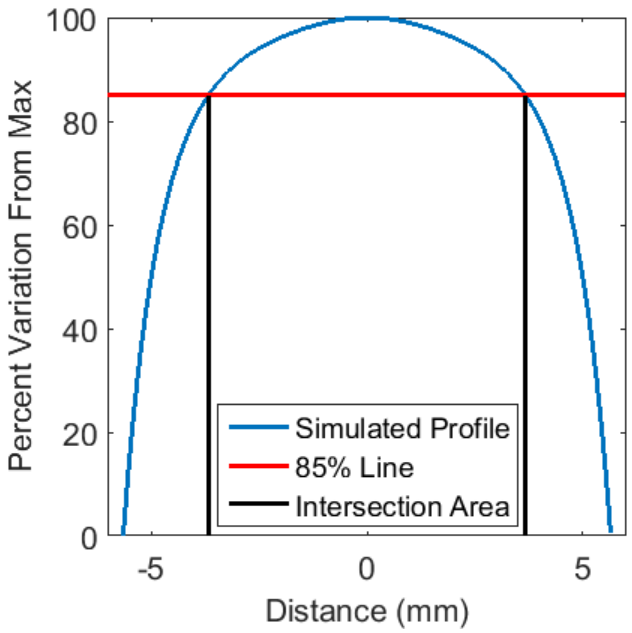

Figure 4.5: Example of acceptable variation in beam current profile across sample area to provide an approximate uniform irradiation.

design operates is quite insensitive to plasma property changes. This shows that a single design can accommodate a varying beam energy and ion density. It also shows high accuracy measurements of plasma properties are not required and average expected value ranges are sufficient. This validates the use of the simple Langmuir probe and corresponding analysis.

A challenge in the design process was creating a single design to work for different beam energies and species. To handle this challenge, the following design philosophy was used. A base case using protons with V_{pl} = 10 kV, T_e = 3 eV and J_{source} = 1 A/m^2 (approximate average J_{Bohm} calculated from Langmuir probe measurements and from expected total beam current values) was created to meet the distribution requirements. The design was then tested with numerous different beam energy and plasma input parameters. If a desired combination did not work in simulation, the design was adjusted and simulated back at the base case. If the new design did not work for the base case, the design was adjusted again until sufficient operation was achieved and the process repeated. This continued through many iterations until the final design was found to work across a large range of beam conditions. The final base case simulation output is shown in Figure 4.6 to provide context for the following sections.

Once the design was accepted, it was constructed and integrated into the larger system

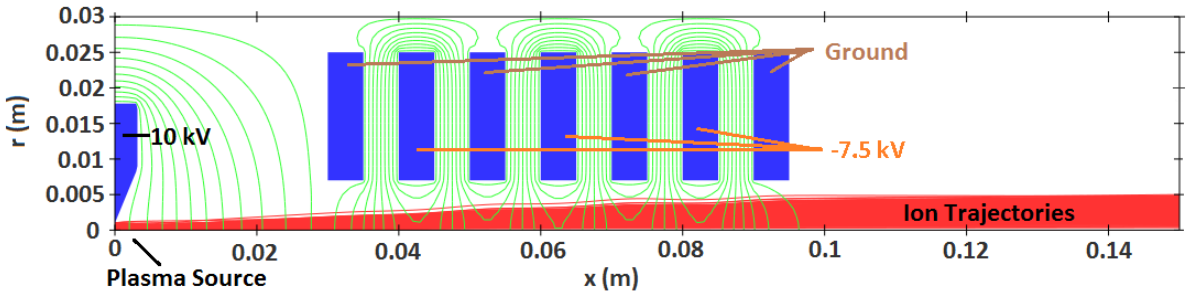

Figure 4.6: IBSimu 'base case' simulation output of ion source design. Electrodes are in blue, ion trajectories in red and equipotential lines in green. Beam stops at 15 cm rather than 42.5 cm to provide higher detail resolution.

for experimental testing. Although it is unlikely for simulation to directly match measured results for a number of potential reasons such as imperfect construction or assumptions (background gas effects in the transport column being negligible), simulation is expected to provide sufficient results that allows experimental implementation without large errors. This allows the next step of experimental design modifications and adjustments to occur.

4.7 Ion Source Design

4.7.1 Plasma Electrode Design

The plasma electrode is typically physically connected to the plasma source chamber and typically doubles as a chamber wall with an aperture in it for ion extraction. In the present system, this wall is the flat face of the hollow cylinder plasma source. The extraction aperture provides a pathway for ions, as well as some unwanted background gas, to enter downstream system components. Therefore, optimal design requires consideration of both effects and must be large enough to produce sufficient beam currents, but small enough to limit gas flow and downstream pressure as this affects ion-neutral collision rates and beam transport success. As IBSimu only provides information on resulting beam current and not on gas flow or pressure effects, the latter requires experimental trial and error investigation. Given the low operational pressure of 1 mTorr, it was assumed that any aperture of reasonably small size would produce a sufficiently small gas leak. Together with the downstream turbo pump, this creates the assumption of negligible downstream pressures for any design. This means IBSimu results alone can be used for aperture size design prior to experimental modifications

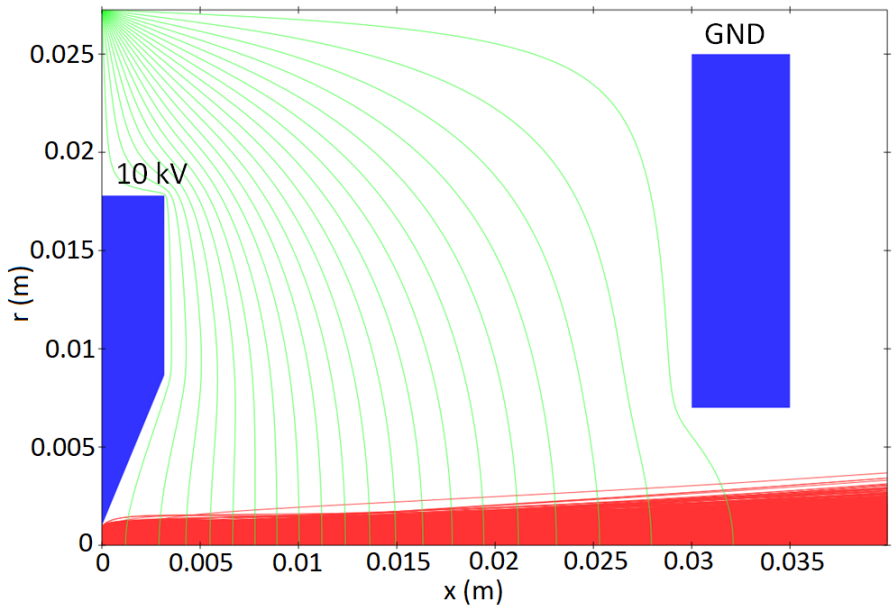

Figure 4.7: IBSimu output of final extractor design. Blue blocks are electrodes, red lines are ion trajectories and green lines are equipotential lines of the electric field. Equipotential shape reveals converging or diverging nature of the beam throughout the path.

and verification. Once implemented and experimental verification of sufficient operation is achieved, the design process ends. The final design for the present system is a single circular aperture with a 2 mm diameter and beamline side edges tapered to the Pierce angle. An IBSimu output of this design with the corresponding ground electrode design is shown in Figure 4.7. The Pierce angle was chosen due to the recommendations of multiple sources, simulations of it in comparison to other angles and the successful experimental results.

4.7.2 Ground Electrode Design and Acceleration Gap Distance

Design of the ground electrode, the first electrode following the plasma electrode, in a system with additional ion optics is not completed in isolation but instead requires consideration of the entire optics chain. This is where the computer simulation code shows its real value. Ground electrode design choices are limited by other factors in the system. Aperture shape is all but set by the choice of extraction aperture shape. The size of the ground electrode depends on extraction aperture size and beam size due to plasma meniscus beam formation. Both the outer shape and diameter are influenced by breakdown requirements and mechanical

mounting within the ion optics system. As the ground electrode is part of the overall ion optics assembly, which requires mechanical mounting, its shape and outer diameter were chosen to be equal to all other ion optics electrodes for mechanical ease. This choice makes the ground electrode circular with a diameter of 5 cm and creates a 5 mm gap between the electrode edge and the chamber wall. As for the aperture size and electrode thickness, both were chosen solely based on simulation results and the general philosophy of allowing the potential map of the system to reach ground within the electrode without reaching a plateau. As was the case with the plasma electrode, only one ground electrode (and additional ion optics electrodes) was machined and tested, which resulted in successful beam creation. The final choice for the aperture diameter and thickness is 1.4 cm and 0.5 cm respectively.

The final design choice is acceleration gap distance (position of ground electrode relative to plasma electrode), which influences the plasma meniscus. As discussed in Section 3.2.1, the plasma meniscus is the boundary emission layer of the plasma-vacuum interface that defines initial ion trajectories. The goal is to create an initial converging effect on the beam using the meniscus formation and electrode tapering. The chosen distance was based solely on beam profile results from simulations of the full ion optics. A starting point for initial simulations was calculated using the Child-Langmuir law and measured plasma properties. The design was then modified to find the final gap distance of 3 cm measured from the plasma side of the plasma electrode to the first face of the ground electrode. As will be discussed in Section 4.8, this distance was also chosen to prevent Paschen breakdown in the gap. The final design is shown in Figure 4.7 where the simulation is focused on the acceleration gap area. The shape of the equipotential lines inside the plasma aperture and the bending of the ion trajectories shows that the meniscus is concave and produces a converging effect. However, even within the short gap, space-charge repulsion causes substantial beam divergence.

4.8 Application of Paschen's Law

As the present system operates in the low mTorr range, which naturally causes pd to tend to the lower pd region, eliminating breakdown conditions is best achieved by designing for a maximum possible pressure that will not be exceeded in operation. If chosen correctly, the maximum pd scenario will be on the left side of the Paschen minimum and capable of holding

off the maximum possible voltage difference. All other operational pressures will only cause *pd* to further decrease and further reduce breakdown conditions. To define the maximum design pressure, recall that the typical operational pressure is of the order of 1 mTorr. The pressure in the acceleration gap and transport column will always be less than the pressure in the source chamber as the amount of leakage gas will be small in comparison to the volume and is removed by the downstream turbo pump. For safety tolerance purposes, an extreme high end estimate for maximum pressure anywhere within the system can be taken as 9 mTorr. The maximum design voltage is taken to be 45 kV; the difference between maximum positive and negative bias sources, +30 and -15 kV. Using these maximum values a maximum safe distance can be calculated, below which breakdown cannot occur.

Inspection of the low *pd* side of hydrogen curve in Figure 3.9, shows that a voltage of 45 kV cannot cause breakdown below a *pd* factor of approximately 0.9 Torr-cm. The gap design and analysis is completed for hydrogen as any designed *pd* that works for hydrogen will also work for helium due to the relative positioning of the helium curve. A pressure of 9 mTorr thus corresponds to a gap length maximum of 100 cm. As the ion acceleration gap length is just under 3 cm, it can be safely assumed that Paschen breakdown cannot occur in the acceleration gap. Furthermore, as the entire beamline is less than this maximum distance, it is also safe to say that Paschen breakdown cannot occur anywhere within the system between two different charged surfaces. Experimental measurements of downstream pressure are of the order of 0.1 mTorr making the true breakdown length over an order of magnitude higher than this high safety tolerant calculation. Even though this result shows breakdown considerations to be negligible for present dimensions, it is still an exercise that should be completed in HV vacuum designs as incorrect assumptions can prove very detrimental. While gap distances in the final design could have been much larger than implemented, the design philosophy was to be as safe as possible at all potential pressures in the mTorr range. Given that there is no harm, other than potential machining challenges, to making distances small, all gaps between charged surfaces, except between the plasma source and grounded target, were designed to be as small as possible to ensure a low operational *pd* value. This also allows the beamline to run at higher pressures within safety tolerances should the need arise.

4.9 Ion Optics Design - Einzel Lens Stack

Prior to simulations, the choice was made to use only electrostatic lenses and of the available options, the choice of using Einzel lenses was made due to their implementation ease and successful history. Recall that an Einzel lens contains three electrodes of altering polarity to create a beam convergence effect. The length of the beamline (42.5 cm $\pm$ 0.5 cm) is sufficient to not require the short focal length of the decel-accel configuration and thus the accel-decel configuration was chosen to take advantage of the benefit of minimal beam abberations and to avoid the issues of the decel-accel lens discussed in Section 3.4.1. Early simulation designs used a single Einzel lens with outer electrodes at ground such that the ground electrode of the extractor could double as a lens electrode. This choice required the middle electrode to be negatively biased. This allows the Einzel lens electrode to double as a suppression electrode, which keeps the number of required HV sources to the minimum of two. Having the final electrode grounded also allows the remainder of the beamline to experience an equivalent potential and result in a zero net electric field as all elements after the ion optics, including the target, are also grounded. If the final electrode was not grounded, the resulting electric field could result in unwanted effects on the beamline.

Simulation revealed a large voltage drop within the Einzel lens was required to create an approximate parallel beam of the order of 1 cm upon exiting the lens. It also showed that a single lens containing the extractor ground electrode results in the beam becoming strongly divergent and obtaining a large diameter before reaching the target. Together, these results showed that a single Einzel lens close to the plasma source is not sufficient to produce the desired target beam characteristics. To address the beam expansion issue, the lens could be moved further from the source, closer to the target. However, this is counterproductive to the overall design as the further the first lens is from the source, the more work it must do on the beam due to the increased beam size as a result of the extra distance under only the space-charge repulsion force. Another option is to keep the first electrode close, and add additional lenses throughout the beamline to continually counteract the space-charge expansion that leads to beam divergence. A version of this idea led to the design of a stack of multiple Einzel lenses connected to the extractor ground electrode rather than just a single lens. The

advantage of the stack design is that multiple lower voltage lenses are used to create the same, if not greater, effect as a single high biased lens. This decreases the HV bias requirement of the negative supply and allows the use of a lower voltage supply, which reduces costs and safety concerns. The lower bias stack can achieve a high focusing power by increasing the distance over which the converging force of the lens system is applied. This also could have been achieved by creating thicker electrodes, but this was avoided with the intent of avoiding potential plateaus at all possible system voltage combinations. Another benefit of the lens stack is the reduction of the travel distance from the lens edge to the target as a result of the additional length. This provides less time and distance for the new ion trajectories to diverge from their optically set paths due to space-charge repulsion before reaching the target.

The final lens stack, shown in Figure 4.9a contains three lenses composed of seven electrodes, the first of which doubles as the extractor ground electrode and the last of which is grounded. The potentials of the electrodes alter between ground and a negative bias. By the time the ions leave the lens system, they travel approximately parallel to each other and are spread far enough apart that space-charge forces are significantly reduced for the operational beam current values. Therefore, the beamline will stay approximately the same diameter as it travels to the target with only a slight expansion that is built into design considerations for the final beam size. The gap between adjacent electrodes was chosen based on simulation results to be 1 cm. Simulation of the final ion optics design was shown in Figure 4.6. The potential map along the beam radial center is shown in Figure 4.8 to showcase the accel-decel design nature of each lens and supplement discussion on effectiveness.

As shown, the negative potential drop does not reach the full -7.5 kV at the beamline radial center. This is due to the choice of electrode aperture diameter and electrode thickness not allowing the potential field to reach full value. In some ways, this may be viewed as a sub-optimal design that should be redesigned to increase performance. The theoretical optimal design would see the potential field decrease to the maximum negative magnitude before instantaneously switching to begin rising and avoiding a potential plateau. However, this can only be achieved for a single energy system or a system where electrode aperture sizes or thicknesses are variable, which is not physically possible. The desire for the present system to operate at a range of energies makes optimal design hard to define. Adding to

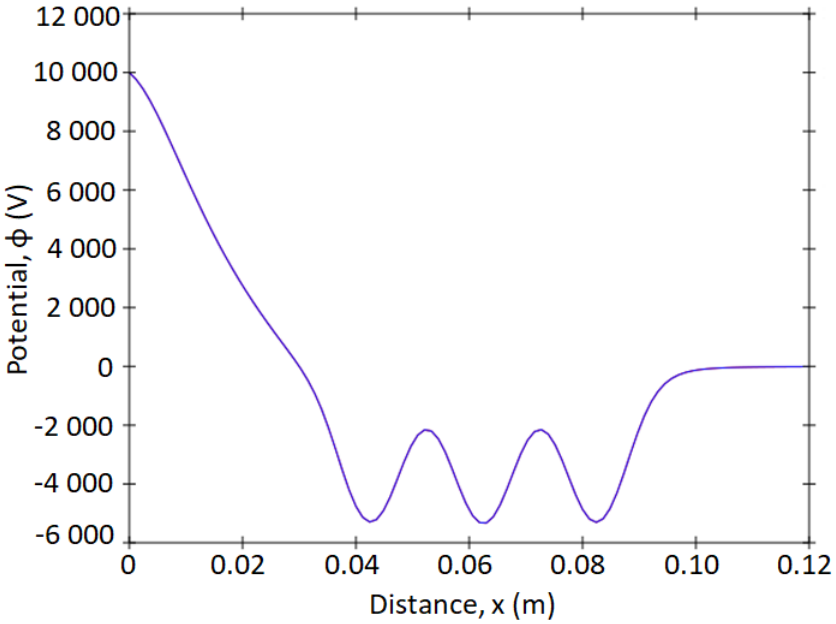

Figure 4.8: Potential map of final design along radial beam center. V_{pl} = 10 kV, V_{Einzel} = -7.5 kV. Note: Full -7.5 kV potential is not achieved. As sufficient operation occurs with this design, this is permissible.

the challenge is the desired variable beam size based on Einzel lens voltage, which requires the fixed electrode design to accommodate all possible beam sizes. This puts constraints on how close the electrodes can be to a given beam, which alters the effectiveness of the applied potential on the potential field map. Overall, the result is a variable optimal design definition that is replaced by a sufficient operation definition. The electrode sizes and positions were chosen such that sufficient results, including beam current, beam size, and avoidance of beam losses, were obtained for a wide variety of beamline settings.

4.10 Ion Optics Assembly and System Mounting

Based on considerations for construction, assembly, and maintenance, all electrodes in the Einzel lens stack were designed with identical dimensions. The inner diameters and thicknesses are equal to the ground electrode at 1.4 cm and 0.5 cm respectively. The outer diameters were chosen based on mounting technique and to reduce the gap between electrode edges and the chamber wall to create a small *pd* value. Each electrode contains three through holes toward the outer edge to allow three ceramic support rods to be inserted. Both

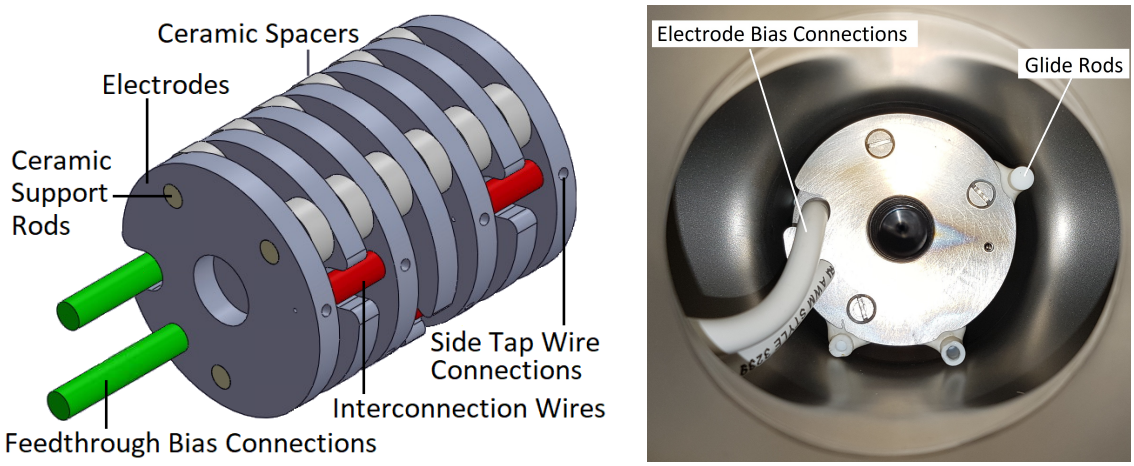

(a) **(b)**

Figure 4.9: (a) SolidWorks drawing of fully assembled Einzel lens stack complete with electrical connections. (b) Picture of lens stack inside transport column taken from the target chamber point of view. Picture shows geometrical centering, attached glide rods and electrical connections. The small diameter extraction aperture can be seen in the center of the electrode aperture.

ends of these rods are tapped to allow screws to fasten the entire assembly together. In between each electrode on top of the support rods are ceramic spacers that keep the electrodes electrically isolated and at a fixed distance from one another. The full assembly is shown in Figure 4.9a. The assembly then has three more ceramic support rods attached to the outer edges using Torr Seal. These outer rods act as glide rails to allow the assembly to slide into the cylindrical transport column and sit such that the geometrical center of the electrodes matches the the geometrical center of the transport column and beamline. Figure 4.9b shows a picture of the stack inside the system. The outer diameter of the electrodes (1.4 cm) is equal to the transport column inner diameter less twice the glide rail diameter (plus machine tolerance). This leaves a 5 mm gap between the electrode edges and the chamber wall, which is small enough to avoid Paschen breakdown at predicted operating pressures.

The electrode stack requires electrical connections between each electrode and the corresponding bias supply. All negative and ground electrodes are connected to each other respectively by connecting every second electrode in the stack. Connections are supplied by 40 kV insulated wire connected to each electrode via a connection hole and side-tapped screw machined into the electrodes. Furthermore, each inner electrode of the stack was machined

with a 'cut out' to allow the wire to pass through without increasing the overall diameter of the electrode stack. Both of these designs can be seen in Figure 4.9a. Each electrode chain is biased by connecting one electrode to the bias supply. A second connection point of the same type was machined into one ground and one negative electrode to complete this connection. The connection wires attach to an isolated HV power feedthough connected to a transport column access port to interface between the electrodes and bias supplies.

4.11 Transport Column

The transport column is the vacuum chamber component that contains the ion optics and links the plasma source to the target chamber thus defining beamline length. This length can be designed to a specific value, but design is typically as simple as keeping the line as short as possible to limit travel time thus limiting space-charge and ion-neutral collision issues. However, the column must also have sufficient length to include all required components such as diagnostic equipment, ports for HV lines or gas management, or, in some systems, mass selection instrumentation. In the present design, beamline length was increased by adding a 4-way cross to the transport column to provide one access port for the ion optics HV bias lines and one port for mid-line diagnostic equipment. Further length was added by the choice of target chamber, discussed in Section 4.12, which is an older, custom built vacuum chamber with five access ports, one of which is custom fit to the downstream turbo pump. The target sits in the middle of the chamber, based on access geometry, which, along with the distance provided by the connection port, adds to the beamline length. As both simulation and experimental results show, this added distance is accommodated by the design to not adversely affect system performance. Another aspect of transport column design is to limit the background pressure by limiting gas flow and adding vacuum pumping. This pressure reduction is required to minimize ion-neutral collision rates that adversely affect the beamline energy and physical distributions. Based on the beamline results covered in Chapter 5, the operational transport column pressure of the order of 0.1 mTorr is low enough to provide sufficient operation.

To limit the amount of HV wire inside the vacuum chamber that could perturb designed electric fields, the HV bias access port is positioned as close as possible to the lens stack

connection point. The HV power feedthrough has two legs (one for ground and one for negative bias) and can hold off 20 kV. While this access point added a significant length to the overall beamline (21 cm) it was required as no other available ports existed in the system. The second access port of the 4-way cross provided a convenient point to measure transport column pressure and determine that the vacuum system design, gas flow rate, and extraction aperture seal keeps transport column pressures below plasma source pressures.

4.12 Target Chamber

Design of the target chamber is similar to the transport column in that its size and number of ports is dictated by the requirements of other elements rather than a specific effect on beamline performance. The target chamber is a cylindrical vacuum chamber with an inner diameter of 9.5 cm and five varying sized access ports. One access port is used to attach the chamber to the transport column, one is used to insert the target sample, one for total beam current monitoring, one to connect to the downstream turbo and one for a radial beam profile measurement device. The chamber is mounted vertically (long axis perpendicular to beam direction) such that the bottom connects to the turbo pump and the top allows vertical sample insertion. All other access ports are on the side of the cylinder. The placement of the turbo pump in the target chamber rather than transport column was chosen based on ease of assembly and mechanical access. The remainder of the access ports, save the connection to the transport column, which is as simple as it sounds, are discussed in the following.

4.12.1 Sample Holder

The sample holder, *i.e.*, the target, shown in Figure 4.10, is a simple design consisting of a base with four screw holes arranged in a square and a hollowed square cover plate, or mask, with four matching through holes. The holder is designed to accommodate approximately 1×1 cm square samples with a thickness of the order of millimeters. The sample is held in place by a press fit between the cover plate and base. Care must be taken to ensure the press fit is not tight enough to cause the sample to fracture under applied pressure. A consequence of this design is that a portion of the sample will not be exposed to the beam. The exposed area is an 8×8 mm square with rounded corners for machining ease. As previously mentioned, the measurement area for present research is further reduced to

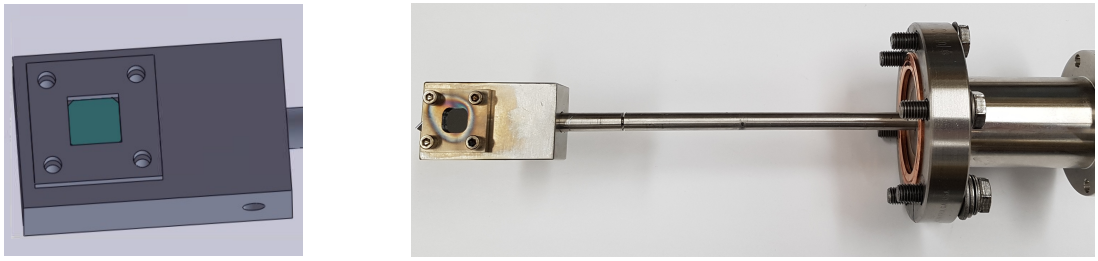

(a) **(b)**

Figure 4.10: (a) SolidWorks drawing close-up of sample holder to show design details. (b) Picture of sample holder and translational vacuum feedthrough.

5×5 mm, *i.e.*, the mask design does not hinder research results. The holder is attached to a translational and rotatable vacuum feedthrough that is attached to the top of the chamber as was shown in Figure 4.2. This mounting places the sample in the center of the target chamber which adds some distance to the beamline, but is the simplest implementation.

The translation and rotation features of the sample holder are used to aid beam diagnostics. Prior to sample irradiation, the target is removed from the beam path, the beam is turned on, measured and given appropriate settings before the sample is returned to the beam path. This allows full characterization of the beam before irradiation to ensure given settings will produce expected results. This measurement step is required due to changes in beam current values, both intentional (different irradiation rates) and unintentional (random fluctuations). As will be discussed in Section 4.14 and throughout Chapter 5, beam current changes do not adversely affect the system as long as they are properly measured. Measurement is required before and after sample irradiation as well as at intervals throughout beam operation which is aided by the ability to remove the sample from the beam. The measurement at intervals also allows adjustments to beam current to be made if necessary or desired. If beam current cannot be actively monitored, it must be calibrated based on system parameters and assumed to stay constant throughout an implant. This was quickly discovered to be a poor assumption in the present system. The random beam current fluctuations and effect mitigation are discussed in Chapter 5. For now it is sufficient to say active monitoring is required, which is not possible in the present design without a movable sample.

Sample sizes were arbitrarily chosen to be approximately 1×1 cm. The target chamber can accommodate much larger samples, with the limiting factor coming from connection flange

inner diameter (3.9 cm). Assuming full irradiation of larger samples is desired, additional limits are obtainable beam size, whose maximum has not been tested, and corresponding beam current density across the larger area. However, the plasma source can produce higher ion densities than have currently been used, and the beamline can create larger beams by decreasing Einzel lens focusing. Therefore, larger samples could be irradiated by the system as is, with only a slight modification to the sample holder and beam diagnostics.

4.12.2 Beam Diagnostics

Along with the connection ports discussed, the target chamber has two additional ports for beam diagnostic equipment and measurements. Directly opposite the connection to the transport column and directly behind the inserted sample holder in the beam path is an access port that contains a total beam current measurement device. The device is a 3 cm diameter stainless steel circular plate attached to an electrical feedthrough. When the target is removed from the beam path, the beam hits the steel plate and current is measured by a 0.1 μA precision ammeter attached outside the chamber. The collection plate should be large enough to ensure collection of the full beam. This includes scenarios in which beam centering or width varies from expected results due to beam focusing or transport issues. It is not the job of the collection plate to identify these conditions, as they will be caught by other diagnostic equipment. As simulation showed expected beam diameters of the order of 1 - 2 cm, the collection plate was designed to be 3 cm in diameter which should meet requirements. Beam current measurement is used to assess beam transport conditions and calculate beam current density and delivered fluence values. Details of this are covered in Chapter 5. As previously mentioned, it is also used to set desired values both before and during irradiation when interval verification measurements are taken.

The other beam diagnostic port contains a radial beam profile measurement device. Radial beam profiles are used to calculate beam current density and fluence delivered to the target area. They are also used to assess the ability of the beam to deliver a less than 15% variation across the sample area and can also give insight into resulting beamline symmetry and position. The profile also gives information on amount of wasted beam, *i.e.*, beam that does not contact the target area; a characteristic that is desired to be minimized but will inevitably be significant based on the desire to perform a large area uniform irradiation. If

only one profile measurement direction is obtained, symmetry arguments are used to assume all other profile measurement directions are equal to create a 2D profile. This can produce significant errors in the profile if the assumption is wrong. As this assumption is unlikely to hold, based on experimental errors and differences from the ideal case, a second, perpendicular, profile measurement is conducted in the system. Together, the two measurements provide a more accurate 2D profile, but still require some assumptions that may not necessarily hold. However, short of taking a true 2D profile measurement, two perpendicular measurements produce sufficient results. Further details and results are given in Section 5.4.

4.13 IBSimu: Additional Details

Inputs to the IBSimu code include: plasma electrode geometry, ion charge, ion mass, ion current density (J_{Bohm}), T_e (parallel and perpendicular), and the starting energy (E_s) of the ions upon leaving the plasma electrode. E_s is not equal to the beamline energy, as this is calculated by providing the potential of the plasma electrode and target, but instead refers to the energy of the ions inside the source in the direction of the extraction aperture. This can be the result of pre-acceleration in the source or simply natural thermal motion. The natural motion of the ions is coupled to T_e through the Bohm criterion [54], which shows that the ion velocity in eV will be of the order of T_e. In the present system, there is no acceleration within the source and thus E_s is of the order of T_e. Therefore, simulations were completed with an E_s of 3 eV (expected average T_e value). As will be shown in Section 4.14, small variations in E_s are negligible with respect to the final beam distribution, primarily due to the small magnitude (eV) in comparison to the beamline energy (keV) and thus approximate values are sufficient. $T_{e\parallel}$ and $T_{e\perp}$ exist in the code for the case of a plasma source with a high magnetic field where T_e can differ parallel and perpendicular to the ion direction of travel. These parameters can be roughly thought of as the variance in E_s along specific directions. While the present source does use a magnetic field, it is assumed that there is no significant difference between $T_{e\parallel}$ and $T_{e\perp}$ and thus in simulation, these values are set equal. In terms of magnitude, the value in theory is zero (for a zero emittance source), but simulations were completed using a small value (a few eV) due to the potential of some variance either from the magnetic field or from random thermal motion not solely directed toward the extraction

electrode. Similar to E_s, Section 4.14 shows variation within the expected range of $T_{e\|}$ and $T_{e\perp}$ (1 - 5 eV) has a small effect on final beam distribution. Average parameter values for design simulations were protons with $T_{e\|} = T_{e\perp} = 3$ eV (approximate value), $E_s = 3$ eV (equal to average measured T_e), and $J_{source} = 1$ A/m^2 (approximate average J_{Bohm} calculated from Langmuir probe measurements and from expected total beam current values).

Other IBSimu input parameters are beamline length, transport column radius, number of ion trajectories to simulate and discrete step size (affects the number of calculations per ion as it traverses the beamline). If the step size is too coarse, results can become quite inaccurate. Therefore, final simulations used a high precision step size (5.5×10^{-5} m/step). The number of ion trajectories also affects the result and is best kept at a large value. It was found that approximately 10 000 trajectories were required for accurate results and that any increase over 50 000 did not significantly increase result accuracy. However, the difference between 10 000 and 50 000 was noticeable and thus all final simulations were completed at 50 000 ion trajectories. To further increase result accuracy, the output profiles from IBSimu underwent post simulation processing in Matlab to remove three artifacts from the results. These artifacts are caused by trajectory binning and the discrete nature of IBSimu. The first artifact was that some profiles produced a large peak or valley, 2 - 3 points wide, in the beam center. For the most part, these features were reduced by increasing the number of particles and step size resolution. However, even at the high resolution used for final simulations, these features would randomly appear. This was fixed by a detection and interpolation algorithm to fill in the central values. The second artifact was that the profiles did not always go to zero at the edges. This was fixed by fitting curves to the profile, with a least squares algorithm, and extrapolating the fit down to zero current. The final artifact was a general 'step-like' appearance to the profiles due to coarse output steps. This was also fixed with curve fitting. All profiles presented in this work have been put through this analysis.

4.14 IBSimu: Input Variation

Given the expected variation in plasma parameters, whether intentional increases to beam current or unintentional random fluctuations, the susceptibility of the beamline distribution to these parameter variations is required to assess performance. Ideally, variation to plasma

parameters does not significantly affect the beam profile at a given voltage pair setting. Achieving this allows the profile to be set independent of plasma properties, which allows characterization and calibration of the beam profile as a function of only voltage settings, as desired. This means active profile monitoring during system operation is not required as voltage settings, once set, are constant. Furthermore, profile independence from plasma properties means the random fluctuations and drifts in beam current become insignificant to the profile. However, these fluctuations still need to be addressed for fluence calculations (Section 5.9). The sensitivity of the beam density profile to changes in the plasma source were investigated with IBSimu by evaluating simulated profiles as a function of individual parameter variation with all others held equal. All following simulations were completed using 50 000 simulated ion trajectories and a high resolution step size of 5.5×10^{-5} m/step.

4.14.1 Current Density Variation

Arguably the most important parameter to test variation sensitivity is current density due to its high planned variation and known influence on the beam profile through space-charge effects. As a result of source prototype testing, the average expected values for n_0 and T_e are known to be of the order of 10^9 ions/cm^2 and 3 eV respectively. This gives a J_{Bohm} of 400 μA/cm^2 or 4 A/m^2 as presented in Section 4.5. Current density variation sensitivity simulations were completed using a defined ion optics geometry and set system voltage pairs to test a range of densities. The resulting profiles were analyzed and compared to the expected average 1 A/m^2 profile. Figure 4.11 displays the simulated beam profiles for two different beam voltage pairs (V_{pl}, V_{Einzel}) equal to (10, -7.5) kV in (a) and (15, -11.2) kV in (b). All simulations were completed using protons with T_e and $E_s = 3$ eV. At both energies there is little difference between the profiles up to 10 A/m^2. Both energies also exhibit a substantial beam width increase at 100 A/m^2 and a small but noticeable increase at 25 A/m^2. The variation between 100 A/m^2 and 1 A/m^2 is noticeably larger at 10 keV due to the increased space-charge repulsion effect as a result of decreased ion velocity. As the velocity decreases, the ion time of flight in the system increases. This increases the time spent in the vicinity of other ions and thus increases the effect of space-charge repulsion. Therefore, the lower energy 10 keV beam should expand more than the 15 keV beam, all else being equal, as is observed in these profiles. The difference between 10 A/m^2 and 1 A/m^2 in beam radius at

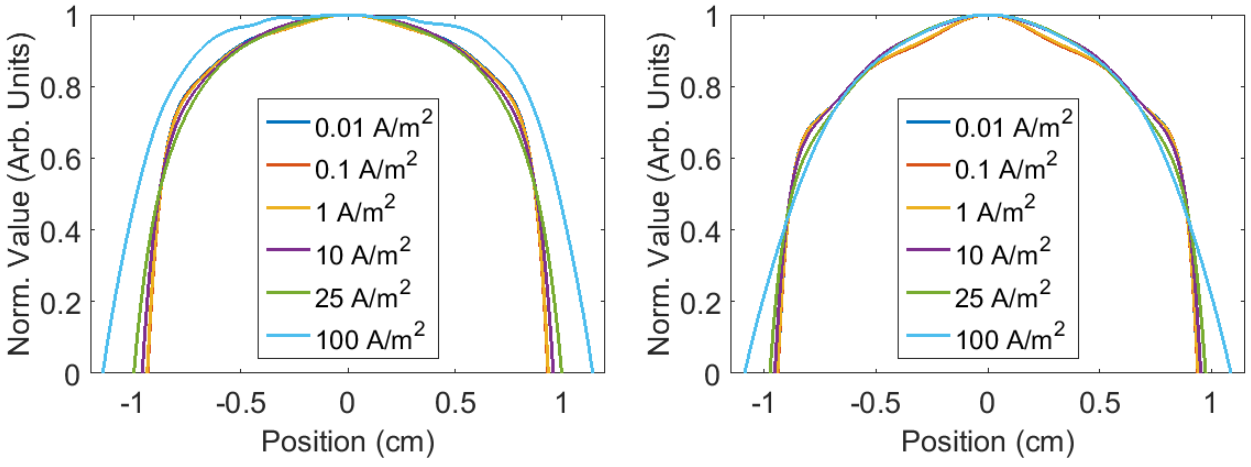

Figure 4.11: Resulting simulated beam profiles at varying current densities. Parameters: protons at $T_e = E_s = 3$ eV for (a) $V_{pl} = 10$ kV, $V_{Einzel} = -7.5$ kV and (b) $V_{pl} = 15$ kV, $V_{Einzel} = -11.2$ kV.

10 keV is 0.025 cm or 0.5 mm in beam diameter and at 15 keV, the difference is 0.1 mm in beam diameter. Looking at current densities below 1 A/m^2 the difference between profiles becomes less than 0.1 mm in diameter. Given the average expected current density is in the 1 to 10 A/m^2 range, this result shows that beam profile is relatively insensitive to density changes as desired. Looking at the 25 A/m^2 case in comparison to 1 A/m^2 as an extreme upper limit comparison, the difference in diameter is 0.5 mm at 15 keV and 1.2 mm at 10 keV. In both of these extreme cases, the difference is still relatively small and in the worst case scenario presents an approximate 10% error in beam size assuming a beam size of the order of 1 cm. If this analysis is kept to the more reasonable comparison of 10 A/m^2 to 1 A/m^2, the error at 10 keV becomes less than 5%; an acceptable error bar. Furthermore, comparison of corresponding current density profiles at each energy shows that beam size can be maintained with proper Einzel lens voltage scaling as was desired.

As will be discussed in Section 5.9, the errors introduced to the beam profile (slight diameter and shape differences) by a varying current density within the expected operating range are acceptable and somewhat negligible in the grand scheme. This analysis was completed for multiple different beam energies from 5 to 25 keV, but with increased emphasis on the 10 keV beam. All current density variation investigations produced the same result of a negligible effect on the beam profile in the 0.01 to 10 A/m^2 range. Special note should be

given to the 5 keV beam where differences up to 20% between 10 A/m^2 and 1 A/m^2 profiles were observed. This error is approaching the point where the effect cannot be ignored or absorbed into error bars and further beam energy reduction will create even greater profile variations. As the present radiation research experiments are conducted at 10 keV, this low energy complication is not an immediate concern. However, potential future (low energy) applications will likely require design changes to produce sufficient operation.

4.14.2 Electron Temperature and Starting Energy Variation

As no pre-acceleration exists inside the plasma source, it is assumed that E_s is solely due to natural ion motion, which is directly related to T_e through the Bohm criterion and thus, E_s is approximately equal to T_e. However, the T_e in the simulation code has a slightly different meaning as the 'true' plasma parameter is accounted for in the current density and E_s parameters. The $T_{e\parallel}$ and $T_{e\perp}$ simulation parameters are components parallel and perpendicular to the ion beam direction of travel. As mentioned, in this system $T_{e\parallel}$ and $T_{e\perp}$ are ideally zero but potentially have a small value of the order of a few eV due to random motion and the applied magnetic field. It is also assumed that these values will be approximately equal, and thus are set as equal in all simulations. Unlike the current density whose value can realistically change by significant amounts (orders of magnitude), these parameters are much more stable and thus have lower possible ranges. The potential range for the plasma T_e is not likely to exist outside of 1 to 10 eV and thus testing was confined to this range. A true upper limit of 5 - 6 eV is more accurate but to show parameter variance, up to 10 eV is investigated. The resulting simulation profiles are shown in Figure 4.12 (a) and (b) for a 10 keV and 15 keV proton beam respectively with varied E_s (measured plasma T_e) values. Little difference exists between profiles at a given energy as expected due to the small magnitude of E_s (eV) in comparison to the beamline energy (keV). The small difference in distribution is due to the increased ion velocity as total beamline energy is E_s plus energy obtained once extracted. Therefore the ion time of flight is decreased by a flat amount throughout the beamline, which decreases space-charge forces and thus the beam width. Figure 4.12 (c) and (d) shows resulting profiles for $T_{e\parallel} = T_{e\perp}$ variation again at 10 and 15 keV, which shows negligible difference in beam diameter, but small noticeable differences in the beam profile center. From inspection, as the 'variance' T_e is increased,

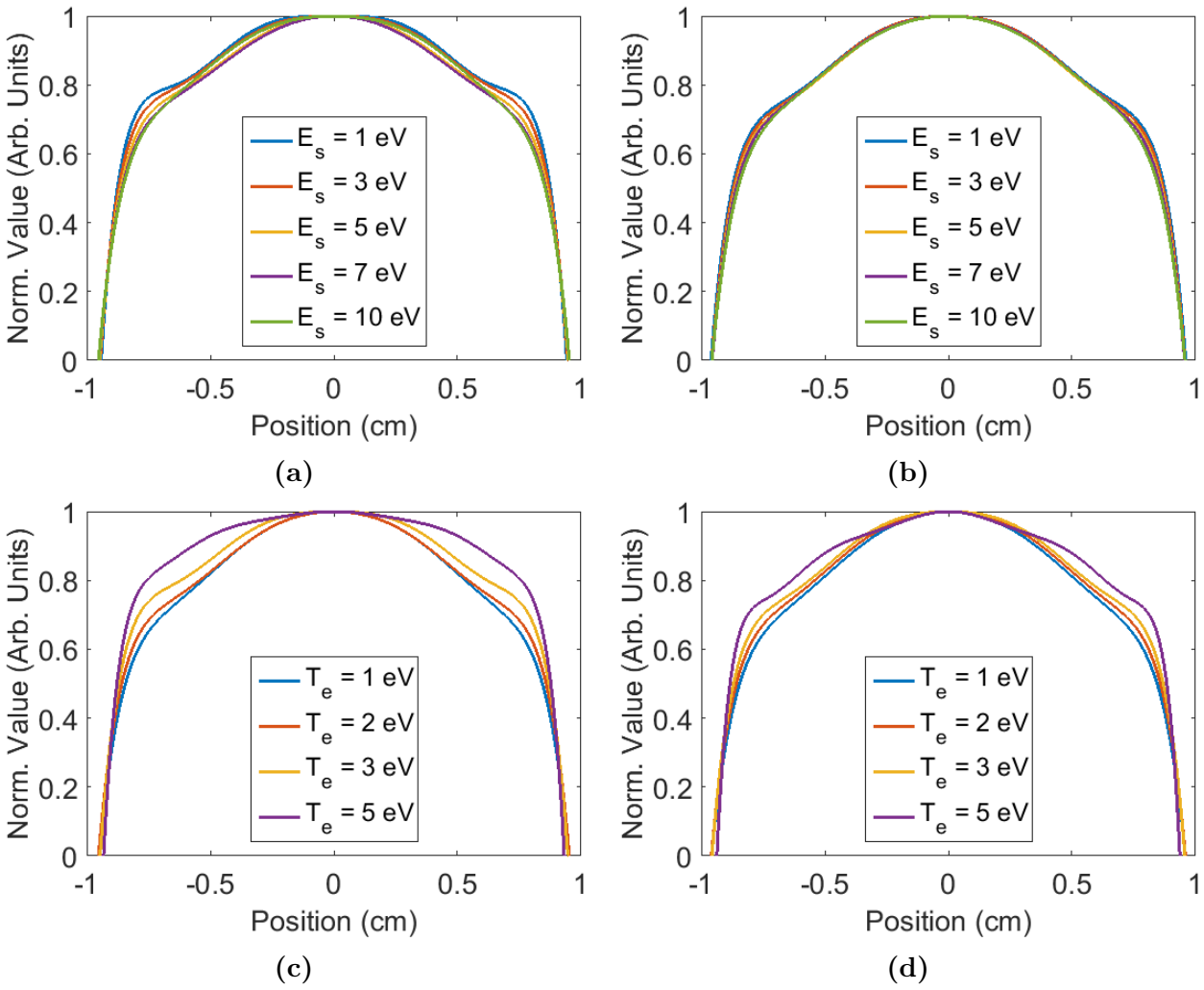

Figure 4.12: Simulated proton profiles for varying E_s (a, b) and T_e (c, d). (a) T_e=3 eV, V_{pl}=10 kV, V_{Einzel}=-7.5 kV (b) T_e=3 eV, V_{pl}=15 kV, V_{Einzel}=-11.2 kV (c) E_s=3 eV, V_{pl}=10 kV, V_{Einzel}=-7.5 kV (d) E_s=3 eV, V_{pl}=15 kV, V_{Einzel}=-11.2 kV. J_{source}=1 A/m^2.

the profile broadens and creates a larger 'flat-top' region in the beam center rather than a more peaked distribution at lower values. This is an expected outcome as the increase to the perpendicular component of ion energy will cause trajectories to naturally diverge more than if this component were zero and thus creates a broader beam profile.

4.14.3 Particle Type Variation

Given the goal of creating a beamline design that can support both hydrogen and helium beamlines, a significant question is, how do different particle types (charge state and mass) affect the beamline? In general, particles with increased mass and the same charge state will have slower velocities at a given V_{pl} which will increase time of flight and thus increase both

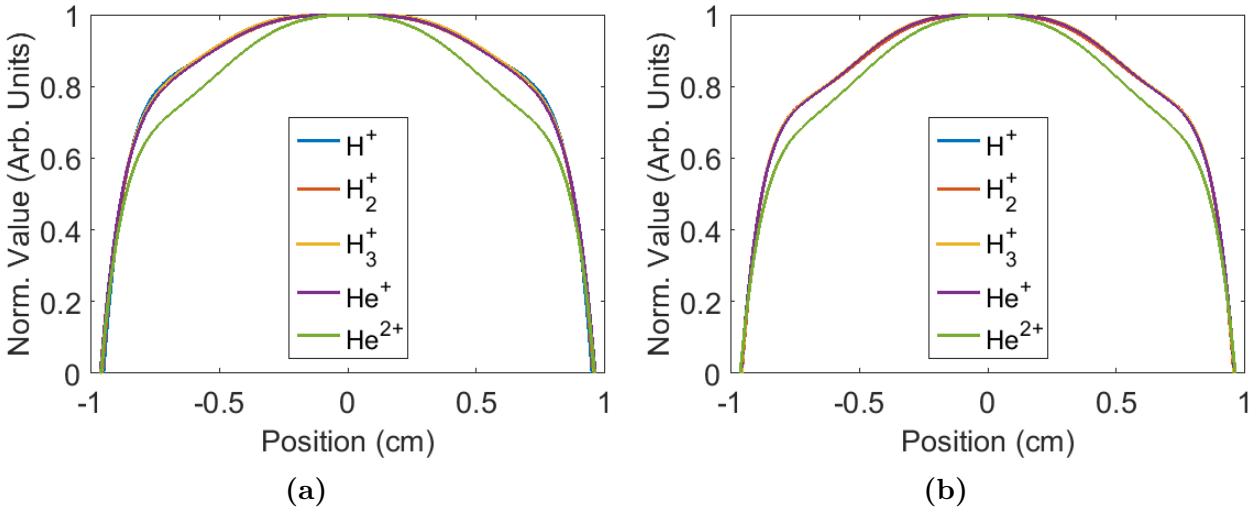

Figure 4.13: Varying particle type simulated profiles. J_{source}=1 A/m^2, T_e=E_s=3 eV for (a) V_{pl}=10 kV, V_{Einzel}=-7.5 kV and (b) V_{pl}=15 kV, V_{Einzel}=-11.2 kV.

the effect of the ion optics and the space-charge repulsion force. The final result is beamline dependent as it depends on beamline length and ion optics strength and sizing. The case of equal mass particles with different charge states is a more involved question. In general, the higher charge state will create stronger space-charge repulsion forces that should cause a more divergent beamline. However, recall that beamline energy is defined as $q\Delta V$. This means the increased charge state increases the ion energy, which increases velocity and decreases time of flight. The time of flight decrease will decrease the time that space-charge repulsion has to affect ion trajectories. This velocity increase also decreases the effectiveness of the ion optics. Again, the end result is beamline dependent. In the hydrogen beamline, there will exist H^+, H_2^+ and H_3^+ as there is no ion selection in the present system. Each particle has a single charge making space-charge forces equal but the different masses will create different velocities. In comparison, the helium beamline will contain He^+ and He^{2+} which quadruples the space-charge force (q^2) for He^{2+} - He^{2+} interactions and doubles the force for He^{2+} - He^+ interactions while also doubling the ion energy of He^{2+} and increasing the velocity by $\sqrt{2}$. In order to test the beamline dependence on particle type and assess whether or not a single design was possible in the expected source operating regime, simulations of H^+, H_2^+, H_3^+, He^+ and He^{2+} using the operational 10 keV design parameters with 5 A/m^2 and $T_e = E_s = 3$ eV were conducted and compared. Resulting profiles are shown in Figure 4.13. Interestingly, all

particle types except alpha particles (He^{2+}) provide virtually identical profiles. The alpha particle profile has identical beam diameters but a slightly different spatial distribution that is slightly stronger peaked in the beam center. This suggests the velocity increase effect outweighs the space-charge force increase for given current densities.

4.14.4 Voltage Variation

The effects of varying either V_{pl} or V_{Einzel} are both straightforward but the final outcome is not necessarily obvious. Changes to V_{pl} affects the particle velocity which affects the time of flight within the Einzel lens and entire beamline. When ion energy is increased, time spent in the Einzel lens is decreased which decreases the lens effectiveness and leads to a wider beam. However, the decreased time spent in the beamline as a whole also reduces the effect of space-charge repulsion, especially after the Einzel lens, which leads to a more narrow beam. The resulting profile is system dependent as current density, travel distance, and base lens strength all influence which effect dominates. For V_{Einzel} variation, the result is more straightforward as this variation only affects the lens strength and does not affect ion velocity outside of the lens. Therefore, an increase in V_{Einzel} magnitude will create a more narrow beam and a decrease in magnitude will create a wider beam. One caveat to this description is the assumption that increases to V_{Einzel} do not create an over convergent lens and a net divergent effect (*i.e.*, the focal length does not become too short).

In regard to application, this question is, how do potential input or equipment errors in applied voltage (50 - 100 V error) affect the resulting beam? As voltages are a set parameter, rather than a created parameter, such as n_0, the range is much more limited. The tested range is based on source setting precision, which for both sources is 100 V. The effect of altering the voltage by $\pm$ 100 V depends on the base setting as a 100 V variation on $V_{pl} = 1$ kV should have a larger effect on the resulting beam than a 100 V variation on $V_{pl} = 10$ kV as the percent variation goes from 10% to 1%. Therefore, voltage variation will be examined at two different (V_{pl}, V_{Einzel}) settings from the operational characteristic curve, at opposite ends of the operational range: (5, -3.9) kV and (20, -14.5) kV. Results are shown in Figure 4.14. The results are best showcased for the lower energy beamline, 5 kV, as the positive voltage changes make up a larger percent of beam energy and the negative voltage changes are also more significant in comparison to the beam energy. When V_{Einzel} is varied, increases

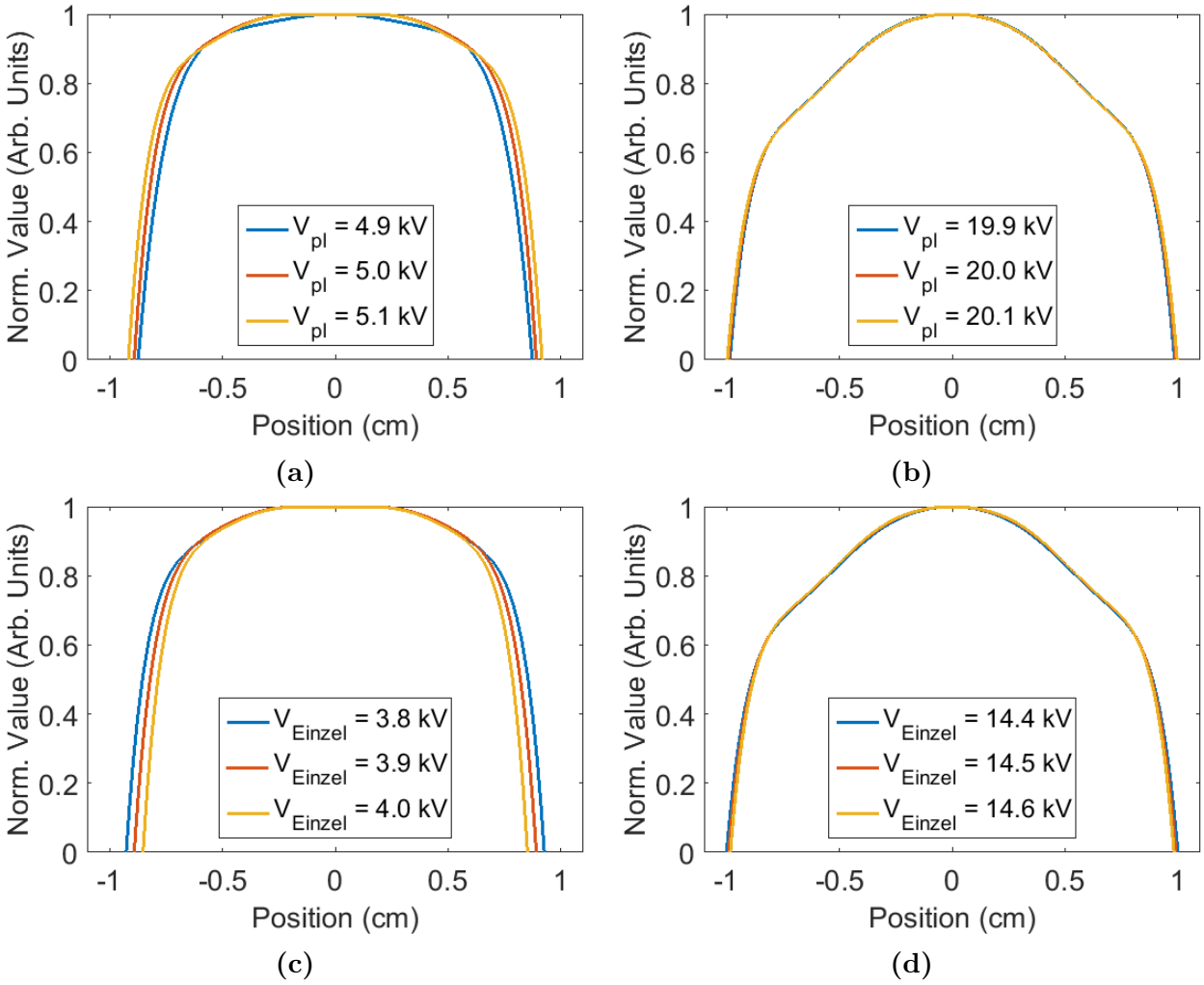

Figure 4.14: Voltage variation simulated profiles. H_2^+, J_{source}=1 A/m^2, T_e=E_s=3 eV. (a) V_{pl}=5 kV ± 0.1 kV, V_{Einzel} = -3.9 kV (b) V_{pl}=20 kV ± 0.1 kV, V_{Einzel} = -14.5 kV (c) V_{pl}=5 kV, V_{Einzel} = -3.9 kV ± 0.1 kV (d) V_{pl}=20 kV, V_{Einzel} = -14.5 kV ± 0.1 kV.

in magnitude result in a more narrow beam as expected. However, when V_{pl} is varied, decreases in magnitude result in a more narrow beam. This shows that, in this system, the increased lens effect outweighs the increased space-charge effect. In all cases, the difference between profiles is relatively small, with higher energy beamlines showing less susceptibility. As the radiation research will be conducted at a constant setting of (10, -7.5) kV, variance in voltages is only an issue of repeatability if the settings get changed, or potential repeatability issues in the sources themselves. Given the relatively high energy of 10 kV, the small variance in profile at 0.1 kV error and that actual repeatability errors will likely be much less than 0.1 kV, this is assumed to be a negligible effect on beam operation and characterization.

4.14.5 Variation Conclusions

The primary conclusion from this investigation of simulation input parameter variation is the strong suggestion that variation of all parameters, and by extension plasma source conditions and system settings, within expected operational ranges, will not produce significant errors in an average parameter beam profile. A summary of these results is shown in Table 4.1. Figure 4.15 shows an average value simulated profile along with maximum and minimum possible simulated profiles. This figure provides a theoretical error bar for an operational profile at 10 keV. As can be seen, there are definite differences between the three profiles in both diameter and distribution. Differences in diameter are easiest to quantify. The maximum difference between these maxima profiles and the central average profile is 1 mm. As will be shown in Chapter 5, error bars of this magnitude and even larger are acceptable for the present radiation damage research. This means source repeatability, plasma instabilities, and variations throughout a single run are acceptable and can be absorbed into an acceptable error calculation. This also conclusively shows, in theory, that a variable density beamline, with a constant profile, is attainable with previously characterized voltage settings, which meets one of the project goals. Finally, this result shows that the measurement and analysis technique used for the Langmuir probe complete with inherent inaccuracies, is sufficient to provide values for simulation as the 'true' values, if different from measured, would not have affected the final outcome as they would fall within the tested ranges.

Parameter	Range	Diameter Effect	Distribution Effect
J_{beam}	0.01 - 10 A/m^2	Small (< 10%)	Negligible
E_s	1 - 10 eV	Negligible	Small
$T_{e\|\|}$ & $T_{e\perp}$	1 - 5 eV	Negligible	Small
Particle Type	H^+, H_2^+, H_3^+, He^+, He^{2+}	Negligible	Small
V_{pl}	± 100 V	Small but Significant	Small but Significant
V_{Einzel}	± 100 V	Small but Significant	Small but Significant

Table 4.1: Summary of tested inputs and ranges with IBSimu along with beam profile diameter and distribution effects. Within the tested operational ranges, varying parameters have a small to negligible effect on resulting profile except when changing voltages. This is as desired - beam is fully adjustable based on applied voltages and small changes to plasma properties have negligible effects on resulting beam.

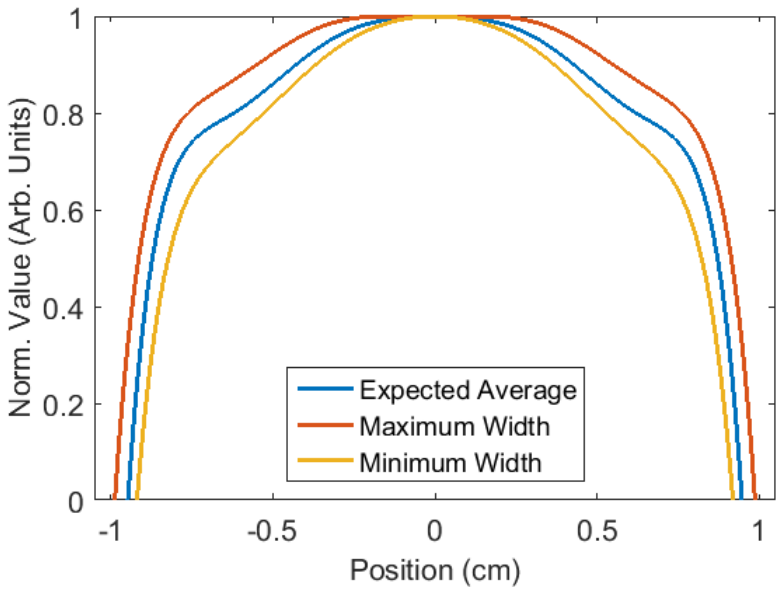

Figure 4.15: Maximum simulation error bounds on expected simulated beam profile. Maximum (red) and minimum (orange) bounds obtained from combination of parameter variations that increase or decrease profile width respectively. All values are extremes of the quoted parameter ranges.

Chapter 5

Beamline Characterization Results

Use of the beamline for charged particle radiation damage research is dependent on sufficient and stable beam characterizations. As shown in Section 4.14, the adjustable beam size allows numerous possible beam sizes and distributions. However, the present project has a specific beam profile of interest, one which meets the sample area uniform irradiation requirement. While multiple beam profiles exist that meet this requirement to varying degrees of success, only one was chosen for full characterization and implementation. Through a combination of simulation and experimental testing, the chosen operational standard beam is created at voltage settings of (10, -7.5) kV for (V_{pl}, V_{Einzel}). From here a family of voltage settings at other beam energies can be found through simulation to provide the same simulated output and, in theory, the same experimental results. An operational characteristic curve is obtained for the chosen beam distribution once experimental results confirm sufficient operation of these voltage pairs. This allows the possibility of research into the energy dependence of radiation effects and variable energy implants of a single sample, all with a constant beam profile. It is known from theory that particle energy primarily affects penetration and implanted layer depth. As examination of implant depth is not part of the present scope, and depth effects can be calculated from any energy result, present research is conducted at a single constant energy of 10 keV (chosen for its relation to the solar wind and expected surface level depth profile), which in turn makes V_{Einzel} constant.

This chapter discusses beamline diagnostic measurement techniques that can be used for any beam size (voltage pair) but with an emphasis on the (10, -7.5) kV beamline. These measurements include total beam current, optimal beam transport and radial current density profiles as well as an attempted 2D beam shape measurement using a crystalline silicon (c-Si) target. Calculations of current density and delivered target area fluence are then presented

based on experimental measurements. Beamline operation is discussed along with implementation challenges including how they were handled. Finally, a brief study of induced structural change in c-Si as a function of fluence is presented using Raman spectroscopy. Measurements of multiple irradiated samples at varying beam currents are compared with published results to provide approximate verification of system operation and fluence calculations.

5.1 Total Beam Current Monitoring

Total beam current, I_{beam}, is measured with a stainless steel collection plate located directly behind the sample holder. Access to the beam is provided before irradiation and at discrete intervals throughout operation by retracting the sample from the beam path. I_{beam} measurements are used with beam size measurements to calculate beam current density and with the HV source current, I_{source}, measurement to assess beam transport. An operational I_{beam} range of the implemented design was measured at a fixed operational pressure of 1 mTorr for a variety of ion densities altered by filament current (temperature).

$$0.1 < I_{beam} < 15\ \mu\text{A} \tag{5.1}$$

This range can be pushed higher by increasing the source pressure if an application requires more current and can tolerate the corresponding increase in transport column pressure. From this range, an approximate expected beam current density range can be calculated assuming a circular beam profile and using a simulated beam diameter range of 0.8 to 2.5 cm. While some assumptions are required to generate this range, it serves as a sufficient preliminary beam performance metric given that the required current density value of 0.445 $\mu\text{A/cm}^2$ previously determined in Section 1.4 is included in, and easily exceeded by, this range.

$$0.02 < J_{beam} < 30\ \mu\text{A/cm}^2 \tag{5.2}$$

5.2 Optimal Beam Transport Measurement

Beam transport comes down to the ability of the ion optics to create a small and contained beam that can traverse the system without colliding with electrodes or chamber walls. This depends on system geometry and the presence and magnitude of ion-neutral collisions. At a high level, optimal beam transport is obtained if

$$I_{beam} = I_{source} \tag{5.3}$$

where I_{source} represents the current leaving the plasma source (ions/s) that must be electrically compensated for by an outside current, *i.e.*, the current from the HV bias source. This is measured by an ammeter connected between the HV source and the plasma chamber. If (5.3) is satisfied, high level beam transport and the absence of beam current losses is confirmed. Insight into losses is also provided by measuring the current of each Einzel lens electrode. If no losses from electrode collisions occur, the current will be zero.

The above measurements were performed at various simulated operational voltage pairs. In all cases, the electrode currents were zero (to 0.1 μA precision) as expected. Comparison of I_{beam} to I_{source} also produced positive results. I_{source} was measured by an analog, galvanometer based, ammeter with 1 μA divisions while I_{beam} was measured by a digital ammeter with 0.1 μA precision. Therefore, these measurements can only be compared to the nearest μA or half μA with some interpolation. For all tested voltage pairs, the two measurements easily matched to the nearest μA giving a possible error of 0.5 μA. Together, these measurements show that first order beam transport is obtained within an error range of 0.1 - 0.5 μA.

A more strict description of optimal beam transport occurs when the experimental beam shape matches the simulated beam shape along with the previous current magnitude matching. As IBSimu does not account for ion-neutral collisions or space-charge compensation, achieving this would suggest these effects have a minimal occurrence and/or negligible effect on beam distribution. This would validate the gas flow and vacuum system designs that attempted to minimize ion-neutral collisions and their effects. Experimental and simulated distribution equivalency would also validate the system construction in terms of producing cylindrical symmetric forces throughout the system (as IBSimu assumes). As will be discussed in Section 5.5, the 2D beam cross section is not symmetric. This suggests either a break in the assumed symmetry or a substantial effect from ion-neutral collisions or space-charge compensation, or a combination of all three. However, the asymmetry is small enough that the resulting profiles still meet desired criteria and can be used for the radiation damage research. Comparison of experimental beam distribution to simulation would be more likely to succeed with a simulation that included ion-neutral collisions and space-charge effects.

While testing beam transport, it was found that in some cases, slight modification to V_{Einzel} (< 200 V) for a given V_{pl} increased I_{beam} by a small (< 0.5 μA) but measurable

amount. To μA precision, this did not alter the measured agreement of (5.3). However, it is assumed that optimal transport for a given V_{pl} should occur at maximum I_{beam}. Therefore, all simulated voltages also underwent a V_{Einzel} adjustment process to ensure maximum I_{beam}. The cause of this effect is unknown but given the small magnitude and experimental adjustment fix, its final, system level, effect is assumed to be negligible. The results of this investigation become the final operational voltage pairs for a given beam diameter.

5.3 The Characteristic Voltage Curve

The implemented design was first completed in simulation for the 10 keV ion beam of singly charged hydrogen ions. As shown in Section 4.14.3, the difference between different hydrogen ion types present in a hydrogen plasma (H^+, H_2^+ and H_3^+) is negligible and thus all simulations were completed with protons. Once the final design was established, simulation was used to find required V_{Einzel} values to produce beam diameters within 5% error of the desired profile for V_{pl} = 5 - 20 kV. Resulting voltage pairs were then experimentally tested for maximum and optimal beam transport in terms of beam current magnitude. The next step was experimental beam size measurement using techniques discussed in Section 5.4. This provided experimental verification of the profile and 5% error variation at all V_{pl} values. This gave final verification that all voltage pairs belong to the same operational, characteristic voltage curve, presented in Figure 5.1. The beam profile associated with this curve is approximately 1.8 cm in diameter with an experimental measured diameter of 1.5 - 1.6 cm. The described creation process can be repeated in the future for any desired beam size or beam characteristic as required.

While V_{pl} can technically range from 0 to 30 kV (HV source range), the operational limit is set to 5 - 20 kV. Below 5 kV, beam transport became challenging to achieve and the experimental distribution started to significantly deviate from the desired distribution. Challenges with low energy beam transport due to the decreased velocity and increased time of flight is a relatively well known issue. As present research only requires the 10 kV beamline, investigation into solutions was omitted and a lower limit of 5 kV, where transport is observed as sufficient, was set. The upper limit of 20 kV is due to the negative Einzel lens source having a limit of -15 kV and not being able to supply the required voltage for higher source voltages of this curve. For a different characteristic curve, both limits, especially the

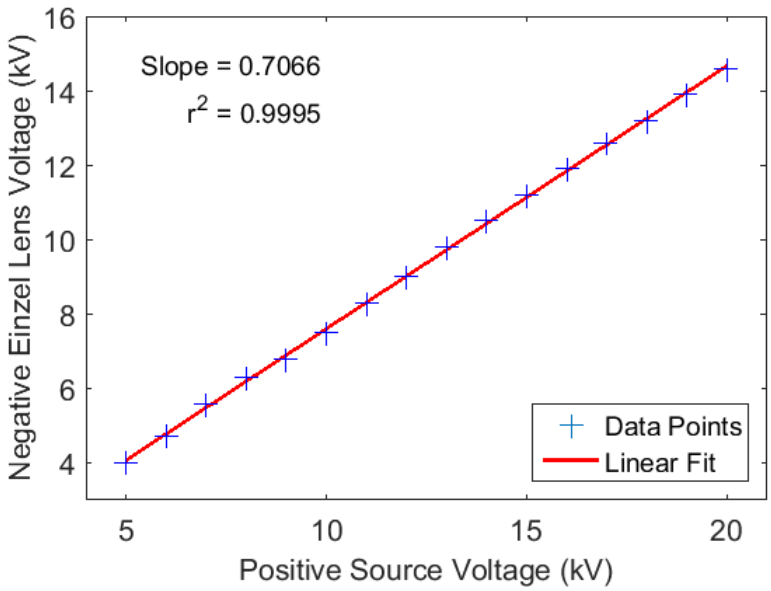

Figure 5.1: Characteristic voltage setting curve for the present research. Resulting beam size ≈1.8 cm simulated and ≈1.6 cm measured diameter. Found through combination of simulation and experimental adjustment.

upper limit, could very well be different. The only hard operational limit is a suggested -14 kV limit for the negative source and 29 kV limit for the positive source. Above these voltages, which are close to source upper limit, some instabilities and source issues were observed. Therefore, for safety reasons, it is advised to stay below these limits.

5.4 Beam Current Density Profile Measurement

Measurement of the beam current density profile is required for performance evaluation and to accurately calculate both the beam current density and delivered target area fluence. Ideally this measurement produces a two dimensional beam cross section. This can be obtained with clever instrumentation such as an array of metal plate collectors [67]. The array of metal plate acts like a CCD for ions where each metal plate is an individual pixel electrically isolated from the rest. Current collected by each plate divided by plate area gives one point of the 2D profile. The limit of this technique is pixel size; reasonable resolution is typically only possible for large beams. Other, higher resolution techniques also exist, such as a scintillation screen and CCD combination, but are proportionally expensive to implement and come with additional challenges such as fitting multiple components into the vacuum system complete

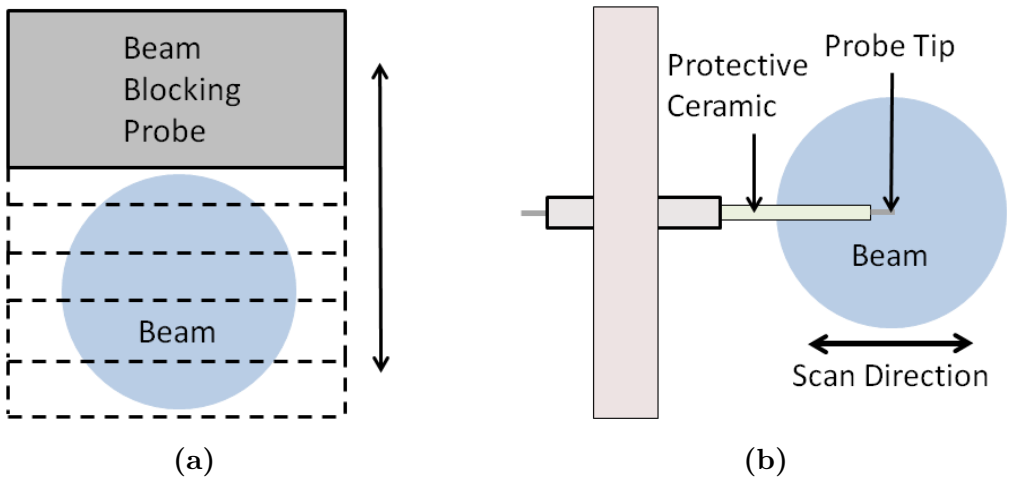

Figure 5.2: Illustrative diagrams (not to scale) of implemented current density profile measurement techniques. Note orientation is representative to alignment in laboratory frame of reference. Perspective is from ion source to target. (a) Vertical Blocked Current Derivative technique. (b) Horizontal Single Line Scan technique.

with electrical interfaces. The present work does not require high resolution measurements and thus more simple, less expensive and lower precision techniques were implemented. Two different techniques are used and both involve scanning a translational probe across the beam to measure current density at discrete intervals. Inherent to both methods is a measurement of beam size as first and last detection of current in the scan denotes the beam edges along the scan direction. The two techniques are referred to as the line scan and blocked current derivative methods. They are implemented with perpendicular scan directions in the system to maximize coverage and, with some distribution assumptions, to give an approximate 2D profile. Figure 5.2 shows illustrative diagrams of the two techniques which are explained, along with results and application to fluence calculations, in the following sections.

5.4.1 Single Line Scan Measurement Technique

The single line scan probe is similar to a Langmuir probe: a conducting metal wire enclosed in ceramic shielding to limit tip size and contained inside an electrically isolated vacuum feedthrough. The difference is in operation as the scan probe is left floating when inserted into the beam where the probe tip collects current through the natural collision of beam ions with the probe. Current measurements are obtained in discrete steps as the probe is scanned across the beam and divided by probe area to give discrete current density measurements.

These are plotted versus position and fitting techniques produce a high resolution profile for fluence calculations. The challenge of this technique is obtaining sufficient signal from low current beams as the probe tip must remain relatively small to allow multiple measurements across the beam diameter. Low signal measurement can be aided with amplifying circuitry such as the current integrator and unity gain buffer in the present setup. The present beam size ($D \simeq 1.6$ cm) permits use of a relatively large probe tip, 3 mm long and 1.5 mm diameter, to increase signal while maintaining sufficient measurement resolution. Profile measurement inevitably disturbs the beam and has an effect on the measured profile. However, if the disturbance is kept small, with a small probe, the effect can be considered to be negligible.

5.4.2 Blocked Current Derivative Measurement Technique

The blocked current derivative technique measures an unblocked portion of the beam current as a continually increasing portion is blocked by a probe inserted into the beam path. The probe is scanned across the beam until the entire beam is blocked. Unblocked current is measured in discrete steps by the collection plate behind the probe. The derivative of this measurement, with respect to probe position, provides a radial beam profile of the line integral of slices perpendicular to the scan direction. This technique perturbs the beam but it is still considered to provide accurate results. The present system utilizes the back of the sample holder as the blocking probe given it is already in the beamline, can fully block the beam and is naturally positioned perpendicular to the line scan probe to provide optimal beam distribution information. Unlike the scan probe technique, the blocked current method does not suffer from low signal level issues due to the larger measurement area. A subtle difference between this technique and the line scan probe is that this technique produces a linear current density (μA/cm) rather than an area current density (μA/cm^2).

5.4.3 Dealing With Plasma Instability Effects

A challenge to all beam diagnostic measurements is inherent beam current fluctuations that are the result of plasma instabilities and fluctuations over short time scales. This includes random HV system internal arcs that occurred throughout development and operation that would cause a brief ($\sim$ 1 s) shutdown of the positive HV supply before ramping back up. These fluctuations made obtaining stable total current and discrete current density readings

challenging. When readings were unstable, average measurements with larger errors were taken. Over longer time scales (minutes), the total beam current was found to potentially change by a small but measurable amount. Over even longer time scales (tens of minutes), the radial profile could drift and profile measurements taken 20 minutes apart could be slightly different. These fluctuations and drifts are further discussed in Section 5.7. For profile measurement and system operation, these observations led to required operation guidelines and measurements during a single run as discussed in Sections 5.7 and 5.8. For beam characterization, this issue led to production of average profiles over large time scales with larger error bars. Every beam diagnostic technique has a varying susceptibility to these issues. For profile measurements, the single line scan technique is very susceptible due to the low measurement area where as the blocked current method is less susceptible due to the large measurement area. However, both are susceptible to profile drifts over a single scan time frame.

The saving grace for this project is that these fluctuations and drifts do not produce large enough errors to cause the system to be unusable. Large errors in fluence, up to as high as 50%, are permissible as radiation damage research requirements are relatively coarse in terms of fluence. Typically research examines changes as a function of fluence for order of magnitude changes, or potentially up to 2 - 3 measurements per order of magnitude. Based on the large scales of fluence measurement and the coarse measurement steps, larger errors can be permissible. For example, the difference between a fluence of 1×10^{15} and 1.25×10^{15} ions/cm^2 (25% error) or even 1.5×10^{15} ions/cm^2 (a 50% error) is negligible as measurement of the induced damage effect cannot discern between these values. In the present work, changes are investigated at coarse fluence values and thus larger error bars in total fluence calculations as a result of larger error bars in the beam profile are acceptable.

5.4.4 Radial Beam Profile Measurement: Results

Extensive implementation and analysis of both beam profile measurement techniques were completed for two different beams, the (10, -7.5) kV beam profile, and a smaller diameter beam, (10, -9.0) kV, as experimental verification of other beam sizes. Measurements were taken over multiple runs at varying beam current values and run times (on start up, 10 minutes in, an hour in, multiple hours in, etc.). The results showed relatively stable profiles, however, some measurements revealed small drifts in the profiles over short runs as well as

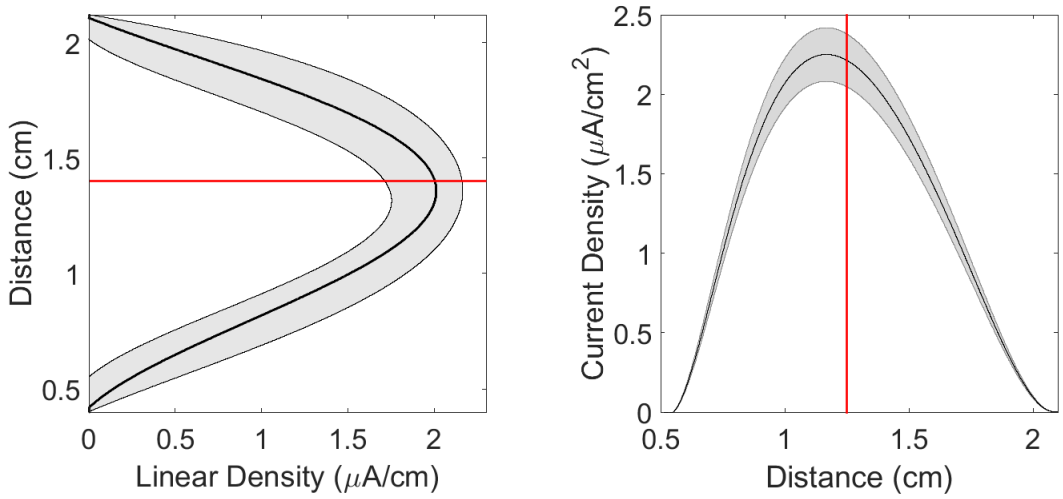

Figure 5.3: Hydrogen beam profiles for (10, -7.5) kV beamline. Left plot is from the vertical blocked current derivative method and the right plot is from the horizontal line scan method. Vertical profile is scaled to $I_{beam} = 2$ μA and horizontal profile is scaled accordingly based on scan area.

larger drifts over longer and multiple short runs. Even with these drifts, the beam profile can always be reported within a confined error range. Multiple measurements were analyzed to produce normalized horizontal (line scan) and vertical (derivative technique) beam current profiles with associated error bars. Horizontal and vertical designations refer to the laboratory frame of reference. The vertical profile area is scaled to equal I_{beam} and the horizontal profile is scaled to the total current collected by the probe over the area swept out of the beam by a scan across the geometric center of the vertical profile. The (10, -7.5) kV hydrogen beam profiles used for fluence calculations are shown in Figure 5.3 scaled to $I_{beam} = 2$ μA. For comparison, the smaller diameter profiles of the (10, -9.0) kV beam are shown in Figure 5.4.

As predicted by theory, profiles are 'Gaussian-like' and produce approximately symmetrical beam diameter measurements: 1.5 - 1.6 cm in the (10, -7.5) kV case and 0.9 cm in the (10, -9) kV case. In the (10, -7.5) kV case, this compares well to the 1.8 cm simulated beam diameter. Two possible explanations exist to account for this discrepancy: the difference between simulation and measurement precision and the unaccounted space-charge compensation in simulation. To define beam size from simulation, the beam radius is taken to be the trajectory position farthest from center. This trajectory position may represent a trivial fraction of I_{beam}, but nonetheless defines radius. When mapping this size to experiment,

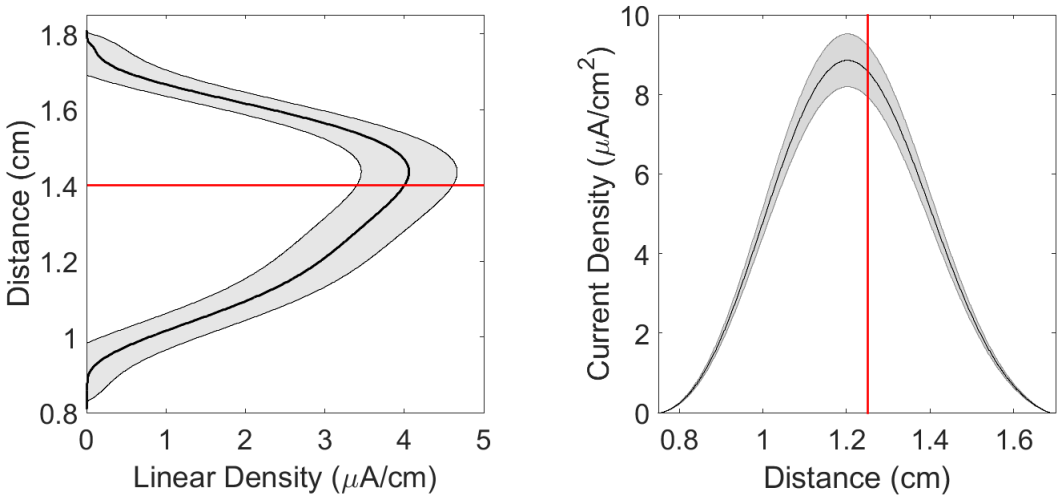

Figure 5.4: Hydrogen beam profiles measured at (10, -9) kV as verification for other beam sizes by changing V_{Einzel}. Vertical blocked current method (left) and horizontal line scan method (right). Scaling is equal to Figure 5.3.

assuming experiment mirrors simulation, the small fraction of beam current this far out may not be measurable with 0.1 μA precision. Furthermore, experimental measurement uses discrete steps equal to the probe tip size which limits measurement precision. Together these two effects can explain a smaller measured beam diameter. In regard to space-charge compensation current, it will exist to some extent in the beamline and will reduce beam diameter by reducing space-charge repulsion in the transport column. However, as this current is not directly measured, the experimental magnitude of the effect cannot be accurately assessed.

The offset from beamline geometrical center (red line in figures) as well as the general asymmetry in the curves appears in all measured profiles. Ideally, the geometrical center should line up with the profile peak and be the point of symmetry. The observed offset and asymmetry suggests error in the machining or alignment of the system, error in geometrical center measurement, or a systematic error in the profile measurement. The most likely is a small machining or alignment error, which would skew the cylindrical symmetry of the system. Even with these slight errors, the profiles can sufficiently approximate uniform irradiation of exposed sample areas. If the sample geometrical center is aligned with the beam profile peak, the exposed 8×8 mm area will see a 33% variation from center to edge with the refined 5×5 mm measurement area seeing a 15% variation, which is within the desired bounds.

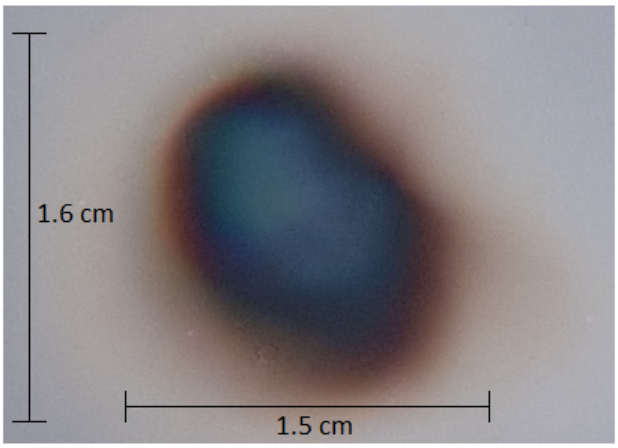

Figure 5.5: Picture of c-Si irradiated with $2{\times}10^{17}$ protons/cm^2 at 10 keV. Image provides a 2D view of beam shape and size. Discolored area measurements agree with horizontal and vertical scan measurements of beam diameter.

5.5 Silicon: 2D Image Result

One of the many radiation induced effects observed in c-Si is a change in reflectivity, color, or appearance as a function of fluence [68]. Unfortunately, the dependence is not monotonic and is fairly erratic, making the mapping of appearance change to exact fluence challenging. However, this appearance change can provide a 2D imprint of the beam and provide insight into beam shape and size. Figure 5.5 shows the irradiated area of a c-Si wafer irradiated with a fluence of $2{\times}10^{17}$ protons/cm^2 at 10 keV without the sample holder mask. Physical measurement of the discolored area provides a vertical diameter of 1.6 cm and a horizontal diameter of 1.5 cm. This closely agrees with the profile measurements. The discoloration also shows a slight skew to the top left of the spot, which agrees with the profile skew in Figure 5.3. The obvious asymmetry in both the horizontal and vertical diameters as well as along the diagonals is undesired. This points to alignment errors in the system. However, the effect is not significant enough to stop the system from being used as is. The primary result of this image is a sufficient verification of the beam profile diagnostic equipment results.

5.6 Helium Beam Profiles

As mentioned, the system was designed to permit other beamline types, such as helium, to run without modification to the system structure, *i.e.*, with only modifications to the applied

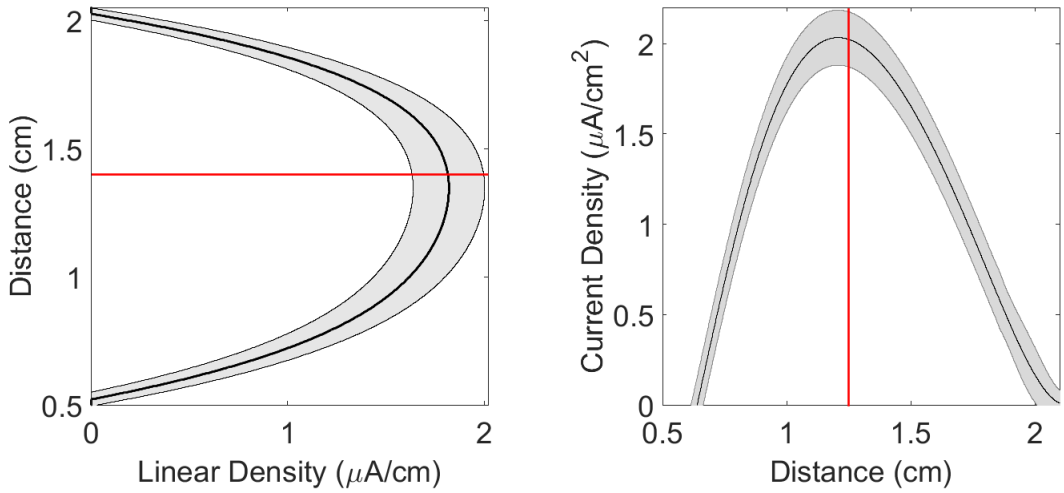

Figure 5.6: Helium beam profiles measured at (10, -7.5) kV to verify the system can operate as a multiple species beamline without system modifications. Left plot is the vertical blocked current derivative method and the right plot is the horizontal line scan method. Scaling is the same as Figure 5.3.

voltages. Based on simulation data, little difference is expected between a hydrogen and helium beamline at current operational ranges. This was tested by running helium in the system. The resulting beam profiles, scaled to the same beam current as the hydrogen profiles, are shown in Figure 5.6. As can be seen, not only did the system create a helium beam, but the profiles are very similar in shape and size to those of hydrogen. This conclusively shows that the system can operate as both a hydrogen and helium beamline.

5.7 Experimental Lessons and System Implications

The beamline characterization process revealed some experimental complexities, some of which were corrected since their discovery and some of which remain in the system due to lack of knowledge of the source or of a solution. In these cases, operational techniques were developed to mitigate or account for the effects. Four major issues along with associated solutions or mitigation are presented here.

5.7.1 Positive HV Source Fluctuations

One remaining complexity is fluctuations in I_{beam} as a result of temporary positive HV source shutdown. The source has internal arc detection and protection circuitry that, when triggered, causes the source to shut down to avoid potential damage. When the arc occurs,

the source instantaneously drops to ground, which turns off the beam, before ramping back up to the set voltage and restoring the beam. Ramp up time depends on voltage setting but is of the order of 1 - 2 seconds. If five arcs are detected within the previous ten seconds, a hard shut off conditions kicks in and a manual restart is required.

Since first implementation, arc detection shutdowns have been an issue. Arc detection has been observed with and without accompanying audible and/or visual arcs within the system. Upon first start up, arcing occurs at the most intense rate due to conditioning effects of conducting surfaces. When the system sits idle at atmospheric pressure, water vapor and other contaminants that enhance arcing conditions can collect on conducting surfaces. When the arcs occur, these contaminants are vaporized and pumped out of the system. Therefore, these types of arcs typically only last for a few minutes on start up. Another type of conditioning exists in which small defects in the conducting surfaces themselves exist and create heightened electric fields in their immediate vicinity. Through continuous arcing, these defects are sputtered off and removed. However, this process takes more time to fully remove the issue. Both types of conditioning were observed in the system as stability would increase after a few minutes of on time and over the course of multiple days of operation.

Once long term conditioning was achieved, system characterization with an operational plasma began. Ideally, arcing only exists on startup, if at all, and becomes absent once the filament is turned on to create plasma. Unfortunately, this was not the case and random arc detection occurred throughout system operation. The randomness of these events made diagnosing the problem challenging, and has yet to be solved. Potential explanations such as random beam fluctuations creating an arcing path between the plasma source and a ground electrode have been entertained, but nothing has been proven. Thankfully, once semi-stabilized, these arcs only occur once every few minutes, which is not enough to shutdown the HV source or cause substantial effects on fluence calculations that cannot be handled. Therefore, due to the minimal effect and the unknown cause, this issue remains in the system.

5.7.2 Beam Current Drift

Another remaining complexity is the drift of I_{beam} over time scales of the order of minutes. During beam characterization, changes in I_{beam}, on time scales as low as 1 - 2 minutes, were observed to be as high as 1.5 μA. Large changes in I_{beam} always occur on beam start

up as the initial measurement starts high and decays over 1 - 2 minutes before reaching a relatively stable value. Once stabilized (constant for $\sim$ 1 minute), the drift speed slows, and in some cases, is non-existent. I_{beam} measurements taken 5 - 15 minutes after stabilization show that I_{beam} can increase or decrease by up to 2 μA or in some cases, remain constant. The drift trend and magnitude appears to be random, making the cause unknown. Potential explanations include battery voltage decay effects, either in the filament battery or filament bias battery, that alter plasma creation conditions and fluctuations in electron emission rate due to unforeseen changes to, or effects of, filament heating. The former explanation is more likely as battery decay will occur and is part of the reason for having an adjustable filament power, to compensate for voltage changes. However, it is thought that effects related to battery decay should occur over longer time scales than those being observed. It also does not explain the high current, fast decay, start up observations. As with the random arcing, this issue remains unsolved and is addressed through beamline operation and error bars.

5.7.3 Moving Beam Spot - Lens Misalignment

During experimental measurement of beam sizes and attempting to verify the success of creating an adjustable beam size, the beam center position was observed to shift as a function of voltage settings, specifically V_{Einzel} at a given V_{pl}. This was first noticed by disagreements in scan probe measurements across multiple voltage settings and confirmed by comparing 2D silicon images of a (10, -7.5) kV beam and a test (10, -10) kV beam originally completed to show successful beam size alteration with V_{Einzel} changes. Further testing revealed a shift range of 0.1 - 1.5 cm depending on compared settings as well as confirmation of a constant shift direction. The issue was traced to an error in the ion optics. One of the ceramic spacers was 1 - 2 mm thicker than the rest which caused a diagonal tilt in the lens, in perfect alignment with the shift direction. Once corrected, the effect was removed from the system.

5.7.4 Vertical Drift of Vertical Profile

Early measurements of the beam profiles included a test of profile stability over long operation times (hours). Profile measurements were taken in 10 - 15 minute intervals for a variety of voltage pairs. Results showed the horizontal (line scan) profile to be fairly stable but showed a gradual upward drift in the vertical profile peak, and eventually the profile

edges, as a function of run time. The cause of this effect was initially thought to involve a temperature dependence. This idea was tested by measuring profiles in 15 minute intervals with a 15 minute cooling 'off' time of the filament in between successive intervals. The results showed a constant vertical drift in successive 'on' time measurements. However, comparison of measurements before and after the cooling period showed the profile to shift back toward the initial position. This confirmed the temperature dependence but did not answer what the temperature change was physically affecting, or how to fix it. To progress past this issue, an operational solution was implemented: all system runs were only allowed 15 minutes of 'on' time before requiring a 15 minute cooling period. This kept the profile within a reasonable error range that could be measured and did not require sample movement throughout irradiation. This primarily affected the high fluence implants that require multiple 15 minute exposures. As present research is not primarily concerned with irradiation rate or time in between doses, this does not adversely affect the final results. This solution simply added to the profile error bars, which as discussed, are sufficient for present needs.

The true source of this drift was discovered near the end of the project, after all sample irradiation had been completed. Upon removal of the filament assembly to change a burnt out filament, the inside of the plasma electrode showed visible discoloration due to interaction with the plasma. While this was expected, the discoloration was not symmetric about the extraction aperture, as was expected, and instead appeared predominantly on the bottom. This suggested that filament heating during operation was causing the tungsten wire to lose rigidity and bend under its own weight. As the average temperature will increase with increasing run time, the filament will continually lose rigidity and fall farther away from the extraction aperture. This would cause the plasma bulk center to fall with it and change extraction properties, conceivably resulting in an asymmetric beam profile with areas of higher concentration, as was observed. This also explains the shift back toward initial position after a cooling period as the filament would partially regain rigidity and pull itself back toward the original position. Thermal expansion and contraction would also add to this effect and the thermal dependence explanation. This theory was verified by completing a test run in which the filament was rotated 90° such that the coil axis became vertical rather than horizontal to provide increased structural strength. Upon measurement, the effect was instantly noticed

as the drift was drastically decreased. This change does not fully eliminate the drift, but does decrease the error bars and increases operational ability as the required cooling time is also decreased. As reference, a continuous one hour run now only results in a 2 mm drift in profile as opposed to the potential 4 - 5 mm drift in 15 minutes previously observed. In the future, this effect can be completely removed by decreasing the filament leg length so that sagging cannot occur or with implementation of an indirectly heated cathode.

5.8 Operational Procedure

The run time dependent profile drift and potential I_{beam} drift produced the need to develop specific operational and analysis techniques to mitigate effects on both delivered and calculated fluence. Beamline operation for run times longer than 15 minutes is as follows:

1. Turn on all voltage supplies and source gas flow. Wait for system to reach steady state.
2. Turn on filament to generate plasma and beam. Wait 1 - 2 minutes for I_{beam} to stabilize.
3. Set I_{beam} to the desired value and monitor for stability.
4. Record I_{beam} and insert sample into beam path. Wait 15 minutes.
5. Remove sample and measure I_{beam}. It may or may not be the same as set value.
6. Turn off the filament and let system sit idle to cool for 15 minutes.
7. Calculate interval and total fluence. Determine desired settings for next interval.
8. Repeat steps 3 - 7 until desired total fluence is achieved.

5.9 Delivered Fluence Calculations

If all beam current intersects the sample area, the calculation for fluence, F, is given by:

$$F = \int_0^T \phi(t)\ dt = \frac{1}{ZeA_{sample}} \int_0^T \int_{beam\ area} J_{beam}(x, y, t)\ dx\ dy\ dt \tag{5.4}$$

where $\phi(t)$ is the incident flux (ions/cm^2/s). If, as is the present case, all beam current is not used to irradiate the measured area, the equation, stated in another way, becomes:

$$F_{meas} = \frac{I_{beam}TP}{ZeA_{sample}} = \frac{NP}{A_{sample}} \tag{5.5}$$

where P is the percentage of the beam intersected by the smaller sample area and N is the total number of ions delivered downstream by the beam in a given time interval, T. This calculation requires a value for the average I_{beam} throughout the irradiation which is calculated from measured values at 15 minute intervals. I_{beam} is assumed to have a piecewise linear trend between successive measurements as shown in Figure 5.7. In the present system, N is the area under each portion of this curve divided by Ze. The total fluence delivered over multiple irradiation periods is the summation of successive applications of (5.5) to each interval. The error in each individual F_{meas} depends on δN, which is found by first calculating maximum and minimum possible values using a 0.1 μA error on each I_{beam} measurement, a 6 second error on irradiation times less than 10 minutes and a 12 second error on irradiation times longer than 10 minutes. δN is then:

$$\delta N = \frac{|N_{max} - N| + |N_{min} - N|}{2} \tag{5.6}$$

As total delivered fluence is the summation of individual calculations, the total error is also the summation of individual errors. Total beam fluence and associated error values are used to scale the average profiles and associated errors as shown in Figures 5.3 and 5.4. These error bars are larger than those found from simulation parameter variation completed in Section 4.14. This effectively means that those errors, for example variations in n_0, are contained within, or absorbed by, the errors discussed here. The use of these profiles and errors to calculate fluence produces fluence values with errors of the order of 20 - 40%, which is sufficiently accurate for the present research requirements. Together, these points further support the claim that changes in plasma properties as a result of repeatability issues or fluctuations in source operation are acceptable to produce sufficient results.

The next step is to define the A_{sample} to use in calculations. The 5×5 mm area was chosen as this is where final measured results will be taken and the higher variation outside of this region would skew the fluence calculation to not accurately reflect that which is observed in the measurement area. This area is used to determine P, by calculating the intersection area of A_{sample} with the profiles. An assumption used in this calculation is that the measured horizontal (line scan) profile is constant, within error, across every horizontal slice of the measurement area. Based on the visual 2D images and general beam knowledge,

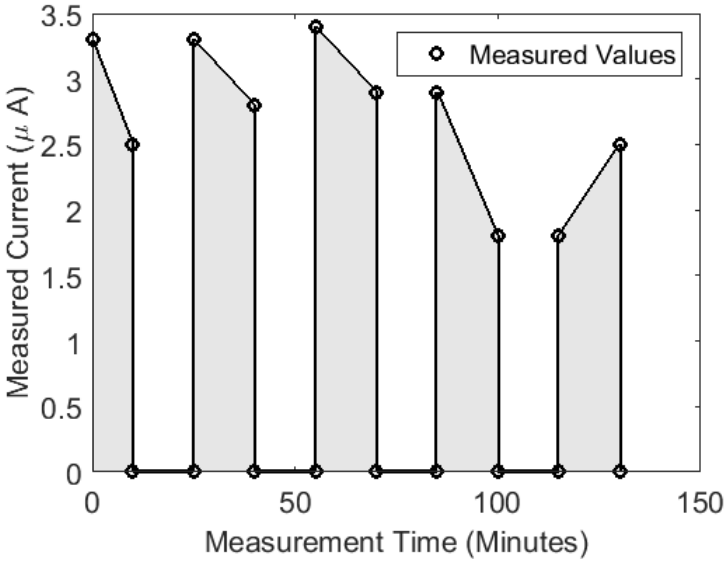

Figure 5.7: Example current measurement throughout system operation. Periods of 0 current represent off times. Variation between measurements is assumed to be linear. The area under each piece, divided by Ze, gives the number of ions delivered in that time interval. The sum of all areas gives total N.

this assumption is not 100% correct. However, within the limited 5×5 mm area, the error this assumption introduces is small and can be absorbed into error calculations to still produce sufficiently accurate fluence calculations. If this assumption were required to extend across the entire beam, its accuracy would significantly decrease and present significant errors. This is another reason for choosing the smaller 5×5 mm area instead of the larger exposed area.

Figure 5.8b shows the normalized horizontal profile intersected by the 5 mm sample area where the covered area is 53% of the horizontal profile. The same steps are performed for the vertical profile, as shown in Figure 5.8a, where 48% of the profile is covered by the 5 mm area. These two percentages are multiplied together to find:

$$P = 0.53 \times 0.48 \approx 0.25 \tag{5.7}$$

While this means roughly 75% of the beam is unused, which is not ideal, it is necessary to obtain variation requirements. This value for P provides the final piece of (5.5) to calculate fluence, which is an average value across A_{sample}. Calculation of δF_{meas} is as follows. The full calculation is completed for the minimum and maximum possible profiles with corresponding minimum and maximum N calculation values. These values are used to calculate δF_{meas} in

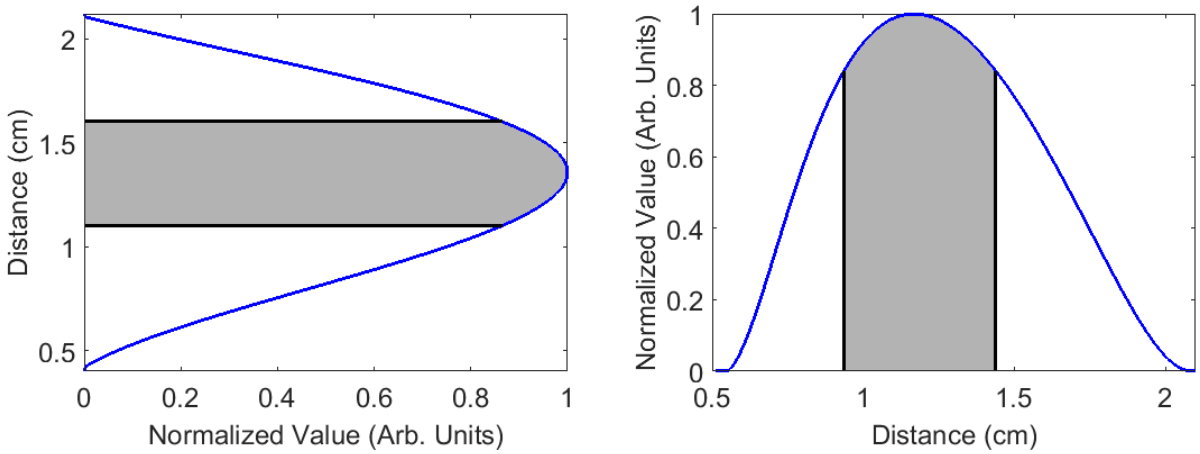

(a) **(b)**

Figure 5.8: Intersections of the 5×5 mm target area with the vertical profile (left) and horizontal profile (right). The shaded area represents the portion of the beam to irradiate the target. The area percentages of each curve multiplied together gives P.

the same fashion as δN in (5.6). The final fluence values are reported with an error range of 20 - 40%. The large range stems from the large errors in single fluence calculations, especially in the cases of short exposures times (10 second error on a few minute measurement becomes a large error) in order to get the low fluence experimental values. For fluence values above 10^{16} ions/cm^2 the error range drops to 20 - 30%. While these errors seem large, recall from previous discussions that the effect on radiation damage research is permissible below 50%. As will be seen in Chapter 6, when induced effect versus fluence plots are presented, the error bars are not as large as one may expect. Measurements of the induced effect will be taken across multiple points in the measured area and averaged together to produce a final result. This will also increase experimental accuracy and decrease potential effects of fluence calculation errors or potential fluence variations across A_{sample}. As a final note on the beam profiles and their intersections with A_{sample}, recall Figure 4.5 in Section 4.6 and the system requirement of creating less than 15% variation across the sample area. Comparison of this value and these figures shows that beamline performance meets this requirement.

5.10 Ion Species Composition

The hydrogen plasma created in the plasma source will contain H^+, H_2^+ and H_3^+ ions that will all be extracted and present in the beamline. Upon collision with the sample surface,

the H_2^+ and H_3^+ ions will separate into 2 and 3 H^+ ions respectively due to the molecular binding energy being much less than the impact energy. Therefore, although the beam is not purely protons, the radiation type, or implant ion type, is effectively pure protons, as desired. The difference is in the proton energies as those created on collision will have an average energy of 5 keV and 3.3 keV respectively in a 10 keV beam. This simply alters the depth profile as shown in Figure 6.1 where weighted SRIM profiles are presented for the three characteristic energies (3.3, 5 and 10 keV: this assumes equal partitioning of energy in the impact collisions). As the depth profile is not a significant concern to this project, this effect is permissible and thus mass selection is not required. If mass selection were required, it would significantly decrease the ion fluence, as the current beam is only approximately 30% protons (this value is obtained from extrapolation of data presented in [69]). The creation of multiple protons from a single ion also increases the delivered proton fluence, which can be used to deliver higher fluences in less time. This 'trick' does not work for all ion species, or radiation damage experiments. However, it works here, and is a beneficial effect.

The plasma composition using H_2 gas is dependent on source pressure due to recombination processes of ions within the plasma [69]. A plot of relative composition for these three species is given in [69] for a pressure range of 0.008 - 0.4 mbar. By extrapolation of this data, approximate composition percentages, 30% H^+, 55% H_2^+ and 15% H_3^+, were obtained for the present beamline at 1 mTorr (0.0015 mbar). As all ions are singly charged, they each contribute one charge to the I_{beam} measurement rather than multiple charges. Therefore, proton fluence can be calculated from ion fluence using beam composition as follows.

$$\left[\frac{\text{protons}}{\text{cm}^2}\right] = C\left[\frac{\text{ions}}{\text{cm}^2}\right] \tag{5.8}$$

$$C = (1 \times 0.3) + (2 \times 0.55) + (3 \times 0.15) = 1.85 \tag{5.9}$$

5.11 Silicon Experimental Study: Raman Spectroscopy

The first experiment with a fully characterized system was a brief study of irradiated crystalline silicon (c-Si). This study required irradiation of multiple c-Si targets at various beam currents and irradiation times, making it highly suitable for a verification run of the system. Silicon was chosen for the first experiment based on the wealth of knowledge of radiation induced effects from various ion implantation studies. By comparing results to those previously

reported as a function of fluence, approximate fluence and system operation verification can be achieved, *i.e.*, verification of a comparable amount of induced damage at correct fluences. The property chosen for investigation as a function of fluence is the Raman spectra as it has been reported to produce a monotonic trend in peak heights as a function of fluence [46] making it ideal for verification purposes. Raman spectroscopy is well suited for induced damage studies as it provides information on bonds present in the material.

Irradiation was completed on optically flat n-type *c*-Si (100) wafers with a resistivity of 10 Ω-cm using the 10 keV hydrogen ion beam setting. The beam was oriented 7° off of the sample normal to suppress channeling effects. The simulated implant range for the beam consisting of 30% H^+, 55% H_2^+ and 15% H_3^+ is shown in Figure 6.1. Recall that material damage as a result of energy deposition (Bragg curve) will be slightly more shallow than the SRIM curves that show where the incident particles finally stop (particle range).

While substrate temperature during irradiation is known to have an effect on the induced damage [47], specifically retained damage, the present experiment does not employ active temperature control or measurement. Therefore the substrate temperature is nominally room temperature. Deviation from room temperature during irradiation is assumed to be minimal due to low induced heating as a result of low beam current densities (3 μA/cm^2 on average), low consecutive implant times due to the 15 minute interval operation and due to passive temperature control provided by the sample holder mounting and convective cooling by the background gas. The sample holder acts as a large heat sink for the sample assuming good thermal contact and conductivity between it and the sample. Irradiation was completed using variable J_{Beam} ranging from 1 - 10 μA/cm^2, with larger densities used to achieve higher fluence implants in a reasonable amount of time (few hours).

5.11.1 Expected Results: Amorphous and Crystal Si Signatures

The Raman spectrum of *c*-Si is dominated by one sharp, characteristic peak centered at 520 cm^{-1}. As *c*-Si is irradiated and damaged, the crystal structure is disrupted and eventually ends up in a state of total disarray. In some cases, this completely damaged lattice can become amorphous silicon (*a*-Si). The creation of *a*-Si due to charged particle irradiation is well observed, especially for high mass ion radiation such as self-implantation, *i.e.*, Si^+ ions into *c*-Si. While there is debate on whether or not low mass ions such as protons are capable

of causing amorphization, they have been observed to destroy the crystal structure and leave the material in an intermediate damaged state, somewhere between crystal and amorphous [46, 49, 70]. This damage causes the 520 cm^{-1} crystal peak to monotonically decrease with increasing fluence, and if amorphization does occur, the characteristic amorphous Raman peak at 480 cm^{-1} will monotonically increase with increasing fluence.

In theory, a plot of the 520 cm^{-1} peak height as a function of fluence should provide a monotonic decreasing trend and all the desired information for system and fluence verification. However, while this trend is known, exact peak intensity values at given fluences cannot be compared to reported results and the general practice of quantitative comparison of Raman peak heights is typically discouraged and avoided. This is because Raman peak heights are very sensitive to a number of parameters such as incident laser power, surface reflectivity, surface flatness, and distance between the surface and the measurement devices to name a few. These parameters cannot be guaranteed to be constant between successive measurements especially when various sample substrates are measured. Therefore, not only can quantitative results not be compared to reported results due to inevitable variation in these parameters, but quantitative comparison within an experiment cannot be highly trusted. This was quickly discovered in the present work when measurements taken over multiple days of the various samples yielded large, unexpected variations in the 520 cm^{-1} peak heights. The solution is to use peak height ratios for quantitative comparisons. Taking the ratio of two values on the same spectra calibrates out the mentioned issues as well as many of the unmentioned issues.

5.11.2 Raman Results: Silicon

Details of the Raman instrument and measurement process are given in Section 6.2. The investigated peak ratio in silicon is the a-peak/c-peak, *i.e.*, the 480 cm^{-1} peak divided by the 520 cm^{-1} peak. The known monotonic trends of these peaks as a function of fluence should produce a monotonic trend in the ratio. Even if amorphization does not occur and only crystal disruption occurs, the ratio should monotonically increase as, in this case, the numerator would stay constant and the denominator would decrease. This results from disordered, but not amorphous, silicon having no Raman signature at these wavenumbers.

Literature was searched for a plot of this ratio versus proton fluence, but no plots were found. However, recall the rule of thumb 'amorphizing dose' is known to be of the order of

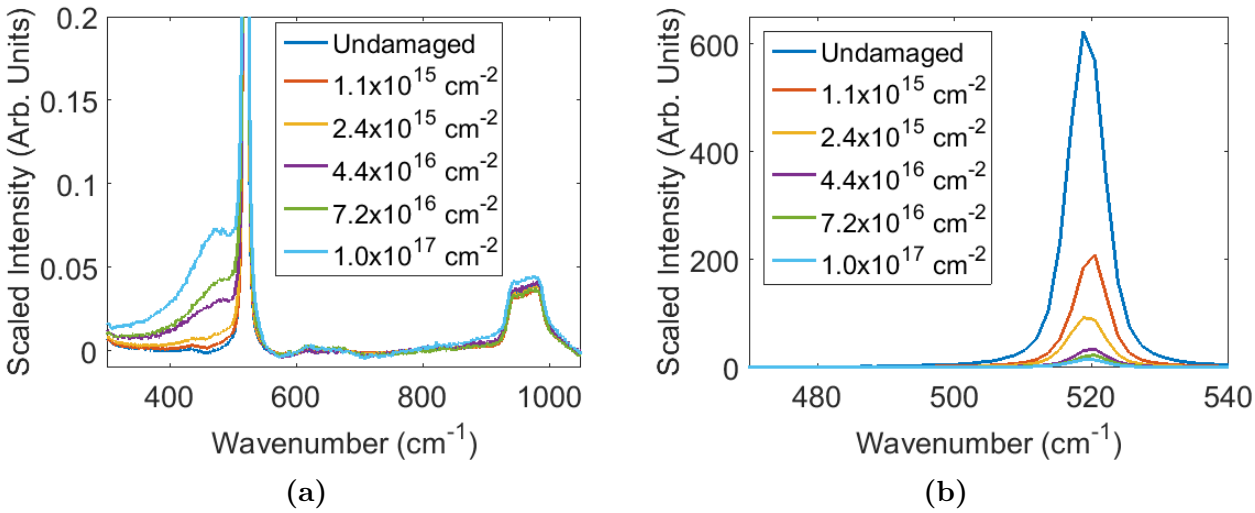

Figure 5.9: Scaled Raman spectra of c-Si irradiated with the 10 keV beamline using variable fluence (protons/cm^2). (a) Spectra normalized by 520 cm^{-1} peak value to show a-peak growth. (b) Spectra normalized by 480 cm^{-1} peak value to show c-peak decay.

10^{16} ions/cm^2 [21]. This fluence generally signifies a point of significant change or the point where the implanted layer can no longer be considered as a pure material. The actual effect is dependent on many factors such as ion mass. In the low mass case, this change may be small where as in the high mass case, the change could be a significant percent amorphization of the implanted layer. The dependence of induced damage on ion mass can make comparison of different mass radiation difficult. However, in the present case, comparison will only be attempted at a qualitative, or approximate quantitative level. If the combination of a noticeable change in the a/c ratio around 10^{16} protons/cm^2 and minimal to no changes at lower fluences is observed, this will provide sufficient verification.

A plot of Raman measurements at selected fluences is shown in Figure 5.9 with normalization completed with respect to the crystal and amorphous peaks in (a) and (b) respectively. In each case, the trend is as expected: the c-peak (relative to the a-peak) decreases in (b) and the a-peak (relative to the c-peak) increases in (a) with increasing fluence. The presence of the a-peak and its growth with respect to any wavenumber (520 cm^{-1} here) as a function of fluence is evidence for induced partial amorphization. This alone is an interesting result as general consensus is that amorphization is not possible with light ion irradiation at room temperature and instead requires cooled substrates along with very high fluences [46].

This partial amorphization result is further backed with comparison to papers on a-Si

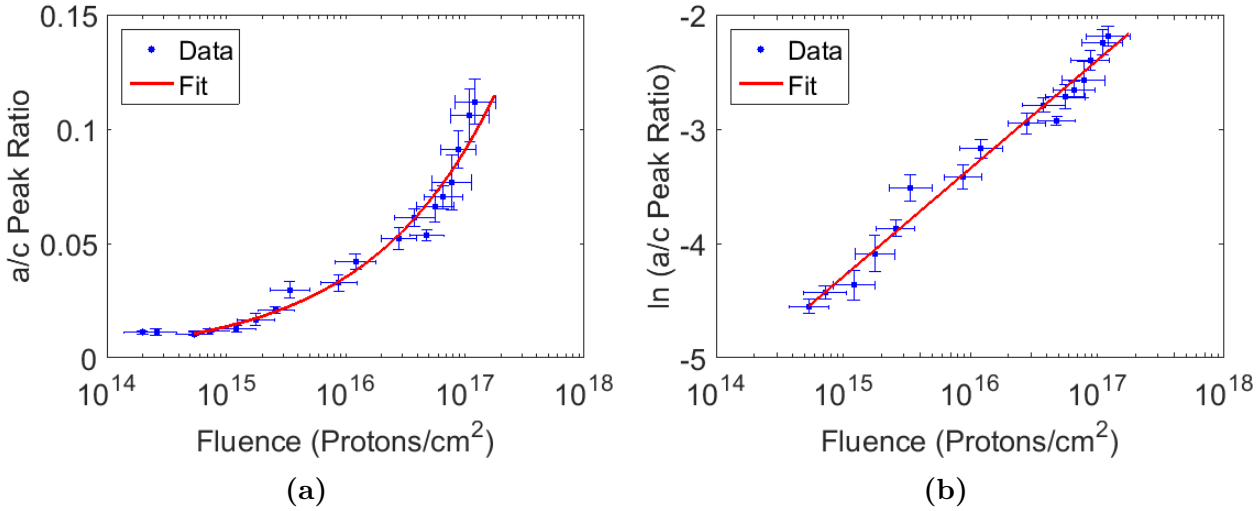

Figure 5.10: (a) a/c ratio versus fluence for proton irradiated c-Si. (b) ln(a/c) ratio versus fluence for proton irradiated c-Si.

deposition onto c-Si substrates [71, 72]. These papers use Raman spectroscopy to investigate the deposited layer and determine percent amorphicity of the deposited layer by examining peak height and peak area ratios. These papers report Raman spectra very similar to those presented here, *i.e.*, a mixture of amorphous and crystal signatures. In these measurements, the 480 cm^{-1} peak is known to come from a-Si, which based on similarities to the current profiles, strongly suggests the Raman signal is indeed a-Si and not from some other radiation effect causing an amorphous-like signal.

A plot of the a/c ratio versus fluence on a logarithmic x-scale is shown in Figure 5.10. The important features to notice are the constant ratio at low fluences ($< 10^{15}$ ions/cm^2), the monotonic trend once the ratio value changes, as predicted, and the noticeable change in ratio growth roughly around 10^{16} ions/cm^2 as expected. Therefore, the fluence calculation method and expected induced damage have been approximately verified as desired. The Raman measurement technique of averaging multiple measurements across A_{sample} also proved to provide sufficient values. The overlaid fit to the data is an exponential fit in log(x) that was found by plotting ln(a/c) vs log(x) and found to produce a linear fit as shown in Figure 5.10. The coefficient of determination (r^2 value) of this fit is 0.98 and gives the equation:

$$\ln(a/c) = 0.411 \log(x) - 18.484 \tag{5.10}$$

where x in this case represents the accumulated fluence.

Mapping this equation back to the overlaying fit of Figure 5.10a results in the equation:

$$a/c = \exp[0.411 \log(x) - 18.484] \tag{5.11}$$

where, again, x is the accumulated fluence.

It is currently unknown if this reported equation of the a/c versus fluence relationship will continue to higher fluences, but there is no reason to suggest that it would not do so. Eventually the ratio will plateau at some value that will depend on the state of the implanted layer once damage has saturated, *i.e.*, is it fully amorphous or only partially amorphous. In the case of a mixed damaged and amorphous layer it is possible that the Raman spectrum still measures a crystal signal from the underlying crystal substrate. This is due to the penetration depth of the Raman laser varying in different states of silicon. In pure c-Si, the penetration depth is of the order of 3000 nm, which is well beyond the present implanted layer depth. However, the penetration depth of pure a-Si is only of the order of 100 nm, which is less than the implanted layer depth. In a damaged state, the penetration is somewhere between these two values and is highly variable. Therefore, if the implanted layer is not fully amorphous, the crystal signal has potential to still be measured. This is definitely the case in present measurements at low fluences and even at high fluences where the amorphous signal is not strong enough to suggest a high enough percent amorphization of the implanted layer to keep the Raman laser from probing into the crystal substrate. This does not affect the trend nor the use of this data for system verification. The only effect is a ratio value change and specifically, an eventual plateau value as the presence of the substrate crystal signal, at least in present measurements, still dominates the ratio.

The result of this investigation into c-Si not only yielded positive results for beamline verification but also a promising data set for future publication. As discussed in Section 7.3, a paper on these results has been submitted to AIP Advances and is currently under review.

Chapter 6

Experimental Proton Radiation Material Results

This chapter presents measurement results of proton irradiated crystal quartz (c-SiO_2), lithium niobate ($LiNbO_3$), and tellurium dioxide (TeO_2). All samples were irradiated using the 10 keV hydrogen ion beamline containing H^+, H_2^+ and H_3^+. Recall that, upon collision with the sample, the H_2^+ and H_3^+ will break into 2 and 3 protons with an average energy of 5 keV and 3.3 keV, respectively. This effectively creates pure proton radiation but at a range of energies rather than monoenergetic 10 keV protons. This energy range causes the damage distribution to become a blend of each individual energy distributions. Figure 6.1 shows an example SRIM output for this situation. As can be seen, the distribution is dominated by the H_2^+ profile, but each profile has a meaningful contribution to the overall summation. As solar wind charged particles are not monoenergetic, use of a range of energies is beneficial as it provides more realistic radiation conditions and induced damage. Measurements of transmittance and reflectance, calculation of absorbance and use of Raman spectroscopy are completed to gain insight into proton induced damage effects. This data is used with expected space environment conditions to calculate a value for spaceborne mission lifetimes.

6.1 Ion Implantation Details

All sample implants are performed at room temperature without temperature control of the sample during irradiation other than passive cooling provided by conductive cooling of the sample holder and convective cooling by the background gas. Estimated heating calculations for quartz shows an average beam current of 3 μA will heat the sample at a rate of $\sim 4\ ^\circ$C/min without considering any cooling mechanisms. Assuming reasonable cooling rates, the sample is expected to remain at room temperature within a small range. As previously discussed,

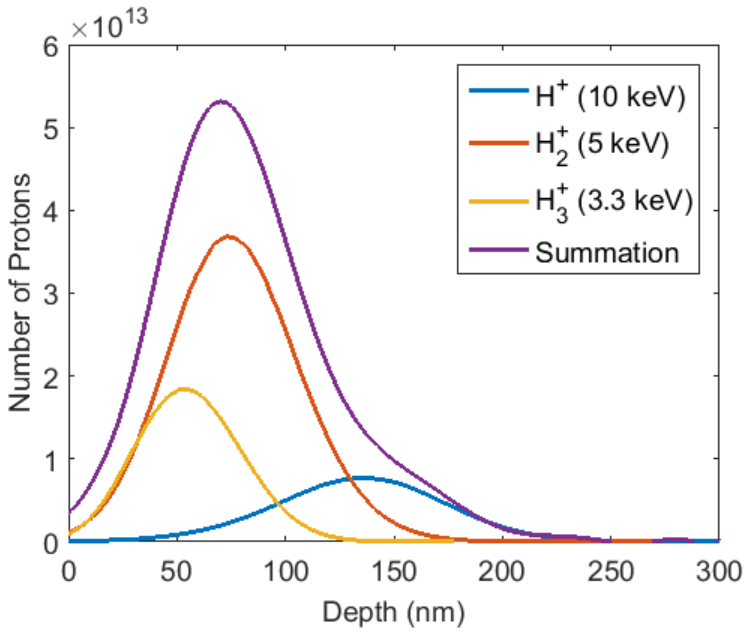

Figure 6.1: SRIM profiles for 10, 5, and 3.3 keV protons into *c*-Si to represent the three different characteristic implant energies as a result of variable beam composition. Profile areas are weighted based on an example beam fluence (2.5×10^{16} ions/cm^2), composition percentages and number of created protons to make total area equal to number of implanted protons. Damage profiles (energy deposition versus depth) will be slightly shallower.

the synopsis of temperature effects is that retained damage decreases with increasing substrate temperature due to enhanced defect recombination. In the present case of comparing experimental conditions to those experienced in space, room temperature is a close approximation as most spaceborne optics are typically heated to close to room temperature to avoid temperature dependent effects in operation. Beam current and radiation flux also affect the substrate temperature as higher currents will increase sample heating and subsequently increase annealing effects. This suggests that lower irradiation rates will induced more retained damage. However, irradiation rate is more involved as some studies show increased damage at higher flux values as a result of causing too much damage in a short period of time to effectively anneal with induced heating [48]. The difference between proton flux in space and in experiment is significant, but is unavoidable when performing accelerated lifetime testing. Any potential effects are ignored for now but are acknowledged when reporting final results.

The quartz, $LiNbO_3$ and TeO_2 studies were completed on a single sample per material,

to minimize costs. To begin, each sample was first irradiated with the lowest fluence followed by completion of all optical measurements. The sample was then inserted back into the beamline in the identical position and orientation to receive the next dose before having all measurements completed again. The total accumulated fluence is the summation of all separate doses. This process repeated until all desired fluences were delivered. This technique is only possible when not examining effects of variable radiation rates. One potential error with this method is sample positioning and maintaining an identical intersection of the exposed sample area with the beam. This error is minimized with careful positioning and effectively accounted for in the beam profile error bar and corresponding fluence calculations. Further minimization is achieved by using the smaller 5×5 mm measurement area to avoid edge effects where differences in exposed area are most likely to occur.

6.2 Optical Measurements

Three different optical measurements were performed on each material to characterize damage and induced effects as a function of fluence: normal incidence transmittance, reflectance and Raman spectroscopy. From transmittance and reflectance, absorbance was also calculated. Transmittance, reflectance and absorbance values provide insight into macroscopic effects whereas Raman spectroscopy provides insight into atomic level structural damage. As was observed in the silicon study, this information can present itself by altering existing Raman lines, producing new Raman lines or a combination of both. Any change to the Raman spectrum is conclusive evidence of induced damage, but the appearance of new lines has elevated significance as this shows new structures and not just peak height altering disorder.

The measurement technique for all measurements, including those performed in the silicon study, is to take multiple, evenly spaced, measurements across the reduced 5×5 mm irradiated area for each fluence. By taking the average of multiple measurements to create a single measurement per fluence, with a corresponding error bar, the measurement accuracy is increased. This also helps average out any potential variation in delivered fluence across the sample area and provides an appropriate error bar given the potential beam variations discussed previously. The number of measurements was variable depending on measurement stability across the sample but the minimum was 10 measurements. An illustrative figure of

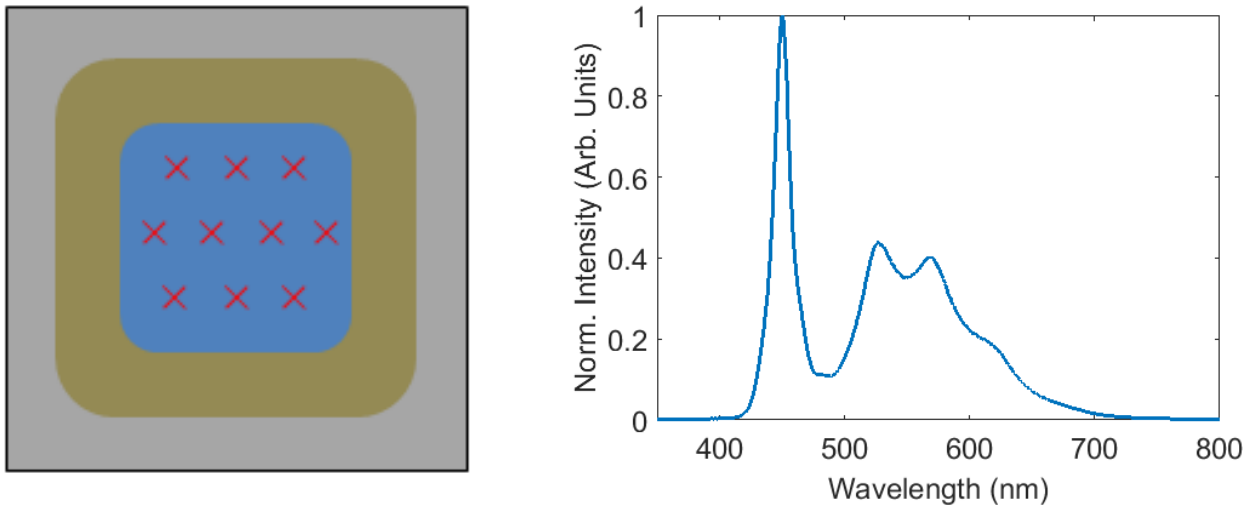

(a) **(b)**

Figure 6.2: (a) Illustrative figure (not to scale) of irradiated sample areas with marked example measurement positions (red crosses). Blue is the measured area, brown is total exposed area and gray is the masked area. (b) Normalized 'white light' LED source spectrum used for transmittance and reflectance measurements.

the irradiated samples with representative measurement positions is shown in Figure 6.2a.

The source used for transmittance and reflectance measurements was a white light LED source with a quoted spectral range of 420 - 780 nm. Figure 6.2b shows the measured spectrum. The wavelength range is appropriate given that all three materials, quartz, $LiNbO_3$ and TeO_2, are all transparent in the visible range. This source was chosen due to its high level of output stability, which decreases experimental measurement error. Transmitted and reflected light is measured by an Ocean Optics Red Tide USB 650 spectrometer that contains 2048 pixels and has a measured spectral range of roughly 340 - 1023 nm, making the resolution approximately 0.34 - 0.36 nm/pixel (variable due to non-linear calibration). Exposure times of individual measurements vary depending on experiment type and signal strength (based on damage condition) but were nominally between 50 - 100 ms. Each measurement position on the sample was automatically measured and averaged by the spectrometer over 20 - 40 scans, depending on exposure time. This was completed to reduce measurement error.

6.2.1 Transmittance Measurements

Transmittance (T) values as a function of wavelength (λ) were measured using the setup shown in Figure 6.3. To begin, the source and detector were aligned to provide maximum

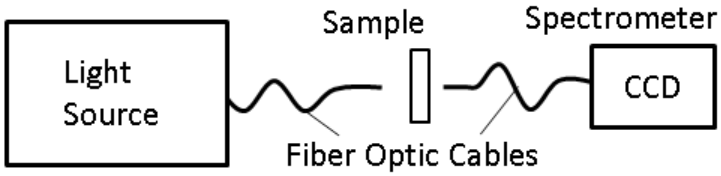

Figure 6.3: Transmittance measurement experimental setup.

detected signal. Once aligned, a series of source intensity ($I_{ref}(\lambda)$) reference measurements were completed and the sample was inserted into the beam path. To eliminate positioning errors between successive spot measurements, the sample was placed on a movable stage that retained relative geometry while enabling discrete scanning across the sample area. Transmitted light intensity ($I_{meas}(\lambda)$) is measured and calculation of $T(\lambda)$ is completed using:

$$T(\lambda) = \frac{I_{meas}(\lambda)}{I_{ref}(\lambda)} \tag{6.1}$$

The sample was positioned such that the source light was normally incident on the irradiated face. Ideally, a collimated light source is used to ensure purely normal incidence light. However, an uncollimated source, such as the one used here, can reduce angular variations by implementing low numerical aperture (0.22) fiber optic cables into the optical path. This limits both the source and collected light to normal incidence rays plus a small cone of angles around normal. In general, light within a small angular range of normal incidence can be considered normal for calculation purposes without producing substantial error in results. The significance of this potential error was experimentally tested by measuring the transmitted signal at multiple different sample angles between normal and normal $\pm$ 10°. The results varied for the different materials but the general result was that slight off-normal incidence did not substantially change measured values. For c-SiO_2, the $\pm$ 10° measurements did not vary by more than 2% of the normal measurement while in both $LiNbO_3$ and TeO_2, a 2% error was observed around $\pm$ 5°, most likely due to their higher birefringence. In both cases, the 2% difference in values is small and was further reduced by accurate sample positioning (off-normal angle $< 5°$). Therefore, these errors were classified as negligible to the final result. Note that this angular check was completed at various points throughout the radiation process at different fluences to ensure that no change to the error percentage occurred with

the induced damage layer. In all cases measurements did not reveal a cause for concern.

The transmittance experiment measures light that has passed through three high level interfaces: the air/damaged front surface layer interface, the damage layer/crystal interface and finally the crystal/air back interface. Modeling of this system using values for the crystal and air components to extract information on the unknown damage layer characteristics is very challenging to achieve for a number of reasons. The most significant reason is that the damage layer interfaces are not sharp like the air/crystal interface and instead exhibit properties gradually varying throughout the damaged layer in a distribution similar to an SRIM plot. This is challenging enough when dealing with monoenergetic particles, but when a range of energies is introduced, it becomes significantly harder due to multiple depth profiles causing further variation within the damaged layer. An attempt was made to model this system using a variety of assumptions such as defining interface boundaries from SRIM plots or implementing a threshold damage criterion to create an effective damage layer in which average characteristics are assumed and outside of which crystal properties are assumed to be normal (this technique was used in [73]). Once layer positions were defined, successive application of the Fresnel equations were used to calculate expected reflectance and transmittance. Unfortunately none of the attempted models produced results that agreed with experimental values. The assumed primary challenges to creating an accurate model are proper handling of the damage layer distribution(s) and inclusion of an appropriate absorption coefficient within a complex index of refraction. Due the failure of these models, information on damage layer properties is left as future work.

Average Value and Error Calculation

As mentioned, each individual intensity measurement ($I_i(\lambda)$), either reference or of the sample, is actually an automatic average of multiple images produced by the spectrometer software and reported as one value per pixel with no error bar. The intensity values used in (6.4) to calculate $\langle T(\lambda)\rangle$ for a single fluence, are also averages of the multiple measurements across the sample area (6.2). The error in these averages is taken to be the standard deviation (6.3). The error in each $\langle T(\lambda)\rangle$ is found with a standard error in quadrature method (6.5).

$$\langle I(\lambda)\rangle = \frac{\sum_{i=1}^{N} I_i(\lambda)}{N} \tag{6.2}$$

$$\delta \langle I(\lambda) \rangle = \sqrt{\frac{\sum_{i=1}^{N} (I_i(\lambda) - \langle I(\lambda) \rangle)^2}{N}} \tag{6.3}$$

$$\langle T(\lambda) \rangle = \frac{\langle I_{meas}(\lambda) \rangle}{\langle I_{ref}(\lambda) \rangle} \tag{6.4}$$

$$\delta \langle T(\lambda) \rangle = \sqrt{\left| \frac{\delta \langle I_{meas}(\lambda) \rangle}{\langle I_{ref}(\lambda) \rangle} \right|^2 + \left| \frac{\delta \langle I_{ref}(\lambda) \rangle \langle I_{meas}(\lambda) \rangle}{\langle I_{ref}(\lambda) \rangle^2} \right|^2} \tag{6.5}$$

6.2.2 Reflectance Measurements

Reflectance measurements were also taken at normal incidence to complement the transmittance measurements. Measurements were taken using a back-scatter fiber optic probe whose experimental configuration is shown in Figure 6.4. Both the source and detector fibers automatically share the same geometry and when positioned normal to a surface ensure, within negligible error, that only normal incident rays are measured. Angular dependence was measured and found to be highly sensitive. Almost any off-normal positioning resulted in complete loss of measured signal, as desired. The goal of this experiment is to only measure light reflected from the front and back crystal/air interfaces as a single summed value. Light incident on the back crystal/air interface from outside the crystal was eliminated by placing the sample on an absorbing black background. The reflectivity of this background was tested by running the collection system without the sample in place. An exposure time of 1 s was required to measure a signal 100 counts above the noise. In comparison, with the sample in place, exposure times of the order of 100 ms accumulated 4000 counts at the same wavelength. Therefore, the black background effectively eliminates unwanted signals.

Reflectance ($R(\lambda)$) was calculated by taking the ratio of the reflected light intensity ($I_r(\lambda)$) to the incident light intensity ($I_{source(\lambda)}$):

$$R(\lambda) = \frac{I_r(\lambda)}{I_{source}(\lambda)} \tag{6.6}$$

This is similar to the transmittance calculation where $I_{source}(\lambda) = I_{ref}(\lambda)$ is obtained by measuring the source in the experimental setup prior to inserting the sample. In the case of reflection, this reference measurement was more involved. In the this experiment, a reference measurement is obtained from the shielded, masked area of the sample which makes $I_{source}(\lambda) = I_{ref}(\lambda) = I_{source}(\lambda) R_{crystal}(\lambda)$. Together with the measured reflected intensity of

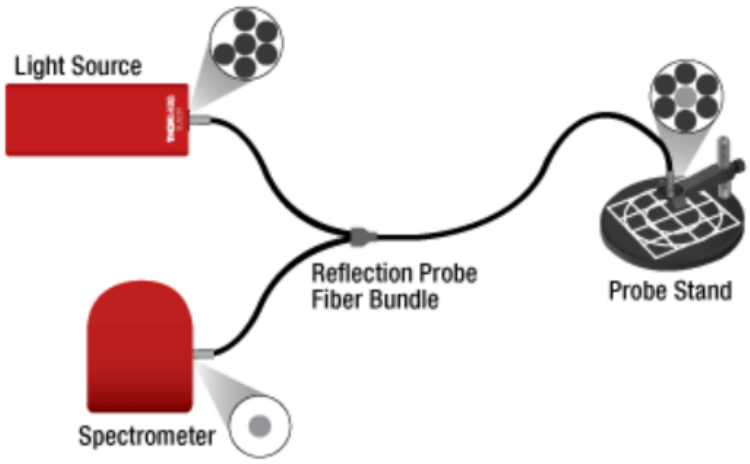

Figure 6.4: Reflectance measurement setup. Image from ThorLabs manual.

the damaged region being $I_r(\lambda) = I_{meas}(\lambda) = I_{source}(\lambda)R_{damage}(\lambda)$ where $R_{damage}(\lambda)$ is the reflectance of the crystal after irradiation, this makes the reflectance calculation become:

$$R(\lambda) = \frac{I_{source}(\lambda)R_{damage}(\lambda)}{I_{source}(\lambda)R_{crystal}(\lambda)} = \frac{R_{damage}(\lambda)}{R_{crystal}(\lambda)} \tag{6.7}$$

Therefore, $R(\lambda)$ from the measurement, calculated as

$$R(\lambda) = \frac{\langle I_{meas}(\lambda)\rangle}{\langle I_{ref}(\lambda)\rangle} \tag{6.8}$$

is actually the reflectance relative to the undamaged crystal reflectance. Actual $R(\lambda)$ values can be found by multiplying out $R_{crystal}(\lambda)$ if this value is known. If the material were isotropic, $R_{crystal}(\lambda)$ could be calculated with the well-known Fresnel equations at normal incidence. However, the materials under investigation are birefringent and the incident light is unpolarized. The incident light could be polarized but challenges still exist with crystal orientation and the effects of unknown damage layer states on the crystal axis, which defines polarization states within the crystal. Analysis at this level is not required for present research goals and is left as future work. Therefore, relative changes to reflectance are sufficient. As an estimation for exact $R(\lambda)$ values that are required to calculate absorbance, an average refractive index value can be used with the Fresnel equation for an isotropic material to gain an approximate $R_{crystal}(\lambda)$ value. The error in this approximation can also be approximated by assuming the true value lies within the bounds of pure ordinary or extraordinary reflection,

Material	Ordinary Refractive Index (n_o)	Extraordinary Refractive Index (n_e)
c-SiO_2	1.544	1.553
$LiNbO_3$	2.272	2.187
TeO_2	2.274	2.429

Table 6.1: List of refractive indices at 590 nm for studied materials.

i.e., perform the same calculation with only $n_o(\lambda)$ and with only $n_e(\lambda)$ to obtain error bounds. Table 6.1 lists the refractive indices for quartz, $LiNbO_3$ and TeO_2 at 590 nm as reference.

Measurement of $I_{ref}(\lambda)$ was completed for each fluence to ensure its measurement under identical conditions to the measurement of the damaged area. Once setup was complete for a given fluence measurement, orientation did not change as the sample was again placed on a movable stage to allow discrete step positional measurements. Measurement of the irradiated area was completed in discrete steps as mentioned and again each spot was automatically averaged over multiple measurements to produce an average value. This averaging is reflected in (6.8). The error calculation for $R(\lambda)$ is the same as for $T(\lambda)$ in (6.5).

6.2.3 Absorbance

Absorbance was strictly calculated from reflectance and transmittance values using:

$$A(\lambda) = 1 - R(\lambda) - T(\lambda) \tag{6.9}$$

$$\delta A(\lambda) = \delta R(\lambda) + \delta T(\lambda) \tag{6.10}$$

6.2.4 Raman Spectroscopy

Raman spectroscopy is a technique used to provide information on the structure of a material, specifically bond types, by measuring vibrational and rotational states. It relies on the inelastic scattering, Raman scattering, interaction of monochromatic light with vibrations, or phonons, of a material to provide up (anti-Stokes) and down (Stokes) shifts in frequency of the incident light. Depending on the shift magnitude, information on the bond type can be discerned. The most common use of Raman spectroscopy is in chemistry as a fingerprinting analysis technique, *i.e.*, it is used to identify unknown materials or induced states. This can be extended to measurement of induced damage. If a new Raman signal is measured, as was

observed in silicon, this points to creation of a new bond type. Another example is changing Raman signal relative intensities showing disruption to specific bond types or general disordering of the material. For induced damage, Raman measurement information alone provides minimal information. However, it can be used as a proxy measurement to relate observable Raman changes to known damage defects measured by other techniques such as electron paramagnetic resonance (EPR), or electron microscopy measurements. These techniques provide the enhanced details on defect types and structures. With this information mapped to Raman signals, Raman becomes more of the well-known fingerprinting technique. As Raman has become a very accessible measurement that is non-invasive and non-destructive, it is often used, once other measurements have clarified damage relationships.

Irradiated sample areas were measured at room temperature by a Renishaw Invia Reflex Raman microscope with a 514 nm Ar^+ laser normally incident on the sample surfaces. Scattered light is also collected normal to the sample surface through a 50x magnification lens and dispersed onto a monochromator with an 1800 lines/mm grating. As mentioned, each fluence is measured in multiple spots across the sample and averaged together to produce a single Raman spectrum and error bar per fluence. The averaging and error approach is the same as was presented for transmittance calculations (6.2) and (6.3).

6.3 Quartz (c-SiO_2)

As a first step into transparent and birefringent materials, c-SiO_2 was irradiated and studied before moving on to the primary materials, $LiNbO_3$ and TeO_2. Quartz served as a test run for measurement techniques due to the availability of reported radiation damage results to compare with present results. The transmittance measurement was validated by comparing experimental results of undamaged c-SiO_2 to calculated results using (6.11) and (6.12), the normal incidence isotropic Fresnel equations, and an average refractive index value.

$$R(\lambda) = \left| \frac{n_1(\lambda) - n_2(\lambda)}{n_1(\lambda) + n_2(\lambda)} \right|^2 \tag{6.11}$$

$$T(\lambda) = 1 - R(\lambda) \tag{6.12}$$

Given the low birefringence of quartz, the error in this assumption and calculation is relatively small as shown in Figure 6.5b. The error is bounded by calculations using only $n_o(\lambda)$ and $n_e(\lambda)$ as the true value cannot lie outside this range. Use of (6.12) is valid as the refractive index of c-SiO_2 is purely real and thus has no absorption component. Together these equations and assumptions allow a bounded calculation of theoretical transmittance to compare with experimental results as shown in Figure 6.5c. The difference in calculated transmittance between different refractive indices is small and the experimental results agree with theory within experimental error, thus validating the use of this technique and all corresponding assumptions. Based on the similarity of techniques and assumptions, this validation can be extended to the reflectance measurement and absorbance calculation.

6.3.1 Quartz: Transmittance

Figure 6.5d shows, for select fluences, transmittance as a function of measured wavelength. The general trend across the spectrum is a decrease in transmittance as a function of fluence, except at low fluences where transmittance is observed to briefly increase before starting to decrease. The decrease in transmittance is expected as darkening of transparent materials is a well known radiation induced effect that was also visually observed. However, the initial increase was not expected. The cause of this is unknown but assumed to be the development of an anti-reflection layer in the damaged region whose properties are changed and removed as fluence (damage) increases. While this explains the observation, there is no further evidence to support this claim and thus it is left as an observational theory. Another interesting behavior is the linear-like trend in transmittance versus wavelength curves and the increasing positive slope with increasing fluence. This shows transmittance is more strongly affected at shorter wavelengths than at longer wavelengths. The cause of this is increased absorbance at shorter wavelengths in this range with strong absorption in the UV [74]. The data reported in [74] does not investigate fluence effects but reports data at a fluence of 2.7×10^{15} protons/cm^2 that is consistent with the trends shown here.

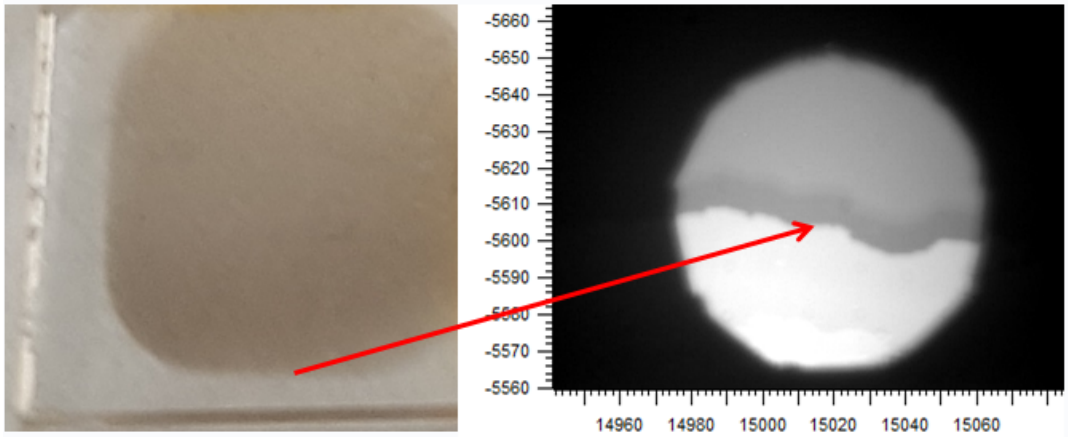

(a) Scale in μm.

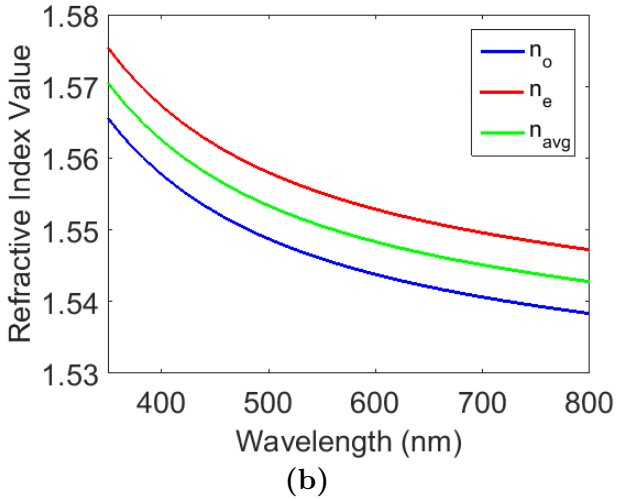

(b)

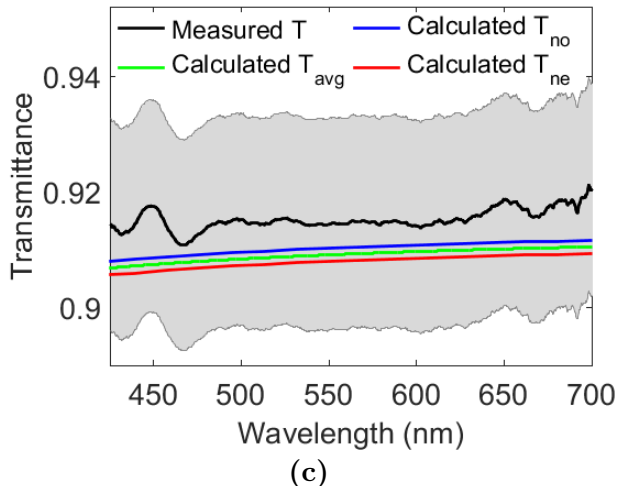

(c)

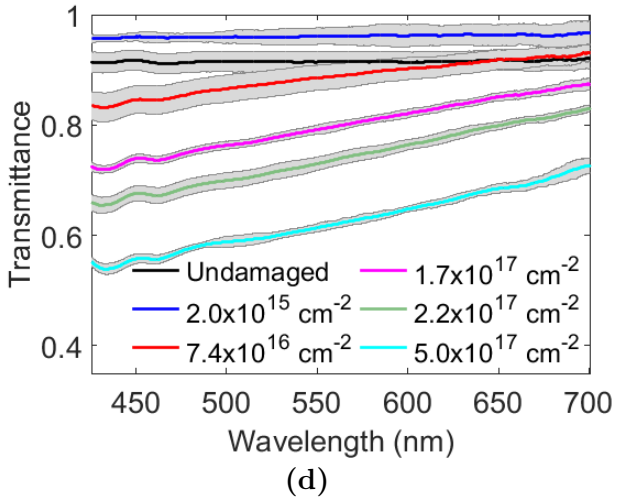

(d)

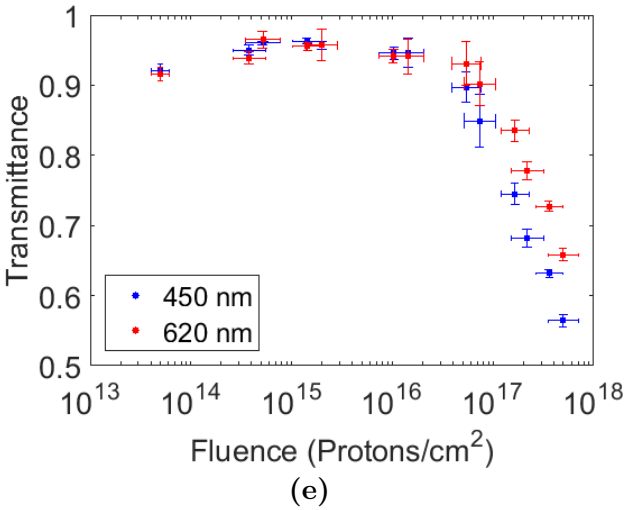

(e)

Figure 6.5: (a) 5.0×10^{17} protons/cm^2 irradiated quartz with microscope image of implant edge. (b) Refractive indices of c-SiO_2 plus average 'isotropic' average value used for calculations. (c) Comparison of measured and calculated $T(\lambda)$ of undamaged crystal to show experimental agreement. (d) $T(\lambda)$ vs wavelength. (e) T vs fluence.

Figure 6.5e shows transmittance as a function of fluence for two selected wavelengths, 450 and 620 nm. These values were chosen to span the measured wavelength range; 450 nm is the maximum of the largest source peak and thus gives the strongest signal, while 620 nm is the farthest point from 450 nm that could be measured with sufficient signal. Other wavelengths were examined and produced similar plots to those shown here. Figure 6.5e clearly shows the initial increase in transmittance before the monotonic decrease. Interestingly, the fluence at which significant monotonic decrease begins, outside of error bars, is roughly around 10^{16} protons/cm^2 (a previously mentioned, general a rule of thumb milestone fluence for radiation damage). This supports the general understanding of radiation induced property changes.

6.3.2 Quartz: Reflectance and Absorbance

Reflectance measurements were taken as described above and plotted versus wavelength for select fluences in Figure 6.6a. As mentioned, the reflectance measurement is relative to the reference measurement of the undamaged crystal; this result at multiple fluences is shown in Figure 6.6a. From this measurement, the actual reflectance value can be approximately calculated or scaled by multiplying out $R_{crystal}(\lambda)$. This requires assumption of an average index of refraction and an isotropic material as was previously discussed. The results of this scaling are shown in Figure 6.6b. The general trend across all wavelengths complements the trend observed in the transmittance measurements, *i.e.*, an initial decrease in reflectance before increasing with fluence. However, there are differences in the plot shapes at different fluences, especially the highest fluence. The cause of this change in shape is unknown.

As the scaled results are scaled by a constant value on a per wavelength basis, the plots of reflectance versus fluence for select wavelengths will have the same shape regardless of which measurement is used. However, scaled results are required to enable a calculation of absorbance. Figure 6.6c shows scaled reflectance values versus fluence at select wavelengths. Again, the trend compliments that of the corresponding transmittance plot. Based on the transmittance measurements, it was somewhat expected for reflectance measurements to have this trend, however, based on the visual appearance of the sample, it was unexpected to see such high reflectance values as, by definition, this will limit absorbance values. Instead, it was expected for absorbance to have a stronger effect and thus limit reflectance.

A plot of absorbance versus fluence is shown in Figure 6.6d. Recall these values are not

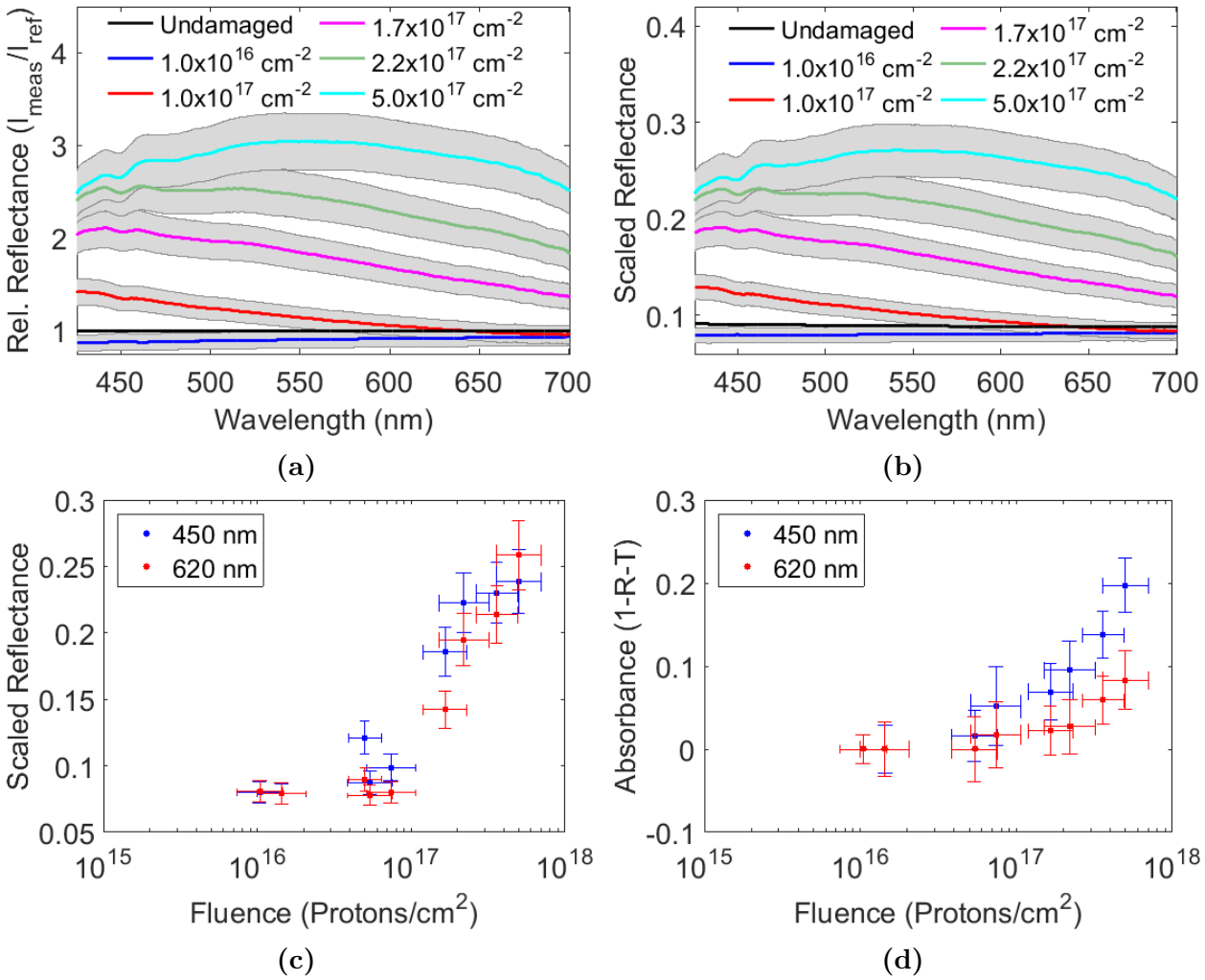

Figure 6.6: $R(\lambda)$ and $A(\lambda)$ results of proton irradiated c-SiO_2. (a) Relative $R(\lambda)$ vs wavelength for select fluences. (b) Scaled $R(\lambda)$ vs wavelength: calculated using $R_{crystal}(\lambda)$. (c) Scaled $R(\lambda)$ vs fluence at 450 and 620 nm. Trend is complementary to that of $T(\lambda)$ in Figure 6.5e. (d) $A(\lambda)$ vs fluence: values calculated from $T(\lambda)$ and $R(\lambda)$.

actively measured but instead calculated from transmittance and reflectance measurements using (6.9). While values are slightly lower than expected based on visual observation of the irradiated crystal, the monotonically increasing trend is as expected. The increased absorbance at shorter wavelengths over longer wavelengths agrees with the data in [74].

6.3.3 Quartz: Raman Spectroscopy

Due to the high use of quartz in various applications, understanding radiation induced effects in all forms of quartz is a well-studied topic. While the structure of different forms of quartz varies in terms of bond angles, all share the same basic bond type of Si-O. In pure quartz, no

other bond type exists as each Si atom is bonded to 4 O atoms and each O atom is bonded to 2 Si atoms. Therefore, on a structural level, defects caused by incident charged particle radiation are the same in all forms of quartz, although they may behave slightly differently in each form. The most common radiation induced defect is called an E' center which occurs when a single O atom has been displaced from a 4-bonded Si atom leaving the Si atom with three bonds and a dangling unpaired electron [75]. Other defect types also occur and are discussed in many reviews such as [75, 76]. The E' center is interesting for this research and Raman spectroscopy due to its high occurrence and creation rate. As E' centers can be radiolytically produced with protons [76] by displacing a lattice atom, creating a Frenkel pair [77], it is clear evidence of an expected type of radiation damage. Evidence for these defects has been reported in many studies for both heavy ion radiation [78, 79], and light ions, specifically protons [74, 77]. Majority of this research uses electron paramagnetic resonance measurements as the E' center is paramagnetic, to identify its existence. Once the existence was shown unequivocally, other research, including Raman measurements, began to take a forefront. In a series of papers by Skuja [80, 81, 82], the existence of a new broad Raman feature was discovered as a result of radiation damage creating E' centers and interstitial O atoms. The source of the new, broad, feature, centered at 1535 cm^{-1} was reported to be from interstitial O_2 luminescence. This was later confirmed by other independent research such as [83]. The basic idea is that incident radiation causes damage resulting in interstitial O atoms that are then mobile in the lattice and can combine with other O atoms into O_2. Once combined, the strong bond of O_2 is challenging to break and remains within the system. The mobility of interstitial O is temperature dependent as expected, and at room temperature has been observed to be highly mobile. Skuja went further with Raman measurements to show that calculations are possible to give approximate values of percent composition of O_2 in the lattice based on peak height and area. This can potentially be used as a measurement of accrued damage. While not pertinent to these specific results, logic dictates that since incident proton radiation creates interstitial O, it should also create interstitial Si that may lead to other effects. However, no reports on such effects have been found.

Unlike the previous measurements (transmittance, reflectance and absorbance) that did not have direct published results to compare with, the Raman measurements can be compared

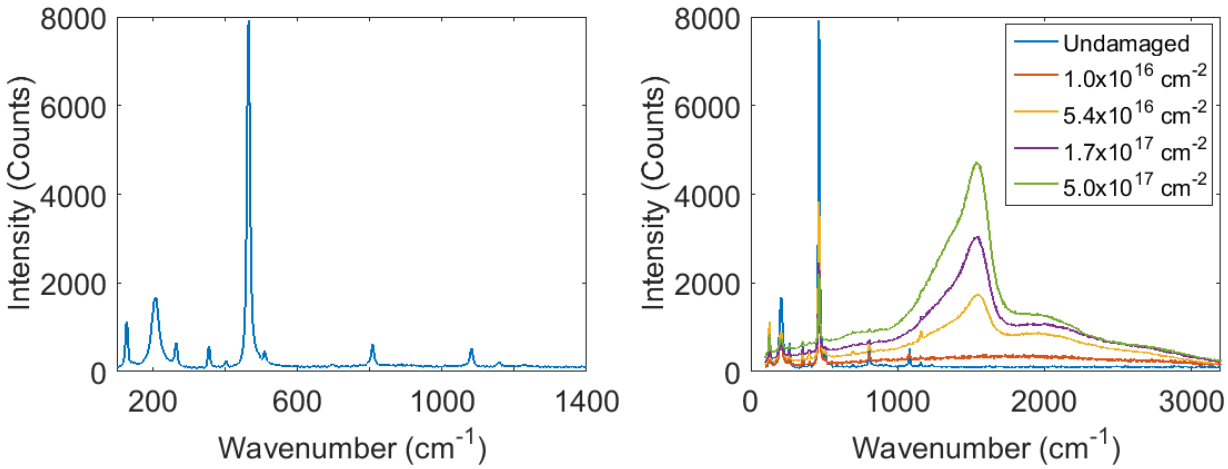

Figure 6.7: (a) Undamaged c-SiO_2 Raman spectrum. (b) Raman spectra at select fluences of 10 keV hydrogen ion (proton) irradiation. First observation of new 1535 cm^{-1} feature (O_2 luminescence) growth with increasing fluence. Smaller, broad peak around 2000 cm^{-1} is a result of Si-H bonds. Overall upward 'bowing' is a background fluorescence effect, common to some Raman measurements, that is later removed.

to the resuts discussed above, specifically, the 1535 cm^{-1} line growth with increasing fluence. Raman measurements were taken as described previously. For reference, Figure 6.7a shows the Raman spectrum of the undamaged c-SiO_2 sample. Higher wavenumbers, past 1400 cm^{-1} have no Raman signal. In comparison to silicon, c-SiO_2 has a large number of Raman peaks. This is due to the higher number of bond types (2 instead of 1) and the more complicated crystal structure. In general, the more complicated a material is, either in structure (bond angles) or number of bond types, the more Raman lines that exist. Figure 6.7b shows a plot of select fluences for irradiated c-SiO_2 and the growth of a new feature at the predicted 1535 cm^{-1} is quite apparent. Another, smaller, broad peak, to the right of the peak of interest, corresponds to a known grouping of Si-H bonds. Given the presence of background hydrogen gas in the system that can diffuse into the top of the lattice and potentially bond with unbonded silicon as a result of the damage, this type of bond makes sense to be observed.

The appearance of the undamaged crystal structure signal below roughly 1000 cm^{-1} is primarily due to the Raman measurement penetrating through the damaged layer and measuring the underlying crystal structure, similar to the occurrence in silicon. While challenging to tell in the presented figures, the crystal Raman signal decreases evenly in intensity with increasing fluence. This clearly shows that its presence is at least partially due to the under-

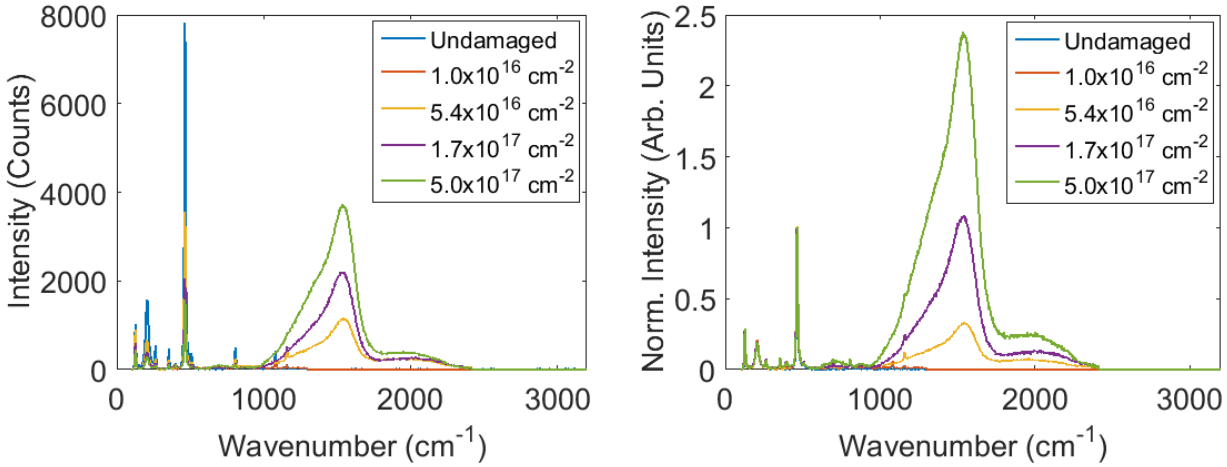

Figure 6.8: (a) Raman spectra of select fluence irradiated *c*-SiO_2 with background signal removed. The new 1535 cm^{-1} signal shape is now much more pronounced. (b) Spectra from (a) normalized to the 464 cm^{-1} peak value to show a clear picture of the 1535 cm^{-1} signal with respect to crystal sructure.

lying crystal structure and is being attenuated by the presence of the damaged layer, which will likely have a growing attenuation coefficient with increasing fluence.

Apart from the desired and expected peak growth with fluence, the overall spectrum at each fluence appears to have an upward bowing that increases with fluence. This is a fairly well-known Raman effect that can appear in spectra as a result of underlying, very broad fluorescence. This type of signal can occur in a variety different measurements and can also be easily removed. Commercially available programs exist to auto analyze Raman spectra, detect effects such as this and remove them from the spectra. However, this effect is simple to remove by taking the data points not included in the undamaged peaks as well as not part of the desired new peaks, performing a polynomial fit and subtracting the result from the spectrum. This was completed in the present work using a least squares fitting method. The spectra, with the 'background' removed, are shown in Figure 6.8a. As learned previously, certain effects and corresponding information can be better presented when observed as an internal ratio, *i.e.*, when the spectra are normalized to a specific wavelength. The result of this normalization, to the 464 cm^{-1} peak (highest undamaged peak) is shown in Figure 6.8b. As can be seen, the removal of the background, as well as the normalization, makes the growth of both peaks quite obvious. Comparison of this peak position and shape to

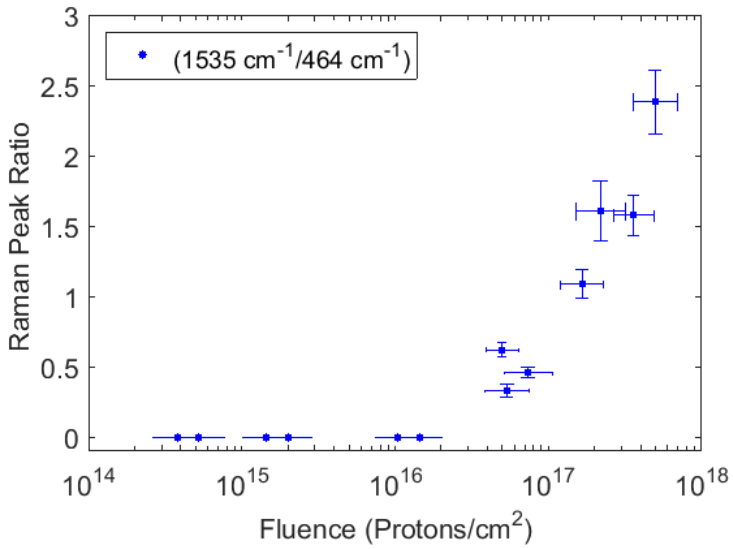

Figure 6.9: Raman peak ratio of the 1535 cm^{-1} O_2 luminescence peak to the 464 cm^{-1} crystal peak versus accumulated fluence.

that reported by [81] and others shows good agreement. The identification of this signal as interstitial O_2 luminescence provides clear evidence of induced structural damage.

As with the silicon data, a plot of peak ratios versus fluence is shown in Figure 6.9. The peak ratio is the new peak maximum, at 1535 cm^{-1}, divided by the strongest crystal peak at 464 cm^{-1}. An interesting result is the obvious change around 10^{16} protons/cm^2 as was expected. In other graphs the existence of the 10^{16} ions/cm^2 rule of thumb switching point theory may be debatable, but here, the effect is obvious. Similar to the silicon plot of amorphous to crystal peak ratio versus fluence, no such plot has been found in literature.

6.4 Lithium Niobate ($LiNbO_3$)

The investigation of $LiNbO_3$ serves as an intermediate study before reaching the pinnacle research material in TeO_2. A picture of the highest fluence (6.8×10^{17} protons/cm^2) irradiated sample is shown in Figure 6.10 along with a microscope image of the damaged area edge. The prominent edge in the microscope image shows a clear distinction between damaged and undamaged material along with the visual darkening effects of charged particle damage. Unlike *c*-SiO_2, $LiNbO_3$ is strongly birefringent and literature on radiation effects is minimal, with literature on radiation damaged $LiNbO_3$ Raman spectra being non-existent to current knowledge. Prior to the present dominance of TeO_2 in AO technology, $LiNbO_3$ was the go to

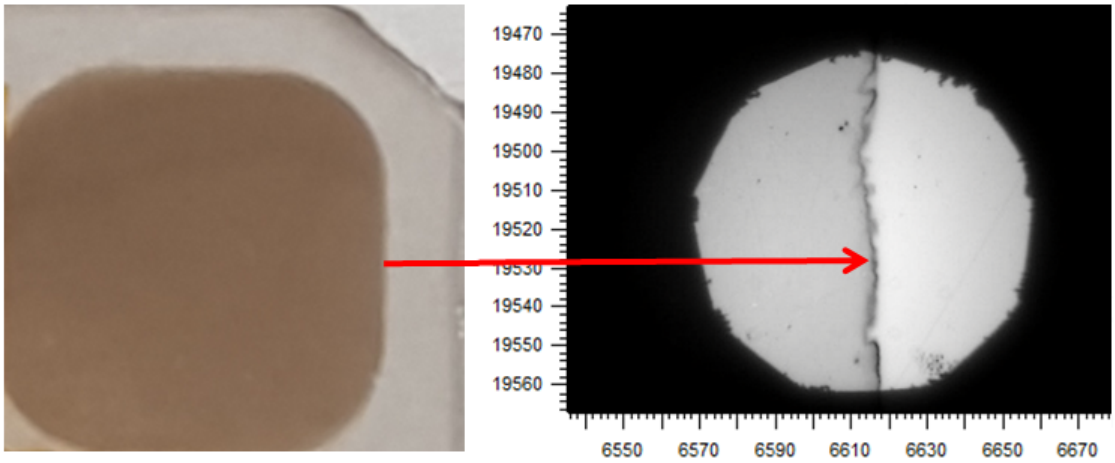

Figure 6.10: Picture of irradiated $LiNbO_3$ and corresponding damaged/undamaged interface under Raman microscope. Scale is in μm. Accumulated fluence: 6.8×10^{17} protons/cm^2.

material, primarily for its large birefringence and ability to be integrated into devices. This makes it a natural choice for study alongside TeO_2. The same irradiation and measurement techniques used for c-SiO_2 were implemented for $LiNbO_3$, with the results shown here.

6.4.1 Lithium Niobate: Optical Measurements

Transmittance measurements are shown in Figures 6.11a and 6.11b, reflectance in Figures 6.11c and 6.11d and absorbance in Figures 6.11e and 6.11f. Overall, trends for transmittance and absorbance agree with results observed in quartz, *i.e.*, linear-like trends versus wavelength with faster increasing absorbance, and decreasing transmittance, at shorter wavelengths making the plots have larger slope magnitudes. The similarities in these trends suggests similar types of damage in the two materials. The trends for reflectance are similar in magnitude changes but are flatter across the wavelength range than trends observed in quartz. Reflectance results show the expected trend in comparison to transmittance results and the substantial absorbance values are consistent with visual darkening observations. Unlike in quartz, transmittance did not initially increase with fluence but instead monotonically decreased once a change was observed. Transmittance again begins decreasing around 10^{16} protons/cm^2, but the 'break point' is at a higher fluence (3×10^{16} protons/cm^2) than in quartz. This shows $LiNbO_3$ is more resistant to radiation induced transmittance changes. This could be due to higher bond strengths or recombination rates as compared to quartz.

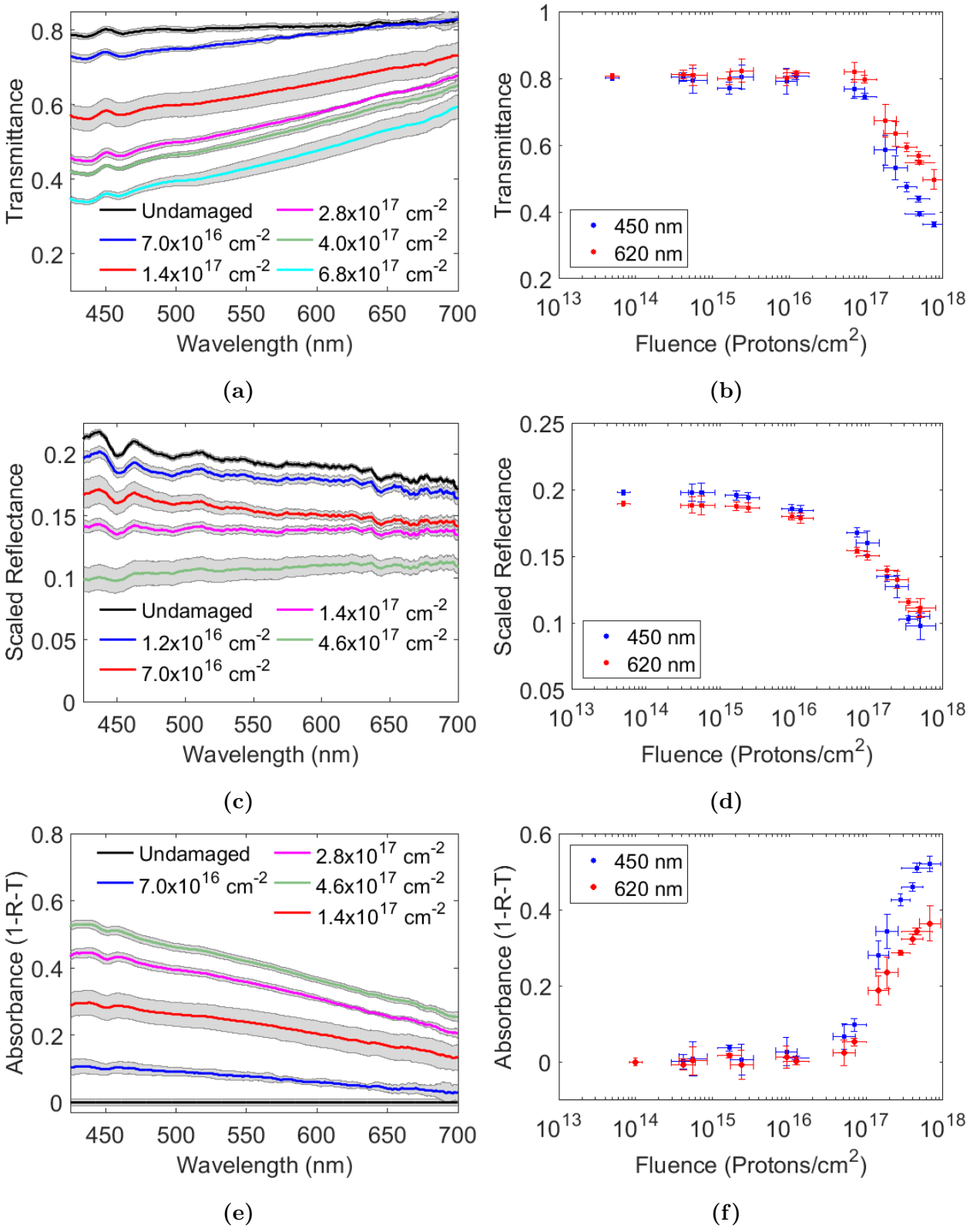

Figure 6.11: $LiNbO_3$ results. (a) $T(\lambda)$ vs wavelength (b) $T(\lambda)$ vs fluence (c) $R(\lambda)$ vs wavelength (d) $R(\lambda)$ vs fluence (e) $A(\lambda)$ vs wavelength (f) $A(\lambda)$ vs fluence.

6.4.2 Lithium Niobate: Raman Spectroscopy

Unlike quartz, where published results exist to guide investigations and compare values to, no such measurements for charged particle radiation damaged $LiNbO_3$ could be found in regard to Raman spectroscopy. The undamaged Raman spectrum is shown in Figure 6.12a along with spectra at select fluences. Again, the spectra is more complicated (has more lines) than previous spectra due to the increased structure and bond type complexity. Similar to c-SiO_2, the underlying crystal signal persists throughout high fluence measurements due to probing of the undamaged material. The peak strengths decrease but peak ratios remain constant to reflect attenuation from the damage layer. As fluence increases, the growth of a new feature appears. The strength of this feature, in comparison to the crystal peaks, is diminished in comparison to the c-SiO_2 spectra. By inspection, this feature looks similar to that which was observed in c-SiO_2 and from analysis, the maximum peak height occurs at 1535 cm^{-1}, the same as in c-SiO_2. To enhance the new feature, Figure 6.12b shows the spectra normalized to the 613 cm^{-1} peak value (largest crystal peak), similar to the process done in c-SiO_2. In this figure it is clear that a new signal is growing with increasing fluence and comparing the position and shape of this feature to that which was found in c-SiO_2 reveals many similarities. This suggests that they are the same peak, due to interstitial O_2 and corresponding vacancies, which is possible, as $LiNbO_3$ is also an oxide. This further supports the speculation of damage similarities based on transmittance and absorbance measurements.

While the luminescence peak signal strength is not as strong in comparison to the crystal peaks as in c-SiO_2, it is still present and obviously growing with fluence. A plot of the ratio of 1535 cm^{-1} to 613 cm^{-1} is shown in Figure 6.12c. The diminished strength coincides with the idea of requiring higher fluences to observe transmittance and reflectance changes *i.e.*, $LiNbO_3$ is more resistant to proton radiation. A small caveat to this statement, in terms of the interstitial O_2 signal, is that the initial interstitial O atoms may have a different mobility in the different materials that may lead to different accumulation rates and thus signatures in the Raman signal. Regardless of these details, the result shows clear evidence of damage as a function of fluence with proton irradiation. Given the scarcity, or potential complete absence, of results such as these in current literature, this data will provide a meaningful contribution to both material science and engineering application literature.

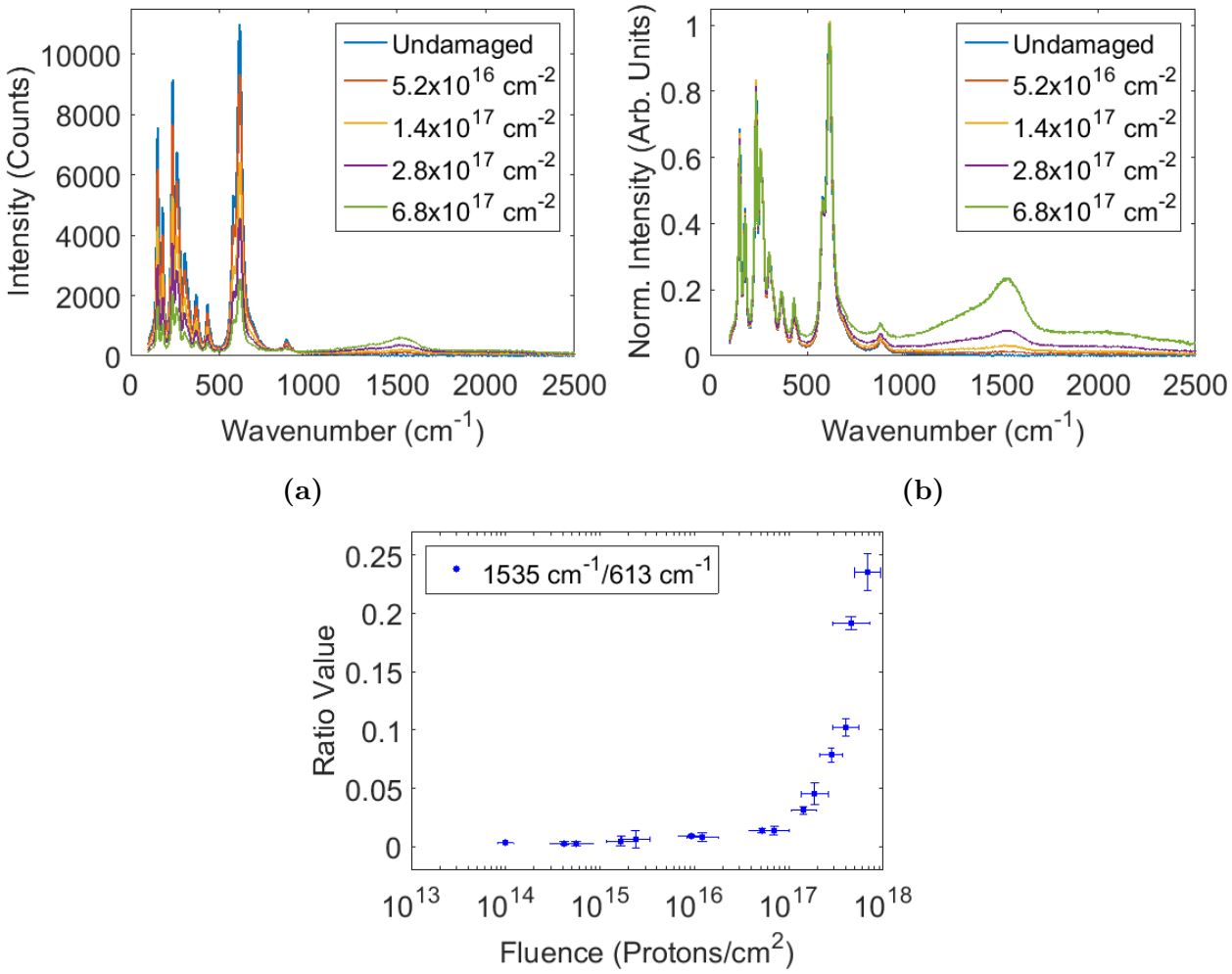

Figure 6.12: (a) $LiNbO_3$ Raman spectra at select fluences. Existence of a broad feature at 1535 cm^{-1}, growing with fluence, is observed. (b) Spectra from (a) normalized to the 613 cm^{-1} peak value to show growth 1535 cm^{-1} signal with respect to crystal structure. (c) Ratio of 1535 cm^{-1} O_2 luminescence peak to $LiNbO_3$ 613 cm^{-1} crystal peak vs accumulated fluence to show relative 1535 cm^{-1} peak growth.

6.5 Tellurium Dioxide (TeO_2)

Results on the final material of study, TeO_2, are the most significant to the general scientific community and specifically to this project due to the widespread use of TeO_2 in AO technology and the lack of radiation damage measurements in current literature, specifically Raman measurements. As discussed in Chapter 1, the current body of work on proton irradiated

TeO_2, and radiation damage in general, concludes that TeO_2 is radiation immune. However, even though the primary proton study is considered accurate in presented data and is widely reference, it was limited to fluences much lower than those delivered in the present work. The results presented here are not meant to refute those of [13] but instead meant to expand the research to higher fluences and present evidence that radiation exposure at low fluences is not enough to fully assess space qualification. It is the current belief that the high fluence data presented here shows that it is inaccurate to say that TeO_2 is radiation immune.

Two key differences, besides delivered fluence, exist between the study in [13] and the present research that should be mentioned. First is the radiation energy, MeV to keV energies respectively. This difference is expected to be minimal as it will only result in a deeper damage layer in the work of [13] in comparison to the surface layer created here. This should not drastically affect measurements such as transmittance. The second difference is in flux values, 1.885×10^{10} protons/cm^2/s in [13] to an average of 4×10^{13} protons/cm^2/s in the present work. As already mentioned, differences in flux can have an effect on induced damage but the exact details are dependent on many other factors. Therefore, if [13] had gone to higher fluences, it would have been very interesting to compare results. Regardless of these differences, based on general retained damage 'rules' it is still unsurprising that the work of [13] did not show radiation damage effects due to the fluences being too low.

6.5.1 Tellurium Dioxide: Transmittance

As with *c*-SiO_2 and $LiNbO_3$, transmittance measurements are shown for select fluences at all wavelengths in Figure 6.13a and for select wavelengths versus fluence in Figure 6.13b. The general shape of the transmittance versus wavelength plots are similar to those observed in both $LiNbO_3$ and quartz, which again suggests a similarity in damage type. This is also echoed in the similarity of absorbance versus wavelength plots. The general trend of a monotonic decreasing transmittance with increasing fluence is observed across all measured wavelengths, similar to that observed in $LiNbO_3$. Interestingly, the TeO_2 takes longer, higher fluences, to begin to observe a transmittance decrease than in $LiNbO_3$. However, once change occurs, it happens at a faster rate and reaches lower values. This was unexpected based on the visual appearance of $LiNbO_3$ being much darker than TeO_2. The increased fluence requirement supports claims of naturally high radiation damage resistance.

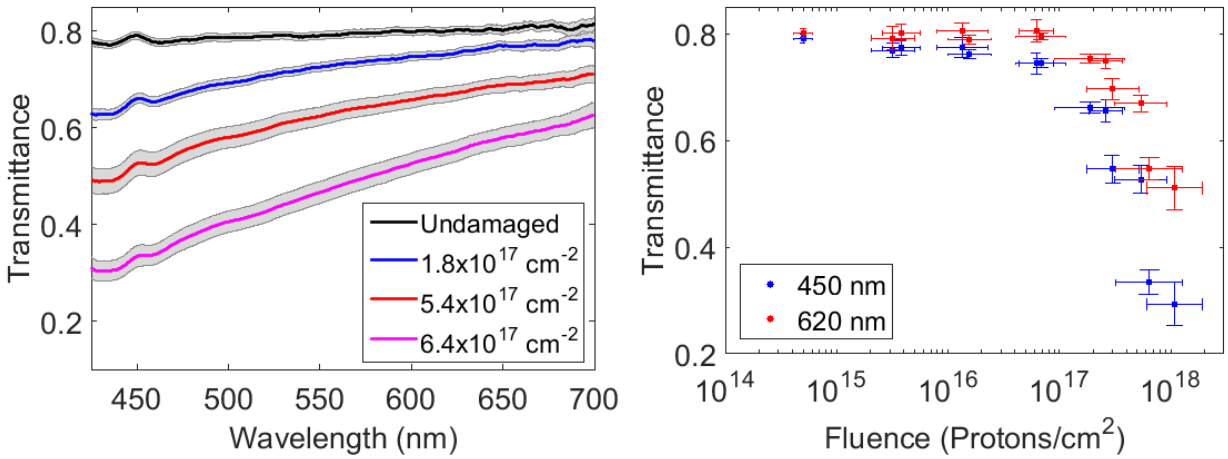

Figure 6.13: (a) $T(\lambda)$ versus wavelength results of proton irradiated TeO_2. General trend is similar to that of $LiNbO_3$, *i.e.*, a monotonic decrease with increasing fluence, once change is observed. (b) $T(\lambda)$ versus fluence for select wavelengths which further shows monotonic decreasing trend. The required fluence for significant change is much higher than in other measured materials.

6.5.2 Tellurium Dioxide: Reflectance and Absorbance

Reflectance and absorbance values for TeO_2 are shown in Figure 6.14. The trends exhibited in the value versus fluence plots are complementary to those for transmittance as expected. The reflectance values interestingly undergo a similar change to that observed in $LiNbO_3$, but take a higher fluence to begin changing, as was observed in transmittance. The more interesting plot may be that of absorbance versus wavelength where substantial changes, reaching almost 55%, are observed. Additionally, the shapes of the absorbance versus wavelength plots are again linear-like and stronger at shorter wavelengths as observed in both $LiNbO_3$ and quartz. This again points to damage type similarities and the creation of an absorbing damage layer. This now suggests that all three oxides have strongly related damage types or effects. This was further investigated with Raman spectroscopy and validated with the presence of the 1535 cm^{-1} feature in all measured materials.

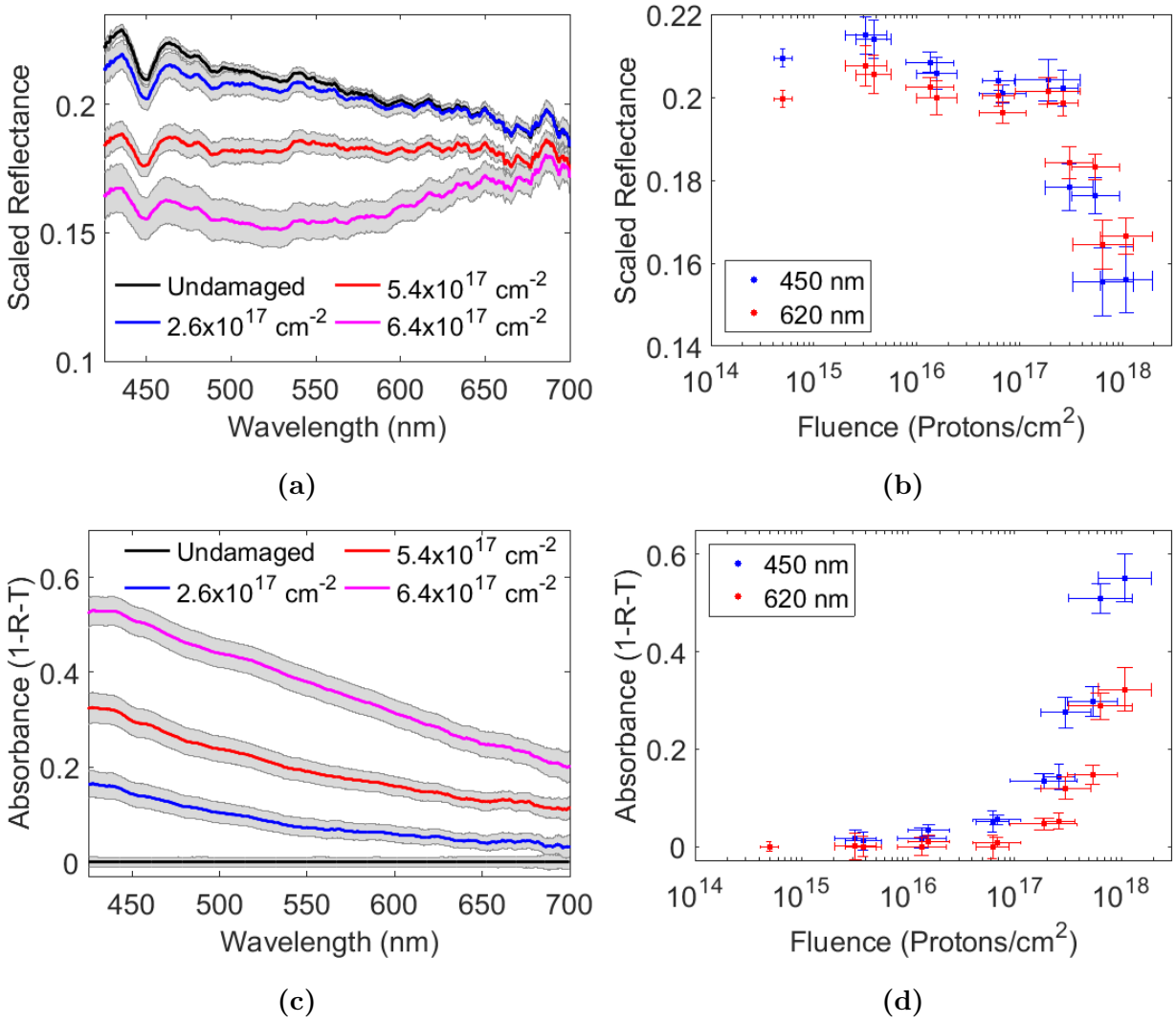

Figure 6.14: Reflectance and absorbance results for proton irradiated TeO_2. General trend is similar to $LiNbO_3$. Trends complement transmittance trend. Required fluence to produce significant change is again large. Low change in reflectance and high change in absorbance, up to 55%, at max fluence was unexpected. (a) $R(\lambda)$ vs wavelength (b) $R(\lambda)$ vs fluence (c) $A(\lambda)$ vs wavelength (d) $A(\lambda)$ vs fluence.

6.5.3 Tellurium Dioxide: Raman Spectroscopy

The Raman measurements for TeO_2 are quite different from those of $LiNbO_3$ and c-SiO_2 in a few ways. First, on a more general level, the visual appearance of the irradiated TeO_2 sample, as shown in Figure 6.15 differs from the other materials in that there is an obvious presence of features and not a simple uniform looking radiated area. The cause of this is

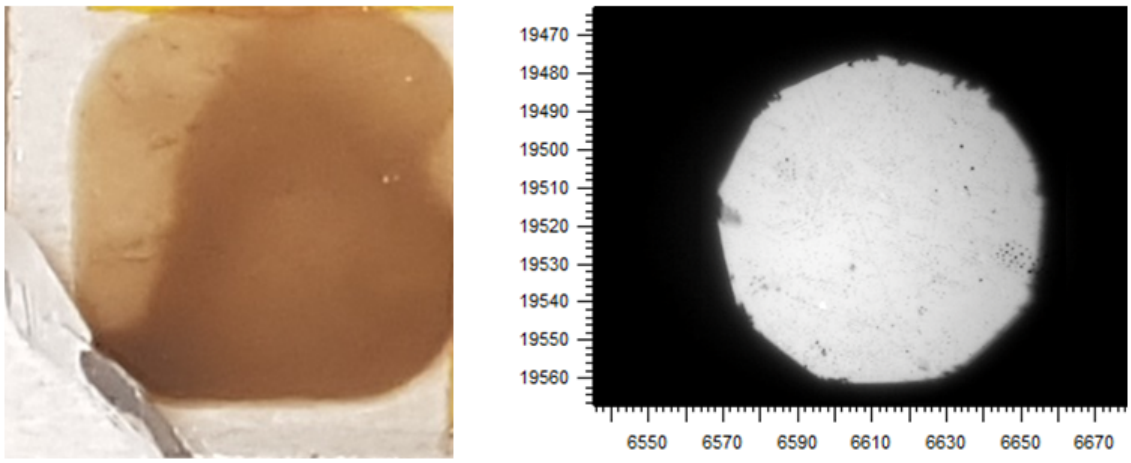

Figure 6.15: Picture of 1.0×10^{18} protons/cm^2 irradiated TeO_2 and corresponding Raman microscope image selected at a random position in irradiated area. Unlike other materials, implant edge was not clearly defined and implant area is not visually uniform.

unknown, but speculated to be due to a high mobility of defects in TeO_2 at room temperature. Furthermore, under the Raman microscope, a clear edge of the implanted area could not be discerned; everything looked reasonably uniform from a damaged position to an undamaged position. The microscope image shown is representative of random positions in the irradiated area that under the microscope appeared quite uniform. However, distributed throughout this uniform background, which is similar to that of the other samples, lies distinct features, which is a stark difference to other samples. Examples of these features are shown in Figure 6.17. When viewing samples of $LiNbO_3$ and c-SiO_2, there were some features throughout the uniform background but where much smaller and different than those shown here. In these cases, these features were determined to be dust or debris on the material surface. However, the size and detail of the features in TeO_2 could not be explained by debris. However, as the features were of unknown origin, they were originally avoided for Raman measurements and measurements of uniform background areas were given preference. The Raman spectra of these featureless measurements are shown in Figure 6.18. Again, the crystal structure appears in all measurements and decays evenly with increasing fluence as was observed in other samples and for the same reasons. However, this time, there is no growth of a new feature. Given the growth of the 1535 cm^{-1} feature in the other materials, and due to the

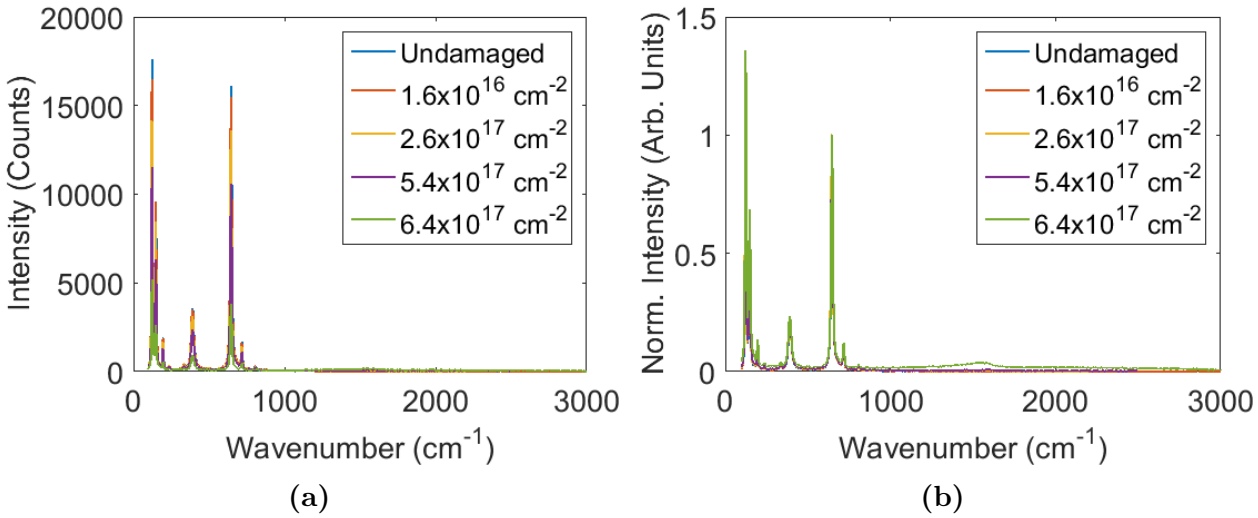

Figure 6.16: TeO_2 Raman measurements of uniform irradiated background - outside of defect features. (a) Raw measurements at select fluences including the undamaged crystal measurement. (b) Spectra of (a) normalized to 646 cm^{-1} crystal peak to show potential small peak growth at 1535 cm^{-1} at high fluence.

presence of oxygen in TeO_2, it was assumed that it would be found again. However, at the highest fluence, observable in the normalized spectra of Figure 6.18, there is a small broad signal around the 1535 cm^{-1} mark. This could simply mean that much higher fluences are required in TeO_2 to obtain significant growth of this peak and the corresponding defect(s).

6.5.4 Raman Measurement of Defect Clusters

The absence of a new feature, specifically the 1535 cm^{-1} feature observed in both $LiNbO_3$ and *c*-SiO_2, was interesting and unexpected based on the similarities of other optical results. Based on the structures of the features shown in Figure 6.17, it was theorized that they were actually defect clusters and would exhibit interesting, possibly desired, Raman spectra. Raman measurements of select defects are shown in Figure 6.18a for raw measurements and in Figure 6.18b for scaled measurements where the 1535 cm^{-1} feature now appears and supports the defect cluster theory. This is not only significant for the appearance of this feature in regard to the similarity with other materials and true evidence of induced structural damage, but also now poses the question, why do these defect clusters form in TeO_2 but not in $LiNbO_3$ or *c*-SiO_2, and why do measurements outside of the features show little to no sign of damage? A proposed explanation for this is simply that defects in TeO_2 have a much higher mobility than in the other materials. This would explain the macroscopic observed features in the

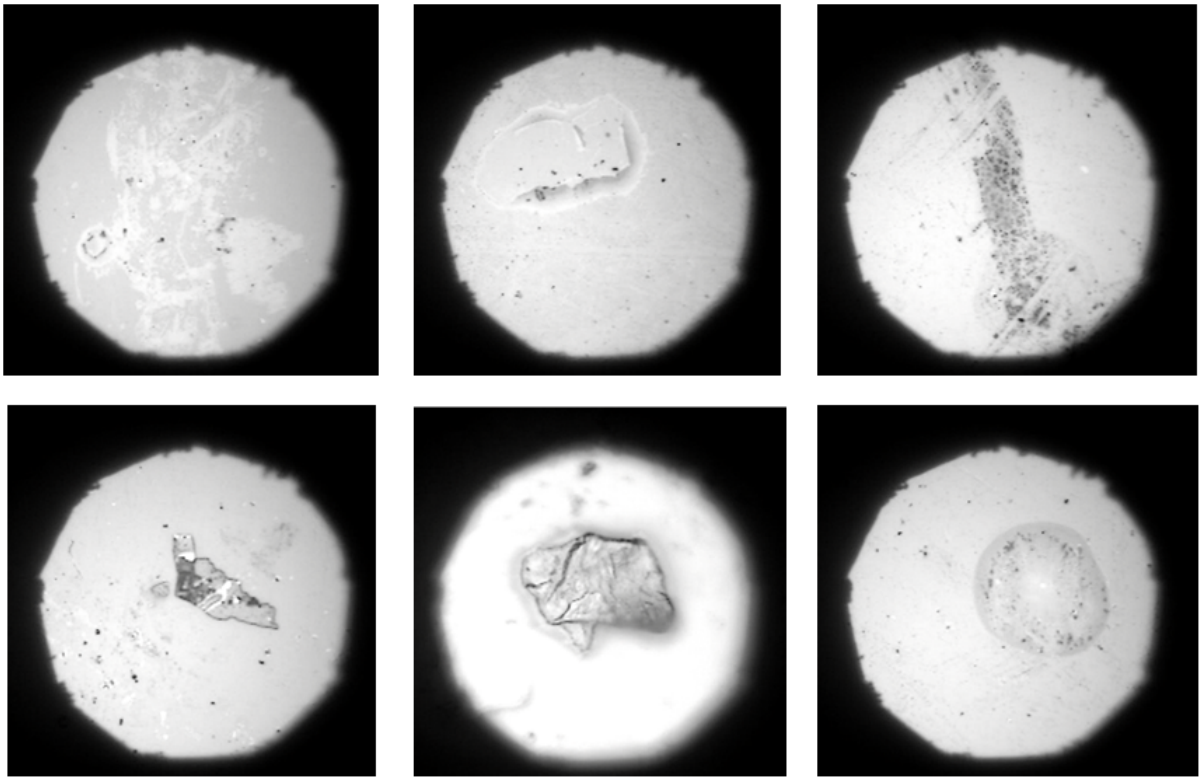

Figure 6.17: Examples of features in TeO_2 observed under the Raman microscope that were later determined to be defect clusters. Features appear at various fluences, beginning at $2{\times}10^{17}$ protons/cm^2 and increasing in frequency and contrast as a function of fluence. Field of view ≈ 80 μm.

irradiated sample and agree with previously reported theories of TeO_2 having a high self annealing ability due to increased mobility.

Assuming that TeO_2 does have an increased defect mobility and a correspondingly high recombination rate, then collisions of same type defects should occur at a statistically similar rate to defect recombination collisions. When collisions of same type defects occur, it is possible for defect clusters to form and grow. This form of explanation is used in other areas of material science, such as amorphization of crystal materials and the clustering, or overlapping, of amorphous pockets leading to large scale amorphous regions. This behavior explains the features observed under microscope and the high mobility can potentially be extended into the macroscopic regime to say that the visible features are just areas of more or less clusters of defects that produce different macroscopic properties.

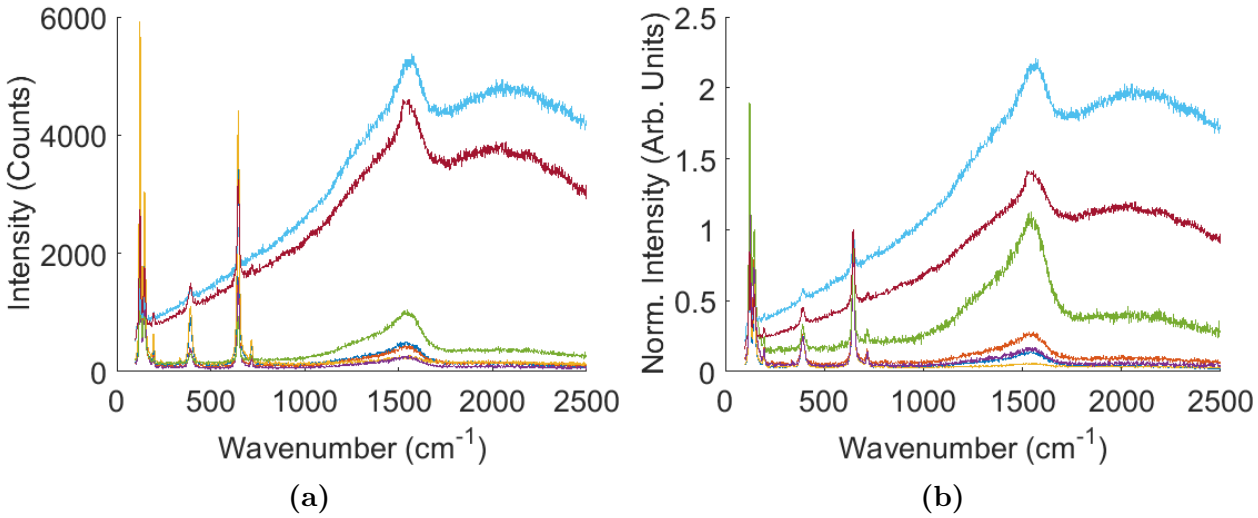

Figure 6.18: TeO_2 Raman measurements of select features at various high fluence values and positions within irradiated area. (a) Raw measurement. (b) Spectra of (a) normalized to 646 cm^{-1} crystal peak to show relative growth of 1535 cm^{-1} signal.

6.6 Comparison of 1535 cm^{-1} Raman Peaks

Throughout the $LiNbO_3$ and TeO_2 results sections, the similarities between the radiation damage induced behavior in all three materials, quartz, $LiNbO_3$ and TeO_2, has been discussed. These similarities appeared in the visual darkening, transmittance measurements and especially the Raman data where the same new Raman feature, at 1535 cm^{-1}, was observed to grow with increasing fluence. The small exception to this is in TeO_2, where the Raman feature was only strongly noticeable inside of macroscopic material features (tens of microns in size), suggested to be defect clusters, rather than throughout the irradiated area as in quartz and $LiNbO_3$. However, the appearance of the same signal in all three materials is strong evidence for a similar type of damage, specifically the radiolytic creation of interstitial O_2 by energetic protons. This fact is further reinforced in Figure 6.19 where the 1535 cm^{-1} feature from each material is isolated, by removal of background signal(s), and normalized to the 1535 cm^{-1} peak value. The two lines shown for TeO_2 come from two visually different features to show agreement across different feature 'types'. As can be seen, all features have good agreement in both shape and position, especially between quartz and $LiNbO_3$. All four spectra have strong agreement in the central peak area (around 1500 cm^{-1}). The TeO_2 lines have small variations toward the edges, but still show good overall agreement.

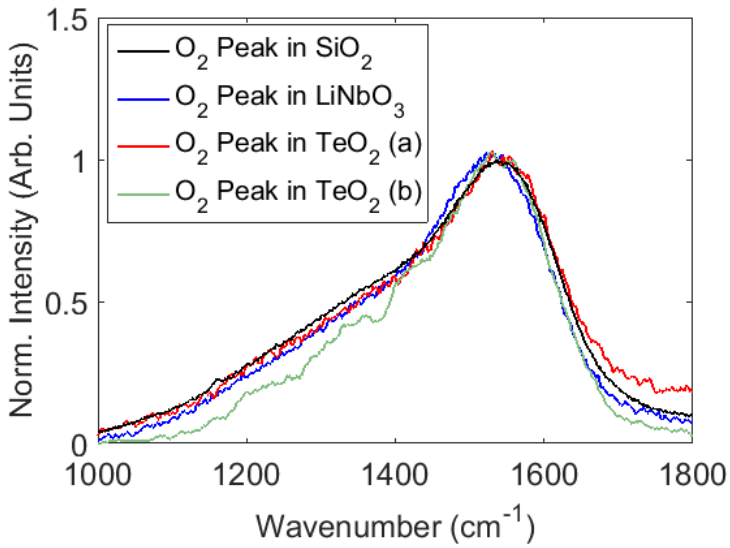

Figure 6.19: Spectral shape comparison of suspected O_2 luminescence features normalized to 1535 cm^{-1} in quartz (black), $LiNbO_3$ (blue) and TeO_2 (red and green). TeO_2 lines show two different defect clusters with two different raw magnitudes to show agreement across visually different features.

6.7 Space Environment Lifetime Calculations

With measurements of induced damage as a function of fluence in hand, the data can be used to discuss operational lifetimes of different materials under different conditions, such as in the space environment. As mentioned in the beginning, charged particles in the space environment are dominated by those from the solar wind for instruments outside of the Earth's protective magnetic field. For instruments inside the magnetic field, radiation conditions are highly variable depending on altitude and orbit, but in general, will experience less radiation than they would if outside the magnetic field. As conditions away from Earth are more easily described as an almost constant, these conditions will be considered here. The lifetime calculations here can serve as an upper limit to radiation damage on materials within the magnetic field where radiation flux is diminished.

The average flux of the solar wind is 3×10^8 particles/cm^2s and is primarily protons (96%). For the purpose of calculations in this work, the flux will be assumed to be 100% protons. The energy range is 1 eV - 10 keV and includes all values throughout this range in varying proportions. Recall that the energy spread only affects penetration depth and concentration

of damage within the damaged layer, which is approximated by the use of a mixed composition hydrogen beam that will result in three characteristic energies, with some statistical spread, rather than a monoenergetic proton beam.

To perform lifetime calculations, a benchmark effect needs to be defined such that once achieved or passed, the material is deemed unusable. For example, looking at transmittance data, a benchmark value could be once transmittance changes by more than 10% from initial value, the material is considered unusable. This benchmark obviously depends on the task of the material in the instrument and on the degree of change in a given property that the instrument can accommodate. In some instances, it may be possible that a 50% change in transmittance is permissible, assuming the rate of change is known to allow system calibrations to adapt to the change. On the other side of things, high precision instruments may only be able to tolerate a few percent change. For example calculations presented here, the 10% change in transmittance estimate will be used.

The lifetime (T_L) calculation, in number of years, is shown in (6.13) where F_c is the critical fluence, *i.e.*, fluence at which the corresponding property reaches an unusable value.

$$T_L = \frac{F_c \text{ particles/cm}^2}{3 \times 10^8 \text{ particles/cm}^2/\text{s}} \times \frac{1 \text{ year}}{3.15 \times 10^7 \text{ s}} \tag{6.13}$$

The critical fluence is estimated from the plots of transmittance versus fluence at 450 nm. Once determined, this value is used with (6.13) to produce the following results.

Material	Critical Fluence (protons/cm^2)	Lifetime (Years)
c-SiO_2	1.0×10^{17}	10.6
$LiNbO_3$	1.2×10^{17}	12.7
TeO_2	1.8×10^{17}	19.0

Table 6.2: Summary of experimental space lifetime calculation results for the three investigated materials assuming a failure metric of a 10% decrease in transmittance from the undamaged value. Critical fluence values are interpreted from graphs. Lifetime values are experimental and may slightly differ in space where flux is diminished.

6.8 Space Environment AOTF Example Calculations

As the primary motivation for present research is to assess the suitability of AOTF materials for the space environment, calculations similar to lifetime calculations can be completed using expected mission times to estimate observed effects in each material type. As has been the case so far, only solar wind radiation levels and details (energies) will be considered with higher energy particles left for future scaling work. Recall that if proper scaling calculations are completed using tools such as SRIM for depth profiles, equivalent fluences at varying depths can be calculated and mapped to the results shown here. This is highly application dependent and given the dominance of the solar wind in charged particle radiation levels that will be experienced by most spaceborne instruments, these calculations are unnecessary to present the purpose and results of the present work.

Table 6.3 shows a summary of results for expected transmittance values and changes relative to initial values for example space mission lifetimes. Values were found by interpolation of previously presented plots of transmittance at 450 nm versus fluence. These results do not present much new information as TeO_2 still comes out as an overall winner for resistance to damage out of the three materials. However, interestingly enough, quartz is not far behind in a lot of categories and may even potentially be ahead. A large part of this success is likely due to the initial increase of transmittance and potentially due to the minimal birefringence. Unfortunately, the low birefringence also makes quartz undesired for AO technology in general. Note that all values presented here are lower limit changes as retained damage is expected to be less in the laboratory than will be found in the space environment, primarily due to the difference in temperature and corresponding effects.

In regard to AOTF technology, the results of this study show that exposure to incident protons with an energy range of the order of 10 keV will result in crystal darkening of the surface layer at high fluences. Even though these energies will not penetrate into the bulk, and the area in which the AO interaction takes place will be undamaged, overall transmittance will drop significantly over time. This transmittance drop is coupled with an increase to absorbance that appears to have a strong dependence on wavelength, with shorter wavelengths experiencing more change than longer wavelengths. The refractive indices will

also change and likely change the birefringence of the damaged layer. The primary result of changes to the refractive indices in the damage layer is changes to device ray tracing and potential changes to system alignment. However, as shown in Table 6.3, it is possible for significant changes to take up to a few years of exposure time, depending on actual accumulation rate. This accumulation rate may permit the use of materials such as TeO_2 and is likely the cause for its observed success in missions completed to date. As mentioned, the tolerance to radiation induced material property changes is application dependent.

Material	Mission Length (Years)	Accumulated Fluence (protons/cm^2)	T ± 0.01	ΔT ± 0.01	$\lvert T-T_0\rvert/T_0$ (%)
c-SiO_2	1	9.5×10^{15}	0.95	0.03	3.3
	2	1.9×10^{16}	0.93	0.01	1.1
	5	4.7×10^{16}	0.90	0.02	2.2
	10	9.5×10^{16}	0.83	0.09	9.8
	20	1.9×10^{17}	0.76	0.16	17.4
$LiNbO_3$	1	9.5×10^{15}	0.79	0.01	1.3
	2	1.9×10^{16}	0.78	0.02	2.5
	5	4.7×10^{16}	0.77	0.03	3.8
	10	9.5×10^{16}	0.73	0.07	8.8
	20	1.9×10^{17}	0.53	0.27	33.8
TeO_2	1	9.5×10^{15}	0.78	0.01	1.3
	2	1.9×10^{16}	0.76	0.03	3.8
	5	4.7×10^{16}	0.75	0.04	5.1
	10	9.5×10^{16}	0.70	0.09	11.4
	20	1.9×10^{17}	0.62	0.17	21.5

Table 6.3: Summary of example mission lifetime accumulated fluence calculations and corresponding changes to transmittance values. Values are obtained through interpolation of the 450 nm $T(\lambda)$ versus fluence plots. Goal of this data is to provide an estimate for resistance to transmittance changes in studied materials.

Chapter 7

Conclusion

Any new material, device, or technology developed for space application must undergo space qualification, including radiation readiness testing, to assess its suitability and projected lifetime under the harsh conditions experienced in space. The focus of this work was on a specific type of radiation, charged particle radiation, specifically protons, and the corresponding induced damage. Further specification saw research focus on optical birefringent materials used in AOTF devices. This primarily stemmed from development of a new satellite instrument, ALI, that implements a TeO_2 AOTF and the fact that published data on charged particle radiation damage and effects, specifically proton radiation, is quite limited. The research that does exist, claims TeO_2 to be highly suited for use in the space environment, and some go as far as to say it is radiation immune. Based on this evidence, AOTF devices have been deployed on a few spaceborne missions, and to current knowledge, have performed well, with no obvious signs of degradation. However, given the limited heritage of use, additional research was completed to add to the knowledge base and aid future instrument qualification. The limited research on this topic also presented an opportunity to provide meaningful results to both the material science and space technology communities.

Alongside TeO_2, both $LiNbO_3$ and crystalline quartz were chosen for complementary studies. Quartz was chosen as a first step into transparent and birefringent materials as the large knowledge base on radiation induced effects in quartz enabled approximate experimental verification of procedures and results. $LiNbO_3$ was an obvious choice for direct comparison with TeO_2 based on its high birefringence and long term use in AO devices prior to the present TeO_2 dominated era. Furthermore, the literature on proton irradiated $LiNbO_3$ is also quite scarce and provides further opportunity to provide meaningful research results. Based on the optical nature of these materials, and the use of TeO_2 in ALI, an imaging instrument,

damage characterization focused on optical properties and related structural defects.

A vast amount of the information known today on radiation damage and induced optical and structural effects in materials comes from nuclear research. This is a result of the naturally radiation rich environment, containing multiple types of radiation, present in nuclear experiments. Along with producing measurable experimental effects, nuclear research was a driving force behind a majority of radiation damage theory, specifically charged particle theory. As charged particle damage became better understood, and its presence in the space environment was confirmed, its effects on spaceborne technology became increasingly important to fully understand. The primary source of charged particle radiation within our solar system is the Sun and the solar wind, which is a constant stream of charged particles, primarily protons (96%) with characteristic energies of the order of 10 keV and an average flux of 3×10^8 particles/cm^2/s. Given that protons in this energy range are obtainable at high flux values to permit accelerated lifetime testing in the laboratory setting, proton radiation was chosen as the focus for the present research.

The most commonly observed radiation induced optical effect is radiation darkening of optical materials. This was also one of the first observed effects in nuclear research, which led to an initial understanding of damage and the accompanied push to further investigate. From here, the list of induced damage effects grew substantially with notable optical effects including changes to the refractive index, or indices, resulting in transmittance, reflectance, and absorbance changes, changes to, or potential complete loss of, birefringence, and an overall loss of crystal structure and properties through disorder of the material. In some cases, the induced structural damage leads to material amorphization which causes substantial changes to material properties. In regard to the studied materials in this work, any of these induced optical effects will negatively affect performance of a corresponding AOTF device.

Radiation readiness testing of these materials involved irradiating samples with fluences equivalent to multiple years of space environment exposure (accelerated lifetime testing) and measuring induced changes as a function of delivered fluence. The present work focused on measuring transmittance and reflectance changes at optical wavelengths (425 - 700 nm) based on the transparency of the materials in this range and the intended imaging use in an AOTF. These measurements also produced the ability to perform an approximate calculation

of absorbance. To gain insight into structural changes of the damaged crystal lattice, Raman spectroscopy was also completed on all irradiated samples. As measurements were taken as a function of fluence, calculations of material lifetimes, dependent on failure metrics, and calculations of expected changes in a defined time frame were able to be completed. These calculations hinge on knowledge of the radiation environment in which the device will operate. This is generally well known for the space environment, and for damage calculations presented in this work, the sole source of radiation was assumed to be the solar wind. Given the low flux of the solar wind (3×10^8 particles/cm^2/s) in comparison to values used in experiment ($\sim 10^{13}$ particles/cm^2/s), and the potential temperature difference experienced in the space environment (depending on implemented thermal control), the expectation is for retained damage to be slightly higher in the space environment than values reported here at equivalent fluences. This makes presented lifetime values an upper limit and expected changes over a given time period a lower limit. However, the difference in retained damage is not expected to be large; likely less than one order of magnitude difference. Also, given the non-obvious effect of differences in flux, it is possible for damage in space to be lower, but again, would not be expected to be substantially lower. The presented calculations can be used as approximate benchmarks for material assessment, and the experimental setup and procedure presented can be used again for future qualification of other materials.

7.1 Summary of Work

In order to perform radiation damage testing, a radiation delivery system was developed. From the dominance of the solar wind in the space environment and its corresponding properties, a hydrogen ion beamline with 10 keV maximum energy was chosen to perform sample irradiation. This energy range also creates a surface damage layer, which makes characterizations such as Raman more easily accessible and interpreted. As the beamline does not contain mass selection, the beam will contain H^+, H_2^+ and H_3^+ in varying composition depending on source operating pressure. At the chosen operational pressure of 1 mTorr, the beam composition will be approximately 30%/55%/15% respectively. This varied composition is beneficial, and actually preferred over a pure proton beam, for the present application. Upon impact with the sample surface, the H_2^+ and H_3^+ ions will separate into 2 and 3 protons with

average energies of 5 keV and 3.3 keV of beam energy respectively. This provides an increase to proton fluence delivered for a given beam current and also creates a range of radiation energies that is more closely related to the energy range observed in the space environment.

Based on the beamline design, specifically the ion optics and adjustable voltages, the system is capable of providing a range of beam energies and sizes. It is also able to create a range of beam currents and beam current densities based on gas pressure and filament temperature control in the plasma source. A summary of beamline performance ranges is given in Table 7.1. In some cases, true range limits were not investigated as characterization was primarily completed for the 10 keV research application beamline. Testing of other beamline energies, sizes and currents not used in the primary research was limited to a minimal number required to show operational variability and stability within reasonable ranges. The beamline was also designed to permit creation of helium plasma and a helium ion beamline. Results for a single helium beamline were investigated and presented to show that it is possible to obtain without system modification. From theoretical considerations and simulations, it is believed that the system could also be used for other beamline ion species with minimal modifications. While this feature, including the helium beam, was not actively used, the existence of the helium beam is a testament to system design success.

For sample irradiation, the beamline voltages (V_{pl}, V_{Einzel}) were set to a constant value of (10, -7.5) kV to produce a slightly asymmetric 1.4 - 1.6 cm diameter beam. The measured beam spot showed a slight skew to the upper left quadrant as viewed in the laboratory reference frame. This asymmetry was likely caused by mechanical misalignments in the system, some of which were corrected and others mitigated as discussed in Chapter 5. Even with this asymmetry, the beam profile was suitable for delivering an approximate uniform irradiation ($< 15\%$ variation from maximum value) across the 5×5 mm sample measurement area. Beam profile and beam current measurements led to calculations of average fluence values, and error ranges, delivered to the sample area.

Samples were irradiated in steps, beginning with the lowest fluence and working up to the highest. With the exception of silicon, all fluences were delivered to the same sample, with total accumulated fluence being the summation of all system runs. Material measurements were conducted as a function of fluence, with all measurements being completed at multi-

Parameter	Range	Controlled By
Beam Current	0.1 - 15* μA	Filament Temperature (PWM) and Pressure (MFC/Pumping)
Beam Size	0.35 - 5 cm^{2}** (0.8 - 2.5 cm Diameter)	Ion Optics (Applied Voltages)
Beam Current Density	0.02 - 43 μA/cm^2	Combination of previous two
Beam Energy	5 - 20 keV***	Plasma Source Bias

Table 7.1: Summary of beamline operational ranges and characteristics.
* Upper limit of beam current was not tested with increasing pressure beyond 2 mTorr. Reported value is largest observed in general operation as reported.
** Upper beam size limit was not fully characterized. Reported value is largest expected.
*** Beam energy range reported in text is 5 - 20 keV for operational reasons, however, technically the system can operate between 1 - 30 keV depending on application.

ple fluences. For silicon, only Raman measurements were conducted. For quartz, $LiNbO_3$ and TeO_2, both transmittance and reflectance measurements were completed as a function of wavelength (from 425 - 700 nm) at each fluence. This data allowed an approximate calculation, using assumptions for reflectance calculation scaling, of absorbance as function of wavelength. From here, transmittance, reflectance and absorbance were all examined as a function of fluence for select wavelengths spanning the visible spectrum (450 and 620 nm). The transmittance, reflectance and absorbance results were generally as expected, but the relationship between trends in all three materials led to some interesting potential connections. In order to gain insight into the induced structural damage, Raman spectroscopy measurments were also completed as a function of fluence. The Raman results produced interesting data sets and strongly suggested similarities and relationships between the induced damage in the three studied materials. All measurements were completed at a minimum of 10 discrete positions across the measured sample area and were averaged to produce a single value per fluence. This increased the measurement accuracy and helped calibrate out any potential variations in fluence delivered, or measured effects, across the measured area.

7.2 Results and Conclusions

The first major results, apart from those related to beamline design and characterization, came from irradiation of silicon. Given the vast knowledge base of charged particle damage in silicon from ion implantation studies, silicon was chosen as a benchmark for system performance as experimental results could be compared with known published values. It was found that, as a function of fluence, or damage, the peak height of the characteristic crystal silicon Raman peak at 520 cm^{-1} monotonically decreased with increasing fluence and, at high fluences, the growth of an amorphous peak at 480 cm^{-1} appeared and monotonically grew with increasing fluence. Other studies in the literature have reported this effect, but with higher mass incident charged particles. The possibility of amorphization with proton radiation is a debated topic in literature, however, the results presented in this work are quite convincing that it is possible. To clearly show the growth of this amorphous signal with respect to the background crystal signal, a plot of the peak height ratio, amorphous/crystal, was produced. The data shows strong evidence for proton irradiation induced partial amorphization of crystal silicon. To current knowledge, no such curve detailing this growth exists in the literature, making this result a meaningful contribution. In regard to the beamline system, the primary result of the silicon irradiation and Raman study was the observation of substantial change in the peak ratio around the 10^{16} protons/cm^2 mark. This provided approximate verification of induced damage and fluence calculations as the general rule of thumb for radiation damage is to expect a fluence of 10^{16} particles/cm^2 to create significant change in the material structure and measurable properties. Silicon was also used to produce a 2D imprint picture of the beamline to aid in verification of other profile measurements.

Following silicon was the study of irradiated crystalline quartz, which provided the first step into transparent and birefringent materials. The results of the transmittance, reflectance and absorbance measurements were more or less what were expected: transmittance decreased with increasing fluence and absorbance increased. This matched visual observations of the material becoming colored and darkened. Interestingly, at low fluences, around 10^{15} protons/cm^2, transmittance was actually observed to slightly increase across all measured wavelengths. However this effect did not last long and transmittance eventually started

to decrease as expected. The assumed cause of this effect was an initial creation of an anti-reflection layer or coating on the sample (a known application of ion implantation) that subsequently went away at higher damage thresholds. Another interesting result of these measurements was an almost linear-like slope to the transmittance and calculated absorbance data versus wavelength whose slope magnitudes both increased with increasing fluence. As a function of fluence, transmittance was observed to decrease faster at shorter wavelengths than at longer wavelengths which created a positively sloped transmittance versus wavelength curve. The opposite effect occurred for absorbance; absorbance increased faster at shorter wavelengths than at longer wavelengths as a function of fluence, which resulted in a negative absorbance versus wavelength slope. This absorbance result agrees with previously reported measurements of proton implanted quartz. In contrast to the substantial changes in value and shapes of transmittance and absorbance versus wavelength, the reflectance value changes were much smaller and less abrupt.

To complement the optical measurements, Raman spectroscopy was used to study irradiated quartz and potential atomic structure changes. From literature, it was found that proton irradiated quartz should exhibit the appearance of a new Raman feature, not present in the original crystal signal, centered at 1535 cm^{-1}, that should grow with increasing fluence. The source of this feature has been reported to be interstitial O_2 luminescence. The source of interstitial O_2 is radiation damage causing destruction of bonds leading to interstitial O atoms that move throughout the lattice to combine with other interstitial O atoms. Once bonded, the O_2 molecule is quite stable. This supports the growth of its signal within the lattice. The production of interstitial O atoms and resulting vacancies is well documented and are known as an E' centers. Upon Raman investigation, the signal, as described in literature, was observed and grew with increasing fluence as predicted. This provided further evidence to the conclusion of silicon that substantial damage to materials is being performed. Similar to its use in silicon, Raman data was used to create a peak ratio versus fluence plot of the new 1535 cm^{-1} feature to a characteristic crystal peak at 464 cm^{-1}. This plot clearly shows the growth of this Raman signal, and corresponding defect, relative to the crystal signal and structure. As was the case for the silicon peak ratio versus fluence plot, this type of plot appears to be absent in the current literature.

After the additional system verification provided by the quartz data, $LiNbO_3$ was the next material of investigation. Unlike quartz, published data on charged particle radiation damaged $LiNbO_3$ is scarce with Raman studies being non-existent. The same irradiation and measurements were completed and the general results of transmittance, reflectance and absorbance were mostly as expected with transmittance again decreasing and absorbance increasing as a function of fluence. In comparison to quartz, the transmittance values reached lower values at high fluence and absorbance increased proportionally. This matched visual data of $LiNbO_3$ being darker than quartz. Neglecting the initial increase in transmittance in quartz at low fluences, the $LiNbO_3$ data is very similar to quartz except that changes require more fluence to be observed. This suggests that $LiNbO_3$ is more resistant to proton radiation induced changes. Interestingly, the linear-like slope of transmittance and absorbance, which increased with fluence, was also observed in $LiNbO_3$ and appeared very similar to the trends in quartz. However, the reflectance versus wavelength results were quite different as they remained fairly constant in shape and simply decreased in magnitude. The similarities in the data led to speculation of similar damage types in $LiNbO_3$ and quartz, with the potential of interstitial oxygen being a common driving factor.

This idea was confirmed in the Raman data which showed the appearance and growth of a similar looking 1535 cm^{-1} feature with increasing fluence. The appearance of this feature required a larger fluence and its magnitude with respect to the crystal structure is diminished in comparison to that in quartz. This reinforces the idea of $LiNbO_3$ being more radiation resistant than quartz. The existence of the 1535 cm^{-1} feature, although with diminished strength, has led to the conclusion that interstitial oxygen also exists in proton irradiated $LiNbO_3$. As with quartz and silicon, a plot of Raman peak ratio versus fluence was created to show the peak growth against the background crystal signal to show clear evidence of its existence. Again, the absence of such a plot in literature makes this a very meaningful result.

The final material to be studied, TeO_2, was also irradiated and measured with the same techniques used for quartz and $LiNbO_3$. Again, the general trends matched visual observations of the material with transmittance decreasing as a function of fluence. The transmittance and absorbance shapes also matched the linear-like trends of quartz and $LiNbO_3$, which led to speculation of a third oxygen containing material developing related induced

damage and macroscopic effects. However, one major difference between TeO_2 and the other materials was the presence of visible features in the irradiated area whereas the other materials looked very uniform. An additional difference was the higher required fluence to induce change in comparison to the other materials, which suggests that TeO_2 is the most radiation resistant of all three investigated materials.

The Raman measurements of TeO_2 revealed very interesting results as the 1535 cm^{-1} signal was not immediately discovered except at a small magnitude in the highest delivered fluence spectrum. Upon further investigation, the irradiated TeO_2 was found to contain small features visible under the microscope (tens of microns in size) that when measured with the Raman instrument showed the expected 1535 cm^{-1} signal. This led to the theory that these features are in fact defect clusters that form due to high mobility of defects in TeO_2. This however opens up additional questions in regard to why these features did not appear in other samples and why outside of these features, where original Raman data was taken, there is no sign of this damage signal. As the goal of identifying the creation of radiation damage as a function of fluence and measurement of induced optical effects has been achieved and given that answers to these new questions will require significant work, it is left as future work.

With damage data as a function of fluence obtained, the final step was to calculate expected lifetimes of each material. Results of this analysis were reported in Tables 6.2 and 6.3. The high level result is that all three materials are quite resistant to change at low fluences (below 10^{14} protons/cm^2). However, this only represents an exposure time of the order of months, which majority of space missions will surpass. Once time frames begin to approach multiple years (10^{16} protons/cm^2), induced effects become much more substantial. Based on the present results, TeO_2 is the most radiation resistant of the three materials in that it takes the highest fluence to start showing substantial changes. However, once changes begin, it is one of the more fast changing materials.

The high level conclusion of this research in regard to space radiation qualification is that all studied materials are susceptible to induced charged particle damage, but at variable rates, with TeO_2 being the most resistant material. This is potentially due to high mobility rates of defects that can lead to high dynamic annealing effects. The effectiveness of this trait at lower fluxes such as those observed in space, has the potential to make TeO_2 a very suitable

space application material. However, results presented here indicate that it is inaccurate to say that TeO_2 is "radiation immune", as the current literature suggests, or in some cases, outright claims. Furthermore, based on the specific application, the induced error as a result of neglecting radiation damage will strongly vary and will be strongly dependent on mission length as it takes multiple years worth of exposure to reach substantial macroscopic material property changing levels. Therefore the suitability of any given material is dependent on the failure metric in terms of property and acceptable magnitude of change.

7.3 Specific Scientific Contributions

Instrument Paper: "Medium Energy Ion Beamline for Optical Material Radiation Testing" [84]

- The beamline designed for this work has the novel capability of providing a range of beam energies, beam currents, beam sizes and beam species, all controllable by user inputs. This is in contrast to other beamlines that are typically more narrowly focused to optimally provide a specific set of beam characteristics for a given application; a wide variety of potential beam characteristics is not a typical project goal. An additional, less common, feature is the use of a broad beam to produce an approximate uniform irradiated area. The more common practice is to scan a smaller beam across the sample area and 'paint' the irradiated area. This requires additional scanning instrumentation and high levels of positioning knowledge and precision. For these reasons, and to provide benchmark, comparison values for other projects, instrument details were compiled into a paper and submitted to Review of Scientific Instruments. It is currently under review.

Silicon Paper: "Production of Amorphous Silicon by Hydrogen Ion Implantation" [85]

- The Raman results found in the irradiated silicon samples were very interesting as they exhibited a clear growth of an amorphous signal with increasing fluence. While this is a known effect with heavy ion implantation, its presence in light ion implantation, specifically protons, is a debated topic with the general consensus being that it does not occur unless extremely high fluences or low temperatures are used. The data found here contradicts this general understanding. Furthermore, the plot of amorphous/crystal

peak ratio versus log(fluence) produces a very defined and well behaved trend, the likes of which has not been found in the literature to current knowledge. Apart from the addition of this data to the literature knowledge base, the result also has potential significant implications to understanding processes in implanted silicon, especially those involving proton irradiation. As silicon is such a widely used and important material, these results may prove very meaningful. Therefore a paper detailing these results has been submitted to AIP: Advances and is currently under review.

Raman Results Paper: "Characterization of Hydrogen Ion Implantation Damage in Quartz, Lithium Niobate and Tellurium Dioxide by Raman Spectroscopy" [86]

- Raman data obtained from the proton irradiated quartz was not new as the growth of the O_2 luminescence feature was already reported in literature. However, a specific plot of peak ratio (1535 cm^{-1}/crystal peak) versus fluence for this effect has been previously unreported. Based on the agreement between previous reported data and measurements obtained in this work, it was concluded that interstitial O_2 was created in the present quartz sample. The same statement cannot be made for $LiNbO_3$ and TeO_2 as measurements of these materials under proton irradiation is limited and in the case of Raman measurements is non-existent. Apart from simply providing this data, results showed high similarities between the three materials in the optical property trends as well as the appearance of the new 1535 cm^{-1} Raman signal in all materials, with TeO_2 showing a slight difference in the formation of defect features or pockets rather than widespread existence. These results and relationships are significant to understanding damage in these materials and, specifically for TeO_2, shows that it is not immune to radiation damage as some works have reported. A paper detailing the Raman results, specifically the creation of interstitial O_2 in $LiNbO_3$ and TeO_2 has been submitted to the Journal of Applied Physics and is currently under review.

Optical Property Results Paper: "Proton Radiation Induced Changes to Transmittance and Reflectance of Birefringent Crystal Materials" [87]

- While the general, high-level, trends of the transparent, crystalline materials changing color and suffering from radiation darkening is not in itself a new result, the specific

trends in the transmittance and reflectance data as functions of wavelength and fluence are important to space engineering applications. The data is specifically useful for instrumentation tolerance design, potential instrument calibrations to mitigate radiation effects and mission lifetime assessment. Furthermore, while the increased susceptibility of these optical characteristics in quartz at shorter versus longer wavelengths was already known or expected based on previously reported absorption data, the same effect in lithium niobate and tellurium dioxide is previously unreported to current knowledge. Based on the engineering applications and general addition to the current knowledge base, the optical effect data is currently being compiled into a more engineering applications focused paper for future submission.

7.4 Future Work

Given the range of work presented, the amount of potential future work is quite large and will strongly depend on the desired direction of future projects. This section highlights some of the more obvious future work paths that, if time had permitted, would have been pursued either to increase validity of results, verify results with complementary data, or narrow the area of focus to eliminate some assumptions made from other works and theory.

7.4.1 Beamline

Future work on the beamline is the largest body of future work as many modifications exist that could be improvements for specific applications. By the nature of the beamline it can also be used for multiple different types of study, not just radiation damage. Some highlights are presented here along with their significance to the present and related future work.

Use of the Helium Beamline to Damage Birefringent Materials

- As was demonstrated, the beamline can also operate with helium ions. Operation was tested and produced results very similar to hydrogen without requiring any system modifications. As mentioned, the second most dominant charged particle in the space environment is alpha particles (helium nuclei). In order to complete the solar wind charged particle damage picture (ignoring the small percentage of other components) the materials used here for proton radiation, silicon, quartz, $LiNbO_3$, and TeO_2, should also be examined under helium radiation. Comparison of these results to the proton

data will be of general application interest but will also carry a theoretical interest as the validity of known scaling rules can be assessed. The latter is of great importance as many assumptions in this work, radiation damage in general, and ion implantation models are based on the validity of both mass and energy scaling.

Additional Beamline Components and Improvements

- Indirectly Heated Cathode
  - Use of an indirectly heated cathode in the system is believed to increase system performance and stability. An indirectly heated cathode replaces the filament electron source with a larger piece of material capable of thermionic emission to supply electrons to the plasma source. This material is usually heated with a filament placed directly behind it. The advantage to this technique is that the electron emitting area is larger and more uniform, which should provide increased plasma stability. Heating rates should also be more stable as the emitting material is not directly pulsed. The heating filament design is very similar to that used here, but does not require biasing. Instead, the new material becomes the biased source. If nothing else, it would be interesting to compare the two source types and evaluate performance differences. The addition of this component would require minimal modification to the present state of the system.
- Mass Selection
  - Although mass selection was not specifically required for this project, many projects would benefit from a single particle type beamline and subsequent narrowing of the incident particle energy range. This would be required for any depth dependent studies. In theory, implementation of mass selection should only require an additional section in the system to perform mass selection and a potential second set of ion optics following the mass selector to manage beam size and compensate for additional travel length. Accurate implementation and the required system characterization and calibration would be a substantial amount of work.

- Other Beam Ion Species
  - Based on examination of ionization cross sections, corresponding creation calculations and beamline simulations, it is suggested that, with some voltage tuning, the system should be able to produce beamlines of other ion types such as argon and nitrogen. While this seems to good to be true in practice, calculations support this claim and it would be interesting to see resulting beamline profiles. A first step to this would be flowing other gas types into the system and testing plasma/beamline creation. If results are promising, the characterization process presented in this work can be completed on the beamline with existing measurement tools. If this works as predicted, it opens up many future research applications with minimal effort at the system development level.

7.4.2 Additional Damage Characterization

Similar to the beamline section, the number of different damage characterization techniques and paths available is quite large. Some of the more obvious measurements include:

- EPR/ESR - Electron Paramagnetic Resonance/Electron Spin Resonance
  - As this was the dominant technique used in the referenced research on radiation induced defects in quartz, running these measurements on irradiated quartz would provide additional verification of the assumed damage type from the Raman measurements. Furthermore, using this technique on $LiNbO_3$, and TeO_2 could provide information on the source of the observed 1535 cm^{-1} Raman feature along with any connections to the feature observed and previously reported in quartz.
- XRD - X-Ray Diffraction
  - This technique is reasonably standard when it comes to identifying specific atomic structures in materials and could be of use to complement other measurements.

7.4.3 Damage Layer Property Calculations

- As mentioned in the text, it should be possible to model the induced damage layer and corresponding material interfaces using Fresnel equations and known indices of

refraction to recreate experimental results and extract material properties of the damaged layer. Also as mentioned, this is a very involved problem as the layer boundaries will be undefined leading to blurring of properties throughout the damage layer, which is further complicated by the range of energies in the system. While not mentioned specifically in the text, a further complication comes from the birefringent nature of the materials and potential intermediate states observed in the damaged layer. This requires polarization information as well as crystal structure orientation and many other intricate details. However, all of these issues can be accounted for and the model is possible. If an accurate model was successfully created, it would provide significant insight into the damage process and resulting optical device consequences. Any spaceborne device that requires, or would benefit from, calibration of induced radiation effects would require a model such as this.

7.4.4 Polarization Sensitive Optical Measurements

- Given the birefringent nature of the materials of interest, an obvious experiment is to examine the birefringent properties of the damaged materials. As mentioned in the text, this was not completed as it was not required for the current work and required a substantial amount of work to accomplish, not to mention the requirement of higher precision equipment. However, if the time and equipment was available, it would be very interesting to examine changes to parallel and perpendicular reflectance and transmittance and potentially obtain information on the corresponding indices of refraction. This would also require precise knowledge of crystal orientation and at higher damage levels, may not be possible due to the unknown damage layer state.

7.4.5 The Dependence of Damage and Induced Effects on Flux and Temperature

- As mentioned throughout the text, it is well-known that different incident flux values and substrate temperatures have an effect on retained damage. However, as also mentioned, the specifics, especially for flux, are not always obvious. By implementing thermal measurement and control of the substrate, these effects could be investigated.

References

[1] H. L. Olesen, "Electronic System Design Techniques," in *Radiation Effects on Electronic Systems*. New York: Plenum Press. 1966.

[2] C. A. Bruch, W. E. McHugh, and R. W. Hockenbury, "Variations in Radiation Damage to Metals," *JOM* vol. 8, no. 10, pp. 1362-1372. 1956.

[3] M. T. Shetter, and V. J. Abreu, "Radiation Effects on the Transmission of Various Optical Glasses and Epoxies," *Applied Optics* vol. 18, no. 8, pp. 1132-1133. 1979.

[4] B. J. Elash, A. E. Bourassa, P. R. Loewen, N. D. Lloyd, and D. A. Degenstein, "The Aerosol Limb Imager: acousto-optic imaging of limb-scattered sunlight for stratospheric aerosol profiling," *Atmospheric Measurement Techniques* vol. 9, no. 3, pp. 1261-1277. 2016.

[5] I. C. Chang, "Tunable Acousto-Optic Filters: An Overview," *Optical Engineering* vol. 16, no.5, pp. 165455. 1977.

[6] N. Gupta, "Investigation of a mercurous chloride acousto-optic cell based on longitudinal acoustic mode," *Applied Optics* vol. 48, no. 7, pp. C151-C158. 2009.

[7] R. Schwenn, "Solar Wind: Global Properties," *Encyclopedia of Astronomy and Astrophysics*, (ed. P Muridin). Bristol: Institute of Physics and Macmillan Publishing. 2001.

[8] C. T. Russell, J. G. Luhmann, and R. J. Strangeway, *Space Physics: An Introduction*, Cambridge University Press. 2016.

[9] NASA Goddard Space Flight Center, *Cosmic Rays*, Accessed: April 20, 2019. Available at: https://imagine.gsfc.nasa.gov/science/toolbox/cosmic_rays1.html.

[10] A. H. Armstrong, F. B. Harrison, H. H. Heckman, and L. Rosen, "Charged Particles in the Inner Van Allen Radiation Belt," *Journal of Geophysical Research* vol. 66, no. 2, pp. 351-357. 1961.

[11] S. N. Vernov, E. V. Gorchakov, P. I. Shavrin, and K. N. Sharvina, "Radiation Belts in the Region of the South-Atlantic Magnetic Anomaly," *Space Science Reviews* vol. 7, no. 4, pp. 490-533. 1967.

[12] E. W. Taylor, J. E. Winter, A. D. Sanchez, and S. J. McKinney, "Proton-induced transient depolarization in gallium phosphide and tellurium dioxide Bragg cells," *Optical Engineering* vol. 36. 1997.

[13] E. W. Taylor, A. D. Sanchez, J. E. Winter, S. J. McKinney, A. H. Paxton, H. Schone, and D. P. Craig, "A Study of Radiation Induced Effects in Photonic Devices: Acousto Optic Modulators and Deflectors," Kirtland Air Force Base, NM: Air Force Research Laboratory. 1998.

[14] S. Trivedi, J. Rosemeier, F. Jin, S. Kutcher, R. Chen, and N. S. Prasard, "Space qualification issues in acousto optic tunable filer (AOTF) based spectrometers," *Solid State Lasers XV: Technology and Devices* vol. 6100, pp. 61001W. International Society for Optics and Photonics. 2006.

[15] N. S. Prasad, E. W. Taylor, S. Trivedi, S. Kutcher, and J. Soos, "Space qualification issues in acousto-optic and electro-optic devices," *Nanophotonics and Macrophotonics for Space Environments* vol. 6713, pp. 67130F. International Society for Optics and Photonics. 2007.

[16] R. Xu, Z. P. He, Z. H. Zhang, Z. Q. Fu, and J. Y. Wang, "The research on characteristics of acousto-optic tunable filter by space radiation experiment," in *International Symposium on Photoelectronic Detection and Imaging 2011: Space Exploration Technologies and Applications* vol. 8196, pp. 819627. International Society for Optics and Photonics. 2011.

[17] O. I. Korablev et al., "SPICAM IR acousto-optic spectrometer experiment on Mars Express," *Journal of Geophysical Research: Planets* vol. 111, no. E9. 2006.

[18] O. I. Korablev et al., "SPICAV IR acousto-optic spectrometer experiment on Venus Express," *Planetary and Space Science* vol. 65, no. 1, pp. 38-57. 2012.

[19] O. I. Korablev, D. A. Belyaev, Y. S. Dobrolenskiy, A. Y. Trokhimovskiy, and Y. K. Kalinnikov, "Acousto-optic tunable filter spectrometers in space missions," *Applied Optics* vol. 57, no. 10, pp. C103-C119. 2018.

[20] L. T. Chadderton, *Radiation Damage in Crystals*. London: Spottiswoode, Ballantyne & Co Ltd. 1965.

[21] P. D. Townsend, P. J. Chandler, and L. Zhang, *Optical Effects of Ion Implantation*, Cambridge University Press, Cambridge. 1994.

[22] E. Rutherford, "The scattering of α and β particles by matter and the structure of the atom," *The London, Edinburgh, and Dublin Philosophical Magazine and Journal of Science* vol. 21, no. 125, pp.669-688. 1911.

[23] J. W. Mayer, "Ion implantation in semiconductors," in *1973 International Electron Devices Meeting*, pp. 3-5, IEEE. 1973.

[24] W. Qin, A. K. Chauhan, and J. A. Szpunar, "Helium bubble nucleation at grain boundaries and its influence on intergranular fracture," *Philosophical Magazine* vol. 99, no. 6, pp. 679-698. 2019.

[25] S. Metzger, H. Henschel, O. Kohn, and W. Lennartz, "Radiation effects in ultraviolet sensitive SiC photodiodes," in *1999 Fifth European Conference on Radiation and Its Effects on Components and Systems. RADECS* 99, pp. 457-460. IEEE. 1999.

[26] G. Matthews, K. Priestley, P. Spence, D. Cooper, and D. Walikainen, "Compensation for spectral darkening of short wave optics occurring on the Cloud's and the Earth's Radiant Energy System," *Earth Observing Systems X*, vol. 5882, pp. 588212. *International Society for Optics and Photonics*. 2005.

[27] N. Bohr, "II. On the theory of the decrease of velocity of moving electrified particles on passing through matter," *The London, Edinburgh, and Dublin Philosophical Magazine and Journal of Science'* vol. 25, no. 145, pp. 10-31. 1913.

[28] H. Bethe, "Zur Theorie des Durchgangs schneller Korpuskularstahlen durch Materie," *Annalen der Physik* vol. 397, no.3, pp. 325-400. 1930.

[29] F. Bloch, "Bremsvermogen von Atomen mit mehreren Elektronen," *Zeitschrift fur Physik A Hadrons and Nuclei* vol. 81, no. 5, pp. 363-376. 1933.

[30] F. Bloch, "Zur Bremsung rasch bewegter Teilchen bein Durchgang durch Materie," *Annalen der Physik* vol. 408, no. 3, pp. 285-320. 1933.

[31] J. Lindhard, and M. Scharff, "Energy Loss in Matter by Fast Particles of Low Charge," *Matematisk-Fysiske Meddelelser Kongelige Danske Videnskabernes Selskab* vol. 27, no. 15, pp. 1-31. 1953.

[32] G. H. Kinchin, and R. S. Pease, "The Displacement of Atoms in Solids by Radiation," *Reports on progress in physics* vol. 18, no. 1, pp. 1. 1955.

[33] P. Sigmund, *Particle Penetration and Radiation Effects: General Aspects and Stopping of Swift Point Charges*, Springer Series in Solid-State Sciences 151, Springer. 2006.

[34] E. Fermi, "The Ionization Loss of Energy in Gases and in Condensed Materials," *Physical Review* vol. 57, no. 6, pp. 485-493. 1940.

[35] L. W. Nordheim, "Theory of Energy Losses of High Energy Particles," *Journal of the Franklin Institute* vol. 226, no. 5, pp. 575-597. 1938.

[36] J. Lindhard, M. Scharff, and H. E. Schiøtt, *Range Concepts and Heavy Ion Ranges,* Copenhagen: Munksgaard. 1963.

[37] NIST, *PSTAR and ASTAR Databases for Protons and Helium Ions.* Accessed: June 22, 2016. Available at: http://physics.nist.gov/PhysRefData/Star/Text/programs.html.

[38] P. L. Grande and G. Schiwietz, *CasP version 3.1.*
URL: www.hmi.de/people/schiwietz/casp.html. (No longer accessible). 2004.

[39] J. F. Ziegler, J. P. Biersack, and U. Littmark, *The Stopping and Range of Ions in Solids,* New York: Pergamon. 1985.

[40] J. F. Ziegler, M. D. Ziegler, J. P. Biersack, *SRIM*, Cadence Design Systems. 2008.

[41] J. F. Ziegler, M. D. Ziegler, J. P. Biersack, "SRIM - The Stopping and Range of Ions in Matter," *Nuclear Instruments and Methods in Physics Research Section B: Beam Interactions with Materials and Atoms* vol. 268, no. 11, pp. 1818-1823. 2010.

[42] H. H. Andersen and J. F. Ziegler, *Hydrogen Stopping Powers and Ranges in All Elements*, Vol. 2 of *The Stopping and Ranges of Ions in Matter*. Pergamon, New York. 1977.

[43] NASA Space Radiation Laboratory, "Bragg Curves and Peaks," Brookhaven National Laboratory. Accessed on April 21, 2019. Available at: https://www.bnl.gov/nsrl/userguide/bragg-curves-and-peaks.php

[44] J. W. Mayer, "Ion Implantation in Semiconductors," in *1973 International Electron Devices Meeting*, IEEE, pp. 3-5. 1973.

[45] L. Pelaz, and V. C. Venezia, H. -J. Gossmann, G. H. Glimer, A. T. Fiory, C. S. Rafferty, M. Jaraiz, and J. Barbolla, "Activation and Deactivation of Implanted B in Si," *Applied Physics Letters* vol. 75, no. 5, pp. 662-664. 1999.

[46] L. Pelaz, L. A. Marqués, and J. Barbolla, "Ion-beam-induced amorphization and recrystallization in silicon," *Journal of Applied Physics* vol. 96, no. 11 pp. 5947-5976. 2004.

[47] T. Motooka, F. Kobayashi, P. Fons, T. Tokuyama, T. Suzuki, and N. Natsuaki, "Amorphization Processes in Ion Implanted Si: Temperature Dependence," *Japanese Journal of Applied Physics* vol. 30, no. 12B, pp. 3617. 1991.

[48] T. Motooka, and O. W. Holland, "Amorphization processes in self-ion-implanted Si: Dose dependence," *Applied Physics Letters* vol. 58, no. 21 pp. 2360-2362. 1991.

[49] T. Motooka, and O. W. Holland, "Amorphization processes in ion implanted Si: Ion species effects," *Applied Physics Letters* vol. 61, no. 25 pp. 3005-3007. 1992.

[50] M. Nastasi, J. W. Mayer, and Y. Wang, *Ion Beam Analysis Fundamentals and Applications*, CRC Press, Taylor and Francis Group LLC. 2015.

[51] L. Spitzer, *Physics of Fully Ionized Gases*, Courier Corporation. 2006.

[52] Electron-Impact Cross Sections for Ionization and Excitation Database, (NIST Standard Reference Database 107). (https://dx.doi.org/10.18434/T4KK5C)

[53] I. G. Brown, *The Physics and Technology of Ion Sources*, 2nd ed., Wiley VCH, Weinheim. 2004.

[54] M. A. Lieberman and A. J. Lichtenberg, *Principles of Plasma Discharges and Materials Processing*, Second Edition. New Jersey: John Wiley & Sons, Inc. 2005.

[55] F. F. Chen, "Langmuir probe diagnostics," In *IEEE-ICOPS Meeting*, Jeju, Korea. 2003.

[56] S. Humphries, *Charged Particle Beams*, John Wiley and Sons. 1990.

[57] F. Paschen, "Ueber die zum Funkenübergang in Luft, Wasserstoff und Kohlensäure bei verschiedenen Drucken erforderliche Potentialdifferenz," *Annalen der Physik* vol. 273, no. 5, pp. 69-96. 1889.

[58] J. D. Cobine, *Gaseous Conductors*, Dover Publications, New York. 1958.

[59] H. Liebl, *Applied Charged Particle Optics*, Springer-Verlag Berlin Heidelberg. 2008.

[60] B. Chapman, *Glow Discharge Processes Sputtering and Plasma Etching*, Jon Wiley and Sons, Inc. New York. 1980.

[61] S. C. Brown, *Basic Data of Plasma Physics*, 2nd ed., MIT Press, Cambridge MA and Jon Wiley and Sons Inc. New York. 1966.

[62] C. F. Barnett, and P. M. Stier, "Charge Exchange Cross Sections for Helium Ions in Gases," *Physical Review* vol. 109, no. 2, pp. 385. 1958.

[63] Y. P. Raizer, *Gas Discharge Physics*, Springer, New York. 1997.

[64] V. V. Zhurin, *Industrial Ion Sources: Broadbeam Gridless Ion Source Technology,* John Wiley and Sons Inc. 2012.

[65] T. Kalvas, O. Tarvainen, T. Ropponen, O. Steczkiewicz, J. Ärje, and H. Clark, "IBSIMU: A three-dimensional simulation software for charged particle optics," *Review of Scientific Instruments* vol. 81, no. 2, pp. 02B703. 2010.

[66] T. Kalvas, "Development and Use of Computational Tools for Modelling Negative Hydrogen Ion Source Extraction Systems," Ph.D. Thesis, University of Jyvaskyla, Finland. 2013.

[67] J. E. Galvin, and I. G. Brown, "Ion Beam Profile Monitor," *Review of Scientific Instruments* vol. 55, no. 11, pp. 1866-1867. 1984.

[68] R. Karmouch, Y. Anahory, J-F. Mercure, D. Bouilly, M. Chicoine, G. Bentoumi, R. Leonelli, Y. Q. Wang, and F. Schiettekatte. "Damage Evolution in Low-Energy Ion Implanted Silicon," *Physical Review B* vol. 75, no. 7, pp. 075304. 2007.

[69] I. Mendez, F. J. Gordillo-Vazquez, V. J. Herrero, and I. Tanarro, "Atom and Ion Chemistry in Low Pressure Hydrogen DC Plasmas," *The Journal of Physical Chemistry A* vol. 110, no. 18, pp, 6060-6066. 2006.

[70] K. P. Jain, A. K. Shukla, R. Ashokan, S. C. Abbi, and M. Balkanski, "Raman Scattering from Ion-Implanted Silicon," *Physical Review B* vol. 32, no. 10 pp. 6688. 1985.

[71] Z. Iqbal, and S. Veprek, "Raman scattering from hydrogenated microcrystalline and amorphous silicon," *Journal of Physics C: Solid State Physics* vol. 15, no. 2, pp. 377. 1982.

[72] D. Ratnayake, M. D. Martin, U. R. Gowrishetty, D. A. Porter, T. A. Berfield, S. P. McNamara, and K. M. Walsh, "Engineering stress in thin films for the field of bistable MEMS," *Journal of Micromechanics and Microengineering* vol. 25, no. 12, pp. 125025. 2015.

[73] P. L. Swart, H. Aharoni, and B. M. Lacquet, "Optical reflectometry of radiation damage in ion-implanted silicon," *Nuclear Instruments and Methods in Physics Research Section B: Beam Interactions with Materials and Atoms* vol. 6, no. 1-2, pp. 365-371. 1985.

[74] V. I. Grafutin, A. G. Zaluzhnyi, S. P. Timoshenkov, O. M. Britkov, O. V. Ilyukhina, G. G. Myasishcheva, E. P. Prokop'ev, and Yu V. Funtikov, "Study of Radiation Damage in Quartz Single Crystals Irradiated with Protons," *Journal of Surface Investigation. X-ray, Synchrotron and Neutron Techniques* vol. 2, no. 4, pp. 518-526. 2008.

[75] D. L. Griscom, "Optical Properties and Structure of Defects in Silica Glass," *Journal of the Ceramic Society of Japan* vol. 99, no. 1154, pp. 923-942. 1991.

[76] R. Salh, "Defect Related Luminescence in Silicon Dioxide Network: A Review," Umea University, Sweden. pp. 135-172. 2011.

[77] H. Hosono, H. Kawazoe, and N. Matsunami, "Experimental Evidence for Frenkel Defect Formation in Amorphous SiO_2 by Electronic Excitation," *Physical Review Letters* vol. 80, no. 2, pp. 317. 1998

[78] R. L. Hines, and R. Arndt, "Radiation Effects of Bombardment of Quartz and Vitreous Silica by 7.5-kev to 59-kev Positive Ions," *Physical Review* vol. 119, no. 2, pp. 623. 1960.

[79] R. A. B. Devine, "Oxygen vacancy creation in SiO2 through ionization energy deposition," *Applied Physics Letters* vol. 43, no. 11, pp. 1056-1058. 1983.

[80] L. Skuja, and B. Güttler, "Detection of Interstitial Oxygen Molecules in Si O_2 Glass by a Direct Photoexcitation of the Infrared Luminescence of Singlet O_2," *Physical Review Letters* vol. 77, no. 10, pp. 2093. 1996.

[81] L. Skuja, B. Güttler, D. Schiel, and A. R. Silin, "Infrared Photoluminescence of Preexisting or Irradiation-Induced Interstitial Oxygen Molecules in glassy SiO_2 and α-Quartz," *Physical Review* B vol. 58, no. 21, pp. 14296. 1998.

[82] L. Skuja, B. Güttler, D. Schiel, and A. R. Silin, "Quantitative Analysis of the Concentration of Interstitial O_2 Molecules in SiO_2 Glass using Luminescence and Raman Spectrometry," *Journal of Applied Physics* vol. 83, no. 11, pp. 6106-6110. 1998.

[83] C. Yan, B. Liu, Xiangcao Li, C. Liu, Y. Li, and X. Ju. "Interstitial O_2 and Si-H Defects Produced in Fused Silica during Laser-Induced Damage," *Optical Materials Express* vol. 8, no. 9, pp. 2863-2869. 2018.

[84] B. J. Taylor, M. P. Bradley, and A. E. Bourassa, "Medium Energy Ion Beamline for Optical Material Radiation Testing," submitted to *Review of Scientific Instruments*. Under review. 2019.

[85] B. J. Taylor and M. P. Bradley, "Production of Amorphous Silicon by Hydrogen Ion Implantation," submitted to *AIP Advances*. Under review. 2019.

[86] B. J. Taylor and M. P. Bradley, "Characterization of Hydrogen Ion Implantation Damage in Quartz, Lithium Niobate and Tellurium Dioxide by Raman Spectroscopy," submitted to *Journal of Applied Physics*. Under review. 2019.

[87] B. J. Taylor, A. E. Bourassa, and M. P. Bradley, "Proton Radiation Induced Changes to Transmittance and Reflectance of Quartz, Lithium Niobate and Tellurium Dioxide," under development. 2019.

Appendix A

High Voltage Circuits and Instrumentation

The positive HV bias of the plasma source chambers requires it, and all electrically connected instrumentation or circuitry, to be isolated from lab ground. The main consequence of this electrical isolation is that no ground based instrumentation or power sources, other than the plasma source HV supply, can be connected to the HV components. For example, a Langmuir probe could not be implemented in the plasma source as it requires a ground based voltage sweep and data acquisition circuitry. Therefore, floating voltage sources, *i.e.* batteries and HV isolation techniques need to be employed to provide electrical systems that can be attached to the HV source as they are required to produce plasma in the source. While many books on plasma sources acknowledge that this must be done, very few, if any, provide details, primarily due to the vast number of ways these electronics can be implemented. The sections in this Appendix discuss all special circuits and techniques (primarily aided with battery sources) implemented in the current system.

A.1 Filament Bias Circuitry

The negative bias of the filament with respect to the plasma source is required to accelerate thermally emitted electrons from the filament toward the plasma electrode to create plasma. For the hydrogen plasma, the bias required is 80 V and for helium the required bias is 110 V. Given the difference in voltage, and that future work, such as the case of other types of plasma, may require other bias voltages, the filament bias must be adjustable. Adjustments cannot be performed during operation but instead need to be set prior to supplying the system HV. The circuit, shown in Figure A.1, is based on the MIC5205 adjustable DC voltage regulator integrated chip. The output voltage of the MIC5205 is controlled by values of the external resistors R1 and R2. Rather than implementing adjustable potentiometers for both resistors, only one resistor is adjustable and the other is set at a fixed resistance value. This provides voltage control via the potentiometer setting. The output voltage from the MIC5205 becomes the input to an EMCO DC/DC converter that provides a 50 times amplification step up to the input voltage. The EMCO converter is 'self powering' which means it draws power from the input voltage line. Power is supplied to the circuit and EMCO by a 6 V rechargeable lead acid battery. When under no external load from source operation, *i.e.*, sourcing the thermal emission electron current, the EMCO draws between 0.01 and 0.02 A of current from the battery. The final bias voltage output of the circuit is connected between the plasma source chamber and the negative leg of the filament. The bias voltage magnitude is given by Equation A.1 which shows that changing the resistor values changes the output voltage. The value of R1 was chosen to be fixed at 26.8 kΩ while the control potentiometer (R2) has a range of 0 - 50 kΩ. The measured output range of the circuit is 64 to 160 V. The capacitors included in the system have no effect on output voltage magnitude but instead exist to 'smooth' the output voltage signal.

$$V_{Bias} = 50 * \left[1.242\ V * \left(\frac{R2}{R1} + 1\right)\right] \tag{A.1}$$

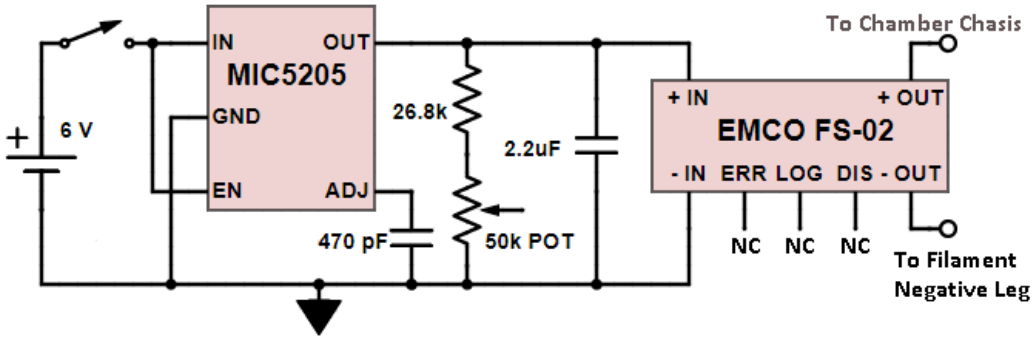

Figure A.1: HV filament bias control circuit. MIC5205 DC/DC converter steps down 6 V battery based on potentiometer setting to provide an adjustable input to the EMCO step up converter. EMCO proves 50 times amplification to input voltage. Current system output range: 64 - 160 V.

A.2 Filament Power Circuit

As the filament is biased negatively with respect to the HV plasma chamber, it also sits at a positive HV with respect to lab ground. This means the power source and any circuitry will become positively biased. The power source is a 12 V 80 AH $LiFePO_4$ rechargeable battery. Connecting this battery directly to the filament would supply the filament with constant power at 12 V and $12/R_{filament}$ A, assuming that the resistance of the filament negligibly changes with temperature. However, as mentioned in the main text, the design calls for filament power, and temperature, control. Therefore circuitry is required to make the average voltage and current delivered to the filament adjustable. This is achieved with a pulse width modulation (PWM) circuit. The idea of this circuit is to pulse the time and duration in which current flows to the filament to create time averaged 'DC' filament voltage and current values less than the 100% up time of a true DC connection. The pulsing time and duration are controllable by adjustable circuit elements such as potentiometers. In this configuration, the filament will experience some off time during which the temperature will decrease. Similar to the voltage and current, the filament will develop a time averaged temperature that will increase over operation time but should reach equilibrium relatively quickly. Unlike the voltage and current, the temperature in the off time will not instantaneously decrease to '0' (room temperature) as significant cooling time would be required. The idea for plasma operation is to pulse the filament at a sufficiently high frequency such that temperature will not significantly vary over one pulse cycle (once at equilibrium) and will emit electrons at an almost constant rate. This is possible as emission rate only depends on instantaneous temperature, not instantaneous current. As plasma results have shown no negative effects from pulsing, this technique is assumed to be working as intended.

The PWM circuit is built around an n-type power MOSFET (Vishay IRFZ44) that can turn the filament on an off depending on the gate voltage supplied by a controllable pulsed timing circuit. The problem for this circuit is active modification to the PWM timing. Ideally the timing, and filament power, is able to be modified by hand and throughout beamline operation. If the circuit were ground based, the timing circuit would be controlled by a manually adjustable potentiometer. Obviously, the HV biasing of this circuit does not allow such

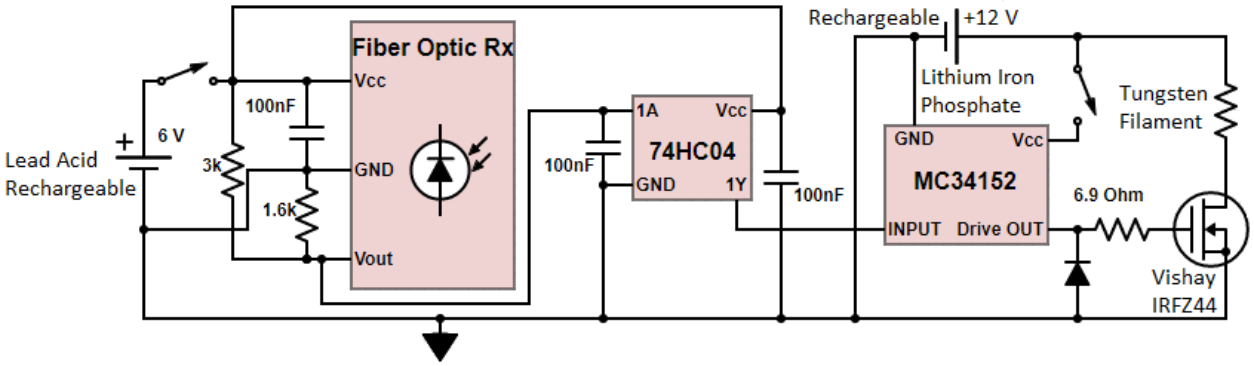

Figure A.2: HV PWM circuit complete with an optical receiver to convert the ground based timing pulses to electrical pulses to control the PWM MOSFET. In between receiver and MOSFET is an inverter to provide correct output logic and buffer the signal, as well as a MOSFET driver IC that ensures sufficient current to fully switch the MOSFET on and off.

a solution. This problem was fixed by breaking the circuit into two components, the timing control circuit, which is ground based, and the power modulation MOSFET circuit, which remains connected to the HV bias. The two circuits are linked together and communicate through a fiber optic line with a transmitter and receiver on each side. This creates HV isolation and allows human modification of the filament power throughout beamline operation. This in turn allows active monitoring and adjustment of beam current by the operator.

The circuit diagram for the high voltage portion of the filament power circuit is shown in Figure A.2. As can be seen, the optical receiver (Rx) is powered by yet another rechargeable 6 V lead acid battery. The receiver converts the light pulse to a 0 - 6 V signal that is sent to an n-type MOSFET Driver IC (MC34152). This chip is powered in parallel by the 12 V $LiFePO_4$ battery and converts the 0 - 6V signal to a 0 - 12 V signal with sufficient current to properly drive the power MOSFET. The power MOSFET is connected between the negative side of the filament and local ground (negative side of 12 V and 6 V batteries) such that the source is connected to the filament and the drain is connected to local ground. Inside this particular MOSFET chip is a protection diode between the source and drain that is not shown in the diagram.

As shown, both the 6 V battery to power the optical receiver and the 12 V battery to power the driver IC are turned on an off with physical switches. These switches are turned on by hand prior to the HV supply and system operation. Once operation is complete, first the HV supply is shut off, the system is grounded by attaching an isolated ground probe and then the circuit battery switches are turned off by hand. The ground probe is a long insulating rod connected to a ground strap that can be inserted into and connected to the plasma source. Once this rod is connected, everything becomes ground referenced and is safe to touch. The length of the rod ensures that the operator inserting the ground strap is a safe distance away from the HV potential components.

A.3 Ground Based Filament Power Control Circuit

The ground based component of the filament power system is the timing pulsing circuit and optical transmission that enables control of the filament power and temperature. The circuit is based on a standard astable configured 555 timer circuit with a potentiometer to change both the frequency and duty cycle of the output signal. Together these parameters influence the average power consumption of the filament as well as the average temperature by altering the duty cycle (heating and cooling times) and frequency of the filament. The 555 timer circuit is shown in Figure A.3. The astable frequency and duty cycle are given by Equations A.2 and A.3.

$$f = \frac{1.44}{(R_A + 2R_B)\,C} \tag{A.2}$$

$$D = \frac{R_A + R_B}{R_A + 2R_B} \tag{A.3}$$

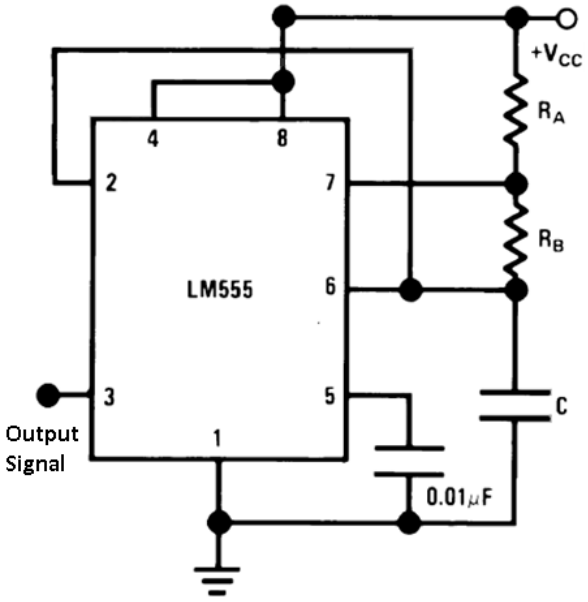

Figure A.3: Ground referenced 555 timer circuit that provides pulse control of the PWM hot deck circuit.

Component	Value
R_A	21.67 kΩ (22 kΩ rated)
R_B	Potentiometer: 0 - 44.4 kΩ (50 kΩ rated)
C	94.7 nF

Table A.1: 555 timer circuit component values.

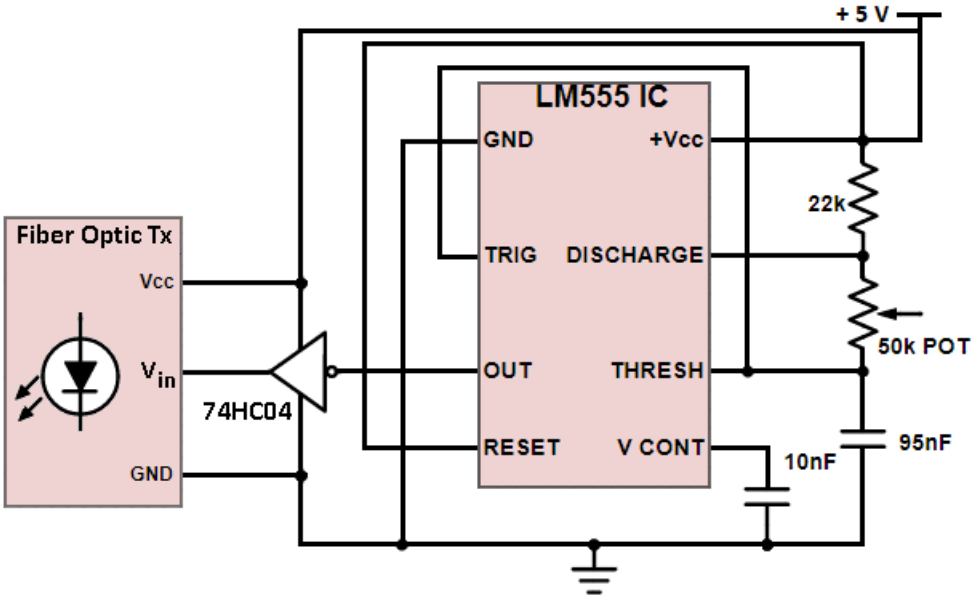

Figure A.4: Ground referenced timing and optical transmission circuit for filament power control. 555 timer is in astable operation mode. Inverter flips duty cycle to appropriate values and provides input buffering to the transmitter to provide an improved signal quality.

With the component values chosen as shown in Table A.1, the duty cycle has a range of 0.51 (maximum R_B) to 1 (minimum R_B (0)). However, from testing, when R_B is set to zero, the circuit output becomes unstable and does not achieve a duty cycle of 1. When implemented in the system to control the filament power, setting R_B to zero actually turns the filament off, further showcasing the unstable behaviour. Therefore the operational upper vale is approximately 0.98. Based on component values, the frequency should have a range of 137 - 700 Hz. The actual measured operational frequency range is 132 - 650 Hz which is in close agreement.

The remainder of the ground based filament power control circuit is then built onto the 555 timer circuit as shown in Figure A.4. As can be seen, the LM555 timer IC and the fiber optic transmitter (Tx) are both powered by a ground referenced 5 V DC supply. The inverter between the output of the LM 555 and the transmitter input is implemented for two reasons. First, it serves as an amplifying buffer for the input signal to the transmitter that helps provide a clean and more distinguished signal and second, it flips the duty cycle of the LM 555 from a range of 50 - 100 % to 1 - 50%, which more accurately matches the system power requirements. The fiber optic transmitter sends the pulse timing to the HV circuit that causes the filament to turn on and off at the timing set by the 555 timer allowing ground based filament control.